



# Evolution pétrologique et déformation des semelles métamorphiques des ophiolites : mécanismes d'accrétion et couplage à l'interface des plaques lors de l'initiation de la subduction

Mathieu Soret

## ► To cite this version:

Mathieu Soret. Evolution pétrologique et déformation des semelles métamorphiques des ophiolites : mécanismes d'accrétion et couplage à l'interface des plaques lors de l'initiation de la subduction. Tectonique. Université Pierre et Marie Curie - Paris VI, 2017. Français. NNT: 2017PA066605 . tel-01980512

HAL Id: tel-01980512

<https://theses.hal.science/tel-01980512>

Submitted on 14 Jan 2019

**HAL** is a multi-disciplinary open access archive for the deposit and dissemination of scientific research documents, whether they are published or not. The documents may come from teaching and research institutions in France or abroad, or from public or private research centers.

L'archive ouverte pluridisciplinaire **HAL**, est destinée au dépôt et à la diffusion de documents scientifiques de niveau recherche, publiés ou non, émanant des établissements d'enseignement et de recherche français ou étrangers, des laboratoires publics ou privés.

# Université Pierre et Marie Curie

ED 398 - Géosciences, Ressources Naturelles et Environnement

*Institut des Sciences de la Terre de Paris*

*Équipe Lithosphère, Structure et Déformation*

Pour l'obtention du grade de :

**DOCTEUR**

## Evolution pétrologique et déformation des semelles métamorphiques des ophiolites : mécanismes d'accrétion et couplage à l'interface des plaques lors de l'initiation de la subduction

Par **Mathieu SORET**

**Thèse de doctorat de Géosciences**

Dirigée par Philippe AGARD et Benoît DUBACQ

Soutenance prévue le 13 janvier 2017 devant le jury composé de :

Philippe AGARD	Professeur (ISTeP – UPMC)	Directeur de thèse
Benoît DUBACQ	Chargé de Recherche (ISTeP)	Co-directeur de thèse
Edwin GNOS	Professeur (NHM. Genève)	Rapporteur
Carl GUILMETTE	Professeur (Univ. Laval, Québec)	Rapporteur
Marco HERWEGH	Professeur (Univ. Bern)	Examinateur
Loïc LABROUSSE	Professeur (ISTeP)	Examinateur
Philippe YAMATO	Professeur (Univ. Rennes)	Invité



## Résumé

Les semelles métamorphiques sont des unités d'origine océanique ( $\leq 500$  m d'épaisseur) situées à la base des grandes ophiolites obductées ( $\leq 20$  km d'épaisseur). Ces unités sont caractérisées par un gradient métamorphique inverse, où les conditions de pression (P) et de température (T) de cristallisation augmentent de la base vers le contact avec l'ophiolite sus-jacente : depuis  $500 \pm 100$  °C et 0.5 ± 0.2 GPa jusqu'à  $800 \pm 100$  °C et 1.0 ± 0.2 GPa. Formées et exhumées au cours des 2 Ma suivant l'initiation des subductions océaniques, les semelles sont des témoins directs de leur dynamique précoce. Les assemblages minéralogiques qu'elles portent et leur déformation fournissent des contraintes majeures, et rares, sur l'évolution de la structure thermique et sur le comportement mécanique de l'interface de subduction naissante.

Au terme d'une étude pétrologique, (micro-)structurale et expérimentale sur les amphibolites naturelles de la semelle de Semail (Oman, UAE) et synthétisées en laboratoire, nous proposons un modèle où la semelle métamorphique résulte d'épisodes multiples d'accrétion d'unités homogènes en P-T (donc sans gradient métamorphique) au cours des premières étapes de subduction océanique. L'écaillage subséquent résulte de changements majeurs dans la distribution de la déformation, du fait des variations des propriétés mécaniques des roches à l'interface de subduction lors de son équilibration thermique et de l'augmentation au cours du temps de la proportion de sédiments entrant en subduction. Ce modèle rend compte d'une grande complexité thermique et mécanique à l'interface de subduction, encore insuffisamment examinée dans les études numériques actuelles.



## Abstract

Metamorphic soles are m to  $\sim$ 500 m thick tectonic slices welded beneath most large-scale ophiolites (usually  $\leq$  20 km thick). They typically show a steep inverted metamorphic structure where the pressure (P) and temperature (T) conditions of crystallization increase upward, from the base of the sole ( $500 \pm 100$  °C at  $0.5 \pm 0.2$  GPa) to the contact with the overlying peridotite ( $800 \pm 100$  °C at  $1.0 \pm 0.2$  GPa). Soles are interpreted as a result of heat transfer from the incipient mantle wedge toward the nascent slab during the first My of intra-oceanic subduction. Metamorphic soles are therefore direct witnesses of petrological processes during early subduction. Their mineralogical assemblage and deformation pattern provide major constraints on the evolution of the thermal structure, on the migration of fluids and on the effective rheology along the nascent slab interface.

We present a detailed petrological, (micro-)structural and experimental study, with refined P–T estimates obtained with pseudosection modelling and EBSD measurements, on the garnet-bearing and garnet-free (natural and synthetized) amphibolite. We suggest a new tectonic–petrological model for the formation of metamorphic soles below ophiolites, which involves the stacking of several homogeneous slivers (without any T gradient) of oceanic crust to form the present-day structure of the sole. These successive thrusts are the result of rheological contrasts between the slab material and the peridotites of the upper plate as the plate interface progressively cools. This model outlines the thermal and mechanical complexity of the early subduction dynamics, and highlights the need for more refined numerical modelling studies.



---

# Remerciements

Voilà c'est (presque) fini. Ces trois ans de thèse viennent conclure quasiment une décennie passée au sein de l'université Pierre et Marie Curie. À l'instar de cette dernière, j'ai changé, évolué (oserons dire mûri ?) en me construisant tour après tour, et cela, grâce aux très nombreuses personnes rencontrées, souvent devenues ami entier.

Tout d'abord, je tiens à remercier Philippe Agard et Pluto ("*ah non moi c'est Benoît Dubacq*") pour ces magnifiques années de recherche et d'aventures au tour du monde. Tout a commencé il y a 4 ans par une belle illumination alpine qui présageait déjà de l'avenir ; à savoir une ampoule (avec son abat jour) sur la semelle plantaire à vouloir suivre ce chamois de Philippe. Peu de temps après, je découvrais Benoît alors sans son bouc hau-tain mais déjà caractérisé par son non moins fameux naturel optimisme ; je cite : "*ces cailloux on n'y comprend vraiment rien*" (euphémisme quand tu nous tiens). Extrêmement complémentaires, ils m'ont permis d'avoir dès le départ toutes les cartes en main pour réaliser ces travaux de recherche, tout en acceptant (voire accompagnant) mes excentricités. Ils ont su me porter et me supporter tout au long de ces années. Merci d'avoir forgé en moi l'envie de fer de la recherche mon métier. J'espère continuer encore longtemps à travailler avec vous. En sus, diverge, plus que la recherche, la plus belle des aventures a certainement été l'aventure humaine. Merci Philippe, Benoît et belle-mamans de thèse, Aline et Barbara, pour tous ces précieux moments passés avec vous. Philippe, j'espère qu'un jour j'aurais l'occasion d'user de ta machine à laver, ce sera sûrement bon signe... Benoît, rendez-vous au prochain café !

Then, I would like to thank Greg Hirth and Keishi Okazaki for the wonderful time spent at Brown University deforming rocks and for their useful help ! J'aimerais remercier Benoît Ildefonse et Patrick Monié pour m'avoir si bien reçu à Montpellier et pour leur aide dans l'analyse micro-structurale et dans la datation des amphibolites de ma thèse et de mon master. Merci également à Alberto Vitale-Brovarone (malgré ses origines turinoises) pour son aide et ses précieux commentaires depuis le master (et merci pour cet excellent restaurant chinois que tu m'as fait découvrir).

Je tiens également à remercier Pink, à la fois acolyte à barbe rousse, joueur de tennis, grand mélomane (ré-écoutez Azis ou Tim Machin pour vous en convaincre), fan inconditionnel de la Fe-Mg carpholite et lanceur professionnel de phallus en carambar pendant mes TP/TD de L1 (à but pédagogique on vous l'assure...). Merci pour tous les grands moments passées ensemble, du labo à Turin en passant par Tanger, que de souvenirs ! Hâte de publier ce fameux papier Plunder & Soret (2045) ! Plus généralement, merci à cette belle clique de Rive Droite complètement improbable : Elsa, Val, Pauline, Anne Claire, Vincent.

Merci à Pipo et Cécile qui, avec Philippe, Benoît et Alexis, ont formé cette belle équipe omanaise chasseuse de semelles, de parata et de chicken tikka masala sous le son de Sugar Man. Merci également au Sultan Kaboos Kimoose ainsi qu'au chameau qui s'est essuyé sur la serviette d'Alexis. Cependant, on ne remerciera ni Philippe ni Benoît d'avoir honteusement triché aux parties endiablées de Uno. C'est moche.

Et puis, que seraient toutes ces années sans cette magnifique équipe LSD dans laquelle j'ai rencontré des gens véritablement formidables ! Tout d'abord, Guillaume le conquérant de lawsonite (qui existe autant que lui est normalien) et il bellissimo cuoco Micatelli ("*Pota ! Perbacco la ragazza !*"), merci pour toutes ses journées et soirées animées, pendant lesquelles on a bien ri, bu, mangé et parlé italien (parfois avec réussite). Merci aussi à vos deux appartements dans lesquels j'ai passé sûrement plus de temps que dans le mien ! Merci aux zippies Marija (and her love for beers) and Io (and her love for Macedonia but only as a salad) qui ont pu nous accompagner dans ces belles soirées. Merci à Léa, ma co-thésarde, avec qui j'ai toujours autant de plaisir de partager des discussions très distinguées, et qui m'aide à m'habiller ! Merci à la petite bande d'anciens avec qui j'ai tant d'excellents souvenirs, notamment lors des pauses cafés de 4h (l'heure ou la durée ?), la maman Anne-Céline et ses éclairs de génie, le futur politicien petit Nico, l'amoureuse de (/du ?) Latex Jordane, la colérique Félicie et la toujours joviale Maë. Merci à mes autres collègues de promo de master et de thèse, Erwann, Michael, Alex, Alexia, Marie, double Ben, Marianne, Aïda, Sylvain, Benjamin L., Tan, Virginie, Mathilde, Zineb, Alma, Leila, Manfred, Emily, Julien et Pauline, avec qui j'ai passé également de très bons moments. Merci enfin au primo homonymus Mathieu R. pour m'avoir introduit... dans la science lors de mon stage de L3 (dont les conclusions ont été réalisées au bar, forcément).

Merci au directeur de l'équipe, Claudio Rosenberg, et à sa secrétaire Bananiera Arrosaia. L'OSU a apprécié toutes ces riches discussions, notamment à l'arrière du bus rose. Merci à Anne Verlaguet, pour sa passion quotidiennement entraînante ainsi que pour ses déjeuners et goûters aromatisés. Merci au ténor Marc Fournier et à Loïc Labrousse pour sa vanne régulière ! Merci à l'équipe microsonde-MEB avec laquelle j'ai eu tant de plaisir à

travailler (gratuitement?) : Michel Fialin et ses envolés matinales, Omar Boudouma et ses récits marocains, et Nicolas Rividi et ses projets lucratifs (on fait 50/50?). Parce que sans eux, on ne ferait pas grand chose (déjà qu'on ne fait pas beaucoup) : un grand merci également à Sandrine Gay, Dovy Tristani et à Marie Jo Queyroy pour leur formidable travail administratif qui nous facilite bien la vie. Merci à Eric Deleris pour l'excellente préparation des lames minces, Marco Moroni pour ses magnifiques photographies et Marc Bruneaux sans qui on ne pourrait pas si bien travailler.

Je souhaite également remercier, et cela tout particulièrement, Farida Ait-Hamoudi pour sa patience et son aide précieuse apportée lors de mes premières années étudiantes à l'UPMC (même si elle lui est arrivée de vouloir me jeter par la fenêtre pour m'éviter de perdre la mention en Licence).

Quite last but not least, je tiens à remercier Sandra, Mélanie et Sybille, mes trois formidables mousquetaires (tout aussi bon vivant et caractériel que les historiques). Sans vous ma vie aurait été bien plus simple, enfin.. bien plus ennuyeuse ! Ensemble, continuons à chercher ma Constance Bonacier.

Enfin, je remercie mes parents, mon frère et ma soeur pour leur soutien indispensable tout au long de ces années d'étude. J'en profite pour remercier le personnel du Consulat Général de France à Tanger (particulièrement Saïd, Fatima Zohra et Rachida) et celui du Mirage pour leur participation à tous ces précieux moments de décompression que m'a offert le Maroc durant ces trois années de thèse.



---

# Table des matières

<b>Remerciements</b>	<b>vii</b>
<b>1 Initiation</b>	<b>1</b>
1.1 Subduction et initiation de subduction . . . . .	1
1.2 Les semelles métamorphiques : des enjeux pétrologique et mécanique majeurs	3
1.3 Structure de la thèse . . . . .	5
<b>2 Semelles, ophiolite, rhéologie : synthèse des connaissances</b>	<b>9</b>
2.1 Les ophiolites obductées : 200 ans de débats . . . . .	9
2.1.1 Brève revue historique . . . . .	9
2.1.2 Des modèles géodynamiques encore en débat . . . . .	15
2.2 Etat des connaissances sur les semelles métamorphiques . . . . .	23
2.2.1 Quelques exemples représentatifs de semelles métamorphiques . . . . .	23
2.2.2 L’Oman : la semelle métamorphique de référence ? . . . . .	29
2.2.3 Synthèse des caractéristiques des semelles métamorphiques mondiales . . . . .	38
2.3 Rhéologie des semelles métamorphiques . . . . .	46
2.3.1 Rhéologie des amphibolites . . . . .	46
2.3.2 Quelles contraintes pour la dynamique de subduction ? . . . . .	51
<b>3 Structure, pétrologie et accrétion de la semelle métamorphique d’Oman</b>	<b>57</b>
3.1 Préambule . . . . .	57
3.2 Abstract . . . . .	60
3.3 Introduction . . . . .	61
3.4 The ophiolite of Semail and the metamorphic sole . . . . .	62
3.4.1 The Semail peridotite . . . . .	62
3.4.2 The Semail metamorphic sole . . . . .	66
3.5 Methods and sample selection . . . . .	67
3.5.1 Electron microscopy . . . . .	68
3.5.2 Raman spectroscopy . . . . .	68

3.6	Field observations on the HT metamorphic sole . . . . .	70
3.6.1	Sumeini . . . . .	70
3.6.2	Khubakhib . . . . .	71
3.6.3	Wadi Tayin . . . . .	73
3.7	Petrography . . . . .	74
3.7.1	Sumeini . . . . .	74
3.7.2	Khubakhib . . . . .	77
3.7.3	Wadi Tayin . . . . .	79
3.8	Mineral composition . . . . .	79
3.8.1	Amphibole . . . . .	79
3.8.2	Garnet . . . . .	82
3.8.3	Clinopyroxene . . . . .	84
3.8.4	Feldspar and micas . . . . .	85
3.9	P-T Estimates . . . . .	85
3.9.1	Empirical geothermometry . . . . .	85
3.9.2	Thermodynamic modelling . . . . .	86
3.10	Discussion . . . . .	89
3.10.1	Stepwise structure of the HT metamorphic sole . . . . .	89
3.10.2	P-T estimates, P-T paths, along strike variations and implications	93
3.10.3	Accretion of metamorphic soles and mechanical coupling: extent and role of partial melting and links with the ophiolite . . . . .	96
3.11	Conclusion . . . . .	99
<b>4</b>	<b>Déformation des amphibolites en contexte d'initiation de subduction</b>	<b>105</b>
4.1	Préambule . . . . .	105
4.2	Introduction . . . . .	109
4.3	The Semail metamorphic sole . . . . .	111
4.4	Methods and sampling strategy . . . . .	112
4.5	Results . . . . .	115
4.5.1	Mineralogy . . . . .	115
4.5.2	Microstructures . . . . .	116
4.5.3	Crystallographic preferred orientation and misorientation . . . . .	120
4.5.4	Mineral composition mapping . . . . .	124
4.6	Discussion . . . . .	126
4.6.1	Deformation processes in amphibole . . . . .	126
4.6.2	Deformation processes in clinopyroxene . . . . .	129
4.6.3	Implications for metamorphic sole formation . . . . .	130
4.6.4	Implications for early subduction geodynamics . . . . .	132

---

4.7 Conclusion . . . . .	133
<b>5 Déformation expérimentale des amphibolites de haute température</b>	<b>137</b>
5.1 Introduction . . . . .	139
5.2 Experimental procedures . . . . .	140
5.3 Mechanical data . . . . .	142
5.4 Analytical methods . . . . .	144
5.5 Mineralogy and Microstructure . . . . .	145
5.5.1 Previous observations . . . . .	145
5.5.2 Amphibolite-mantle coupling simulation . . . . .	145
5.5.3 Garnet-bearing amphibolite . . . . .	150
5.6 Interpretation and discussion . . . . .	151
<b>6 Discussion générale</b>	<b>155</b>
6.1 Synthèse des résultats pétrologiques et structuraux . . . . .	155
6.1.1 Nouvelles structure et conditions P-T des semelles métamorphiques de haute température . . . . .	155
6.1.2 Mécanismes de déformation des amphibolites et couplage mécanique à l'interface des plaques . . . . .	158
6.2 Un modèle conceptuel d'évolution : accrétion et exhumation des semelles métamorphiques . . . . .	161
6.2.1 Accrétion de la semelle amphibolitique à grenat-clinopyroxène : première " <i>inversion rhéologique</i> " à l'interface de la subduction . . . . .	161
6.2.2 Accrétion de la semelle amphibolitique à plagioclase ± biotite : seconde " <i>inversion rhéologique</i> " à l'interface de subduction . . . . .	165
6.2.3 Accrétion de la semelle de faciès des schistes verts : troisième (et dernière ?) " <i>inversion rhéologique</i> " à l'interface de subduction . . . . .	166
6.2.4 Accrétion, amincissement et exhumation : une distribution ubiquiste sous l'ophiolite . . . . .	166
6.3 Implications pour la genèse des ophiolites . . . . .	170
6.4 Les implications pour la base de croûte continentale . . . . .	173
<b>7 Conclusion</b>	<b>177</b>
<b>Annexes</b>	<b>205</b>
7.1 Agard et al. (2016) : <i>Plate interface rheological switches during subduction infancy : Control on slab penetration and metamorphic sole formation</i> . . . . .	205
7.2 Soret et al. (2016) : <i>Strain localization and fluid infiltration in the mantle wedge during subduction initiation : Evidence from the base of the New Caledonia ophiolite</i> . . . . .	221



---

# Table des figures

1.1	Distribution des zones de subduction et d'accrétion océanique actuelles à l'échelle mondiale, d'après Stern (2002) . . . . .	1
1.2	Schéma évolutif d'une subduction océanique menant à l'obduction à grande échelle d'une ophiolite, comme en Oman ou en Turquie. . . . .	3
1.3	Formation de la semelle métamorphique au contact du coin de manteau encore jeune et chaud, impliquant un saut précoce de l'interface de subduction. Figure modifiée d'après Agard et al. (2016) (voir Annexes). . . . .	4
2.1	Extrait de la définition d'une ophiolite par Brongniart (1827) et représentation de la Trinité de Steinmann par Prof. E. den Tex (Coleman, 1977). . .	10
2.2	Représentation schématique de différents type d'obduction. . . . .	12
2.3	Géochimie isotopiques des laves V1 et V2 de l'ophiolite d'Oman. . . . .	14
2.4	Modèle de subduction intra-océanique à la ride, d'après Boudier et al. (1988). .	16
2.5	Modèle d'évolution magmatique de l'ophiolite de Mirdita (Albanie), d'après Dilek et al. (2008). . . . .	18
2.6	Modèle d'initiation sur une faille transformante, d'après Whattam & Stern (2011). . . . .	18
2.7	Modèle numérique de subduction intra-océanique initiée sur une faille transformante, d'après Duretz et al. (2016). . . . .	19
2.8	Modèle de subduction intra-océanique avec une initiation sur un détachement océanique, d'après Van Hinsbergen et al. (2015). . . . .	20
2.9	Modèle d'initiation à la transition océan-continent, d'après Hässig et al. (2016b). . . . .	22
2.10	Distribution des ophiolites et des semelles métamorphiques à l'échelle mondiale, d'après Dilek & Furnes (2011). . . . .	24
2.11	Carte géologique simplifiée de l'ophiolite d'Oman et de la semelle métamorphique associée (Gnos, 1992). . . . .	30
2.12	Log pétro-structurale représentatif de la semelle métamorphique à Sumeini en Oman (Searle & Malpas, 1982). . . . .	32

2.13	Compilation des compositions des amphiboles constituant la semelle métamorphique d’Oman. . . . .	34
2.14	Compilation des compositions des grenats et des clinopyroxènes de la semelle métamorphique d’Oman. . . . .	35
2.15	Compilation des conditions P–T de formation des amphibolites de la semelle métamorphique d’Oman. . . . .	36
2.16	Structure des semelles métamorphiques à l’échelle mondiale. . . . .	38
2.17	Distribution pression-température des semelles métamorphiques haute et basse températures à l’échelle mondiale. . . . .	39
2.18	Distribution temporelle des ophiolites (Dilek & Furnes, 2011), des plumes majeurs (Vaughan & Scarrow, 2003) et des semelles métamorphiques. . . . .	40
2.19	Modèles de formation des semelles métamorphiques et leur accrétion à la sus-jacente future ophiolite. . . . .	42
2.20	Vue schématique des principaux modèles rhéologiques de la lithosphère continentale. . . . .	47
2.21	Mise en évidence le fort adoucissement de la croûte inférieure gabbroïque en présence de bandes de cisaillement. . . . .	48
2.22	Diagramme de phase du plagioclase déterminé expérimentalement. . . . .	49
2.23	Contraintes différentielles en fonction de la température estimées par Getsinger et al. (2013). . . . .	50
2.24	Compilation des conditions P–T des semelles métamorphiques de haute et basse températures à l’échelle mondiale (cette étude). . . . .	52
2.25	Modèle schématique d’accrétion des semelles métamorphiques par un saut précoce l’interface (1 vers 2) de subduction intra-océanique. . . . .	53
2.26	Courbes de viscosité en fonction de la température pour différents matériaux à l’interface de subduction. . . . .	54
3.0	Geodynamic setting of metamorphic sole formation during intra-oceanic subduction infancy. . . . .	64
3.1	Schematic cross-sections of the three classical outcrops of metamorphic soles and its overlying mylonitic peridotites (in Sumeini, Khubakhib and Wadi Tayin) all along the Semail ophiolite. . . . .	65
3.2	Photographs of the base of the Semail ophiolite outcropping in the Sumeini region. . . . .	69
3.3	Representative structure of the base of the Semail ophiolite outcropping in the area of Khubakhib and Wadi Tayin. . . . .	72
3.3	Representative mineral assemblages in the garnet-clinopyroxene amphibolite (zone 2a) of the Sumeini metamorphic sole. . . . .	76

3.4	Representative mineral assemblages in the Semail metamorphic sole. . . . .	77
3.5	Composition of Ca-amphibole in selected samples from Khubakhib, Sumeini and Wadi Tayin. . . . .	80
3.6	Composition of garnet in selected samples from Khubakhib, Sumeini and Wadi Tayin. . . . .	81
3.7	Composition of clinopyroxene in selected samples from Khubakhib, Sumeini and Wadi Tayin. . . . .	82
3.8	Composition of feldspar, white mica and biotite in selected samples from Khubakhib, Sumeini and Wadi Tayin. . . . .	84
3.8	Estimated P-T conditions for the Semail metamorphic soles. . . . .	88
3.9	Simplified geological map of the Semail ophiolite with the position of the inferred ophiolitic ridge axis (black lines), after Nicolas et al. (2000). Compilations of P-T estimates and associated P-T paths calculated in this study for the metamorphic soles. . . . .	92
3.10	Two different <i>scenarii</i> proposed for the formation and exhumation of the HT metamorphic soles (and later the LT soles) and its present-day distribution beneath the ophiolite. . . . .	94
3.11	Evolutive model for metamorphic sole formation and structuration during the early subduction dynamics by stepwise accretion and exhumation of successive slices from the downgoing slab to the LT deformed base of the ophiolite. . . . .	95
4.1	Geodynamic setting of metamorphic sole formation during intra-oceanic subduction infancy. Simplified geological map of the Semail ophiolite. Compilations of P-T estimates and associated P-T paths (Soret et al., subm). Ti content vs. Si content showing the continuous decrease of T conditions during the exhumaiton of the metamorphic sole. Evolution of modal proportion in mafic rocks with PT conditions. . . . .	110
4.2	Maps of phases from a garnet-clinopyroxene bearing amphibolite. . . . .	114
4.3	Maps of phases from a garnet-clinopyroxene bearing amphibolite. . . . .	115
4.4	Micro-structure quantification of amphibole and clinopyroxene. . . . .	118
4.5	Photographs of microstructures in amphibole grains from amphibolite at different distance from the peridotites. . . . .	119
4.6	Pole figures illustrating crystal lattice orientation (CPO) of amphibole of the analyzed samples (one measurement per grain). . . . .	121
4.7	Pole figures illustrating crystal lattice orientation (CPO) of clinopyroxene of the analyzed samples (one measurement per grain). . . . .	122

4.8	Quantified fabric (using the J-index) of amphibole, clinopyroxene and plagioclase. . . . .	123
4.9	Compositional map of Ti and (2-10°) intracrystalline misorientation (to the mean) of amphibole. . . . .	125
4.10	Evolutive model of the deformation of the high temperature metamorphic sole of Oman, as a witness of the former slab crust during subduction infancy.	128
4.11	Pole figures illustrating crystal lattice orientation (CPO) of plagioclase of the analyzed samples (one measurement per grain). . . . .	134
5.1	Experimental conditions and sample descriptions. . . . .	141
5.2	Shear stress vs. shear strain curves for each experiments. . . . .	143
5.3	Backscattered electron emission image of a fine-grained experimental amphibolite from (Getsinger & Hirth, 2014) synthetized at hydrostatic conditions. Fabric (quantifying with the J-index) vs. total experiment strain. . .	144
5.4	Post experimental back-scattered images of finite microstructures in the two-layers samples W2006 and W2009 deformed during shear strain experiments. . . . .	146
5.5	EBSD maps of sample W2009 showing the quality of the indexation and pole figures of olivine and clinopyroxene. . . . .	147
5.6	Post experimental back-scattered images of finite microstructures in garnet-bearing amphibolite (W2013, W2016). . . . .	149
5.7	Photographs of the press Griggs apparatus during an experiment and the pieces forming the sample assembly. . . . .	153
6.1	Compilation des conditions P-T des semelles métamorphiques de haute et basse températures estimées au cours de cette étude. . . . .	157
6.2	Modèle de subduction intra-océanique avec une initiation sur un détachement proche d'une ride de type MOR, (Figure modifiée d'après Van Hinsbergen et al., 2015) . . . . .	160
6.3	Schéma en deux dimensions illustrant la déshydratation importante de la plaque plongeante peu de temps après l'initiation de la subduction. . . . .	163
6.4	Modèle évolutif de formation des semelles métamorphiques par les accrétions successives de différentes portions écaillées de la plaque pongeante issues de changements rhéologiques majeurs à l'interface des plaques dans un régime thermique en cours de ré-équilibration. . . . .	164

6.5	Carte géologique simplifiée de l'ophiolite de Semail (Oman, UAE) avec la position de sa ride et de sa semelle métamorphique sous-jacente ubiquiste. Compilation des conditions P–T estimées dans notre étude pour chaque écaille de semelle métamorphique dans les localités de Khubakhib, Sumeini et Wadi Tayin. Modèles évolutifs opposés de (dé)formation et d'exhumation des semelles métamorphiques expliquant leur distribution ubiquiste sous l'ophiolite. . . . .	168
6.6	Illustration du couplage mécanique et des déformation associées à l'interface croûte–manteau lors de l'initiation de la subduction. . . . .	169
6.7	Compilation d'âges obtenues par méthode $^{206}\text{Pb}/^{238}\text{U}$ sur zircons dans la croûte ophiolitique et dans la semelle métamorphique du complexe ophiolitique de Semail. . . . .	171
6.8	Illustrations de bande de cisaillement amphibolitique dans la base de croûte continentale, d'après Tatham et al. (2008) et Kenkmann & Dresen (2002). . . . .	173



---

# 1 Initiation

## 1.1 Subduction et initiation de subduction

Les zones de subduction sont des frontières de plaques convergentes le long desquelles une plaque plonge sous une autre. Introduit pour la première fois par Amstutz (1951), ce phénomène se traduit à la surface du globe par la présence d'environ 55 000 km de marges actives (Figure 1.1 ; Lallemand, 1999). Les zones de subduction sont la source majeure des activités sismogéniques et volcaniques sur Terre, et elles représentent un des principaux moteurs de la tectonique des plaques. À l'échelle des temps géologiques, elles contrôlent au premier ordre l'évolution profonde comme superficielle de la Terre. La compréhension du fonctionnement des zones de subduction est donc un enjeu majeur.

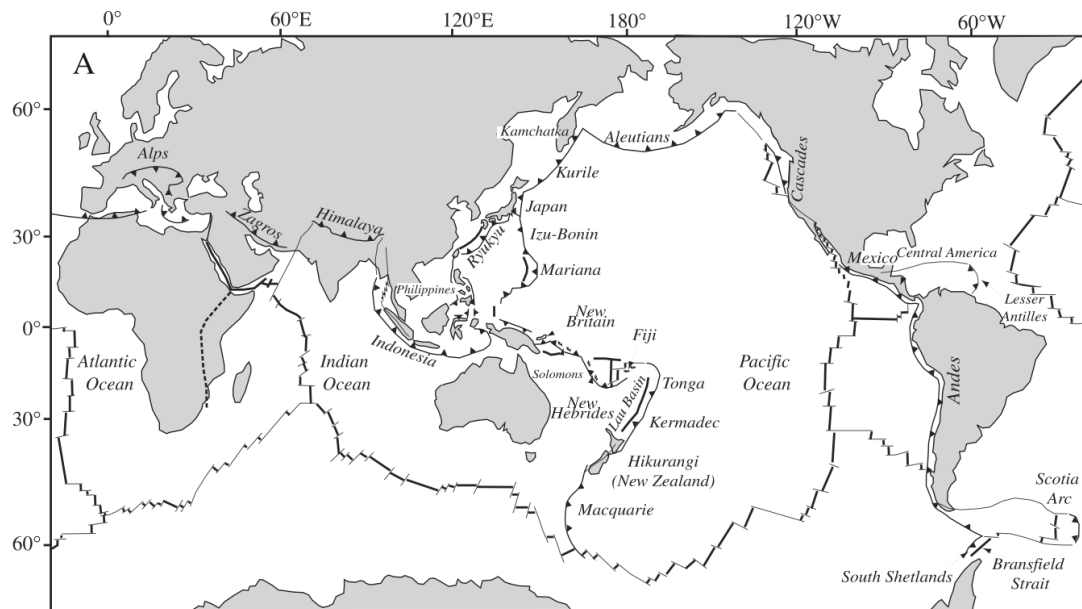


FIGURE 1.1 – Distribution des zones de subduction et d'accrétion océanique actuelles à l'échelle mondiale, d'après Stern (2002)

Les zones de subduction sont trop profondes pour être observées directement, au travers de forages par exemple. Elles peuvent être cependant imaginées à l'aide d'outils

---

géophysiques, mais à des résolutions spatiales encore bien insuffisantes pour analyser en détails les mécanismes à l'interface des plaques en zone de subduction.

Les zones de subduction peuvent également être examinées au travers des roches enfouies (parfois à grandes profondeurs) et exhumées le long de l'interface des plaques. La structure des unités de roches métamorphisées en zone de subduction sont des témoins directs, et donc d'importance majeure, de la dynamique des zones de subduction (états thermique et mécanique, transfert de matière). Couplées aux données géophysiques, ces roches sont des marqueurs clefs pour suivre et quantifier, par le biais de la modélisation numérique, les processus dans les zones de subduction.

Depuis le premier modèle numérique publié (par Minear & Toksöz, 1970), la plupart des travaux sur les zones de subduction portent sur la dynamique long terme (Gerya et al., 2002, Facenna & Becker, 2001, Peacock et al., 2005), notamment au travers des informations apportées par les roches de haute pression et basse température (HP-BT) (Burov & Yamato, 2008, Agard et al., 2009). Par contraste, l'initiation de la subduction est un phénomène relativement peu examiné, et de ce fait énigmatique. Dans la plupart des modèles numériques et analogiques, cette étape reste prédéfinie géométriquement par une zone de faiblesse (Faccenna et al., 1999), faute de contraintes thermo-mécaniques suffisantes (Gerya, 2011, Dymkova & Gerya, 2013). Les exemples actifs d'initiation de zone de subduction sont très limités voire absents. Bien que les subductions actives soient dans une grande proportion relativement jeunes (près de la moitié des zones de subduction actives ont été initiées au cours du Cénozoïque ; Gurnis et al., 2004), elles ne renseignent que sur des incréments déjà tardifs de la subduction.

Depuis l'avènement de la tectonique des plaques, deux grandes problématiques sont associées à l'initiation de la subduction (Dewey, 1976, Stern, 2004) :

- La naissance : où et comment les subductions se nucléent ? Quels sont les mécanismes à l'origine de leur activation (Gurnis et al., 2004) ?
- L'enfance : **comment les zones de subductions une fois nucléées se développent dans les premiers millions d'années le long d'une interface en cours de refroidissement jusqu'à atteindre l'état d'équilibre** (Hacker, 1991, Stern & Bloomer, 1992) ?

**Les seuls témoins de la dynamique précoce des zones de subduction ( $\leq 1$  à 2 Ma après l'initiation) sont les semelles métamorphiques.**

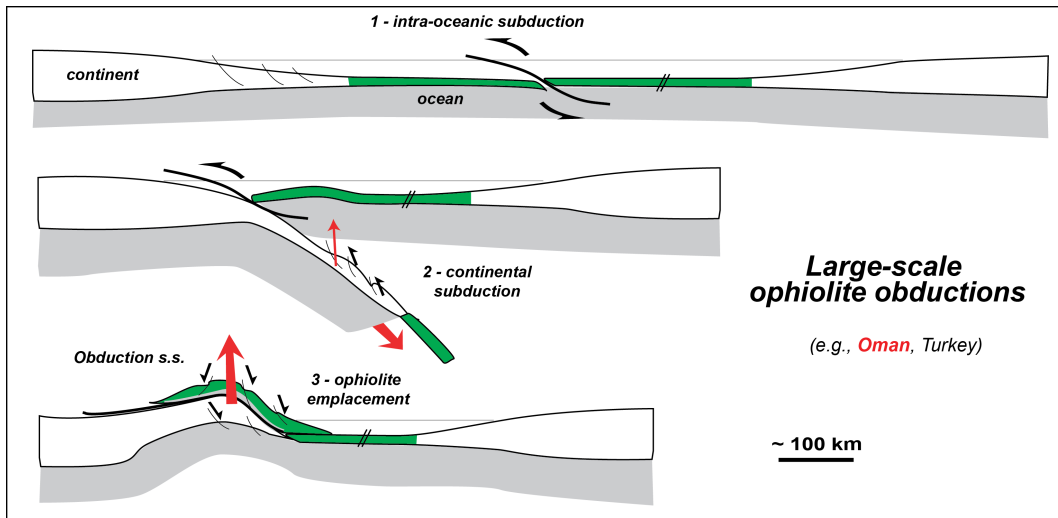


FIGURE 1.2 – Schéma évolutif d'une subduction océanique menant à l'obduction à grande échelle d'une ophiolite, comme en Oman ou en Turquie.

## 1.2 Les semelles métamorphiques : des enjeux pétrologique et mécanique majeurs

Les semelles métamorphiques sont des ensembles de roches métamorphiques d'affinité océanique (Dewey, 1976, Jamieson, 1986, Wakabayashi & Dilek, 2000), d'épaisseur généralement infra-kilométrique. Leur conditions P-T, réparties autour de  $700 \pm 300^\circ\text{C}$  et  $1.0 \pm 0.5 \text{ GPa}$ , ébauchent un gradient de haute température et moyenne pression (HT-MP). Ces roches sont ubiquistes à la base des larges fragments d'ophiolite obductée (comme en Oman où les conditions d'affleurement exceptionnelles favorisent leur étude ; Gnos, 1992).

Les ophiolites obductées sont des portions d'épaisseur pluri-kilométrique de lithosphère océanique charriées sur plusieurs centaines de kilomètres (Coleman, 1971, Nicolas, 1981). Elles sont observées le long des grandes paléo-sutures mondiales (Dilek & Furnes, 2011). Leur mise en place est généralement interprétée comme le résultat de l'initiation de subduction océanique menant à l'enfoncement de la partie distale de la marge continentale (comme indiqué par la présence sous-jacente de roches de haute pression ; Agard et al., 2007, 2009). L'obduction, *sensu stricto*, de la lithosphère océanique a lieu lors de l'exhumation de la lithosphère continentale, essentiellement par rebond isostatique lié au contraste de densité entre les deux lithosphères.

La base des ophiolites, directement en contact avec les semelles métamorphiques, présente une déformation très importante (Boudier et al., 1988), cohérente en terme de structure et de conditions P-T avec celle des semelles métamorphiques ( $700$  à  $1000^\circ\text{C}$  ; Linckens et al., 2011, Herwegh et al., 2016, Soret et al., 2016). L'épaisseur de ces péridotites

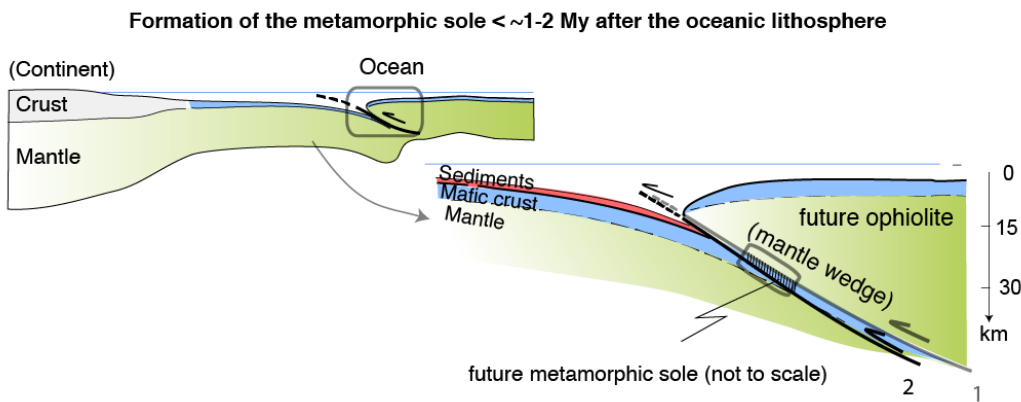


FIGURE 1.3 – Formation de la semelle métamorphique au contact du coin de manteau encore jeune et chaud, impliquant un saut précoce de l’interface de subduction. Figure modifiée d’après Agard et al. (2016) (voir Annexes).

déformées, dites rubanées, peut atteindre plusieurs centaines de mètres (comme en Oman ; Nicolas et al., 2000).

De par leur nature, leurs conditions P-T et leur étroite association structurale avec la base des ophiolites sus-jacentes, les semelles métamorphiques ont rapidement été interprétées comme des portions de lithosphère océanique (croûte + sédiment) d’abord subductées puis sous-plaquées et métamorphisées par d’importants transferts de chaleur au contact du manteau de la plaque supérieure (l’ophiolite) (Williams & Smyth, 1973, Dewey, 1976). Autrement dit, le contact péridotites–semelles métamorphiques est précoce dans l’histoire des subductions. Cette interprétation implique (Figure 1.2) 1 – l’existence d’au moins un saut de l’interface de subduction afin d’expliquer le sous-plaquage des semelles métamorphiques aux péridotites de la plaque supérieure et 2 – l’exhumation du complexe ophiolitique et de la semelle métamorphique se produit de manière conjointe et simultanée (Figure 1.3). Les âges attribués aux semelles métamorphiques (Hacker et al., 1996, Vergely et al., 1998, Parlak & Delaloye, 1999), proches des âges d’accrétion des ophiolites sus-jacentes ( $\leq 1-2$  Ma ; Rioux et al., 2012, 2013, 2016) sont en accord avec cette hypothèse. De plus, la faible dispersion des âges des semelles métamorphiques ( $\leq 1-2$  Ma) suggère que leur formation représente probablement un très bref épisode dans l’histoire de la subduction.

**La base des ophiolites obductées représente donc le témoin fossile d’interface de subduction naissante.**

**Cependant, la formation des semelles métamorphiques reste à ce jour fortement débattue :**

- Les estimations des conditions P-T-t des semelles métamorphiques sont encore associées à de grandes incertitudes ( $\pm 0.4$  GPa –  $\pm 300$  °C –  $\pm 2$  Ma), et peuvent fortement différer en fonction des méthodes thermo-barométriques utilisées.
- La structure et les modalités d'accrétion et d'exhumation sont encore incomprises et demandent à être mieux intégrées aux modèles d'initiation de subduction. La distribution spatiale ubiquiste des semelles métamorphiques et l'écart important entre leurs estimations de pression et les épaisseurs actuelles des ophiolites ( $\leq 15$ – $20$  km ; Lippard, 1986, Hacker & Gnos, 1997, Dilek & Furnes, 2009) ne sont notamment pas encore résolus.
- Le comportement rhéologique des roches des semelles métamorphiques reste méconnu, malgré les implications sur l'évolution mécanique précoce des zones de subduction.

**L'objectif de ce travail de thèse est donc de préciser les conditions thermiques et mécaniques de formation des semelles métamorphiques afin de clarifier :**

- l'évolution de la déformation et de la rhéologie à l'interface manteau–croûte de subduction jeune.
- les mécanismes d'accrétion et d'exhumation des roches à l'interface de subduction.
- l'environnement de genèse des subductions océaniques.

### 1.3 Structure de la thèse

La second chapitre de cette thèse présentera une revue des connaissances sur les semelles métamorphiques et sur le comportement mécanique des amphibolites.

- Dans un premier temps, nous aborderons de manière critique les modèles géodynamiques (numériques ou conceptuels) de formation des systèmes de subduction–obduction. Puis, nous présenterons une revue succincte des différentes semelles métamorphiques mondiales et des complexes ophiolitiques associés. Une description pétro-structurale plus détaillée sera effectuée sur la semelle métamorphique d'Oman. L'objectif final est de proposer une synthèse originale des semelles métamorphiques à l'échelle mondiale.
- Dans un second temps, nous présenterons un bilan des connaissances sur les lois rhéologiques des différents matériaux constituant la base des complexes ophioli-

---

tiques obductées (manteau, serpentinite, amphibolite, métasédiments). L'objectif est d'envisager les contraintes mécaniques qu'imposent l'accrétion des semelles dans la dynamique précoce des zones de subduction océanique.

Le troisième chapitre de cette thèse présentera le travail pétro-structural que j'ai réalisé sur la semelle métamorphique de l'ophiolite de Semail (Oman, UAE) le long de trois affleurements "classiques" : Khubakhib et Sumeini au nord et Wadi Tayin au sud de l'ophiolite. Une ré-interprétation structurale sera proposée et discutée, en lien avec la construction d'un nouveau modèle dynamique de formation des semelles métamorphiques.

Le quatrième chapitre de cette thèse abordera les mécanismes de déformation des amphibolites de la semelle métamorphique via la réalisation de cartographies d'orientation cristallographique réalisées à l'EBSD couplées à des cartographies chimiques réalisées à la microsonde. L'objectif est de préciser l'évolution et les mécanismes de mise en place des semelles métamorphiques à l'interface de subduction naissante.

Le cinquième chapitre présentera les premiers résultats issus des expériences analogiques effectuées sur presse à confinement solide Griggs avec pour enjeux : 1 – simuler le couplage mécanique entre des péridotites et des amphibolites à l'interface de subduction et 2 – examiner l'influence du grenat dans le comportement mécanique des amphibolites. L'objectif est de comparer ces résultats à la déformation des amphibolites de la semelle métamorphique. Le travail présenté ici est essentiellement exploratoire.

La sixième et dernière partie intègrera et discutera les résultats majeurs obtenus dans les différentes chapitres de ma thèse. L'objectif est de réaliser une synthèse afin d'élaborer un modèle générale de la formation des semelles métamorphiques permettant de préciser et de contraindre la dynamique précoce des zones de subductions océaniques. Nous finirons ce travail de thèse par la présentation d'une série de conclusion et de perspectives.

---

*N.B : une part non négligeable de mon temps de doctorat a été occupée à la publication de mes travaux de master, portant déjà sur des amphibolites déformées à haute température, cette fois situées dans la base des péridotites de l'ophiolite de Nouvelle-Calédonie. Cet article est présenté en annexes.*





---

## 2 Semelles, ophiolite, rhéologie : synthèse des connaissances

Nous présentons dans ce chapitre une synthèse originale sur les semelles métamorphiques à l'aide d'une compilation des connaissances à l'échelle mondiale et l'apport de données nouvelles sur :

1. les modèles géodynamiques actuellement proposés.
2. les caractéristiques intrinsèques et génériques des semelles métamorphiques.
3. le comportement mécanique des amphibolites.

### 2.1 Les ophiolites obductées : 200 ans de débats

#### 2.1.1 Brève revue historique

Avant de trouver un consensus en 1971 avec la conference de Penrose, le terme d'ophiolite a été employé dans l'histoire de manière très différente. La première utilisation connue remonte au règne de l'empereur Napoléon Bonaparte par Brongniart (1813) afin de décrire des roches (et non une unité) serpentineuses (Figure 2.1). Le nom d'ophiolite est dérivé de la racine grecque "*ophi*" signifiant *serpent*, en raison de l'apparence tachetée et brillante que peut avoir la serpentinite et comparable à l'aspect de certains de ces animaux répugnantes. Cette première définition a été par la suite utilisée pour décrire toute roche serpentinisée, que le protolith soit une péridotite, un basalte ou un mélange.

*Pour la petite histoire, 1813 n'est pas la meilleure des années pour Bonaparte. L'année suivante, il signe le traité de Fontainebleau et abdique sans condition. Il conserve cependant le titre impérial et acquiert la souveraineté de l'Île d'Elbe, choisie sans nul doute, seulement dis-je certain, en raison de ses affleurements ophiolitiques dont Moret (1951) rapporte la description.*

## 20. OPHIOLITE. (*Serpentin, Leozia.*)

Pâte de Serpentine ou de Talc et de Diallage, enveloppant du Fer oxidulé. — Structure massive, presque compacte.

(a)

Parties accessoires et accidentnelles. Mica (râtement), Felspath, Pétrosilex, Grenats, Quarz, Calcaire, Grammatite, Asbeste, Fer oxidulé, Pyrites.

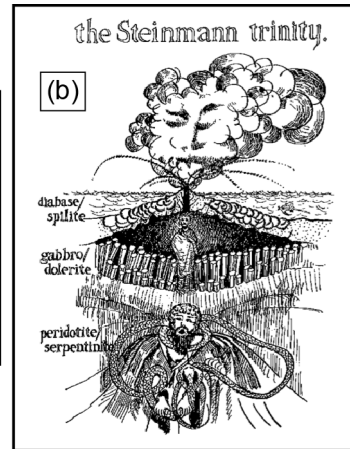


FIGURE 2.1 – (a) Extrait de la définition d'une ophiolite par Brongniart (1827) ;(b) Représentation de la Trinité de Steinmann par Prof. E. den Tex (Coleman, 1977).

### 1927 – Assemblage de roches ultrabasiques et basiques

Steinmann (1927) est le premier à employer le terme d'ophiolite comme un assemblage de roches ultrabasiques et basiques génétiquement et structuralement liées, issu d'une même évolution magmatique : la Trinité de Steinmann (Figure 2.1).

*"Le magma ultrabasique, le plus dense et le moins enrichi en volatiles, se solidifie en premier et forme les péridotites. Cette évolution se fait par séparation gravitaire, mais aussi par des processus de différentiation à la source afin d'expliquer que des dykes basiques — dont l'origine doit se trouver plus en profondeur — recoupent cette unité. La première unité basique, associant des gabbros et des dykes de pyroxénites, se solidifie ensuite au-dessus des péridotites. Les diabases représentent la dernière unité à cristalliser. Elle est recouverte à la surface par une couche de sédiment"*

Il est aussi le premier à associer ces complexes ophiolitiques aux sédiments pélagiques environnants, définissant ainsi un paléoenvironnement marin pour ces intrusions platoniques. Benson (1926) remarque que ces sédiments sont déformés. Il émet alors l'idée que les ophiolites se forment lors d'orogenèses.

Dans le même temps, en Amérique, Bowen (1927), en développant le concept de crystallisation fractionnée, rejette la théorie de Brongniart (1827) en démontrant qu'une intrusion magmatique périclitique demanderait des conditions de température trop élevées pour exister au sein de la croûte terrestre. Ainsi, il dissocie génétiquement, au contraire des européens, les roches ultrabasiques des roches basiques.

Hess (1938) propose alors que l'injection de magma périclitique ait lieu à plus basse température, en supposant une proportion en eau importante — de l'ordre de 5 à 15 %.

Dans cette hypothèse, la serpentisation des périclites représenterait le dernier stade de la cristallisation du magma. Cette hypothèse est compatible avec l'absence sur le terrain d'évidence d'auréole de haute température au contact de ces structures ophiolitiques. Cependant, Bowen & Tuttle (1949) rejettent une nouvelle fois cette idée en démontrant expérimentalement qu'un liquide ultrabasique contenant de l'eau ne pouvait exister à des températures inférieures à 1000 °C.

Ce n'est qu'au début des années 1960 que les ophiolites sont considérées comme des témoins d'une différenciation de magma basaltique (Brunn, 1960) dans les premiers stades de construction de géosynclinaux (Aubouin, 1965). Peu de temps après, Wyllie (1967) réalise pour la première fois une revue générale des publications mêlant 33 auteurs (américains et européens) afin d'établir une grande synthèse des connaissances sur les complexes ultrabasiques et des roches associées. Cette revue dissocie alors clairement les périclites de type "alpin" — comme celle d'Oman ou de Terre Neuve (Canada) — des autres complexes comme le Skaergaard, les nodules de périclites ou les kimberlites. De ce fait, l'idée européenne d'associer génétiquement les périclites avec les roches basiques dans les cortèges ophiolitiques alpins commence à faire consensus en Amérique. Malgré cela, alors que l'hypothèse d'une origine mantellique pour les ophiolites devient majoritaire, de nombreuses divergences persistent sur leurs mécanismes de mise en place.

## 1971 – Lithosphère océanique obductée

Avec l'avènement de la tectonique des plaques à la fin des années 1960 et la publication des premiers sondages géophysiques la lithosphère océanique médio-océanique, de nombreux auteurs reconnaissent rapidement l'origine et les processus de mise en place des ophiolites. Il est maintenant suggéré que ces complexes proviennent de fragments de lithosphère océanique — structuralement analogues aux ophiolites observées à terre, mis en place par de chevauchements sur la marge continentale. Le terme d'*obduction* — en opposition à la *subduction* — est pour la première fois employé par Coleman (1971) pour définir un tel mécanisme géodynamique. Le terme d'**ophiolite** définit, depuis la conférence de Penrose (1972), l'association de roches basiques et ultrabasiques représentant une portion de lithosphère océanique, complète ou non, métamorphique ou non, en position allochtone. Analogues à la lithosphère océanique présente en contexte océanique ou en bassin marginal et accessible uniquement par forage ou dragage en mer, les ophiolites obductées sont d'abord une opportunité unique d'étudier à terre les mécanismes de formation de la lithosphère océanique. Elles représentent également les seuls indices de croûte océanique plus âgés que 200 Ma.

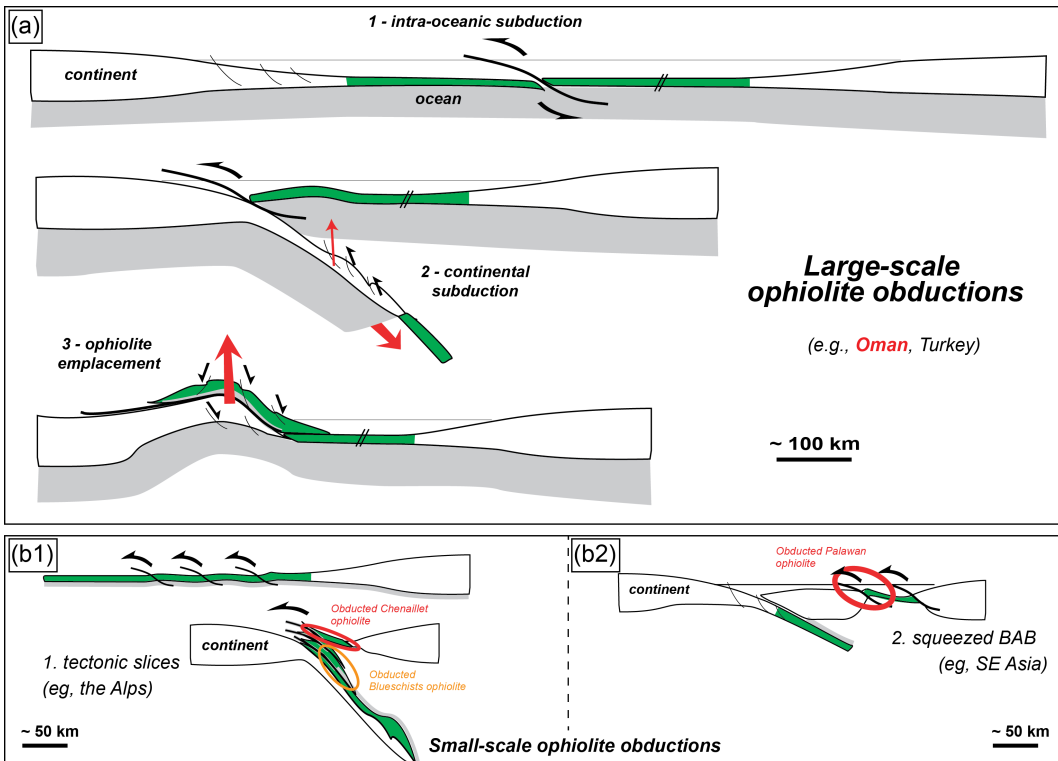


FIGURE 2.2 – Représentation schématique (a) d'une obduction à grande échelle d'une lithosphère médio-océanique comme celle de l'Oman, (b) d'une obduction à petite échelle d'une écaille de lithosphère océanique non métamorphique comme le Chenaillet ou métamorphique comme le Mont Viso, et (c) d'une obduction à petite échelle d'un bassin marginal comme au Palawan en Asie.

L'**obduction** est un phénomène géodynamique particulier caractérisé par la mise en place d'une ophiolite sur de la lithosphère continentale, pourtant moins dense et plus épaisse. Bien que leur mise en place soit mécaniquement contre-intuitive (la lithosphère océanique étant plus dense et plus rigide), les ophiolites obductées sont décrites à l'échelle mondiale (Coleman, 1971, Dilek & Furnes, 2011). Situées au niveau de limites de plaques actuelles et fossiles, elles ont été rapidement considérées comme des marqueurs d'anciennes ceintures orogéniques (Benson, 1926, Steinmann, 1927, Hess, 1955). Suivant leur nature et leur taille, trois grandes familles d'ophiolites obductées peuvent être différenciées (Figure 2.2) :

- 1. les ophiolites métamorphiques.** Ces fragments infrakilométriques, souvent très déformées, représentent une portion variable de la lithosphère océanique subductée, écaillées puis exhumées sur la marge continentale arrivée en subduction (e.g., Mont Viso, Erro Tobio (Alpes) ; Figure 2.2).
- 2. les ophiolites non métamorphiques infrakilométriques.** Peu ou pas déformées, elles résultent de la mise en place de petites écailles de lithosphère océanique (ap-

partenant à la plaque supérieure) sur la lithosphère continentale subductante (e.g. le massif du Chenaillet (Alpes) ; Figure 2.2).

**3. les ophiolites non métamorphiques d'échelle plurikilométrique** (e.g., Oman ; Nouvelle-Calédonie ; Terre Neuve ; Turquie). L'obduction de ces larges portions d'ophiolite résulte de l'initiation d'une subduction intra-océanique menant ensuite à la subduction de la partie distale de la marge continentale. L'obduction de la lithosphère océanique de la plaque supérieure (la future ophiolite) sur de la lithosphère continentale se fait lors de l'exhumation de celle-ci (Figure 2.2). L'obduction peut être alors considérée mécaniquement comme un phénomène passif. Il est essentiellement lié à l'évolution géodynamique d'un cas particulier de la subduction. **C'est à la base de ces ophiolites obductées que l'on peut observer la présence de semelles métamorphiques.** Seule cette famille d'ophiolite sera donc traitée ici.

Comme précisé en préambule de cette section, les larges ophiolites obductées, dites non métamorphiques, sont constituées d'une épaisse unité de roches ultra-basiques (i.e., ~ 15–20 km d'épaisseur comme en Oman ; Lippard, 1986) et d'une unité de roches basiques d'échelle kilométrique à pluri-kilométrique (i.e., 5-6 km à Terre Neuve (Canada) et en Oman , 10-12 km ; Girardeau & Nicolas, 1981, Ernewein et al., 1988), plus rarement conservée. Ces deux ensembles représentent respectivement les parties mantellique et crustale des cortèges ophiolitiques obductés. L'ensemble ultrabasique est constitué généralement de harzburgites dans lesquelles la foliation magmatique est localement observable. Les lherzolites n'ont été observées que très localement comme dans le massif de Tiebaghi (Prinzhofer et al., 1980, Ulrich et al., 2010), dans la "*ceinture ouest*" de l'ophiolite de Mirdita en Albanie (Pamić et al., 2002, Dilek et al., 2008) ou à la base de l'ophiolite omanaise (Godard et al., 2000, Yoshikawa et al., 2015).

Les harzburgites sont des roches très appauvries en éléments traces les plus incompatibles. Au premier ordre, elles sont généralement interprétées comme les résidus de fusion de la cristallisation de la croûte à partir de péridotites sources plus enrichies comme les lherzolites. En fonction du degré de fusion partielle, le manteau est plus ou moins appauvri. Ainsi, les lithosphères de type lherzolite (LOT) sont considérées comme des témoins d'accrétion océanique rapide (type Pacifique) alors que les lithosphères de type harzburgite (HOT) sont considérées comme des témoins d'accrétion lente (type Atlantique). Cependant, de nouvelles études démontrent que les lherzolites peuvent être également le résultat d'une refertilisation secondaire d'un manteau plus appauvri (Figure 2.3 ; Godard et al., 2006). Cette refertilisation peut avoir lieu soit en position de fore-arc via des transferts de fluides issus de la déshydratation du panneau plongeant (e.g. Ishikawa et al., 2005, Ulrich et al., 2010), soit par une remontée asthénosphérique locale (e.g. Takazawa et al., 2003).

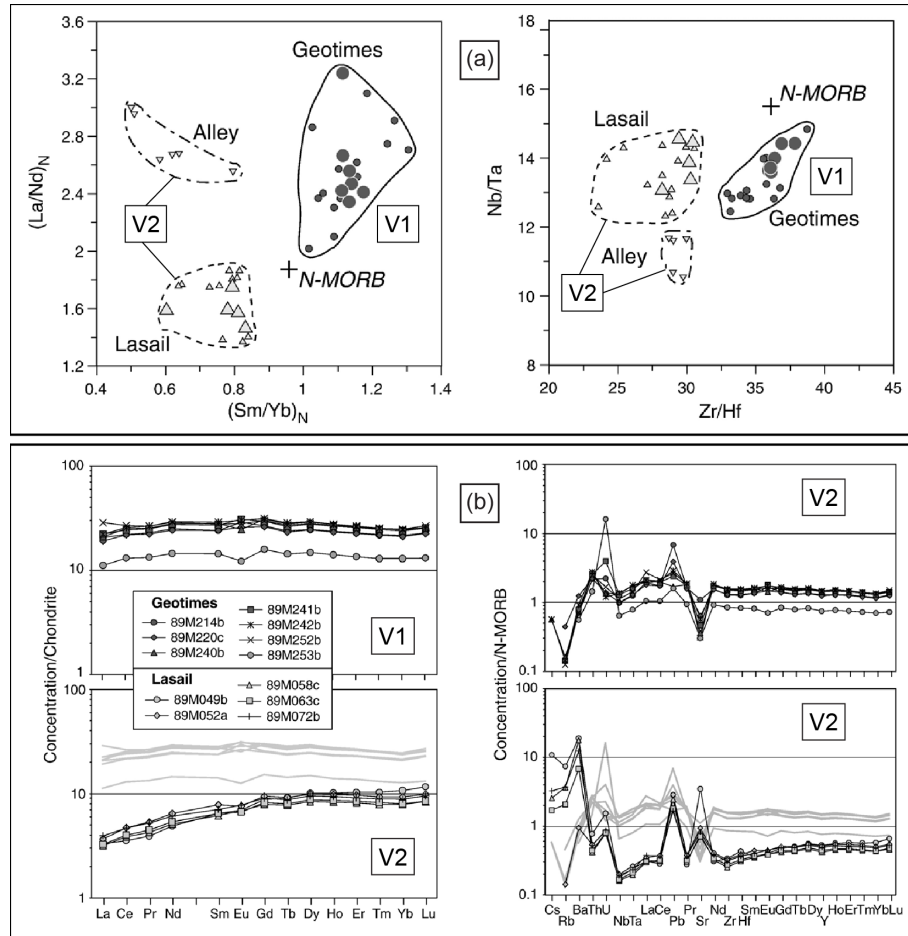


FIGURE 2.3 – Analyses (a) isotopiques et (b) élémentaires réalisées par Godard et al. (2006) sur la croûte de l'ophiolite d'Oman. Deux signatures magmatiques sont distinguées : V1 (dit aussi Geotimes) et V2. Les valeurs de normalisation proviennent de Sun & McDonough (1989).

La nature et la compositions géochimique de ces roches nous renseignent donc sur leurs conditions de formation.

Bien que souvent absente, la partie crustale des ophiolites, composée principalement de basaltes et de gabbros, présente l'intérêt d'être moins sujette aux processus d'hydronium supergène, d'être plus enrichie en éléments traces que les péridotites et d'être plus propice à la datation. Dans ces niveaux basiques, les données de géochimie élémentaire et isotopique montrent l'existence voire la co-existence (e.g., Oman ; Ernewein et al., 1988, Godard et al., 2006) de deux signatures distinctes. Présentes également dans les dykes basiques recoupant la partie mantellique des ophiolites (e.g., Nouvelle-Calédonie ; Soret et al., 2016), ces deux signatures sont (Figure 2.3) :

- une signature N-MORB ou BABB, compatible avec une accrétion médio-océanique ou en bassin marginal (e.g. magmatisme V1 en Oman ; Boudier et al., 1988)

- une signature E-MORB, IAB ou OIB marquée par un enrichissement en éléments traces les plus mobiles et les plus incompatibles par rapport aux basaltes de type MOR. (magmatisme V2 en Oman ; Ernewein et al., 1988)

La présence de cette deuxième signature est considérée par certains auteurs comme témoins d'une formation partielle (Ernewein et al., 1988, Beccaluva et al., 2004, Saccani & Photiades, 2004) ou totale (MacLeod et al., 2013, Marchesi et al., 2009, Arculus et al., 2015) de l'ophiolite en contexte de supra-subduction (ou SSZ pour supra-subduction zone Pearce et al., 1984, Pearce, 2003) lors des stades précoce de la subduction intra-océanique. La présence de ce néo-magmatisme enrichi en incompatibles est ainsi expliquée par des transferts de fluides de la plaque plongeante vers la lithosphère océanique de la plaque supérieure (de type MOR) et/ou par des remontées à la surface de manteau asténosphérique potentiellement engendrées par le retrait du slab (Stern & Bloomer, 1992, Stern, 2004, Whattam & Stern, 2011).

**La nature et les mécanismes de mise en place des larges ophiolites obductées demandent donc, comme l'initiation des zones de subduction, encore à être précisés.**

### 2.1.2 Des modèles géodynamiques encore en débat

Le choix des modèles de formation des ophiolites et d'initiation des subductions intra-océaniques (Stern, 2004) a un rôle fondamental sur la paramétrisation des conditions thermo-mécaniques initiales des modèles de subduction-obduction (Duretz et al., 2016). Les conditions HT-MP enregistrées par les semelles métamorphiques imposent un régime thermique de formation anormalement élevé, restreignant fortement l'environnement de nucléation de la subduction. La structure et la chimie des complexes ophiolitiques sont également des contraintes fortes dans l'initiation des zones de subduction.

#### Modèle d'initiation à la ride

Dans le cas de l'ophiolite d'Oman, l'axe de la paléo-ride océanique est subperpendiculaire à sa direction de propagation enregistrée par les bandes de cisaillement basse température ( $\leq 1000^{\circ}\text{C}$ ) situés à sa base (Boudier et al., 1988, Girardeau & Nicolas, 1981). Les premiers modèles de formation ont donc proposé une formation au niveau de la ride océanique avec un axe de subduction parallèle à celle-ci. Cette ride agit alors comme une zone mécaniquement faible permettant la nucléation de la subduction sous l'effet de la dynamique régionale compressive.

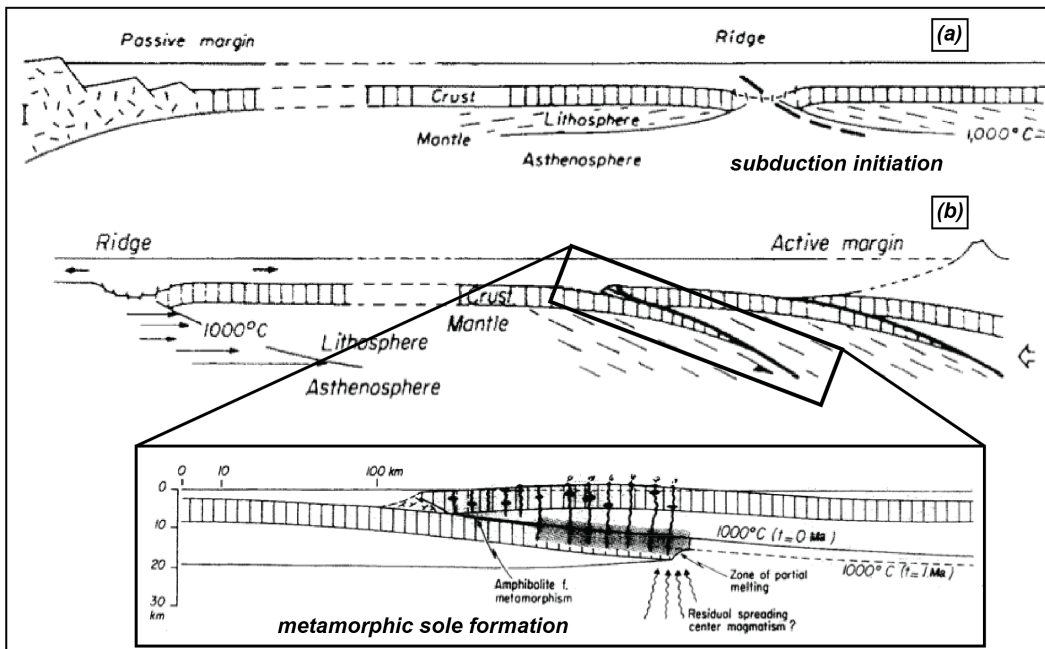


FIGURE 2.4 – Modèle de subduction intra-océanique avec : a) initiation à la ride ; b) formation de la semelle métamorphique par transfert de chaleur depuis le manteau de la plaque supérieure vers le panneau plongeant, d'après Boudier et al. (1988).

Ce modèle est privilégié par les auteurs favorisant la thèse d'une accrétion magmatique classique de la lithosphère océanique à la ride (Ceuleneer et al., 1988, Nicolas et al., 1988, Godard et al., 2006). La signature d'arc est alors expliquée par l'infiltration de fluides hydrothermaux à la ride (Boudier et al., 2000) ou par des interactions tardives entre l'ophiolite et des fluides silicatés produit par un fort degré de fusion partielle du manteau supérieur précédemment appauvri à la ride (Ernewein et al., 1988, Godard et al., 2006).

**Si cet environnement thermique, anormalement fort, répond aux critères de formation des semelles métamorphiques (Figure 2.4 ; Boudier et al., 1988). leurs modalités d'accrétion et d'exhumation ne sont pas discutées.** De plus, ces modèles d'initiation sont fortement remis en question du point de vue mécanique. Numériquement il est en effet très compliqué d'initier une subduction à la ride. Le fort régime thermique a tendance à d'avantage distribuer les contraintes qu'à les localiser, malgré les nombreux accidents tectoniques environnants.

### Modèle de formation en arrière d'une zone de subduction

La signature d'arc observée dans la plupart des ophiolites (e.g., Oman, Nouvelle-Calédonie, Mirdita (Albanie), Terre Neuve (Canada), Turquie Pearce et al., 1984, Pearce, 2003) est interprétée par de nombreux auteurs comme le résultat d'une forma-

tion partielle ou complète d'une nouvelle lithosphère océanique au-dessus d'une zone de subduction.

L'ophiolite de Mirdita présente latéralement et verticalement deux signatures géochimiques distinctes (Bébien et al., 1998, Beccaluva et al., 1994, Bortolotti et al., 2002, Dilek et al., 2008). À l'ouest, la partie crustale de l'ophiolite, d'une épaisseur de 3 à 4 km, est dominée par une signature d'affinité MOR alors qu'à l'est celle-ci, plus épaisse (10–12 km), présente une affinité essentiellement de SSZ. Ce contraste structural et géochimique est fonction de la distance au front de propagation. De plus, ces mêmes caractéristiques sont reportées dans l'ophiolite grecque de Pindos (Capedri et al., 1980, Dilek et al., 1990, 2007, Saccani & Photiades, 2004), qui se trouve dans la continuité latérale de l'ophiolite albanaise.

Dilek et al. (2008) proposent un modèle de formation polyphasée de l'ophiolite de Mirdita (Figure 2.5). Tout d'abord, une lithosphère océanique est accrétée au niveau d'une ride médio-océanique. Puis, l'initiation d'une zone de subduction intra-océanique occasionne le métasomatisme d'une partie de cette lithosphère océanique. D'affinité MOR, la lithosphère océanique sus-jacente à cette nouvelle subduction s'enrichit alors d'une signature d'arc via l'interaction avec des fluides aqueux et silicatés originaires de la plaque plongeante. Cette nouvelle étape de fusion partielle de la plaque supérieure, enrichit en éléments incompatibles, est ensuite accentuée par la remontée du manteau asthénosphérique et l'extension arrière-arc provoquée par le retrait de la plaque plongeante. Ce modèle permet donc la juxtaposition latérale et verticale de deux lithosphères océaniques d'affinité différente. La première lithosphère formée à la ride, et peu affectée par la subduction, forme la ceinture "ouest" du complexe de Mirdita lors de son obduction. La lithosphère formée en contexte d'arrière-arc formera la ceinture "est", caractérisée par une dominance SSZ.

En revanche, **ce modèle est difficilement compatible avec une formation de la semelle métamorphique** sub-synchrone à celle de l'ophiolite comme observé en Albanie (Vergely et al., 1998, Dimo-Lahitte et al., 2001). De plus, le modèle proposé par (Dilek et al., 2008) semble fortement incompatible avec une formation et surtout une exhumation des semelles métamorphiques conjointes avec les ophiolites sus-jacentes. Enfin, les semelles métamorphiques situées à la base des ceintures ophiolitiques "est" et "ouest" ne présentent pas de différences structurale, géochimique ou temporelle majeures (Gaggero et al., 2009).

### Modèle d'initiation sur une faille transformante

Afin de répondre à ce problème, un modèle d'initiation sur une zone de fracture d'échelle lithosphérique comme une faille transformante est proposé (Casey & Dewey, 1984,

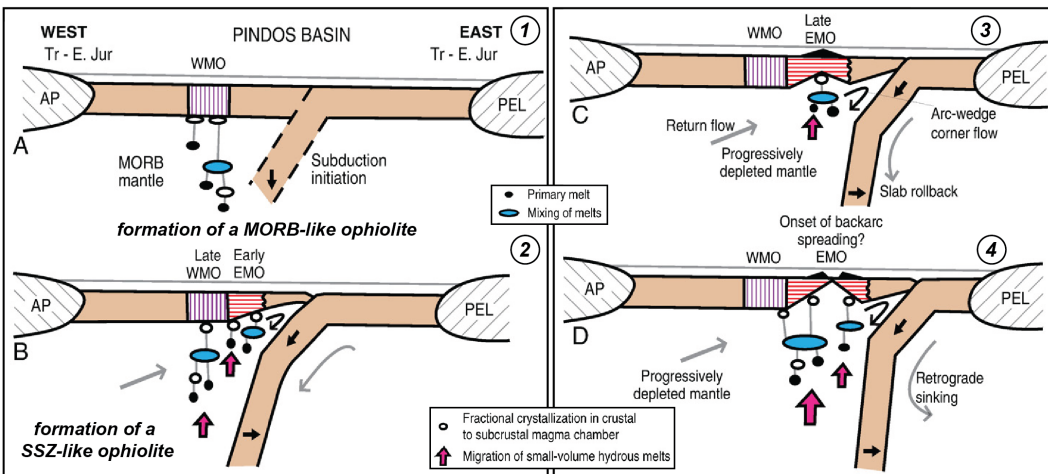


FIGURE 2.5 – Modèle d'évolution magmatique dans le temps et l'espace des ceintures "ouest" (d'affinité MOR) et "est" (d'affinité SSZ) du complexe ophiolitique de Mirdita (Albanie), d'après Dilek et al. (2008).

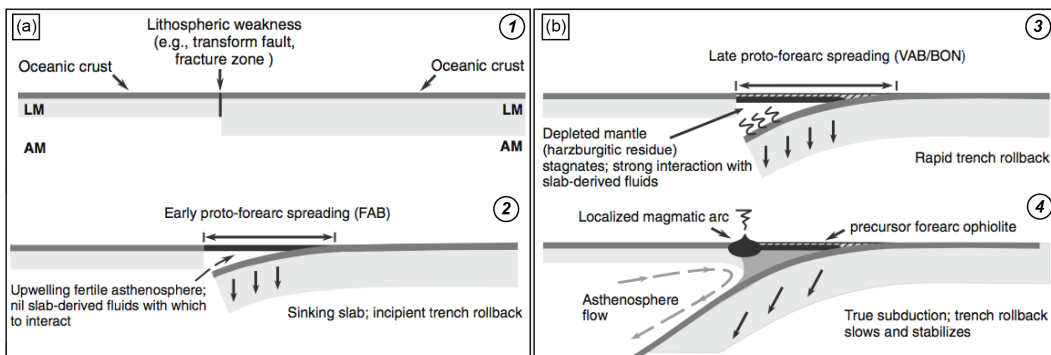


FIGURE 2.6 – Modèle de subduction intra-océanique impliquant : a) une initiation au niveau d'une zone de fracture (faille transformante) ; b) une accrétion magmatique de l'ophiolite en supra-subduction, d'après Whattam & Stern (2011).

Stern & Bloomer, 1992, Hall et al., 2003, Gurnis et al., 2004, Stern, 2004, Whattam & Stern, 2011). Ce modèle a été paramétré à partir des structures de déformation basse température observées à la base de nombreuses ophiolites obductées, qui montrent un sens de cisaillement parallèle à la présumée paléo-ride, et également à partir de la signature d'arc (SSZ) enregistrée par celles-ci et par certaines lithosphères océaniques actuelles comme Izu–Bonin–Mariana (Pearce et al., 1984, Pearce, 2003, Arculus et al., 2015).

Dans ce modèle (Figure 2.6), l'ophiolite est entièrement formée au niveau de la zone de fracture par remontée adiabatique du manteau asthénosphérique, provoquant sa fusion partielle. Dans les premières phases succédant à la nucléation de la subduction, les transferts de fluides entre la plaque plongeante et la plaque supérieure sont limités (Figure 2.6a). Ainsi, la nature de la naissante lithosphère présente est similaire à celle d'une lithosphère formée sur une ride médio-océanique. Dans un second temps (Figure 2.6b), les

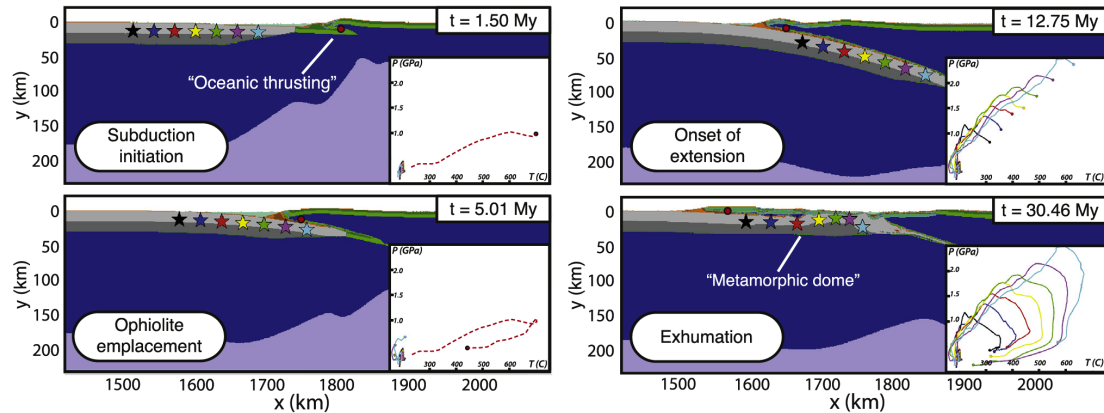


FIGURE 2.7 – Modèle thermique de subduction intra-océanique initiée sur une faille transformante avec la formation puis l'exhumation de l'ophiolite et de la semelle métamorphique sous-jacente, d'après Duretz et al. (2016).

interactions entre les deux plaques s'accentuent. Les fluides libérés par la plaque plongeante provoquent la fusion partielle du manteau lithosphérique préalablement appauvri. Le retrait continu de la plaque plongeante entretient l'extension arrière-arc et l'accrétion de cette nouvelle lithosphère océanique dont la composition évolue vers une signature de SSZ.

Si ce modèle, avec une plaque supérieure jeune et/ou avec la remontée du flux asthénosphérique chaud, rend thermiquement possible la formation d'une semelle métamorphique sub-synchrone avec l'ophiolite sus-jacente (Hall et al., 2003, Gurnis et al., 2004), il n'existe dans la littérature que très peu d'exemples l'incorporant. Duretz et al. (2016) ont testé thermiquement la faisabilité de cette formation avec une initiation au niveau d'une anomalie thermique majeure, comme pouvant exister au niveau des failles transformantes (Figure 2.7). Le chemin P-T calculé de la semelle métamorphique est similaire à celui attendu. Cependant, leur modèle n'inclue ni extension arrière-arc ni fusion partielle permettant la formation dans un second temps de l'ophiolite de type SSZ, comme suggéré précédemment. L'extension dans la plaque supérieure est tardive, elle résulte de l'étape d'exhumation de la marge continentale. Ce mécanisme d'amincissement est une des hypothèses permettant d'expliquer le désaccord (ou *conundrum*) entre les pressions de formation des semelles métamorphiques et l'épaisseur actuelle des ophiolites ( $\leq 20$  km).

Enfin, le modèle d'une néo-formation complète au niveau d'une zone de fracture est incompatible avec les produits magmatiques dans les ophiolites dont l'âge de formation est bien antérieure à la dernière initiation de subduction, comme observé en Nouvelle-Calédonie (Soret et al., 2016).

## Modèle d'initiation sur un détachement océanique

Van Hinsbergen et al. (2015) et Maffione et al. (2015) ont adapté le modèle d'initiation de subduction intra-océanique proposé par (Stern, 2004) au cas d'une subduction parallèle à la ride, comme observé en Oman (Boudier et al., 1988, Hacker, 1994). Dans leur modèle (Figure 2.8), l'initiation de la subduction a lieu au niveau d'un détachement d'échelle lithosphérique proche d'une ride pré-existante. Ce détachement, parallèle à la ride, est la zone de faiblesse mécanique sur laquelle est accommodée la dynamique compressive régionale. Avec leur modèle, les auteurs proposent également une solution à l'inadéquation persistante entre les conditions P-T des semelles métamorphiques et les épaisseurs actuelles des ophiolites.

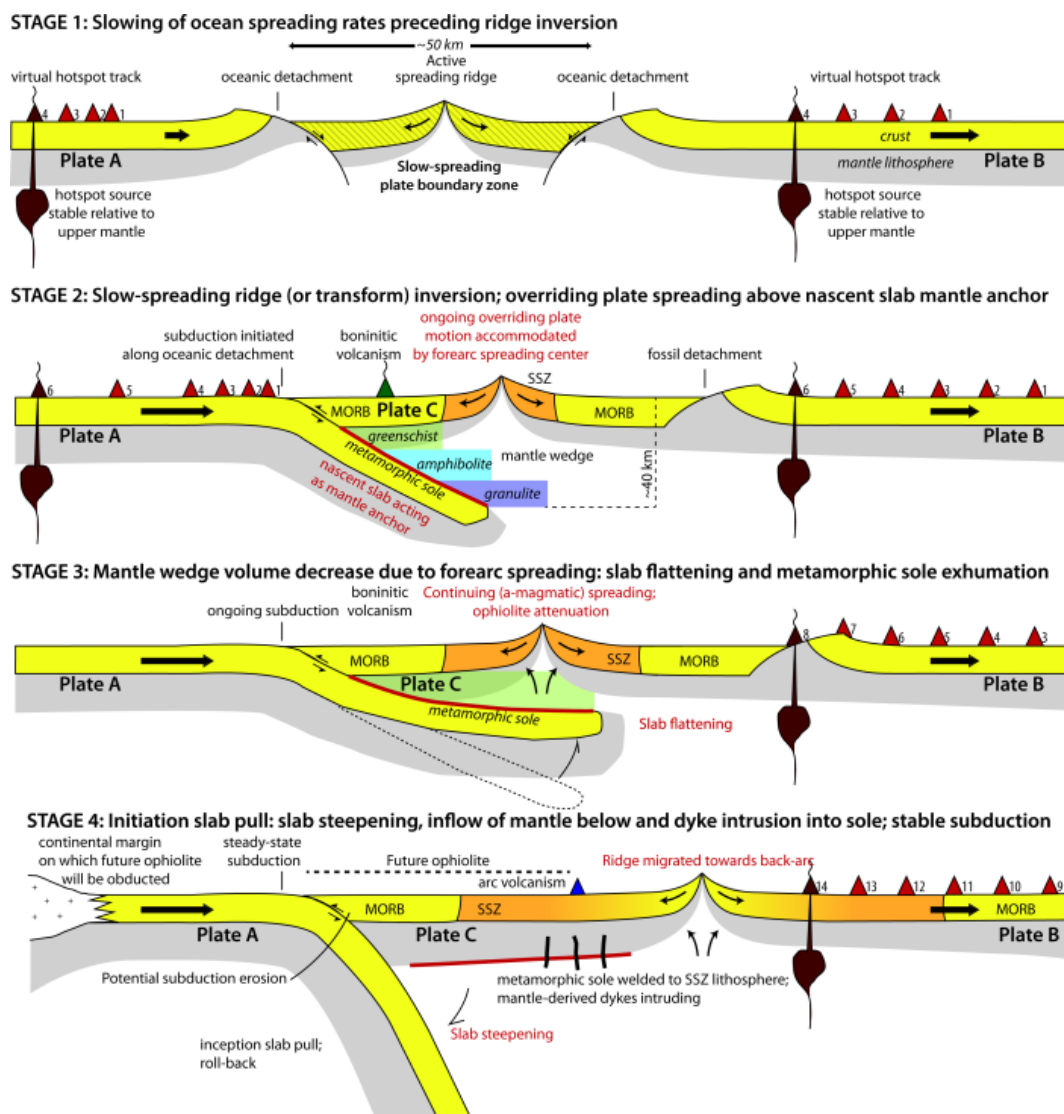


FIGURE 2.8 – Modèle de subduction intra-océanique avec une initiation sur un détachement océanique, d'après Van Hinsbergen et al. (2015).

Ce modèle de subduction intra-océanique débute proche d'une ride afin de répondre aux conditions thermiques nécessaires à la formation de la semelle métamorphique. Celle-ci se forme alors le long de la plaque plongeante, depuis le faciès des schistes verts à moyenne profondeur ( $\sim 10\text{--}15$  km) au faciès granulitique à plus grande profondeur ( $\sim 35\text{--}45$  km), par transfert de chaleur avec le manteau chaud. En effet, l'ophiolite sus-jacente continue, dans le même temps, son accrétion magmatique avec cette fois une signature de supra-subduction. Différentes écailles de la plaque plongeante métamorphisée sont ensuite accrétées lors de leur exhumation alors que le régime thermique de la subduction s'est refroidi pour atteindre un état proche de l'équilibre. Cette exhumation est associée à un aplatissement de la plaque plongeante ("*slab flattening*") du fait du fort amincissement de la lithosphère sus-jacente lors de son accrétion (Van Hinsbergen et al., 2015). Cette hypothèse explique la différence entre les profondeurs de formation estimées pour les amphibolites de la semelle métamorphique et l'épaisseur actuelle des ophiolites  $\leq 20$  km. La semelle métamorphique est ensuite totalement découpée de la subduction lors de l'éclogitisation et du retrait de la plaque plongeante (Figure 2.8). Elle se trouve alors intégrée au sein des péridotites de la future ophiolite obductée et non plus à l'interface des plaques au sein du chenal de subduction.

L'accrétion syn-exhumation n'est pas explicitée dans leur modèle géodynamique (Figure 2.8), tout comme les mécanismes à son origine et la mise en place finale du complexe ophiolitique sur la marge continentale. L'absence de la semelle métamorphique au sein du chenal de subduction lors de la formation des unités HP-BT est notamment problématique. En effet, en Oman comme en Turquie, ces unités de haute pression sont structurellement très proches de la semelle métamorphique, sans traces de manteau intercalé. Les modalités d'obduction du complexe ophiolitique demeurent également énigmatiques. Leur modèle impliquent un saut pluri-kilométrique de l'interface des plaques, non expliqué dans leur étude.

### Modèle d'initiation à la transition océan-continent

L'hypothèse d'une initiation au niveau de la transition océan-continent (TOC) est également invoquée dans la mise en place de certaines ophiolites obductées, remettant en cause celle de la subduction intra-océanique généralement privilégiée. Alors que les premiers modèles de formation et d'obduction des ophiolites NE anatoliennes et du Petit Caucase (Rolland et al., 2009b, Sosson & Rolland, 2010) impliquaient une subduction intra-océanique, les derniers modèles favorisent désormais une subduction continentale à la TOC (Hassig et al., 2015, Hässig et al., 2016a,b).

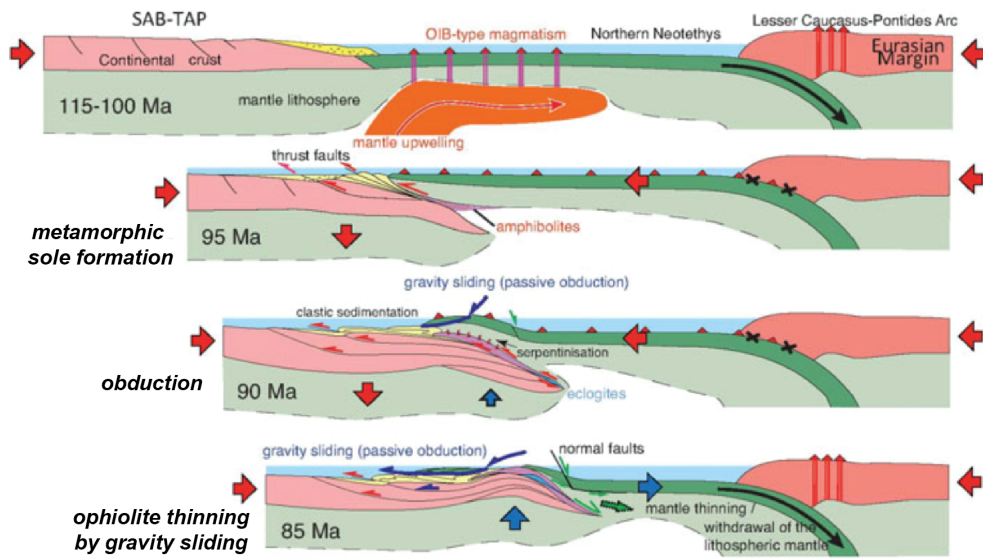


FIGURE 2.9 – Modèle de subduction océanique avec une initiation à la transition océan–continent basé sur le complexe ophiolitique NE anatolienne (Hässig et al., 2016b).

Dans ce modèle (Figure 2.9), la lithosphère océanique est préalablement réchauffée par la remontée d'un flux asthénosphérique. Ce réchauffement a pour conséquence de réduire la densité, la viscosité et l'épaisseur de la la future ophiolite. D'après les auteurs, cette étape est attestée par la mise en place de laves de chimie OIB (*Ocean Island Arc*) 10 à 25 Ma antérieurs à l'obduction. Puis, à partir de fragments de roches de faciès schistes bleus observés à la base du complexe ophiolitique (Rolland et al., 2009a) dont le pic de métamorphisme est contemporain à celui de la semelle métamorphique et du dépôt des sédiments scellant l'obduction, les auteurs proposent que la subduction continentale s'initie au niveau de la TOC (Figure 2.9) sur une zone fortement serpentinisée. L'absence d'éclogite continentale observée à la surface est interprétée comme en accord avec l'hypothèse d'une subduction proche de marge continentale, limitant son enfouissement (Hässig et al., 2015). Enfin, l'exhumation de la marge continentale sous-charriée sous l'ophiolite obductée permet l'exhumation de cette dernière. Cette exhumation entraîne la flexure et l'érosion par glissement gravitaire de l'ophiolite. L'amincissement de l'ophiolite est un des mécanismes proposés pour résoudre le problème posé par les profondeurs de formation des semelles métamorphiques (Lagabrielle et al., 2013, Duretz et al., 2016).

En accord avec les datations, la semelle métamorphique est formée au moment de l'initiation de la subduction de la marge continentale. L'environnement thermique élevé due à la remontée préalable d'un flux asthénosphérique (type point chaud) est également compatible avec les estimations de formation à haute température. Cependant, bien que dessinée dans ce modèle, l'origine et les mécanismes de formation et d'exhumation de celles-ci (non détaillés par les auteurs) restent fortement énigmatiques.

## 2.2 Etat des connaissances sur les semelles métamorphiques

### 2.2.1 Quelques exemples représentatifs de semelles métamorphiques

La caractérisation des premières semelles métamorphiques a débuté au cours des années 1970, avec notamment les travaux de Williams & Smyth (1973), et Coleman (1977) sur la semelle métamorphique de Bay of Island (Terre Neuve, Canada), le complexe ophiolitique de référence à cette période. Ces travaux ont permis d'établir une première description pétro-structurale de la semelle métamorphique, et d'affirmer le lien entre cette dernière et les ophiolites sus-jacentes (Figure 2.10 ; Table 2.1).

C'est cependant à la fin des années 1970 (Malpas, 1979, McCaig, 1983, Jamieson, 1981) et surtout au cours des années 1980, que les premières conditions pression-température de formation des semelles métamorphiques et les premiers modèles géodynamiques sont proposés (Jamieson, 1986), notamment avec l'apparition des premiers travaux sur la semelle métamorphique d'Oman (Ghent & Stout, 1981, Searle & Malpas, 1982), plus étendue et plus continue latéralement.

Les années 1990 sont ensuite marquées par un désintérêt relatif de l'ophiolite canadienne et un transfert important des études vers la semelle métamorphique d'Oman (e.g. Gnos, 1992, Gnos & Kurz, 1994, Hacker, 1994, Hacker et al., 1996, Hacker & Gnos, 1997, Gnos, 1998), qui est ainsi devenu l'objet de référence.

Dans les années 2000, la semelle métamorphique en Oman, alors très étudiée, est à son tour quelque peu oubliée au dépend de l'ophiolite sus-jacente (Boudier et al., 2000, Godard et al., 2000, 2003, 2006, Takazawa et al., 2003, Le Mée et al., 2004, Python et al., 2008) et des roches de HP-BT sous-jacentes (El-Shazly et al., 2001, Warren et al., 2003, Yamato et al., 2007). L'attention est également détournée vers les semelles métamorphiques des autres complexes ophiolitiques néo-téthysiennes (Albanie, Turquie, Grèce ; Parlak & Delaloye, 1999, Önen & Hall, 2000, Dimo-Lahitte et al., 2001, Saccani & Photiades, 2004, Dilek et al., 2007, 2008, Gaggero et al., 2009).

Les semelles métamorphiques "*alpines*" affleurent de façon assez continue depuis l'ophiolite d'Oman jusqu'aux ophiolites des Dinarides en Albanie, en passant par les ophiolites de Turquie et de Grèce (Figure 2.10 ; Table 2.1). Leur distribution spatiale est-ouest est héritée de la fermeture de la Néo-Téthys entre le Jurassique et le Crétacé. Deux principales tranches d'âges marquent leur formation. À l'ouest, les semelles métamorphiques des ophiolites albanaise et grecque sont datées autour de  $160 \pm 10$  Ma alors que plus à l'est les semelles métamorphiques turques et omanaises sont datées autour de  $93 \pm 3$  Ma. En raison de leur continuité spatiale et de leur facilité d'accès, ces semelles font partie des semelles

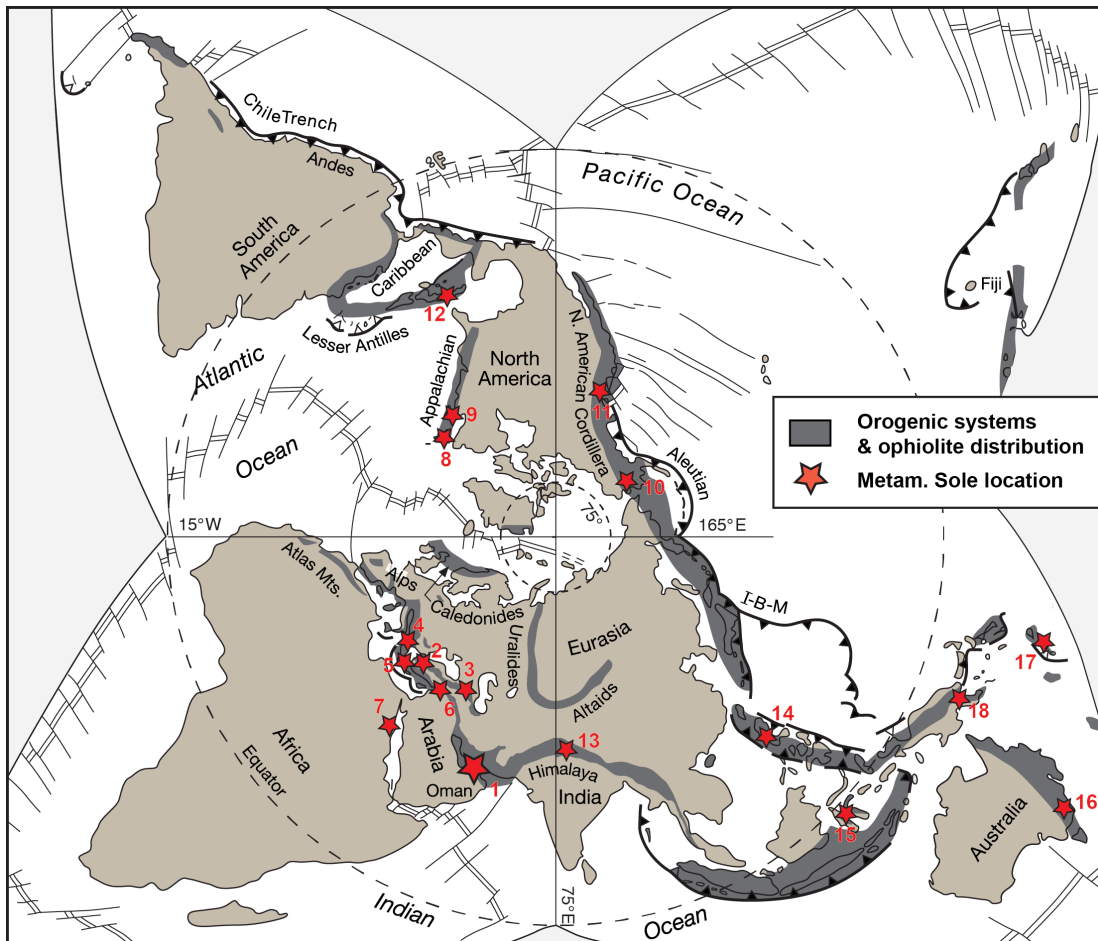


FIGURE 2.10 – Distribution des ophiolites et des semelles métamorphiques à l'échelle mondiale, figure modifiée d'après Dilek & Furnes (2011).

les plus étudiées. Dans la chaîne himalayenne, au niveau du Tibet (Guilmette et al., 2012), une portion de semelle métamorphique est également décrite, avec un âge de  $123 \pm 3$  Ma.

Le nord-est du Canada est l'autre région présentant d'importants affleurements de semelles métamorphiques, au niveau de la terminaison nord de la ceinture des Appalaches (Figure 2.10 ; Table 2.1). Cette région regroupe les ophiolites de Terre Neuve (Bay of Island) et du Québec (Thetford Mines et le Mont Albert).

**C'est à Terre Neuve que la semelle métamorphique est précisément décrite pour la première fois (e.g. Dewey & Bird, 1971, Williams & Smyth, 1973) et que des conditions pression-température sont estimées (Malpas, 1979).** Cette semelle métamorphique, datée autour de  $480 \pm 3$  Ma (Jamieson, 1981, McCaig, 1983), affleure principalement sur 4 grandes localités (i.e. du nord au sud : White Hills, Table Mountain, Blow-Me-Down Moutain et Lewis Hills) dispersées sur 400 km de long et 100 km de large, pour une épaisseur maximale d'environ 100 m (e.g Malpas, 1979, McCaig, 1983).

**Au Québec, la semelle métamorphiques apparaît discontinue le long de la Baie – Verte Brompton Line (BBL) séparant les zones de Humber (i.e. relique de la marge continentale Laurentienne et de sa couverture) et de Dunnage (i.e. relique de l'océan Iapétus) accrétées à partir de 400 Ma lors de l'orogène taconienne (e.g. Pagé et al., 2008). Au sud de cette ligne affleurent l'ophiolite de Thetford Mines et sa semelle métamorphique sur 15 km<sup>2</sup>. La semelle métamorphique a une épaisseur maximale d'environ 700 m. Elle est datée de 477 ± 5 Ma par méthode <sup>40</sup>Ar–<sup>39</sup>Ar sur amphibole (Pagé et al., 2008). Au nord de la BBL, affleure dans la région de Gaspé, l'ophiolite du Mont Albert et sa semelle métamorphique dite "du Diable", sur une surface d'environ 50 km<sup>2</sup> (e.g. Trzcienski, 1988). Cette dernière affleure de façon continue sous les périclites sur une épaisseur moyenne de 500 m (e.g. Trzcienski, 1988). Sa formation est datée de l'Ordovicien, à 465.2 ± 2 Ma par méthode <sup>40</sup>Ar–<sup>39</sup>Ar sur amphibole (Malo et al., 2008).**

**Dans la cordillère nord américaine, deux semelles métamorphiques affleurent localement** (Figure 2.10). La première est située dans la chaîne des Cascades, dans la baie de San Francisco. Elle est associée à l'orogène du Franciscain. La semelle métamorphique affleure sous forme de blocs de tailles allant de 600 m de long pour 400 m de large jusqu'à des blocs d'échelle métrique. Ces blocs sont inclus dans une matrice composée d'un mélange d'argile et/ou de serpentinite (Wakabayashi, 1990). La semelle métamorphique est datée du Jurassique supérieur, entre 160 et 163 Ma (e.g. Ross & Sharp, 1988, Wakabayashi, 1990) par méthodes K–Ar et <sup>40</sup>Ar–<sup>39</sup>Ar sur amphiboles.

**Une autre semelle métamorphique affleure également plus au nord, en Alaska dans la chaîne des Brooks** (Figure 2.10 ; Table 2.1). La semelle métamorphique est située de manière discontinue sous une ophiolite mesurant 350 km de long, 50 km de large, avec une épaisseur de 3–4 km. Sa séquence la plus complète et la plus continue verticalement est observée à Misheguk où elle affleure sur épaisseur maximale de 200 m (Harris, 1998). Les analyses radiochronométriques par méthode K–Ar et <sup>40</sup>Ar–<sup>39</sup>Ar sur amphiboles donnent un âge de formation entre 164 et 169 Ma (Harris, 1998), comparable à l'âge de la semelle métamorphique du Franciscain.

**Dans les Caraïbes, la seule ophiolite associée à une semelle métamorphique est répertoriée à Cuba** (Figure 2.10 ; Table 2.1). La semelle métamorphique affleure sous l'ophiolite de Moa–Baracoa, à l'est de l'île. Ces ophiolites forment un complexe long de 170 km et large de 20 km pour une épaisseur moyenne de 4 km. La semelle métamorphique forme le complexe du Guira de Jauco dont l'épaisseur n'a pas été estimée (Lázaro et al., 2013). Son âge de formation est également assez mal contrainte. Deux âges ont été obtenus, 72 ± 3 Ma et 58 ± 4 Ma, respectivement par méthode K–Ar sur amphibole et sur roche totale. Lázaro et al. (2013) suggèrent que l'âge tardi-crétacé est le

---

plus probable considérant la géodynamique régionale connue. La semelle métamorphique témoignerait alors des stades précoces d'une subduction initiée dans le nord des Caraïbes datée entre 90 et 70 Ma (Lázaro et al., 2013).

Dans le sud-ouest Pacifique, on retrouve une autre ceinture ophiolitique, plus étendue et bien plus récente (Figure 2.10 ; Table 2.1). Cette ceinture résulte de la fermeture de multiples bassins marginaux, relativement continus latéralement, avec pour finalité leur obduction sur la marge continentale distale est-australienne au Paléogène. Cette ceinture ophiolitique est composée principalement des ophiolites de Papouasie Nouvelle-Guinée, de Nouvelle-Zélande et de Nouvelle-Calédonie.

**La semelle métamorphique de Papouasie Nouvelle-Guinée affleure au sud-est de l'île, sous l'ophiolite PUB (textitPapuan Ultramafic Belt).** L'ophiolite a une épaisseur maximale de 12 km et la semelle métamorphique fait entre entre 200 et 300 m d'épaisseur. C'est dans la localité de Musa-Kumusi que la semelle métamorphique est la mieux préservée (Lus et al., 2004). Les datations  $^{40}\text{Ar}$ - $^{39}\text{Ar}$  réalisées sur des amphiboles de la semelle métamorphique contraintent sa formation autour de  $58.3 \pm 0.4$  Ma (Lus et al., 2004).

**L'autre semelle métamorphique de la région sud-ouest Pacifique affleure de manière sporadique au sud de la Nouvelle-Calédonie,** sous l'ophiolite du Massif du Sud qui couvre environ un tiers de la surface totale de l'île (e.g. Paris, 1981, Prinzhofer, 1981, Cluzel et al., 2012). Cette ophiolite s'est formée depuis le Crétacé Supérieur ( $\sim 95$  Ma) jusqu'à l'Éocène ( $\sim 55$  Ma ; Cluzel et al., 2012). Les principaux affleurements de la semelle métamorphique sont situés à Pinjen, Mueo, Petchecara et Ouenghi (Cluzel et al., 2012). La semelle métamorphique fait au maximum une cinquantaine de mètres d'épaisseur et n'est jamais continue sur plus de 600–700 m de long (Cluzel et al., 2012). À Pinjen et Mueo, la semelle métamorphique est composée exclusivement d'amphibolites à clinopyroxène alors qu'à Petchecara, ce sont des amphibolites à epidote. À Ouenghi, la semelle métamorphique affleure dans la rivière sous forme de blocs éboulés principalement basiques mais avec des passées plus riches en quartz (Cluzel et al., 2012). Les datations radiochronométriques réalisées par les méthodes  $^{40}\text{Ar}$ - $^{39}\text{Ar}$  sur amphiboles et U/Pb sur sphènes et zircons de la semelle métamorphique de différentes localités montrent un âge constant autour de  $55.9 \pm 0.8$  Ma (Cluzel et al., 2012). Cet âge, à la limite Paléocène-Éocène, est similaire ( $\leq 2$  Ma) à celui obtenu sur la semelle métamorphique de Papouasie Nouvelle-Guinée.

**La semelle métamorphique la plus récente dans l'ouest-Pacifique affleure plus au nord, sous l'ophiolite du Sulawesi en Indonésie.** L'ophiolite affleure de façon discontinue sur une longueur totale de 500 km et sur un maximum 15 km d'épaisseur (Parkinson, 1998). Son âge de formation est sujet à débats. De nombreuses datations par

méthode K–Ar sur roche totale portées sur la croûte océanique de cette ophiolite ont été réalisées. Les âges obtenus couvrent un spectre compris entre 93 Ma à 32 Ma (e.g. Mubroto et al., 1994, Monnier et al., 1995). La semelle métamorphique est comprise entre 500 à 1000 m d'épaisseur. C'est dans la région de Mowomba que sa séquence est la plus complète. Située sous l'ophiolite, elle repose structuralement sur un mélange de blocs amphibolitiques à schistes verts avec un overprint schistes bleus (Parkinson, 1998). Le sommet de la semelle métamorphique, directement sous l'ophiolite, est composée d'amphibolites à grenat. Le contact entre les péridotites de l'ophiolite et la semelle métamorphique est caractérisé localement par la présence de pseudotachylites (Parkinson, 1998). Sous les amphibolites à grenat, d'une épaisseur de 300 à 500 m, la semelle métamorphique est constituée d'une unité d'amphibolite à epidote puis d'une unité schistes verts riche avec une proportion en quartz et en carbonate augmentant fortement en descendant dans la séquence (Parkinson, 1998). Les datations réalisées par méthode K–Ar sur amphiboles de la semelle métamorphique indiquent qu'elle s'est formée à l'Oligocène, autour de 30 Ma (Parkinson, 1998).

**Au voisinage du Sulawesi on retrouve une dernière ophiolite, sur l'île de Palawan dans les Philippines** (Figure 2.10 ; Table 2.1). L'origine de cette ophiolite porte à controverse. Il semblerait que l'ophiolite de Palawan soit en réalité composée de deux unités ophiolitiques d'âges différents. L'ophiolite, qui couvre la majeure partie de l'île, serait d'âge Eocène (i.e. 44–45 Ma) et elle chevauchera une ophiolite plus ancienne, d'âge Crétacé, qui n'apparaîtrait que localement en fenêtre uniquement dans le sud-ouest de Palawan. La mise en place de l'ophiolite Eocène serait alors le résultat de l'initiation d'une subduction au niveau d'une faille transformante découpant deux lithosphères océaniques d'âges différents en proto-mer de Chine, au sud de la marge eurasiatique. La semelle métamorphique est observée sous l'ophiolite d'âge Eocène au nord de l'île, sur une épaisseur comprise entre 80 et 205 m. C'est dans la Baie d'Ulugan qu'elle est la mieux préservée. Cette semelle est principalement constituée d'amphibolites basiques avec localement des niveaux plus riches en quartz, en micas et en disthène. Les amphibolites à grenat sont restreintes aux niveaux directement sous le contact avec les péridotites. Elle a été datée par méthode  $^{40}\text{Ar}$ – $^{39}\text{Ar}$  sur amphiboles à  $34.0 \pm 0.6$  Ma et à  $34.3 \pm 0.2$  Ma sur muscovites, des âges comparables à l'âge de la semelle métamorphique de Sulawesi.

**La plus vieille semelle métamorphique serait située au sud-est de l'Egypte**, à Wadi Haimur au niveau du bouclier Arabo-Nubien (Figure 2.10 ; Table 2.1). Cette semelle métamorphique d'âge Protérozoïque, est génétiquement liée à l'orogène pan-africaine. Elle est composée d'un ensemble de métagabbros, d'amphibolites et d'hornblendites, chevauché localement par des gneiss mylonitiques ou des roches de type ultrabasique (El-Naby et al., 2000). Les amphibolites sont caractérisées par un assemblage à amphibole – plagioclase – quartz ± grenat ± clinopyroxène. L'épidote est uniquement présente dans les amphibolites

#	Loc.	Ref.	Thickness		HT sole		LT sole	
			HT(m)	LT(m)	P(GPa)	T(°C)	t(Ma)	P(GPa)
1	Oman	Gnos (1998)	70		1.1±0.2	800±100	95	0.5±0.05
		Gnos & Kurz (1994)	2000		0.77±0.12	825±25		
		Ghent & Stout (1981)	30–40	80–85	0.5±0.2	810±55		
		Hacker & Mosenfelder (1996)				825	92.6–95.7	
		Hacker & Gnos (1997)				825±50		
		Searle & Cox (2002)			1.16±0.16	840±70		
		Searle & Malpas (1982)			0.5 ?	825±50		
		Bucher (1991b)					0.4±0.1	500±50
		Hacker et al. (1996)	≤500				92.6–95.7	
		Hacker (1994)	≤500				92.4–95.7	
2	Turkey	Warren et al. (2003)					94.5±0.23	
		Cowan et al. (2014)	80	150	1.2±0.1	840±60		
		Okay et al. (1998)			0.85±0.35	700±50		
		Plunder et al. (2015)			1.1±0.2	800±60		
		Dilek & Whitney (1997)	10–150			≥ 560	90–92	
		Önen & Hall (1993)	35	122	0.3±0.1	750±50	90–93	
		Önen (2003)					93±0.2	
		Parlak & Delaloye (1999)					92.6±0.2	
		Çelik & Delaloye (2006)	≤500				91.3±2.3	0.55±0.05 575±25
		Hassig (2014)					91–94	
3	Caucasus	Hassig et al. (2015)					88–95	
		Pamić et al. (2002)	≤600		0.83±0.1	710±40	136±15	
4	Dinarides	Gaggero et al. (2009)	600		0.7	730±110	162–172	0.6±0.1 624±9
		Gartzos et al. (2009)	≤250				150–155	
5	Cyclades Greece	Saccani & Photiades (2004)					159–175	
		Al-Riyami et al. (2002)	200–300			≥ 600		
6	Syria	Parlak et al. (1996)				≥600	93.4±2.0	
		El-Naby et al. (2000)			0.75±0.15	700	590–630	0.62±0.15 550±80
7	Egypt	Farahat (2011)			0.6	670±50	93.4±2.0	
					±0.15			
8	Newfoundland	Malpas (1979)	70			750±50		0.6±0.2 625±75
		Jamieson (1981)			0.85±0.15	875±25	480±5	0.42±0.07 600±50
		McCaig (1983)	70	80	0.9±0.2	800±50	477±5	
		Jamieson (1986)			0.80±0.25	900±50		0.4±0.1 575±75
9	Québec	Savic (1988)	100		0.75±0.15	750±100		0.4±0.1 575±75
		O'Beirne-Ryan et al. (1989)			0.85±0.05	800±50		0.6±0.2 625±75
		Trzcienski (1988)	50	450	1.2	840		
		Clague et al. (1981)			0.65±0.15	775±35		
10	Brooks Range	Malo et al. (2008)					465±2	
		Harris (1998)	500		0.5	≥650	164–169	
11	California	Wakabayashi (1990)			0.95±0.05	645±15	160–163	
		Lázaro et al. (2013)			0.86±0.01	655±10	70	
13	Tibet	Guilmette et al. (2012)			1.2±0.25	850±100	127–132	
		Encarnacion et al. (1995)	80–250		0.95	730±30	34±0.6	
14	Philippines	Parkinson (1998)	300	300		700±60	30	
		Meffre et al. (2012)			0.85±0.15	725±25	511±4	0.5±0.1 555±15
15	Sulawesi	Mulder et al. (2016)	200		0.8	875	510–515±4	
					0.6±0.3	800±100	55±2	660
17	N. Caledonia	Cluzel et al. (2012)						
		Lus et al. (2004)	40	160	0.4	900	58.3±0.4	

TABLE 2.1 – Revue mondiale des localités, des épaisseurs, des âges et des conditions P-T de formation des semelles métamorphiques

sans grenat, dite massives par El-Naby et al. (2000). Les amphibolites à clinopyroxène ou à grenat apparaissent uniquement au sommet de l'unité de la semelle métamorphique. Leurs conditions pression – température de formation sont estimées autour de 0.65–0.85 GPa et 700 °C (El-Naby et al., 2000). Les amphibolites "massives" (i.e. sans grenat), qui représentent la partie basale de la semelle métamorphique, sont estimées à des conditions de plus basses pressions et températures, autour de 0.47–0.78 GPa et 450–620 °C. La datation par la méthode Sm/Nd sur roche totale fournit des âges autour de 630 Ma et de 590 Ma, respectivement pour les amphibolites à clinopyroxène et les amphibolites à grenat.

## 2.2.2 L’Oman : la semelle métamorphique de référence ?

### Distribution spatiale ubiquiste sous l’ophiolite

Le complexe ophiolitique de Semail (ou d’Oman) présente la plus grande extension et les meilleures conditions d’affleurement au monde (150 km de large pour 600 km de long ; Nicolas et al., 2000). Ainsi, la semelle métamorphique, qui est ubiquiste à sa base, est également une des plus importantes au monde en terme de continuité spatiale et d’affleurement.

D’une épaisseur maximale d’environ 500 m (excepté dans la fenêtre d’Asimah–Khubakhib), elle est généralement interprétée comme la juxtaposition de deux unités majeures. Directement sous les périclases, la semelle métamorphique de haute température (HT) est toujours située structuralement au-dessus de la semelle de plus basse température (BT) de manière plus ou moins continue sous l’ophiolite (Figure 2.11 ; Gnos, 1992) depuis Wadi Tayin au sud-est à Khubakhib au nord-ouest. Lorsque la semelle de haute température est absente, cette unité affleure directement sous les périclases. Les semelles de haute et basse températures montrent une fabrique planaire importante, sub-parallèle à celle des périclases, avec localement des preuves de déformation en cisaillement simple. La semelle de plus haut grade métamorphique est localement épaissie par quelques plis couchés d’échelle centimétrique. La semelle de basse température est bien plus fréquemment plissée et avec des longueurs d’ondes régulièrement pluri-métriques.

La semelle de haute température (aussi appelée semelle amphibolitique) est essentiellement composée de métabasalte métamorphisé dans le faciès amphibolitique à granulitique. La proportion de quartzite et de roches riches en micas augmente en s’éloignant du contact avec les périclases alors que l’intensité du métamorphisme décroît. Du sommet jusqu’à la base de l’unité, la semelle métamorphique évolue depuis des niveaux basiques à grains fins à amphibole ± grenat ± clinopyroxene ± plagioclase vers des niveaux plus grossiers à amphibole ± plagioclase ± epidote, également plus hétérogènes avec l’imbrication de niveaux transitionnels plus acides riches en amphibole ± plagioclase ± quartz ± biotite ± muscovite ± grenat (e.g., Searle & Malpas, 1982, Gnos, 1992). Proches du contact avec les périclases de l’ophiolite sus-jacente, des traces de fusion partielle dans la semelle métamorphique sont également décrites sous forme de fines intrusions de composition tonalitique à dioritique (~ 5–10 % ; Searle & Malpas, 1982, Boudier et al., 1988, Hacker & Gnos, 1997, Searle & Cox, 1999). Au contact avec les périclases de l’ophiolite sus-jacente, la semelle haute température est généralement recoupée par des veines de rodingite à quartz ± calcite ± epidote ± tremolite ± prehnite ± wollastonite ± xonotrite.

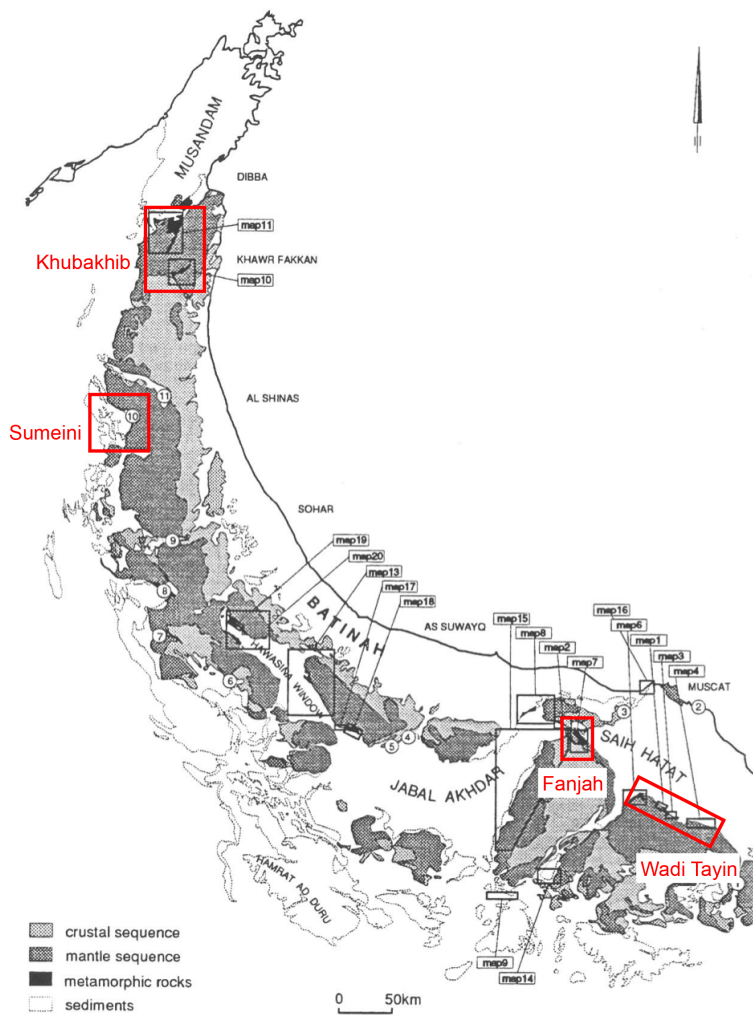


FIGURE 2.11 – Carte géologique simplifiée de l’ophiolite d’Oman et de la semelle métamorphique associée (Gnos, 1992).

La semelle de basse température est essentiellement composée de metachert dans le faciès des schistes verts avec des intercalations de métatuffe à albite  $\pm$  chlorite  $\pm$  tremolite  $\pm$  epidote et de métacarbonate à quartz, trémolite, épидote ou piémontite (Bucher, 1991b, Gnos, 1992). Cette portion de la semelle métamorphique a été relativement peu étudiée et donc il n’existe que peu d’informations pétro-structurales à son sujet.

Les semelles de haute et basse températures montrent une fabrique planaire importante avec localement des preuves de déformation en cisaillement simple. La déformation est moins claire dans la semelle métamorphique à grenat. Les niveaux de plus bas grade métamorphique, marqués par une plus forte hétérogénéité compositionnelle sont marqués par la présence de nombreux plis couchés, d’échelle centimétrique dans la semelle haute température à pluri-métrique dans la semelle de basse température.

La semelle métamorphique de Green Poole dans la région de Wadi Tayin est située dans le sud-est de l'Oman, à une centaine de kilomètres du front de propagation de l'ophiolite (map 3 ; Figure 2.11). Elle fait partie des semelles les plus étudiées au monde (Ghent & Stout, 1981, Gnos, 1992, Hacker & Mosenfelder, 1996, Cowan et al., 2014). Son sommet est composé d'amphibolite à grenat + clinopyroxène + plagioclase sur 2 m d'épaisseur. Puis, le grenat disparaît et sur 80 m la semelle métamorphique haute température est composée d'amphibolite à clinopyroxène + plagioclase. Les 50 derniers de mètres de la semelle amphibolitique sont caractérisés par la disparition du clinopyroxène et par une plus grande proportion de niveaux micacés à albite ± quartz ± calcite ± grenat manganifère, alternant avec des niveaux basiques riches en amphibole + epidote + chlorite. La biotite dans les niveaux micacés est rare et souvent rétromorphosée en chlorite. Sous cette semelle amphibolitique, la semelle métamorphique est composée de métachert avec de rares passées métabasiques sur une épaisseur non spécifiée. Ghent & Stout (1981) interprètent cette dernière partie comme l'unité de faciès des schistes verts. Cependant, Hacker & Mosenfelder (1996) revisitent cette structure et interprètent la partie basale de cette semelle métamorphique comme appartenant originellement au faciès amphibolitique basse température puis rétromorphosée dans le faciès des schistes verts.

Toujours dans la région de Wadi Tayin (map 1 et map 4 ; Figure 2.11), Gnos (1992) décrit latéralement une semelle métamorphique relativement similaire à celle de Green Poole, mais avec la particularité de ne pas présenter d'amphibolites à grenat. Localement, la semelle basse température affleure directement sous les périclases. À Ghubrat Tam (map 4 ; Figure 2.11), Gnos (1992) évoque également la présence de métagabbro alors qu'habituellement les amphibolites sont interprétées comme dérivant d'un protolith basaltique. De plus, tout comme à Green Poole, la semelle métamorphique est recoupée par veines de métacarbonates à epidote et xonotrite à l'interface avec les périclases (Ghent & Stout, 1981, Gnos, 1992).

À Bidbid dans la région de Fanjah, toujours à l'arrière de l'ophiolite (map 7 ; Figure 2.11), Gnos (1992) qualifie la séquence de la semelle métamorphique comme "idéale" avec la présence des unités de haute et basse température. La semelle repose sous les périclases et sur les sédiments non métamorphiques de l'Hawasina d'affinité continentale. À Rustaq, les amphibolites à grenat forment le sommet de la semelle métamorphique sur 10 à 15 m d'épaisseur.

À Sumeini, Searle & Malpas (1982) réalisent (Figure 2.11) une des premières descriptions pétro-structurales fines de la semelle métamorphique au front de propagation de l'ophiolite d'Oman (Figure 2.12). Ils y décrivent une semelle métamorphique d'une épaisseur de 250 m située sous les périclases de l'ophiolite d'Oman. La base des périclases

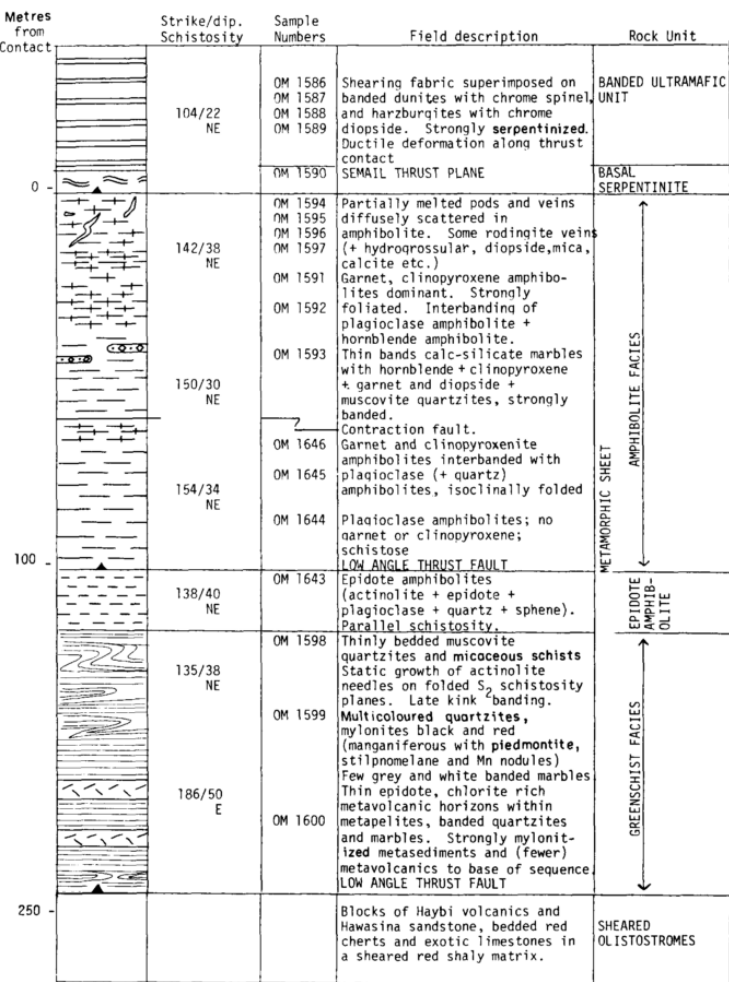


FIGURE 2.12 – Log pétro-structurale représentatif de la semelle métamorphique à Sumeini en Oman (Searle & Malpas, 1982).

est caractérisée par une importante déformation ductile. Comme à Wadi Tayin, le contact entre les deux formations est caractérisé par la présence de veines de métacarbonates. La semelle métamorphique, directement sous les péridotites, est constituée d'amphibolite à plagioclase  $\pm$  grenat  $\pm$  clinopyroxène sur une épaisseur d'une centaine de mètres. Searle & Malpas (1982) décrivent également la présence de niveaux riches en quartz et micas, ainsi que la présence de petites poches et de veines à feldspath potassique et amphibole qu'ils interprètent comme des évidences de fusion partielle in-situ. La deuxième moitié de la semelle est caractérisée par la disparition du clinopyroxène et du grenat dans les niveaux basiques. Sous la semelle de haute température affleure la semelle de basse température sur une centaine de mètres également. Elle est principalement composée de métachert à muscovite  $\pm$  actinote, alternant avec de rares métatuffes à albite  $\pm$  chlorite  $\pm$  epidote. A la transition entre les unités de haute et basse température, la semelle métamorphique est composée de niveaux basiques à fin grains à epidote + plagioclase + actinolite + quartz.

Au nord-ouest de l'ophiolite d'Oman, dans la région d'Asimah au front de propagation de l'ophiolite (map 10-11 ; Figure 2.11), la semelle amphibolitique à grenat est la plus épaisse d'Oman, avec une épaisseur maximale de 70 m dans la fenêtre de Khubakhib (Searle & Malpas, 1982, Gnos, 1992, 1998) dont une majorité présente du clinopyroxène. Dans le nord de Masafi, Gnos (1992) décrit la présence de disthène dans une amphibolite à grenat, ce qui en fait l'unique observation de silicate d'alumine dans la semelle métamorphique d'Oman. Les rares niveaux micacés intercalés entre les niveaux métabasiques sont constitués de grenat, de biotite, de quartz et de muscovite. La suite de la semelle haute température est composée d'amphibolite à plagioclase, alternant avec des niveaux riches en quartz de plus en plus nombreux jusqu'à être dominants dans la semelle métamorphique de faciès schistes verts.

### Des hétérogénéités minéralogiques et chimiques

Les **amphiboles** proches du contact avec les péridotites sont de couleur brune alors qu'en s'éloignant du contact, leur couleur évolue vers le vert ce qui témoigne d'une évolution de composition. La composition des amphiboles des niveaux métabasiques de la semelle métamorphique de haute température varie entre le pôle de la pargasite et les pôles de la magnésio- et tschermakite- hornblende (Figure 2.13). Ces amphiboles font partie des minéraux index du faciès des amphibolites. Les amphiboles dont la composition est proche du pôle de l'actinolite-trémolite sont, quant à elles, caractéristiques du faciès des schistes verts (Figure 2.13). Dans la semelle haute température, ces amphiboles sont rétrogrades alors que dans la semelle basse température ces amphiboles appartiennent au pic de métamorphisme. Malgré cette variabilité, les amphiboles des semelles haute et basse températures sont très peu zonées (Gnos, 1992, Hacker & Mosenfelder, 1996).

Les amphiboles dans la semelle amphibolitique à grenat ont une teneur en Ti élevée, entre 1.5 et 2.5 wt% (Hacker & Mosenfelder, 1996, Cowan et al., 2014). Cette teneur diminue avec la distance aux péridotites (Figure 2.13a,d). Ces variations de composition en Ti sont interprétées comme des différences de températures de métamorphisme (Searle & Malpas, 1982). L'effet d'une variation de la composition de roche totale est exclue en raison de la présence ubiquiste de phases titanées. De plus, Gnos (1998) et Hacker & Mosenfelder (1996) mettent en évidence une corrélation positive entre le ratio FeMg des amphiboles et la distance aux péridotites, qu'ils interprètent comme une diminution de la température (Figure 2.13c).

Les **clinopyroxènes** de la semelle métamorphique sont des diopsides (Figure 2.14). Inclus dans les grenats et dans la matrice des amphibolites de haute température au niveau du contact, ils sont également présents plus loin du contact dans les amphibolites à plagi-

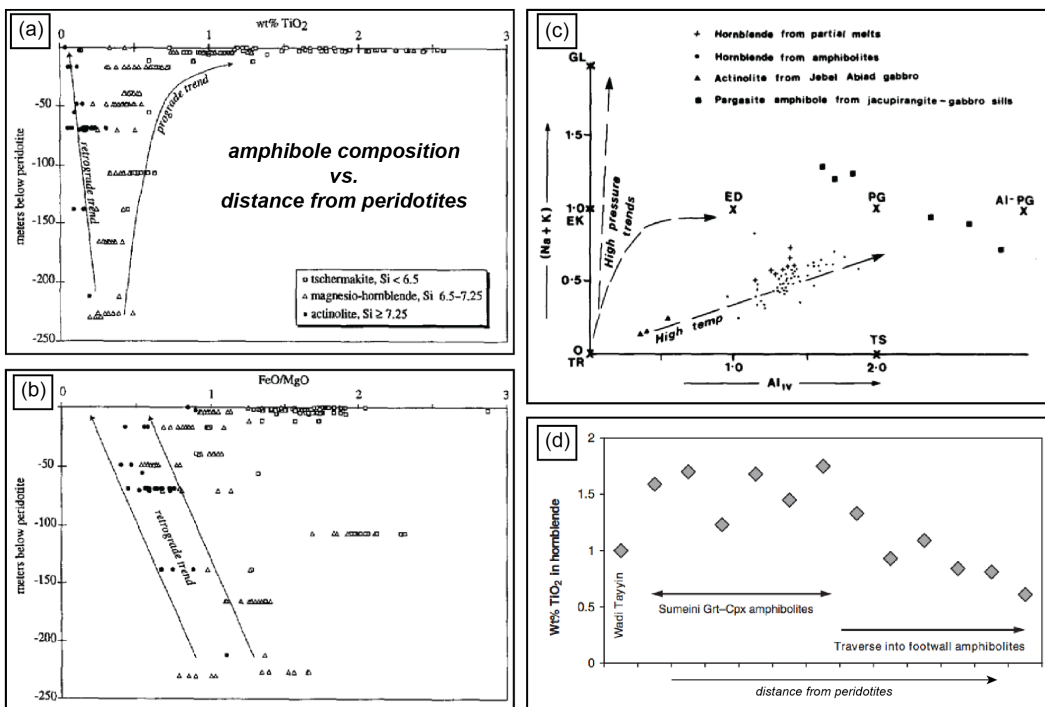


FIGURE 2.13 – Composition des amphiboles constituant la semelle métamorphique d’Oman : a) b) à Wadi Tayin, d’après Hacker & Mosenfelder (1996) ; c) à Sumeini d’après Searle & Malpas (1982) ; d) à Wadi Tayin, d’après Cowan et al. (2014).

clase sans grenat. Hacker & Mosenfelder (1996) décrivent une légère augmentation en Mg# sur la bordure externe de certains clinopyroxènes inclus dans des grenats (Figure 2.14a) tandis que Gnos (1992) rapporte un enrichissement en Ti, Fe et Na dans les clinopyroxènes avec l’augmentation de la distance avec les péridotites.

Les **grenats des niveaux basiques** sont riches en almandin avec une proportion plus réduite en pyrope et en grossulaire (Figure 2.14c). Ils présentent de nombreuses inclusions d’amphiboles brunes, de clinopyroxènes et des phases titanées (rutile, sphène, ilménite). Les grenats sont non à faiblement zonés (Ghent & Stout, 1981, Gnos, 1992, 1998, Searle & Malpas, 1982, Hacker & Mosenfelder, 1996), ce qui est interprété comme le résultat d’une homogénéisation à haute température par diffusion (Hacker & Mosenfelder, 1996). Gnos (1998) observe également une augmentation du contenu en Fe anti-corrélée avec le contenu en Ca dans les grenats avec la distance par rapport au contact avec les péridotites (Figure 2.14d).

Les **grenats dans les métacherts** sont riches en spessartine et montrent une zonation plus marquée (Ghent & Stout, 1981, Searle & Malpas, 1982, Gnos, 1992, 1998, Hacker & Mosenfelder, 1996). Ghent & Stout (1981) décrivent un enrichissement en Mn et un appauvrissement en Fe et Mg du cœur vers la bordure. Hacker & Mosenfelder (1996)

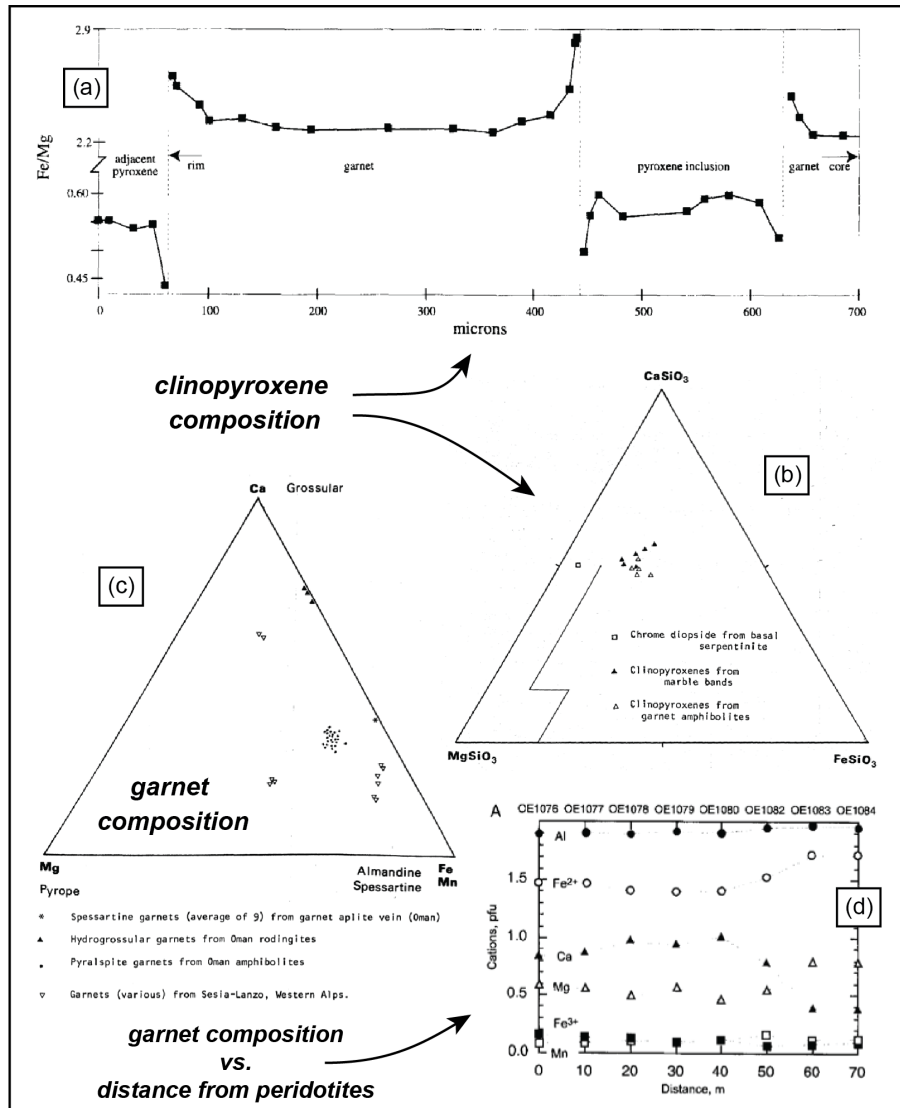


FIGURE 2.14 – Composition des grenats et des clinopyroxènes de la semelle métamorphique d’Oman : a) à Wadi Tayin, d’après Hacker & Mosenfelder (1996) ; b) et c) à Sumeini, d’après Searle (1980) ; d) à Khubakhib, d’après Gnos (1992, 1998).

décrivent une zonation tout aussi importante mais inverse dans des grenats pourtant issus de la même localité (Wadi Tayin).

Les **plagioclases** sont souvent observés à l’état de relique en raison d’une importante rétromorphose tardive en albite + epidote + muscovite. La concentration en anorthite au pic de métamorphisme varie fortement en fonction des études. Dans la semelle amphibolitique de Wadi Tayin, Ghent & Stout (1981) observent des plagioclases avec 25% d’anorthite alors que Hacker & Mosenfelder (1996) rapportent des pourcentages qui montent jusqu’à 55%. À Khubakhib, Gnos (1998) décrit des plagioclases avec un contenu en anorthite entre 20 et 30%.

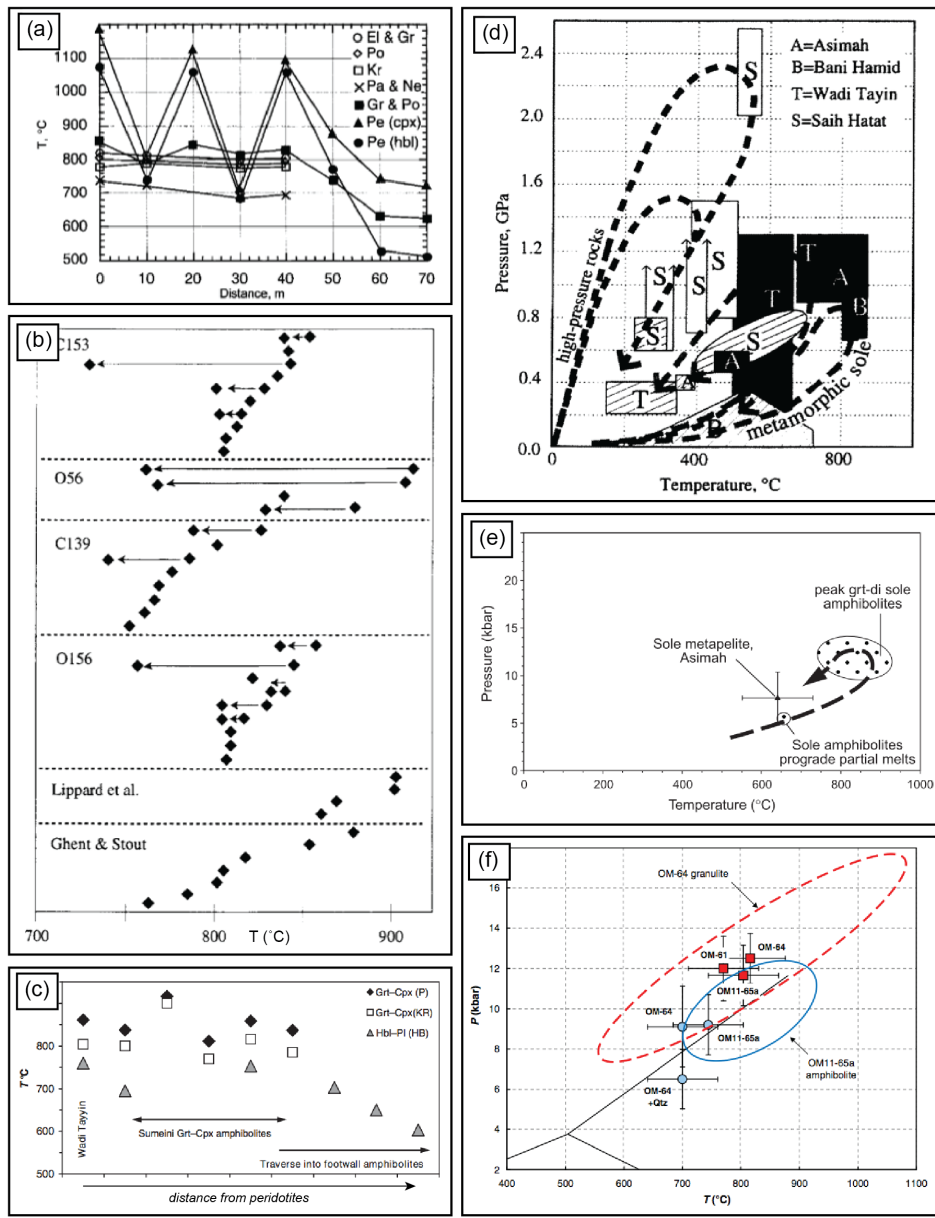


FIGURE 2.15 – Conditions P-T de formation des amphibolites de la semelle métamorphique d’Oman : a) températures estimées à partir de géothermomètres grenat-clinopyroxène dans les amphibolites de Khubakhib, d’après Gnos (1998) ; b) températures estimées à partir de géothermomètres grenat-clinopyroxène dans les amphibolites de Wadi Tayin, d’après Hacker & Mosenfelder (1996) ; c) températures estimées à partir de géothermomètres amphibole-plagioclase dans les amphibolites de Sumeini, d’après Cowan et al. (2014) ; d) présentation des chemins P-T de la semelle métamorphique d’Oman pour les régions de Khubakhib-Asimah (A) et de Wadi Tayin (T), d’après Hacker & Gnos (1997) ; e) chemin P-T pour la semelle métamorphique de Khubakhib-Asimah, obtenues par la méthode d’*Average PT* de THERMOCALC<sup>®</sup>, d’après Searle & Cox (2002) ; f) Conditions P-T les plus récentes pour les semelles métamorphiques de Sumeini et Wadi Tayin, obtenues par la méthode d’*Average PT* de THERMOCALC<sup>®</sup>, d’après Cowan et al. (2014).

## Des conditions pression–température incertaines

Au début des années 1980, Ghent & Stout (1981) et Searle & Malpas (1982) apportent les premières estimations pression-température (P-T) de formation pour la semelle métamorphique d'Oman grâce à l'utilisation de géothermomètres basés sur les échanges cationiques entre le grenat et le clinopyroxène (Green & Ringwood, 1967, Råheim & Green, 1974, Ellis & Green, 1979, Ganguly, 1979). Ghent & Stout (1981) obtiennent à Wadi Tayin des températures comprises entre 755 et 865 °C pour une pression de 0.2 GPa. La pression a été estimée suivant la réaction d'équilibre : albite = jadéite + quartz (Newton & Smith, 1967). Cependant, à partir de la composition du clinopyroxènes et du plagioclase, Ghent & Stout (1981) ré-estiment la pression entre 0.44 et 0.53 GPa. Searle & Malpas (1982) calculent à Sumeini des températures autour de 900 °C pour des pressions de 0.4 GPa.

Ces conditions thermiques obtenues sont comparables à celles estimées dans le même temps à Terre Neuve au Canada ((Malpas, 1979, Jamieson, 1981), respectivement de 750 ± 50 °C et de 875 ± 25 °C. Les pressions obtenues sont, à l'inverse, très inférieures à celles établies outre-Atlantique par qui se situent autour de 0.85 ± 0.15 GPa (Jamieson, 1981).

Les nouvelles conditions thermiques calculées à Khubakhib (Figure 2.15a ; Gnos, 1992, 1998), à Wadi Tayin (Figure 2.15b ; Hacker & Mosenfelder, 1996, Cowan et al., 2014) et à Sumeini (Figure 2.15f ; Cowan et al., 2014), toujours à l'aide des méthodes thermo-barométriques conventionnelles, demeurent autour de 800 ± 50 °C. Cependant, la variabilité des estimations est importante (~ 400 °C) entre les géothermomètres utilisés et en fonction de la distance par rapport aux péridotites (Figure 2.15a,b). Avec la découverte du disthène dans la semelle de haute température de Khubakhib, les pressions calculées sont réévaluées à la hausse, autour de 1.1 ± 0.2 GPa (Gnos, 1992, 1998).

Les conditions P-T calculées à partir de la méthode *average P-T* de THERMO-CALC<sup>©</sup> (Powell & Holland, 1994) sur la semelle métamorphique de Khubakhib sont autour de 840 ± 70 °C et 1.16 ± 0.16 GPa (Figure 2.15e ; Searle & Cox, 2002). A Wadi Tayin et Sumeini, des conditions P-T sont comprises entre 770 et 900 °C et entre 1.1 et 1.3 GPa (Figure 2.15f ; Cowan et al., 2014). Ces résultats sont cohérents avec les estimations réalisées par les méthodes thermo-barométriques conventionnelles.

À l'inverse du chemin P-T classique dessiné pour les roches de HP-BT formées lors de la subduction continentale, les chemins produits pour la semelle métamorphique sont anti-horaires (Figure 2.15d,e ; Hacker et al., 1996, Searle & Cox, 2002). Ces chemins résultent notamment de simulations thermiques de l'interface de subduction lors de l'initiation d'une subduction océanique impliquant une lithosphère nouvellement formée (Hacker, 1991). La plaque plongeante est métamorphisée à haute température au contact des péridotites de la plaque supérieure encore chaude ( $\geq 1000$  °C) lorsqu'une portion de la plaque plongeante est accrétée à la plaque supérieure. Cette écaille, la future semelle métamor-

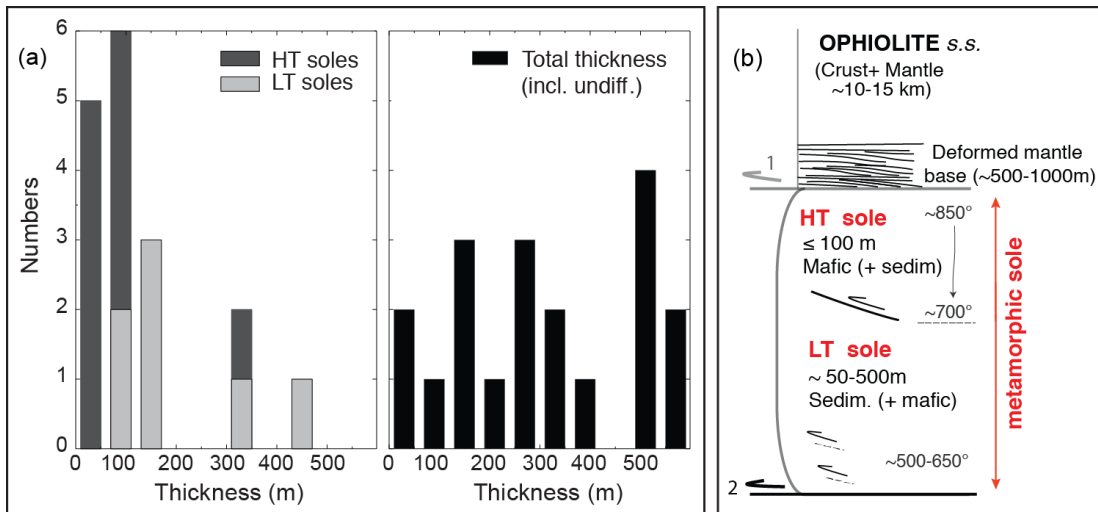


FIGURE 2.16 – Structure des semelles métamorphiques à l'échelle mondiale : a) histogrammes de fréquence des épaisseurs des semelles métamorphiques de haute et basse températures ; b) séquence structurale et métamorphique schématique de la base des complexes ophiolitiques. Figure modifiée d'après Agard et al. (2016).

phique, est ensuite exhumée le long d'une interface en refroidissement, donc le long d'un gradient thermique plus faible.

### 2.2.3 Synthèse des caractéristiques des semelles métamorphiques mondiales

Directement situées les péridotites des grandes ophiolites obductées, les semelles métamorphiques ont généralement une épaisseur maximale de  $\sim 500$  m. Lorsque leur séquence est la plus complète, leur sommet est majoritairement constitué de roches métabasiques sombres dans lesquelles peuvent être intercalées localement des passées métasédimentaires. Les roches métabasiques évoluent généralement depuis des niveaux massifs mylonitiques à amphibole + plagioclase + grenat + clinopyroxène (Searle, 1980, Gnos, 1998) et plus rarement à orthopyroxène (Terre Neuve; Jamieson, 1981) vers des niveaux moins déformés essentiellement composés d'amphibole + plagioclase avec une taille de grains plus importante en descendant dans la séquence. La présence de silicates d'alumine est rare. En Oman, seul le disthène a été décrit dans des amphibolites (Gnos, 1992). Ces assemblages minéralogiques sont caractéristiques d'un métamorphisme de haute température – moyenne pression (HT-MP) dans les faciès amphibolitique et granulitique. Les conditions pression-température (P-T) du pic de métamorphisme sont généralement estimées autour de  $800 \pm 200$  °C et  $1.0 \pm 0.4$  GPa (McCaig, 1983, Jamieson, 1986, Gnos, 1998, Hacker & Gnos, 1997, Cowan et al., 2014, Plunder et al., 2015, 2016, Agard et al., 2016), soit entre 30 et 40 km de profondeur pour des températures au-dessus du solidus hydraté des basaltes.

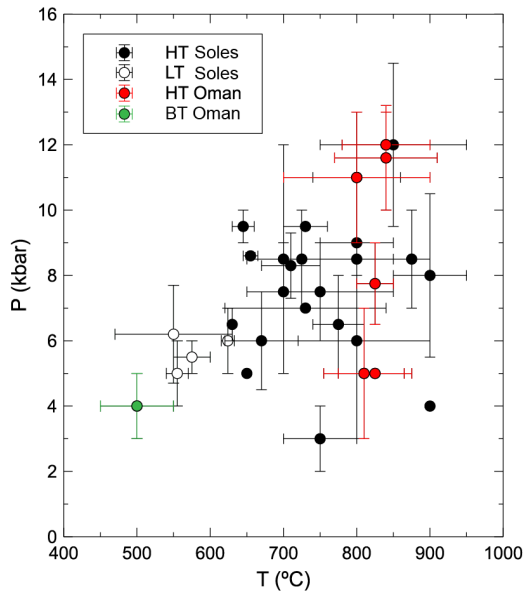


FIGURE 2.17 – Distribution pression-température des semelles métamorphiques haute et basse températures à l'échelle mondiale. En rouge sont indiquées les conditions estimées pour les semelles métamorphiques de Semail (Oman, UAE).

La base des semelles métamorphiques est caractérisée par un ensemble de roches de teinte plus claire. Il repose dans la plupart des cas sur des sédiments non à peu métamorphiques de la marge continentale. Il contient une importante fraction métasédimentaire composée de méta-radiolarites et de méta-carbonates. Il est constitué de quartz avec des minéraux annexes typiques du faciès des schistes verts comme la muscovite, la chlorite, l'actinote et la piémontite ainsi que la calcite et la tremolite dans les passées plus carbonatées. Les quelques intercalations métabasiques sont composées principalement d'épidote, d'albite et d'actinote. Cette séquence de bas grade métamorphique est souvent peu étudiée. Les conditions de formation de cette unité, rarement estimées, sont autour de  $550 \pm 100^\circ\text{C}$  et  $0.5 \pm 0.2 \text{ GPa}$  (Jamieson, 1986, Bucher, 1991a, Gaggero et al., 2009) avec, là encore, des incertitudes marquées en terme de pression et de température.

Un changement abrupt de métamorphisme et de lithologie peut localement exister entre ces deux ensembles. Certains auteurs suggèrent alors la présence d'un contact tectonique entre ces deux séquences. Cependant, cette discontinuité structurale dans les semelles métamorphiques reste débattue (Hacker & Mosenfelder, 1996).

Les datations radiométriques révèlent que les semelles métamorphiques se forment généralement dans les 1 à 2 Ma après l'accrétion magmatique des ophiolites sus-jacentes. Corrélée aux ophiolites, l'exhumation de semelles métamorphiques n'est pas un processus régulier dans le temps. De plus, il ne semble pas y avoir de semelles métamorphiques plus vieilles que 600 Ma. Enfin, selon les études, les âges attribués aux unités de haute et de basse

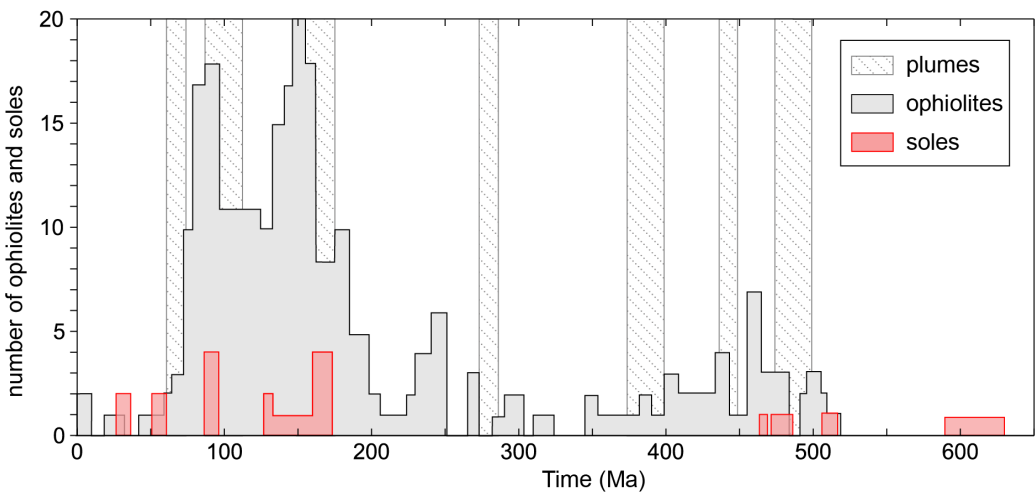


FIGURE 2.18 – Distribution temporelle des ophiolites (Dilek & Furnes, 2011), des plumes majeurs (Vaughan & Scarrow, 2003) et des semelles métamorphiques.

températures de la semelle métamorphique sont selon les études similaires ou légèrement différents (la seconde succédant de quelques centaines de milliers d'années la première).

L'interprétation des données radiométriques est très importante puisqu'elle constraint fortement les modèles de formation des semelles métamorphiques. Les données indiquant un même âge pour la semelle métamorphique permettent de suggérer que la semelle métamorphique se forme dans un très court moment (au moins dans l'incertitude de la mesure des méthodes utilisées) après l'initiation des zones de subduction. Les âges indiquant une mise en place différée de l'unité du faciès des schistes verts par rapport à l'unité du faciès amphibolitique à granulitique sont compatibles avec les conditions de pressions différentes estimées pour ces deux formations et leur position structurale actuelle. Cette hypothèse est aussi renforcée par le fait que l'on retrouve toujours l'unité basse température sous l'unité haute température, ce qui suggère que le contact entre cette dernière et les péridotites précède la formation de l'unité du faciès des schistes verts). Cependant, l'incertitude sur les données radiochronologiques ne permet pas de confirmer définitivement cette hypothèse, et ne permettent pas non plus de distinguer des différences à l'intérieur de chaque unité.

De plus, les méthodes radiométriques, selon la gamme de température subie, ne datent pas tant l'âge du métamorphisme que l'âge auquel la semelle métamorphique a franchi la température de fermeture du système (propre à chaque minéral). Les températures de fermeture peuvent varier en fonction de la taille des grains et de la vitesse du refroidissement, des fluides et de la déformation. Dans le cas de la méthode  $^{40}\text{Ar}/^{39}\text{Ar}$ , les températures de fermeture respectives de l'amphibole et de la muscovite varient autour de 550 °C (Harrison, 1982) et de 400 °C (Harrison et al., 2009). Ces températures sont proches de celles de l'unité du faciès des schistes verts mais très éloignées de celles estimées

pour l'unité de faciès amphibolitique à granulitique. Ce faisant, si cette dernière est déjà exhumée aux conditions de formation de la semelle de basse température lorsque celle-ci se forme, des âges similaires seraient attendus pour ces deux formations.

## La structure thermique

S'il a été rapidement admis que les semelles métamorphiques résultent d'une formation à des conditions HT-MP nécessitant un contexte thermique particulier, celui-ci reste encore très discuté. Or, contraindre leur origine et leurs mécanismes de mise en place sont des enjeux majeurs afin de mieux comprendre la dynamique des zones de subduction au moment de leur initiation.

La séquence litho-métamorphique inverse des semelles métamorphiques pose de nombreuses questions encore non résolues, notamment quant à sa formation. D'une épaisseur de moins de 500 m, les semelles métamorphiques sont interprétées comme structuralement continues, donc présentant un gradient thermique très élevé ( $\geq 1000^\circ\text{C/km}$ ; Hacker & Mosenfelder, 1996). Ce gradient est deux ordres de grandeurs supérieurs à celui calculé à l'interface des plaques dans les modèles numériques actuels (Gerya, 2011, Maffione et al., 2015, Duretz et al., 2016) et jusqu'à 10 fois supérieurs à ceux préservés au niveau des anciennes interfaces de subduction aujourd'hui exhumées (Peacock, 1987). La valeur de ce gradient supposé est également à mettre en regard du gradient thermique de la zone de subduction lors de la formation des semelles métamorphiques qui est  $\sim 20^\circ\text{C/km}$ . De plus, bien que leur foliation principale et leurs isogrades métamorphiques sont sub-parallèles entre elles, certaines études ont montré l'existence d'un léger changement de linéation entre les unités de haute et basse températures, comme en Oman (Boudier et al., 1985, Gray & Gregory, 2000, Cowan et al., 2014) ou à Terre Neuve (Dewey & Casey, 2013).

Les températures maximum ( $\geq 800^\circ\text{C}$ ) estimées pour les semelles métamorphiques sont bien supérieures aux températures données pour la fusion partielle des basaltes et des sédiments hydratés. Dans leur partie sommitale, caractérisée par les températures les plus élevées, les niveaux métasédimentaires (plus sensibles à la fusion partielle) sont régulièrement absents. Pourtant, très peu de preuves de fusion *in-situ* sont rapportées dans la semelle métamorphique et celles-ci sont limitées à 5–10% du volume total (Searle & Malpas, 1982, Boudier et al., 1988, Hacker & Gnos, 1997, Searle & Cox, 1999). À l'inverse, la refertilisation de la base des péridotites par percolation de liquide silicaté est plus communément observée (Boudier et al., 1988, Takazawa et al., 2003, Pirard, 2012, Yoshikawa et al., 2015, Haase et al., 2016, Soret et al., 2016).

### How metamorphic soles get welded to the overlying ophiolite?

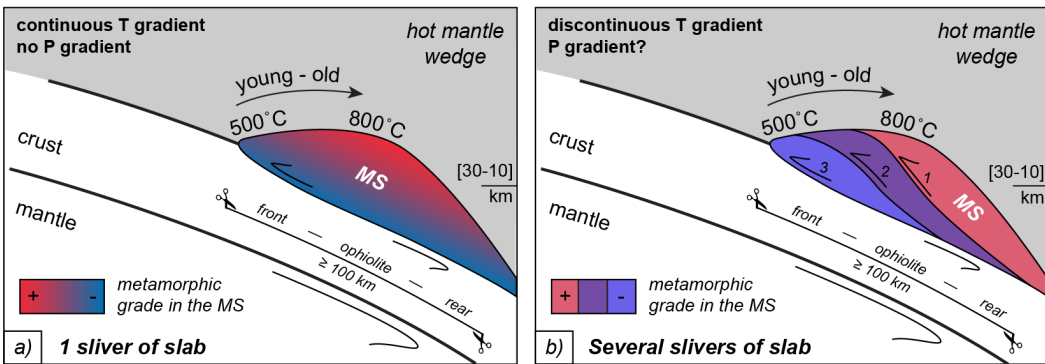


FIGURE 2.19 – Modèles de formation des semelles métamorphiques et leur accrétion à la sus-jacente future ophiolite.

- La structure des semelles métamorphiques est-elle continue ? Est-il possible de distinguer des variations de lithologie et de métamorphisme cohérentes le long d'une même séquence permettant de définir des sous-unités ?
- Les semelles métamorphiques ont-elles fondu et dans quelle proportion ?
- Peut-on raffiner les estimations P-T de formation des semelles métamorphiques ?

### Le *conundrum*

Il est admis que les semelles métamorphiques se forment au contact des périclites mylonitisées formant la base actuelle des ophiolites. Autrement dit, le contact périclites-semelles métamorphiques est supposé précoce dans l'histoire des subductions. Cela signifie que l'exhumation du complexe ophiolitique se produit de manière conjointe et simultanée.

Or, les épaisseurs actuelles des ophiolites sus-jacentes ( $\leq 15\text{--}20$  km ; Lippard, 1986, Dilek & Furnes, 2009) ne sont pas compatibles avec les estimations barométriques au pic de métamorphisme pour les semelles métamorphiques ( $\sim 1$  GPa soit 30–40 km de profondeur ; Gnos, 1998, Wakabayashi & Dilek, 2000, Searle & Cox, 2002, Cowan et al., 2014, Guilmette et al., 2012, Plunder et al., 2015). Cet écart entre les pressions estimées et les épaisseurs ophiolitiques observées représente le "*metamorphic sole conundrum*" (Hacker & Gnos, 1997), par opposition à l'*"ophiolite conundrum"* qui souligne les controverses autour de la nature et l'origine des ophiolites obductées (Moores et al., 2000).

Plusieurs études ont tenté de répondre à cette problématique en proposant des modèles d'amincissement tectonique (Searle & Malpas, 1982, Boudier et al., 1988, Gray &

Gregory, 2000, Agard et al., 2010, Lagabrielle et al., 2013) ou magmatique (Maffione et al., 2015, Van Hinsbergen et al., 2015) de l'ophiolite. Toutefois, aucun de ces modèles n'expliquent l'accrétion des semelles métamorphiques. En effet, ils ne s'intéressent pas ou que très peu à la formation des semelles métamorphiques, qui sont pourtant des contraintes rares et essentielles.

Une autre explication avancée à ce *conundrum* est la surévaluation des profondeurs de formation des semelles métamorphiques de haute température. Les pressions estimées seraient en partie augmentées par de la surpression tectonique survenant à l'interface des plaques (McCaig, 1983). Cette surpression affectant les péridotites et les semelles métamorphiques lors de leur (dé-)formation pourrait réduire jusqu'à un facteur 2 les profondeurs estimées (Petrini & Podladchikov, 2000). Ces nouvelles profondeurs ( $\sim 15\text{--}20$  km) correspondraient d'avantage aux épaisseurs des ophiolites actuelles. Elles seraient également équivalentes à celles estimées pour la semelle de basse température.

- Les semelles métamorphiques mondiales se forment-elles toutes à une même profondeur ? Les estimations barométriques peuvent-elles être précisées et généralisées ?
- Comment expliquer l'écart entre les pressions estimées (converties en profondeur) et l'épaisseur actuelle des ophiolites ?
- Peut-on discriminer 1 - exhumation relative des semelles métamorphiques ; 2 - amincissement de l'ophiolite ; 3 - surpression tectonique ?

## La distribution spatiale sous l'ophiolite

La distribution spatiale des semelles métamorphiques sous les ophiolites soulève également des questions. Certaines ophiolites ont des dimensions qui atteignent plusieurs centaines de kilomètres de long et/ou de large (Oman, Turquie, Terre Neuve, Albanie), et sous ces ophiolites la semelle métamorphique est ubiquiste.

Seule une récente étude, réalisée sur les semelles métamorphiques de Turquie occidentale, fait mention d'une disparité dans les conditions P-T des semelle métamorphiques corrélée à leur répartition spatiale sous l'ophiolite. L'ophiolite de Turquie occidentale s'étend sur plus de 200 km de large. Plunder et al. (2016) ont démontré que la semelle métamorphique sous-jacente n'enregistrait pas les mêmes conditions P-T selon qu'elle affleurait au front de propagation ou à plus de 200 km en arrière de l'ophiolite. Au contraire de la semelle métamorphique présente au front de propagation, celle située en arrière de l'ophiolite est affectée par une rétromorphose dans le faciès des schistes bleus ( $\sim 1.2$  GPa –  $425^\circ\text{C}$ ).

---

Or, les deux semelles métamorphiques présentent originellement les mêmes conditions P–T–t (1 GPa – 850 °C à 93 Ma; Plunder et al., 2016). En partant de ce constat, Plunder et al. (2016) proposent un modèle évolutif polyphasé impliquant un différentiel de dynamique d'exhumation entre la semelle métamorphique non affectée et celle affectée par la rétromorphose dans le faciès des schistes bleus. En effet, l'absence d'évidence de cette rétromorphose dans la semelle métamorphique au front de propagation de l'ophiolite implique une exhumation rapide dans l'histoire de la subduction, avant que celle-ci n'ait atteint l'état d'équilibre thermique. À l'inverse, la semelle métamorphique présente à plus de 200 km du front de propagation de l'ophiolite est restée plus longtemps à sa profondeur de formation, alors que le régime thermique de la subduction se refroidissait, passant de 850 à 425 °C à ~ 35 km de profondeur, soit proche de son état d'équilibre.

Aucune autre étude ne mentionne précisément de telles disparités. Dans la semelle métamorphique d'Oman, de la Mg–riebeckite et de la stilpnomelane sont rapportées dans la région d'Asimah–Dibba (Allemand & Peters, 1972, Gnos & Kurz, 1994), à l'extrême nord de l'ophiolite. Du disthène dans la semelle haute température de Khubakhib (Gnos, 1992, 1998) et de la crossite dans la semelle basse température de Sumeini (Searle, 1980, Searle & Malpas, 1982, Searle & Cox, 1999) sont également observés au nord du Samail Gap. Au sud de celui-ci, seule la crossite est décrite (Rabu, 1987). Cependant, ces minéraux ne sont pas des phases index du faciès des schistes bleus. De plus, ces minéraux semblent être présents au pic de métamorphisme et non secondaires.

- Les semelles métamorphiques enregistrent-elles toutes les mêmes conditions P–T sous les plus grandes ophiolites (comme en Oman) ?
  - Quelles implications sur l'environnement et la dynamique en trois dimensions des zones de subductions lors de leur initiation ?

## La déformation

Les conditions P–T(–t) sont de fortes contraintes sur la dynamique de formation et d'exhumation des semelles métamorphiques. Si les semelles métamorphiques enregistrent les mêmes conditions P–T–t alors le fait de les retrouver à plus de 100 km à travers l'ophiolite implique probablement l'existence de mécanismes d'extension importants.

Or, malgré une foliation souvent marquée, les semelles métamorphiques ne sont pas (sauf rares exceptions) caractérisées à petite échelle par des déformations importantes qui pourraient expliquer cette extension. Les nombreux plis observés dans les semelles

métamorphiques épaissent leur séquence et donc limitent leur étirement. De nombreuses failles normales structurent également ces unités. Cependant, elles sont souvent reliées au bombement de la lithosphère continentale sous-jacente lors de son exhumation (Agard et al., 2010), donc lors d'épisodes tardifs et froids.

En Oman comme en Turquie, la semelle métamorphique affleure en avant et en arrière du front de propagation de l'ophiolite. Cependant les affleurements ne sont pas continus. La continuité spatiale des semelles métamorphiques sous les ophiolites est difficile à évaluer. Pourtant, la distribution spatiale des semelles métamorphiques, corrélée à leurs conditions P-T-t, est une contrainte essentielle dans la quantification de leur déformation.

- Les semelles métamorphiques sont-elles latéralement continues sous les ophiolites ?
- Par quels mécanismes se déforment-elles ? Peuvent-ils expliquer leur distribution spatiale sous les ophiolites ?
- Compte tenu de son épaisseur actuelle, peut-on quantifier le taux d'extension subi par la base de l'ophiolite ? Quelle est et comment se répartie cette extension dans la semelle métamorphique et les péridotites rubanées sus-jacentes ? Cette extension peut-elle expliquer l'épaisseur "anormale" des ophiolites et être une réponse au *conundrum* ?

---

## 2.3 Rhéologie des semelles métamorphiques

Les semelles métamorphiques de haute température sont constituées principalement de métabasaltes cisaillées à  $\sim 800^\circ\text{C}$  – 1 GPa. Elles sont composées d'amphibole  $\pm$  plagioclase  $\pm$  clinopyroxène  $\pm$  grenat. Ces roches dérivent de portions de lithosphère océanique subduite et métamorphisée à haute température lors de leur juxtaposition au coin de manteau sus-jacent. Leur importante déformation au pic de métamorphisme est interprétée comme synchrone de leur accrétion au manteau de la plaque supérieure qui formera la base de l'ophiolite obductée. Cette déformation renseigne donc directement sur les processus mécaniques et la rhéologie effective à l'interface des plaques lors de l'initiation des zones de subduction. Cette déformation n'a pourtant été que très peu explorée (Hacker and Christie, 1990).

### 2.3.1 Rhéologie des amphibolites

Les amphibolites sont communément associées au développement de grandes bandes de cisaillement ductile au sein des lithosphères continentales et océaniques (Kirby, 1985). **Elles témoignent de fortes rétroactions positives entre localisation de la déformation et circulation de fluides.** Le comportement mécanique des amphibolites participe donc à la rhéologie des croûtes inférieures continentales et océaniques (Fig. 2.20), et de l'interface des plaques en zone de subduction.

Sur la base d'observations des profondeurs sismogéniques, des épaisseurs élastiques et des extrapolations des lois rhéologiques expérimentales, il a été suggéré que la croûte inférieure a une viscosité faible, à l'inverse de la croûte supérieure et du manteau sous-jacent qui se comportent de manière cassante. C'est le modèle du "*jelly sandwich*" (Fig. 2.20 ; Burov & Watts, 2006). Cependant, ce contraste de viscosité important en base de croûte est remis en question par d'autres études géophysiques qui évoquent la possibilité d'une croûte inférieure plus résistante, avec des viscosités proches voire supérieures à celles de la croûte supérieure. C'est le modèle de la "*crème brûlée*" (Fig. 2.20 ; Maggi et al., 2000, Jackson, 2002, McKenzie & Jackson, 2002, Burov & Watts, 2006). Enfin, il existe un dernier modèle dans lequel toute la colonne lithosphérique (et notamment la croûte inférieure) est faiblement résistante en raison de la présence de nombreuses zones de cisaillement (Fig. 2.20 ; Bürgmann & Dresen, 2008).

De nombreuses études expérimentales ont permis d'augmenter l'état des connaissances sur la rhéologie des roches océaniques en fonction de la vitesse de déformation, de la taille de grains ou encore de la fugacité en H<sub>2</sub>O (Hacker & Christie, 1990, Mackwell et al.,

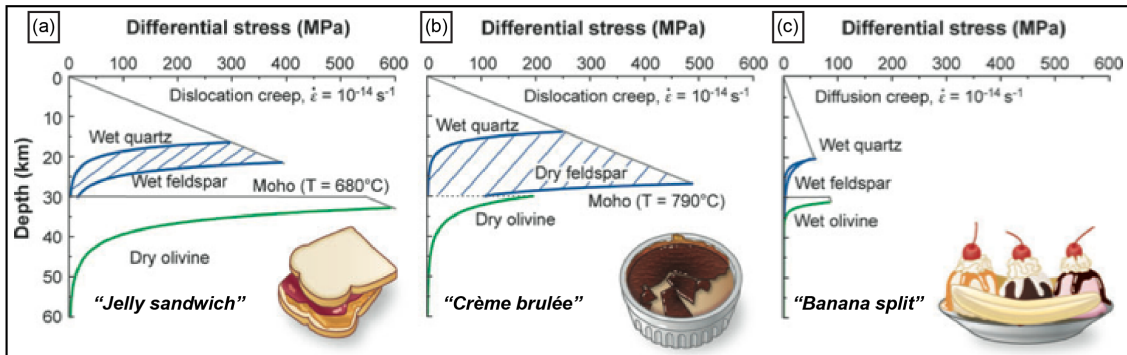


FIGURE 2.20 – Vue schématique des principaux modèles rhéologiques de la lithosphère continentale. Figure modifiée d'après Bürgmann & Dresen (2008). a) Modèle du "jelly sandwich" (Burov & Watts, 2006) caractérisé par une croûte moyenne à inférieure faiblement résistant et un manteau supérieur composé d'olivine anhydre très résistant (Hirth & Kohlstedt, 2003). b) Modèle de la "crème brûlée" (Burov & Watts, 2006) composé d'une croûte inférieure plus résistante que le manteau supérieur, affaibli par un géotherme élevé et une plus forte teneur en eau. c) Modèle du "banana split" caractérisé par une croûte et un manteau faiblement résistants, affaiblis par la présence de nombreuses zones de cisaillement (Bürgmann & Dresen, 2008).

1998, Rybacki & Dresen, 2000, Stunitz et al., 2003, Dimanov & Dresen, 2005, Mehl & Hirth, 2008, Homburg et al., 2010, Getsinger et al., 2013, Getsinger & Hirth, 2014). Différentes lois rhéologiques ont pu être établies à partir de ces études et extrapolées aux conditions naturelles, mais le comportement mécanique de ces roches à la transition fragile-ductile reste encore à être éclairci (Hacker & Christie, 1990).

À partir de gabbros mylonitiques et non déformés récoltés in-situ, Mehl & Hirth (2008) concluent que la viscosité des roches gabbroïques anhydres à grains grossiers composées de 50% de plagioclase et 50% de clinopyroxène est similaire à celle de l'olivine aux conditions du Moho (Fig. 2.21a). Ce résultat est en faveur d'un faible contraste de viscosité entre la croûte inférieure et le manteau supérieur, sans toutefois prendre en compte la présence possible de phases hydratées stables jusqu'à 800-900°C, les amphiboles. Ils indiquent cependant que la localisation des contraintes dans des bandes de cisaillements adoucit fortement la résistance de la croûte (en diminuant sa viscosité d'un facteur 2 à 4 ; Fig. 2.21a).

Homburg et al. (2010) ont également examiné le contraste de viscosité croûte–manteau en analysant des dikes gabbronoritiques intrudant le manteau ophiolitique d'Oman. À partir de leurs observations et des lois de fluages pour le plagioclase (Rybacki & Dresen, 2004) et l'olivine (Hirth & Kohlstedt, 2003), les auteurs démontrent qu'à haute température ( $T \geq 700^\circ\text{C}$ ) le plagioclase est moins visqueux que l'olivine en conditions hydratées comme anhydres (Fig. 2.21b). Ils concluent donc qu'une proportion forte de plagioclase peut introduire de grands contrastes rhéologiques en base de croûte. L'effet adoucissant

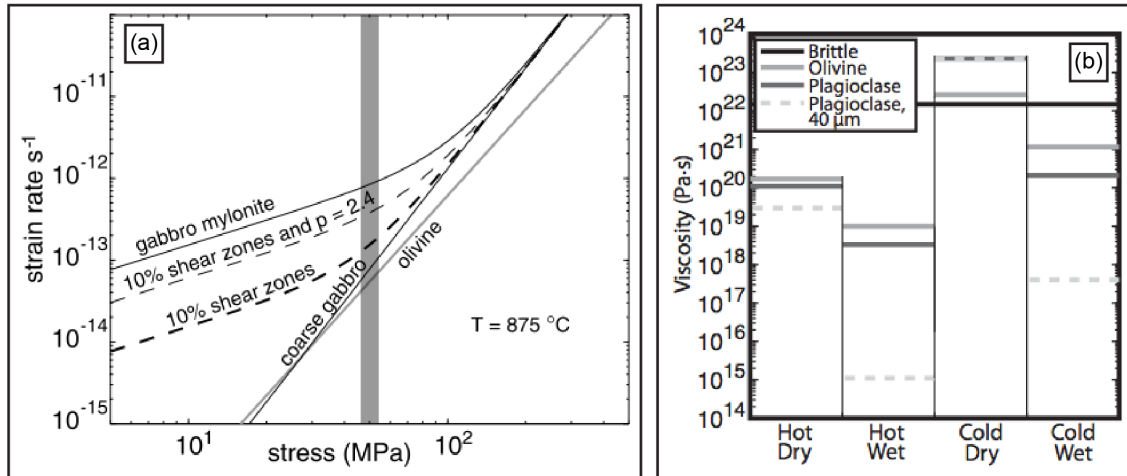


FIGURE 2.21 – a) Graphique mettant en évidence le fort adoucissement de la croûte inférieure gabbroïque en présence de bandes de cisaillement. Les courbes représentent les vitesses de déformation en fonction des contraintes pour un gabbro à grains grossiers ( $\sim 3000 \mu\text{m}$ ) et un gabbro mylonitique à grains fins ( $\sim 35 \mu\text{m}$ ) contenant 50% d'anorthite et de clinopyroxène, une olivine anhydre (3000  $\mu\text{m}$ ) et une colonne crustale avec 10% de bandes de cisaillement. Pour une contrainte de 50 MPa, la vitesse de déformation d'une croûte gabbroïque avec 10% de bandes de cisaillement est 2 fois plus rapide que pour une croûte gabbroïque non déformée. Ce différentiel de vitesse s'accroît dans le cas d'une réduction de la taille de grains. Figure modifiée d'après Mehl & Hirth (2008). b) Viscosités calculées pour le plagioclase et l'olivine en conditions hydratée et anhydre pour une croûte continentale de 70 km d'épaisseur (comme observée au Tibet) et une vitesse de déformation de  $10^{-13} \text{ s}^{-1}$ . Avec un géotherme froid, il existe un fort contraste entre les systèmes hydratés et anhydres. En conditions hydratées, le plagioclase est beaucoup moins résistant que l'olivine alors que le contraste est inversé en conditions anhydres. En présence d'un géotherme élevé, le plagioclase est moins visqueux que l'olivine, indépendamment de la fugacité en  $\text{H}_2\text{O}$ . Figure modifiée d'après Homburg et al. (2010).

peut être davantage augmenté dans le cas d'une localisation durable de la déformation sur des bandes de cisaillement riches en plagioclase, d'autant plus si elle est associée à des réactions d'hydratation.

Stünnitz & Tullis (2001) suggèrent que le contraste de viscosité peut être encore accru lors de la formation syn-cinématique de nouvelles phases de tailles plus réduites par réaction d'hydratation. Les auteurs ont mené des déformations expérimentales en cisaillement simple sur des agrégats de plagioclase de composition intermédiaire avec ajout de 0.1 à 0.4 wt% d'eau. Durant la déformation à des conditions de déséquilibre chimique, les agrégats de plagioclase réagissent avec l'eau pour former un mélange de zoisite + plagioclase (enrichi en sodium) + mica + quartz + disthène le long de fines bandes de cisaillement accommodant l'essentiel de la déformation (Fig. 2.22a). Dans le même temps, les échantillons enregistrent une forte réduction des contraintes de cisaillement (Fig. 2.22b). À micro-échelle, le mélange de grains extrêmement fins nouvellement créé ne présente pas

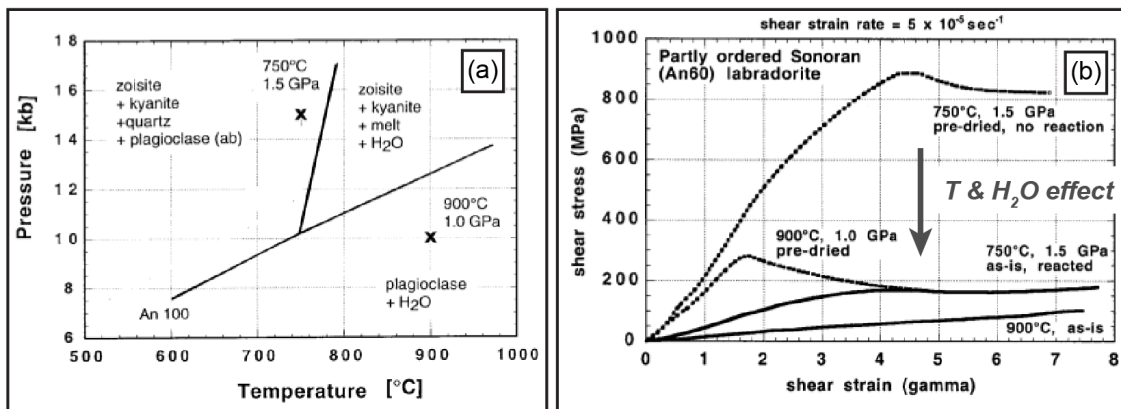


FIGURE 2.22 – a) Diagramme de phase du plagioclase déterminé expérimentalement. Les croix représentent les conditions P-T des deux types d'expérience menés par Stünitz & Tullis (2001), b) Comportement mécanique du plagioclase, de type labradorite, déformé en cisaillement simple. À l'inverse des échantillons "*pre-dried*", les échantillons "*as-is*" contiennent 0.4 wt% de H<sub>2</sub>O afin de permettre la réaction plagioclase = zoisite + mica + quartz + disthène à 750 °C. La flèche souligne l'effet adoucissant provoqué par l'augmentation de température et la formation de nouvelles phases à grains très fins par réaction d'hydratation. Figure modifiée d'après Stünitz & Tullis (2001).

de dislocation, à l'inverse des agrégats de plagioclase. Les auteurs en concluent que la formation de nouvelles phases et/ou leur petite taille peut affaiblir localement la résistance des roches crustales, par le biais d'un changement dans les mécanismes de déformation (passant d'un fluage par dislocation à un fluage par diffusion accommodé par l'apparition de glissements aux joints de grains).

Getsinger et al. (2013) ont également étudié l'influence des circulations de fluides dans la localisation de la déformation et la rhéologie de la croûte inférieure continentale, mais cette fois dans des roches polycristallines à plagioclase et amphibole. Les auteurs se sont, pour cela, intéressés à des roches gabbroïques localement mylonitisées et hydratées dans des bandes de cisaillement de croûte inférieure. Leurs analyses indiquent que la localisation de la déformation est directement liée à des infiltrations de fluides permettant l'hydratation des roches basiques. En favorisant la déformation plastique des plagioclases, la formation de nombreuses amphiboles et une déformation par fluage diffusion, les auteurs estiment que ces circulations de fluides diminuent dramatiquement la viscosité des roches gabbroïques (Fig. 2.23a). La déformation est alors localisée sur ces niveaux, dont la viscosité plus faible contraste avec celle des roches encaissantes non hydratées. La réduction de taille des grains, proposée par Stünitz & Tullis (2001) comme mécanisme essentiel à la localisation de la déformation, est donc replacée au second ordre.

Une étude expérimentale en cisaillement simple sur des amphibolites naturelles et synthétiques (Fig. 2.23b ; Getsinger & Hirth, 2014) semble confirmer que la rhéologie des

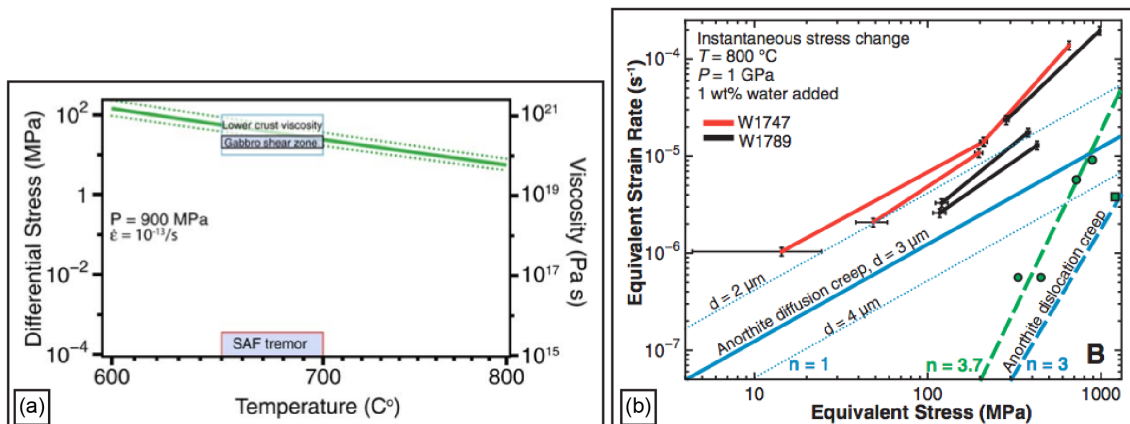


FIGURE 2.23 – a) Contraintes différentielles en fonction de la température estimées par Getsinger et al. (2013). Les courbes vertes représentent la loi de fluage pour l'anorthite (Rybacki et al., 2006). b) Vitesses de déformation équivalente en fonction des contraintes équivalentes définies à partir des données expérimentales sur amphibolites synthétiques, d'après Getsinger & Hirth (2014). Les lois de fluage par diffusion et par dislocation pour l'anorthite hydratée par diffusion (Rybacki et al., 2006) sont représentées en bleu. La courbe verte représente la loi de fluage par dislocation pour les amphibolites (Hacker & Christie, 1990). Le carré vert correspond à l'amphibolite naturelle déformée expérimentalement.

amphibolites à plagioclase est proche de celle établie pour le plagioclase hydraté. Cette dernière fournirait donc une bonne approximation de la résistance de la croûte inférieure hydratée. Toutefois, les auteurs reconnaissent que la déformation des amphiboles et son influence sur la rhéologie de roches polycristallines restent encore à préciser. En effet, certaines études avaient précédemment démontré que les amphiboles avaient un comportement mécanique très résistant et cassant (Brodie & Rutter, 1985, Hacker & Christie, 1990). La déformation ductile n'avait été atteinte que lors d'expériences en cisaillement simple sur des amphibolites synthétiques à grains très fins ( $\sim 75\text{--}100 \mu\text{m}$ ; Hacker & Christie, 1990). Les auteurs avaient alors interprété cette déformation par l'introduction de défauts dans le réseau cristallin des amphiboles lors de leur synthèse et/ou par une plus faible taille de grains.

Le comportement mécanique des amphiboles doit donc être précisé. Les métabasaltes de haute température de la semelle métamorphique, équilibrés en faciès amphibolitique à granulitique, formés pour une bonne part d'amphbole, constituent donc un objet d'étude particulièrement adéquat pour préciser les modalités de déformation des amphiboles (phase cristallographiquement complexe et chimiquement hautement variable). Ces métabasaltes présentent une minéralogie et des conditions P-T de formation similaires aux amphibolites de base de croûte continentale et océaniques. Certaines parties des amphibolites de la semelle métamorphique contiennent également des proportions importantes de clinopyroxène et de grenat ( $\geq 20\%$ ), permettant d'appréhender l'influence mécanique de ces phases.

### 2.3.2 Quelles contraintes pour la dynamique de subduction ?

Les semelles métamorphiques répertoriées à travers le monde partagent de nombreuses caractéristiques communes. Aidées des lois rhéologiques existantes pour des différents matériaux, ces similarités ont été des contraintes essentielles nous permettant d'élaborer un modèle général de formation des semelles métamorphiques. Ce modèle apporte un éclairage nouveau sur les modalités d'accrétion et d'exhumation de ces roches à l'interface des plaques. De manière plus générale, ce modèle permet de préciser les processus thermomécaniques responsables de la mise en place des jeunes zones de subduction océanique.

**La compilation pétro-structurale que nous avons établie montre que les conditions de formation des semelles métamorphiques sont remarquablement similaires, indépendamment de leur âge et de leur environnement de genèse.** Lorsque leur séquence est complète, les semelles métamorphiques sont généralement composées de l'accrétion de deux unités avec des lithologies et des conditions P-T intrinsèques. L'unité de plus haute température est composée essentiellement de métabasalte métamorphisé autour de 800 °C et 1 GPa. Cette unité affleure toujours au-dessus de la seconde unité, composée principalement de métasédiments, équilibrée autour 600 °C et 0.5 GPa et généralement plus épaisse : son accrétion s'effectue donc à moindre profondeur et plus tardivement que l'unité de haute température. Enfin, ces unités ne présentent que très rarement un re-équilibrage le long d'un gradient de haute pression – basse température.

Les estimations P-T-t des semelles métamorphiques sont à comparer à celles des roches éclogitiques. Malgré des lithologies parfois similaires, ces dernières résultent d'une accrétion toujours plus tardive (au moins 5 Ma après l'exhumation des roches de semelles métamorphiques), à plus grande profondeur et dans un régime de subduction plus froid (Wakabayashi, 1990, Agard et al., 2009). De plus, contrairement aux semelles métamorphiques qui sont systématiques sous les ophiolites obductées, la présence de roches éclogitiques exhumées (ou en tout cas observées) sous celles-ci est rare.

**La structuration des semelles métamorphiques témoigne donc des accrétions précoces et brèves de deux unités (d'abord riche en basalte, puis riche en sédiment) à l'interface des plaques et à des conditions P-T différentes, compatible avec un refroidissement continu de la zone de subduction.** Ces accrétions sont suivies d'une exhumation partielle rapide (conjointement avec la base du manteau ophiolitique montrant des déformations et des températures similaires ; Linckens et al., 2011, Herwegen et al., 2016, Soret et al., 2016), avant d'atteindre un régime de subduction plus mature, caractérisé par les rares exhumations des roches de haute pression basse température, schistes bleus ou éclogites.

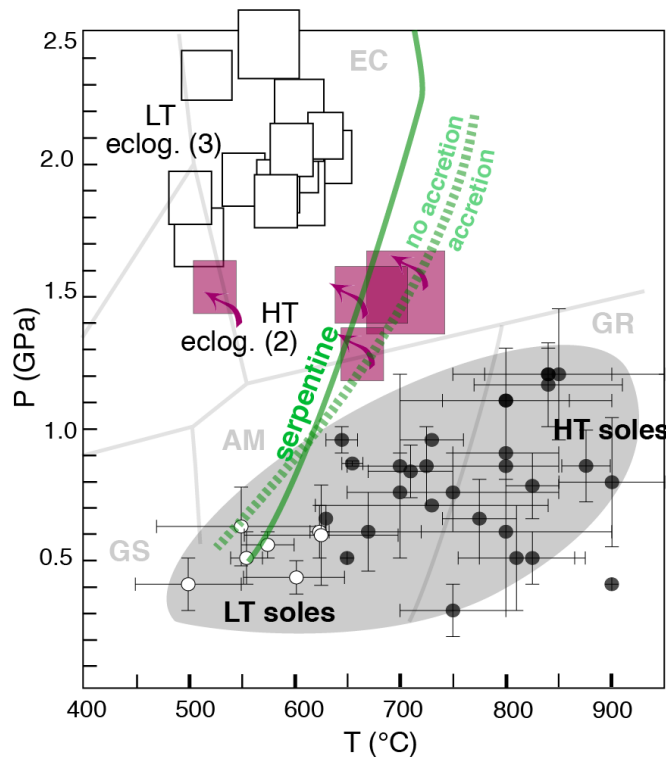


FIGURE 2.24 – Compilation des conditions P–T des semelles métamorphiques de haute et basse températures à l'échelle mondiale (cette étude). Ces conditions sont à comparer aux conditions P–T des roches de HP–BT (ici les éclogites) formées 10 à 15 Ma plus tard dans l'histoire des subductions.

Ces accrétions successives (et les déformations associées dans les semelles métamorphiques et dans les périclites basales des ophiolites) attestent d'éisodes successifs de couplage importants à l'interface de subduction. Elles témoignent également d'hétérogénéités (localisant la déformant) à l'intérieur de la plaque plongeante pour permettre le détachement de chaque unité, provoquant ainsi des sauts de l'interface de subduction.

Or il est essentiel de réaliser que l'interface des plaques sera d'autant plus couplée que les viscosités effectives des matériaux de part et d'autre seront proche — a contrario, un différentiel fort de part et d'autre entraînera une localisation de la déformation et un découplage de l'interface (c'est d'ailleurs l'argument généralement utilisé pour le rôle lubrifiant de la serpentine dans le coin de manteau; ?). Il est donc important de caractériser, à l'aide des lois de fluages existantes, l'évolution de la viscosité en fonction de la température des différents matériaux présents à l'interface des plaques en zones de subduction.

C'est l'objet de la compilation présentée ici.

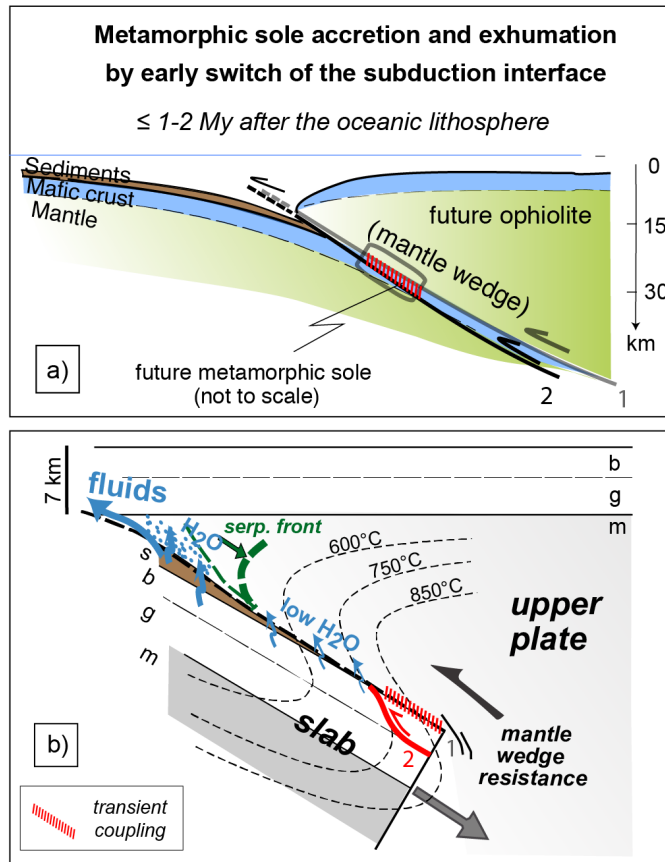


FIGURE 2.25 – (a) Modèle schématique d'accrétion des semelles métamorphiques par un saut précoce l'interface (1 vers 2) de subduction intra-océanique. L'exhumation partielle de la semelle métamorphique se fait ensuite conjointement avec la base de la future ophiolite obductée ; (b) Schéma d'une zone de subduction précoce caractérisant les processus d'hydratation du naissant coin mantellique et d'écaillages de portions de la plaque plongeante (les semelles métamorphiques) lors de couplage à l'interface des plaques.

Le comportement du coin de manteau de la plaque est reproduit à partir des lois de fluage des olivines anhydres et hydratées (ichiro Karato, 2010, Hirth & Kohlstedt, 2015) et de la serpentine. Compte tenu de leur nature et du peu de lois existant sur ces roches métamorphiques, les unités basiques et sédimentaires des semelles métamorphiques sont respectivement étudiées à partir des lois de fluages sur les amphibolites (Hacker & Christie, 1990) et sur le quartz (Ranalli & Murphy, 1987).

Ces lois de fluage montrent au premier ordre que, indépendamment de la température (et de la vitesse de déformation), la résistance mécanique des périclases (approchée par les lois pour l'olivine "dry" ou "wet") est toujours plus élevée que celle de la croûte océanique. De manière analogue, les sédiments, quoique de plus faible viscosité que la croûte océanique, sont plus résistants que la serpentine.

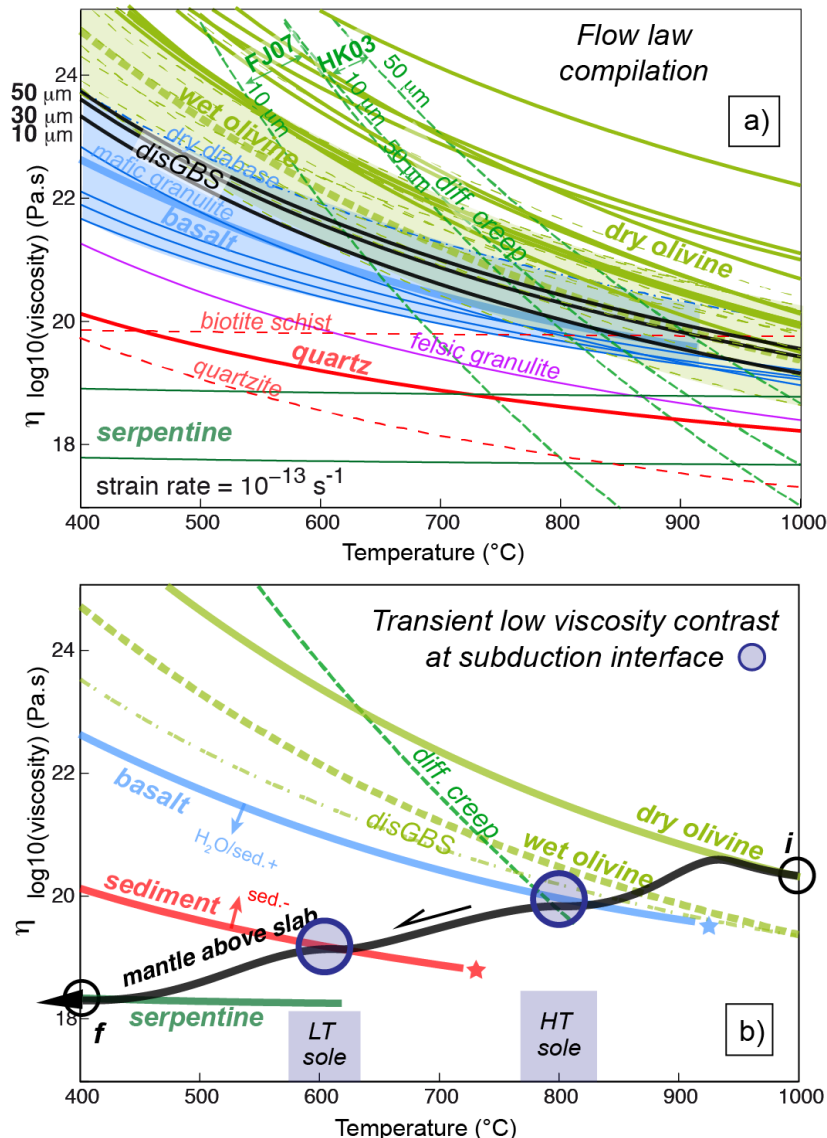


FIGURE 2.26 – (a) Courbes de viscosité en fonction de la température pour différents matériaux à l’interface de subduction déterminées à partir des lois de fluage existantes. (b) Mise en évidence de contraste de viscosité faible à l’interface de subduction lors du refroidissement et de l’hydratation du coin de manteau.

Un point, cependant, n'a pas reçu toute l'attention qu'il méritait : une fois la subduction initiée, le régime thermique à l'interface des plaques diminue, jusqu'à atteindre un état d'équilibre. Au fur et à mesure du refroidissement, les fluides libérés par la plaque plongeante au cours de son enfouissement vont permettre l'hydratation progressive du coin de manteau. Celle-ci se traduit par la stabilisation de phases hydratées (par ex., amphiboles) puis la serpentinisation progressive des péridotites de la plaque supérieure.

La viscosité des péridotites diminue alors progressivement jusqu'à approcher celle de la serpentine (Escartín et al., 2001). Il est donc possible de prévoir que, à mesure de la

mise en place de la subduction et de son refroidissement progressif, la viscosité du coin de manteau doit nécessairement diminuer. Les lois rhéologiques permettent de prédire qu'elle rejoindra dans un premier temps celle des roches crustales (autour de 800 °C) puis celle des roches sédimentaires (autour de 600 °C) au sommet de la plaque plongeante.

**Deux constatations s'imposent :**

- ces températures de "croisement rhéologique" correspondent approximativement aux conditions thermiques estimées pour les semelles métamorphiques ;
- de si faibles contrastes de viscosité peuvent être à l'origine d'épisodes de couplage important à l'interface de subduction.

A la lumière des observations et des données présentées dans les trois chapitres qui suivent, nous intégrerons ces considérations dans la discussion, afin de préciser les modalités d'accrétion durant la dynamique précoce des zones de subduction.



---

# 3 Structure, pétrologie et accrétion de la semelle métamorphique d’Oman

## 3.1 Préambule

Ce chapitre correspond à un article soumis dans la revue *Journal of Metamorphic Geology*.

Nous présentons un réexamen de la structure et des conditions de formation des semelles métamorphiques de haute température de Semail, le long de trois coupes principales dans les localités de Khubakhib et de Sumeini au nord, et de Wadi Tayin au sud. Sur la base d’observations structurales, de changements brusques dans la composition et dans les assemblages minéralogiques et de nouvelles estimations P–T, deux sous-unités tectoniques ont été définies dans l’unité amphibolitique de haute température. Leurs conditions P–T ont été calculées notamment au moyen de pseudosections à l’aide d’un nouveau modèle de fusion partielle dans le système des métabasites. Avec l’observation de zonations fortes dans les grenats des amphibolites des semelles métamorphiques d’Oman, des chemins P–T progrades sont également présentés. Un résultat de spectroscopie Raman sur la matière carbonée dans l’unité de basse température permet de confirmer les rares conditions thermiques préalablement estimées pour cette unité. En conclusion, la comparaison des trois coupes "classiques" de semelles métamorphiques a permis :

- d'affiner leurs modalités de formation, en démontrant qu'elles se forment toutes à des mêmes conditions P-T, sans preuve de gradient thermique continu.
- d'élaborer un modèle évolutif générique dans lequel la structuration des semelles métamorphiques résultent de la juxtaposition de multiples portions de la plaque plongeante écaillées et accrétées à différentes conditions P–T aux péridotites de la plaque supérieure.
- de préciser la dynamique de couplage mécanique à l'interface des plaques à l'initiation de la subduction.



## Petrological evidence for stepwise accretion of metamorphic soles during subduction infancy (Semail ophiolite, Oman and UAE)

Submitted in *Journal of Metamorphic Geology*

**Mathieu Soret<sup>1</sup>, Philippe Agard<sup>1</sup>, Benoît Dubacq<sup>1</sup>, Alexis Plunder<sup>1,2</sup>, Philippe Yamato<sup>3</sup>**

<sup>1</sup>Sorbonne Universités, UPMC Univ. Paris 06, CNRS, Institut des Sciences de la Terre de Paris (ISTeP), 4 place Jussieu 75005 Paris, France

<sup>2</sup>Department of Earth Sciences, Utrecht University, Heidelberglaan 2, 3584 CS Utrecht, The Netherlands

<sup>3</sup>Géosciences Rennes, Université de Rennes 1, CNRS, F-35042 Rennes, France

---

### 3.2 Abstract

Metamorphic soles correspond to tectonic slices welded beneath most large-scale ophiolites. These slivers of oceanic crust metamorphosed up to granulite facies conditions are interpreted as forming during the first My of intra-oceanic subduction from heat transfer from the incipient mantle wedge towards the top of the subducting plate. This study reappraises the petrological model for formation of metamorphic sole through detailed field and petrological work on three classical key sections from the Semail ophiolite (Oman and United Arab Emirates). Based on geothermobarometry and thermodynamic modelling, data show that metamorphic soles do not record a continuous temperature gradient, as expected from simple heating by the upper plate or by shear heating, and proposed by previous studies. The upper, high-temperature metamorphic sole is subdivided in at least two units, testifying to the stepwise formation, detachment and accretion of successive slices from the downgoing slab to the mylonitic base of the ophiolite.

Estimated peak pressure-temperature conditions through the metamorphic sole are, from top to bottom, 850 °C – 1 GPa, 725 °C – 0.8 GPa and 530 °C – 0.5 GPa. These estimates appear constant within each unit but separated by a gap of 100 to 200 °C and ~0.2 GPa. Despite being separated by hundreds of kilometres below the Semail ophiolite and having contrasting locations with respect to the ridge axis position, metamorphic soles show no evidence for significant petrological variations along strike.

With these new constraints, we suggest a new tectonic-petrological model for the formation of metamorphic soles below ophiolites. This model involves the stacking of several homogeneous slivers of oceanic crust and its sedimentary cover to form the present-day structure of the sole. These successive thrusts are the result of rheological contrasts between the sole, originally from the top of the subducting slab, and the peridotite above as the plate interface progressively cools down. This model brings important information on the thickness, the scale and the coupling state at plate interface during the early history of subduction/obduction systems.

### 3.3 Introduction

Metamorphic soles are thin (m to ~500 m thick), amphibolite to granulite facies slivers of oceanic crust with variable proportions of basaltic and sedimentary material underlying most large-scale ophiolites worldwide (Williams & Smyth, 1973, Wakabayashi & Dilek, 2000). They are interpreted as formed during the first few My of intra-oceanic subduction (Fig. 3.4a; Dewey, 1976, Spray et al., 1984, Boudier et al., 1988, Hacker, 1990, Dewey & Casey, 2013), when the crust of the subducted plate gets heated up by the mantle, scrapped off and accreted to the upper plate (the future ophiolite). In this paper "subduction initiation" or "subduction infancy" (Stern & Bloomer, 1992) is defined as the period immediately following intra-oceanic subduction nucleation, when a newly born subducting slab starts to penetrate into a young and hot mantle (Hacker & Gnos, 1997, Agard et al., 2016, Plunder et al., 2016) until reaching steady-state (Peacock & Wang, 1999, Syracuse et al., 2010). Metamorphic soles are therefore direct witnesses of deep processes over the first few million years of the existence of subduction zones, and provide key constraints for numerical modelling of young subduction zones (Hacker, 1990, Gurnis et al., 2004, Gerya, 2011, Duretz et al., 2016). Their emplacement, by accretion process at the base of the ophiolitic mantle and transfer across the subduction plate interface, testifies of mechanical coupling during that period, with implications for crustal and mantle rheologies (Agard et al., 2016). Interestingly, although very thin ( $\leq 500$  m) compared to the thick ( $\leq 10\text{-}20$  km) fragments of oceanic lithosphere (Coleman, 1971, 1981, Nicolas, 1981), metamorphic soles are found welded and distributed below ophiolites across equally vast distances (i.e., typically 100-1000 km; Fig. 3.4b).

Uncertainties remain on the detailed structure of metamorphic soles (e.g., continuous or not? representing a very high thermal gradient or not?; Searle, 1980, Hacker, 1991, Gnos, 1992, Hacker et al., 1996), on their exact pressure-temperature (P-T) conditions of formation, on the amount of associated melting and on the genetic link with localized magmatic intrusions in the ophiolite (Searle & Malpas, 1982, Boudier et al., 1988, Hacker & Gnos, 1997, Searle & Cox, 1999, Ishikawa et al., 2005, Rioux et al., 2013, Soret et al., 2016). This is partly due to the fact that analytical and modelling methods with contrasting accuracy were used over the last 30 years, with estimates for depth (considering P estimated only as lithostatic pressures) appearing much greater than the ophiolite thickness above, giving rise to the "metamorphic conundrum" (Hacker & Gnos, 1997). The emplacement of metamorphic soles has been largely ignored too (as noted by Dewey & Casey, 2013, Plunder et al., 2016). In particular, how thin metamorphic soles get welded along such distances and how they can show the same approximate P-T conditions regardless of their location at the front or rear of the ophiolite thrust (i.e., across 100-150 km) remains enigmatic. Is

---

there a significant thinning of metamorphic soles during accretion/emplacement and what are the implications in term of rheology at the subducting plate interface?

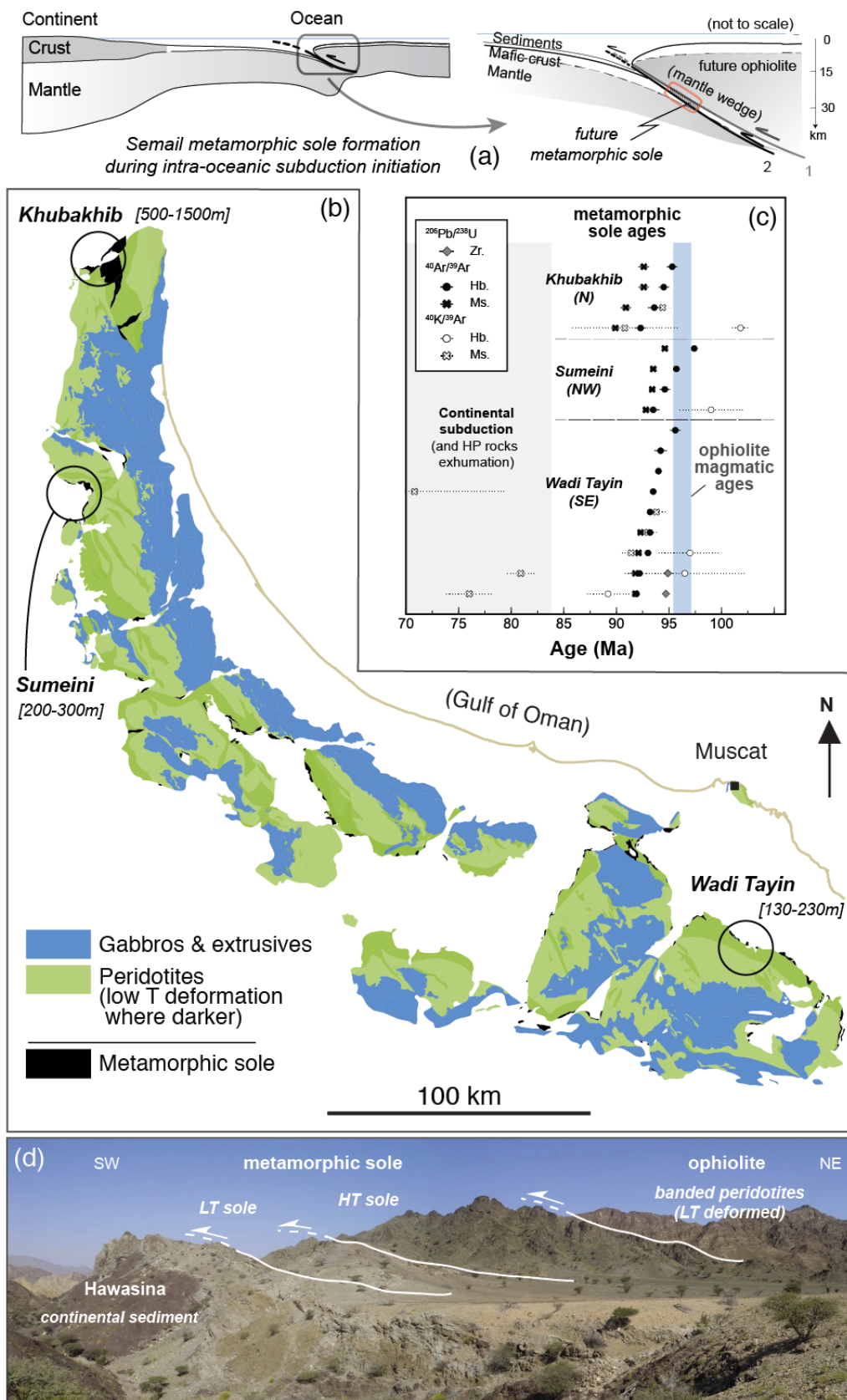
The aim of the present petrological study is to reappraise one of the best-studied metamorphic sole, the metamorphic sole of Oman/UAE, which has unrivalled exposure. Detailed field and petrological work is reported here together with thermodynamic modelling performed by using the latest data for the mafic systems allowing of partial melting (Green et al., 2016, Palin et al., 2016). This contribution focuses on three classical but fundamental sections, deemed representative of the Oman metamorphic sole and already well documented independently (from north to south: Khubakhib: Gnos and co-workers; Sumeini: Searle and co-workers; Wadi Tayin: Hacker and co-workers). The aim is to track changes in lithologies and P-T conditions in each section but also along strike between sections (i.e., ~400 km apart) in order to understand how they relate to the overall structure of the ophiolite (e.g., to the location of the former oceanic ridge) and how strain localizes within metamorphic soles during subduction initiation. Implications are then discussed, with emphasis on the importance of the progressive character of metamorphic and rheological changes which lead to progressive accretion of the metamorphic sole.

## 3.4 The ophiolite of Semail and the metamorphic sole

### 3.4.1 The Semail peridotite

#### Nature and origin: a brief review

The Semail ophiolite (also referred to as the Oman ophiolite) stretches across Oman and the United Arab Emirates (UAE; Fig. 3.4b). This 600 km long and 150 km wide ophiolite is one of the best-exposed on Earth. This ophiolite is thought to represent a portion of oceanic lithosphere formed at a fast-spreading ridge (Lippard, 1986, Searle & Cox, 1999, Goodenough et al., 2010) during the Cenomanian (Tilton et al., 1981, Warren et al., 2003, Rioux et al., 2012, 2013) and obducted onto the Arabian continental margin along thousands of kilometers during the Campanian-Maastrichtian (Glennie et al., 1974, Coleman, 1981, Agard et al., 2010). Unlike other Upper Cretaceous Peri-Arabic ophiolites (from Turkey to Iran), the Semail ophiolite has not been affected after its emplacement by the later (Tertiary to present) Arabia-Eurasia collision. The oceanic crustal sequence ( $\leq$  4-8 km thick) is composed of thick gabbros, sheeted dikes and pillow lavas with imbricated radiolarian cherts. The underlying upper mantle ( $\leq$  10 km thick) is mainly composed of harzburgites and dunites (Allemand & Peters, 1972, Glennie et al., 1974, Coleman, 1981, Lippard, 1986).



---

Figure 3.0: (a) Geodynamic setting of metamorphic sole formation during intra-oceanic subduction infancy. The later geodynamic evolution will lead to continental subduction and obduction s.s.; (b) Simplified geological map of the Semail ophiolite, highlighting the systematic outcrops of metamorphic sole beneath the mantle ophiolite (modified after Nicolas et al., 2000); (c) Review of radiometric ages for metamorphic sole formation along the Oman ophiolite (Hb: hornblende; Ms: white mica; Zr: zircon; (see Agard et al., 2016, for references); (d) overview of the basal ophiolitic complex, with the mylonitic peridotites overthrusting the high-temperature (HT) and the low-temperature metamorphic soles which overlying unmetamorphosed continental sediment of the Hawasina complex.

Despite being the most-studied ophiolite, its exact petrological nature and origin remain uncertain (see Rioux et al., 2013, 2016, for extended discussion). While the structure of the ophiolite, mostly composed of variously-tectonized harzburgite with a typical near-axis mantle flow fabric, advocates for formation beneath an ocean ridge (Ceuleneer et al., 1988, Nicolas et al., 1988), the geochemistry of the crust displays two distinct patterns highlighting a more complex geodynamic environment of formation. Lavas and dikes from the Geotimes unit (Ernewein et al., 1988, Godard et al., 2006) show a MORB-like composition, consistent with the interpretation of the ophiolite structure. In contrast, lavas from Lasail and Alley units (Ernewein et al., 1988) have a signature requiring hydrous partial melting of the peridotite (Alabaster et al., 1982), usually interpreted as taking place in a supra-subduction zone environment (Pearce & Alabaster, 1981, Alabaster et al., 1982, Lippard, 1986, Shervais, 2001, Goodenough et al., 2010, MacLeod et al., 2013). Other authors explain the presence of water by descending hydrothermal fluids near a ridge axis (Boudier et al., 2000) or by late melt/rock interaction between the shallow upper mantle and melts produced by high degree of melting of the previously depleted Geotimes mantle (Ernewein et al., 1988, Godard et al., 2006).

Radiometric dating of mafic dikes and crustal samples displays a cluster of ages at ca. 95 Ma (Fig. 3.4c; Tilton et al., 1981, Goodenough et al., 2010, Rioux et al., 2012, 2013, 2016, Roberts et al., 2015) indicating that most of the ophiolite was formed within ca. 2 Ma. Rioux et al. (2013) suggest a model where most of the ophiolite was accreted in a short period of time, first at an oceanic spreading centre and then over a supra-subduction environment.

### The mylonitic basal peridotite

The Semail ophiolite was early thrust onto the lower plate (subducted oceanic crust) over a ductile shear zone (Fig. 3.4b). This shear zone outcrops as a several-km thick mylonitic to ultramylonitic peridotite referred to as banded peridotite (Searle & Malpas,

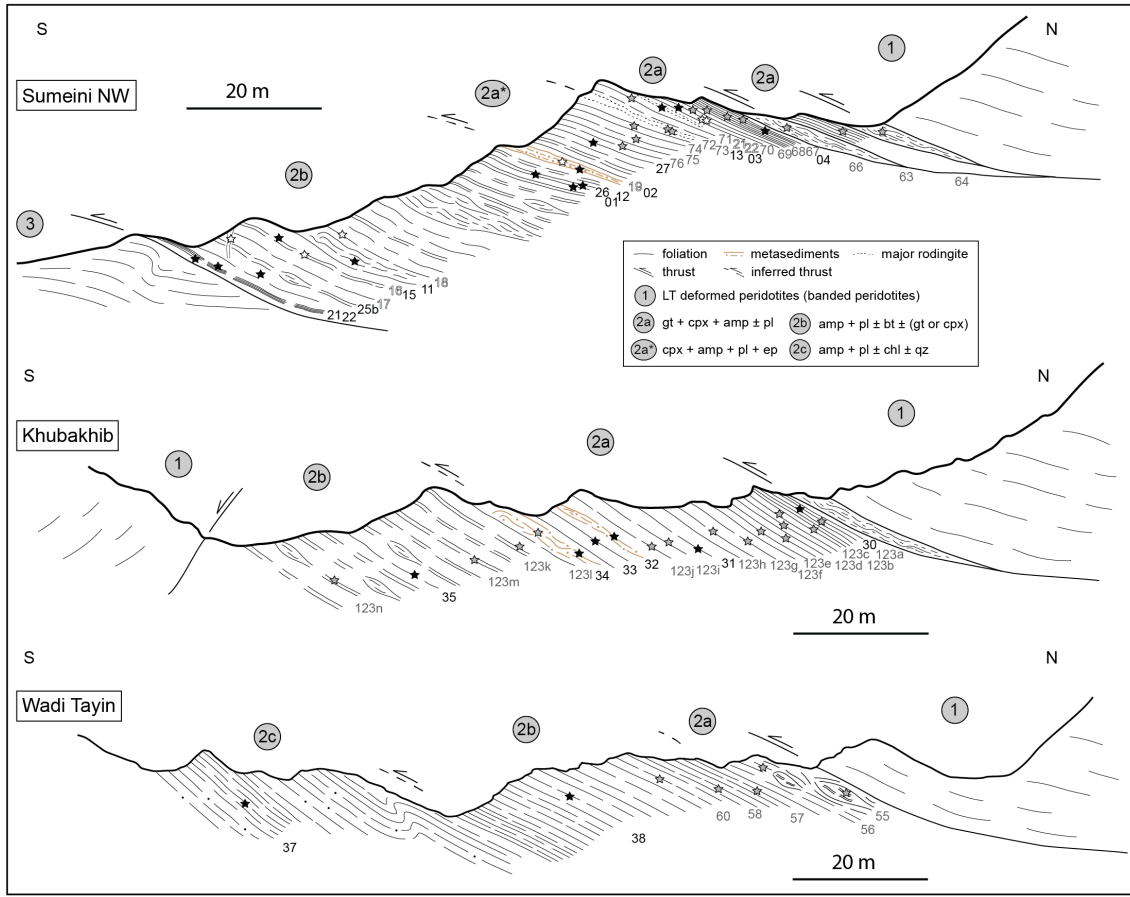


Figure 3.1: Schematic cross-sections of the three classical outcrops of metamorphic soles and its overlying mylonitic peridotites (in Sumeini, Khubakhib and Wadi Tayin) all along the Semail ophiolite. Numbers and stars refer to the sample numerotation (grey, white and black stars correspond respectively to the year of sampling 2013, 2014 and 2016). Three major units are reported: (1) the basal mylonitic peridotites; (2) the high temperature metamorphic sole, composed of metabasalt and rare metasediment metamorphosed in the amphibolite to granulite facies; (3) the low temperature metamorphic soles metamorphosed in the greenschist facies and mainly composed of metasediment.

1982) overlying 10 to 500 m thick, highly strained and metamorphosed slivers of oceanic crust and associated sediments (Fig. 3.4b). Together, they form the basal sole of the ophiolite (Jamieson, 1981), even if the term "metamorphic sole" commonly refers to the basal crustal part.

High-T ( $\sim 1200^\circ\text{C}$ ) plastic deformation is reported in the tectonized harzburgite (Boudier et al., 1988). A mylonitic overprint found at the base of the peridotite along shear zones (Fig. 3.4b) is assigned to lower-T deformation ( $700\text{-}1000^\circ\text{C}$ ; Boudier et al., 1988, Linckens et al., 2011, Herwegen et al., 2016) together with the crystallization of secondary phases (chiefly amphibole and clinopyroxene).

---

### 3.4.2 The Semail metamorphic sole

#### Outline of the structure and composition

The crustal part of the Semail metamorphic sole is generally interpreted as the juxtaposition of two major units (Hacker & Mosenfelder, 1996), strained and metamorphosed by heat transfer from the still warm upper plate mantle toward the slab (associated with fluid transfer and possible shear heating) during the first My of intra-oceanic subduction (Fig. 3.4a). Its thickness is commonly 10-100 m and does not exceed 500 m (except in the Asimah-Khuabkhil window; Fig. 3.4b).

Directly underlying the banded peridotite, the high-temperature (HT) sole structurally overlies the low-temperature (LT) sole all along the Semail ophiolite (Fig. 1a; see Gnos, 1992, for detailed mapping) from Wadi Tayin (south-east, Oman) to Asimah-Khubakhil (north, UAE). The HT sole is essentially composed of metabasalt from amphibolite to granulite facies. From top to bottom, the Semail HT sole changes from a homogeneous, fine-grained garnet-clinopyroxene-plagioclase bearing amphibolite to a more heterogeneous, coarser-grained plagioclase and/or epidote bearing amphibolite with imbrications of metacherts rich in biotite, muscovite and/or garnet. Previous authors report localized partial melting of the metamorphic sole, limited to a few % (Searle & Malpas, 1982, Boudier et al., 1988, Hacker & Gnos, 1997, Searle & Cox, 1999).

The LT sole is mainly composed of greenschist facies metachert, with imbrications of metatuffs and metasediments. Metabasalts in the LT sole are essentially composed of fine-grained chlorite, albite, actinolite and/or epidote (Searle & Malpas, 1982, Gnos, 1992). The LT sole is thickened by numerous folds and faults (Hacker & Mosenfelder, 1996, Gray & Gregory, 2000).

Structurally, the entire metamorphic sole shows a strong planar fabric with evidence of simple shear deformation: lineation and lattice preferred orientation of quartz in the inter-bedded quartzite indicate a dominant simple shear regime with a sense of shearing consistent with that of the basal banded peridotites (Boudier et al., 1985). Fabric orientation measurements also indicate a change in foliation and lineation from the HT to LT soles (Boudier et al., 1985, Gray & Gregory, 2000). Deformation is less conspicuous in garnet-bearing HT sole amphibolites than in the garnet-free HT and LT soles where lithological heterogeneities underline deformation. Complex recumbent folding is only locally observed in the plagioclase and/or epidote bearing amphibole (cm- to 10 cm-scale) while frequent in the LT sole (m- to 10 m-scale).

### Conditions and timing of formation

Previous P-T estimates for the HT sole are mostly based on garnet-clinopyroxene geothermobarometry and spread over the range 700-900 °C and 0.4-1.3 GPa (Ghent & Stout, 1981, Searle & Malpas, 1982, Gnos & Kurz, 1994, Hacker & Mosenfelder, 1996, Hacker & Gnos, 1997, Gnos, 1998, Searle & Cox, 2002, Cowan et al., 2014). Multi-equilibrium thermobarometry gives estimates of 770 °C and 1.1-1.4 GPa for amphibolites from Sumeini and Wadi Tayin (Searle & Cox, 2002, Cowan et al., 2014). P-T conditions for the LT sole are poorly constrained. Amphibole-plagioclase geothermobarometry yielded 450-500 °C and 0.45 -0.55 GPa (Bucher, 1991a).

Wherever the metamorphic sole is complete (i.e., not disturbed by later obduction related deformation), the LT sole always underlies the HT sole. The entire sequence shows therefore an inverted T gradient, with isograds sub-parallel to the basal peridotite foliation, grading steeply from the granulite/amphibolite facies down to greenschist facies ( $\geq 1000$  °C/km; Hacker & Mosenfelder, 1996). This gradient is two orders of magnitude higher than those inferred at the slab/mantle wedge interface in most numerical models (Gerya, 2011, Maffione et al., 2015, Duretz et al., 2016) and ten times steeper than any inverted thermal gradient preserved at paleo-subduction interface (Peacock, 1987).

Radiometric ages indicate that the HT and LT soles were formed and exhumed within about 1 My (Hacker, 1994, Hacker et al., 1996), preceding the formation of high pressure (HP) rocks from the Saih Hatat dome by 10-20 My (see Yamato et al., 2007, Agard et al., 2010, for the compilation of ages). The accretion and exhumation of the metamorphic sole was coeval to slightly younger than the ophiolite crust by 1-2 My (Fig. 3.4c; Hacker, 1994, Hacker & Mosenfelder, 1996, Hacker et al., 1996, Hacker & Gnos, 1997, Gnos, 1998, Warren et al., 2003, Rioux et al., 2012, 2013, 2016). Temperature estimates for the base of the mylonitic mantle, ranging from 1000 to 700 °C (Boudier et al., 1988, Michibayashi & Mainprice, 2004, Linckens et al., 2011, Herwegh et al., 2016) confirm that a still hot thermal regime prevailed in the upper plate during metamorphic sole accretion.

### 3.5 Methods and sample selection

Coupled observations and sampling were made all along and across the Semail metamorphic sole (Oman, UAE; Tables 3.1, 3.2, 3.3). The collection comprises samples from both the HT and LT soles from three classical areas: Khubakhib, Sumeini and Wadi Tayin (see Fig. 3.4). 45 samples mainly corresponding to amphibolite (15 from Khubakhib, 23 from Sumeini, 7 from Wadi Tayin), cut in the XZ plane of deformation, were selected for

---

chemical analysis and thermobarometric estimations. The present study focuses essentially on the HT metamorphic sole. The LT sole has not been studied in detail. However, one maximum T condition has been obtained by Raman Spectrometry.

### 3.5.1 Electron microscopy

Electron scanning microscopy was used to complete optical microscopy at ISTeP (UPMC, Univ. Paris 6) using Zeiss Supra 55VP associated to an SSD detector PTG Sahara for imaging and elemental mapping in energy-dispersive spectroscopy mode. Additional observations were made using a Zeiss Sigma scanning electron microscope (SEM) at Laboratoire de Géologie (ENS, Paris).

Electron probe micro-analysis were carried out at CAMPARIS (Jussieu, Univ. Paris 6) after optical and scanning electron microscopy work, with both Cameca SX-5 and SX-100 instruments. Point measurements were made using classical analytical conditions (15 kV acceleration voltage and 10 nA beam current allowing  $\sim 2 \mu\text{m}$  beam size in wavelength-dispersive spectroscopy mode) using diopside (Ca, Mg, Si), MnTiO<sub>3</sub> (Mn, Ti), orthoclase (K, Al), Fe<sub>2</sub>O<sub>3</sub> (Fe), albite (Na) and Cr<sub>2</sub>O<sub>3</sub> (Cr) as standards to measure elements indicated in brackets. Representative analyses are given in Table 3.4.

### 3.5.2 Raman spectroscopy

Raman spectroscopy of carbonaceous material (RSCM) provided a maximum T estimates (Tmax) for an unoxidized carbonaceous-rich sample from the Semail LT metamorphic sole (SE11-17b; Khubakib-Asimah area). This thermometry, with an absolute accuracy of  $\pm 25^\circ\text{C}$ , is based on the irreversible transformation of organic matter (Beyssac et al., 2002). Raman spectra were obtained using a Renishaw InVIA Reflex microspectrometer (IMPMC Paris) using a 514 nm Laser Physics argon laser in circular polarization, and the laser power at the sample surface was set at  $\sim 1 \text{ mW}$ . The laser was focused on the sample by a DMLM Leica microscope with a 100x objective (NA = 0.85). Carbonaceous material was systematically analysed below a transparent adjacent mineral (i.e., quartz). Twenty spectra were acquired in the 1000-2000 cm<sup>-1</sup> range under with acquisition time between 30 to 60 s. Spectra were then processed using the software Peakfit and the calibration of Beyssac et al. (2002).

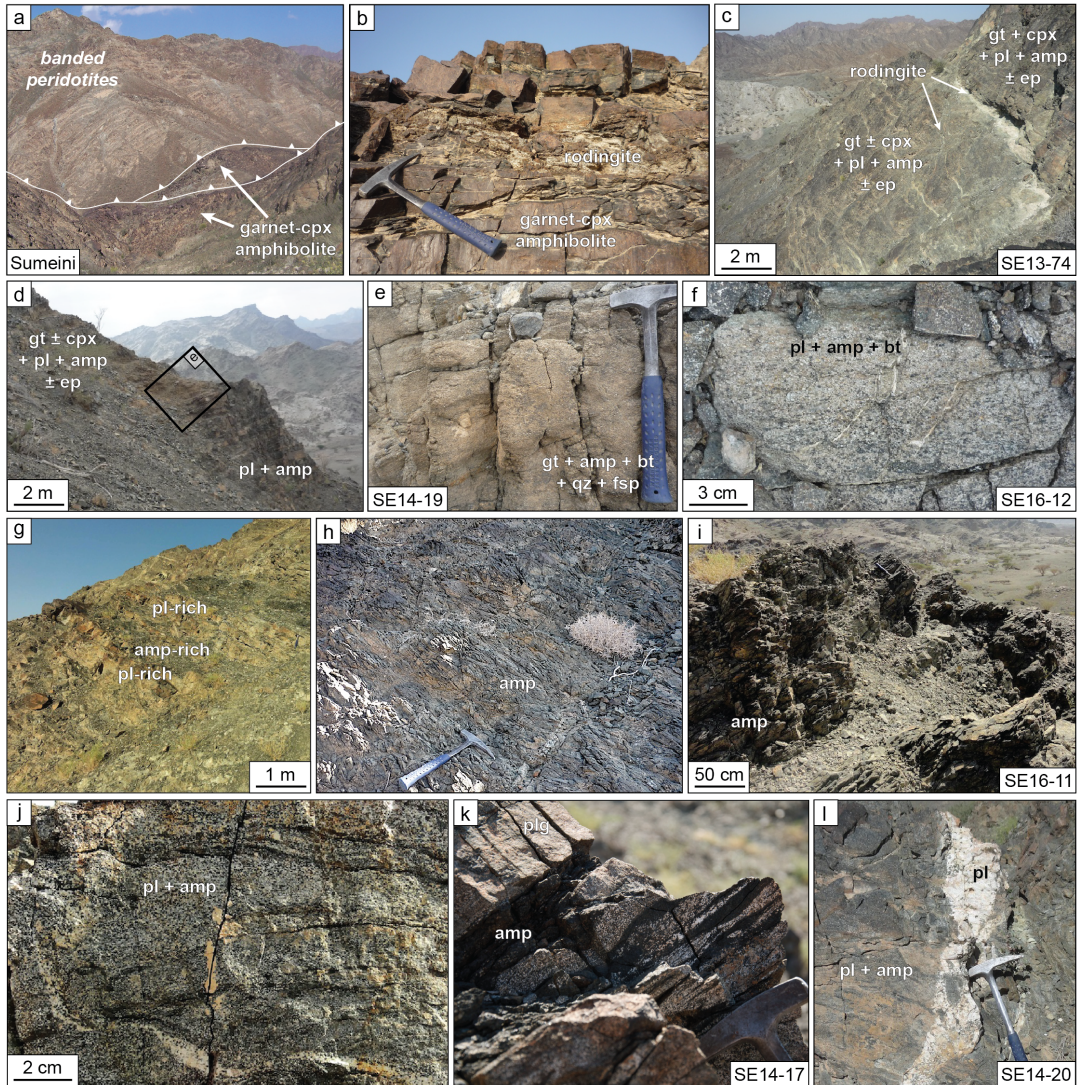


Figure 3.2: Photographs of the base of the Semail ophiolite outcropping in the Sumeini region. (a) Basal contact between the banded peridotites (zone 1) and garnet-bearing metamorphic sole (zone 2a) with general foliation subparallel to the contact; (b) garnet-clinopyroxene amphibolite (zone 2a) covered by a superficial ferruginous cap and crosscut by rodingite veins locally subparallel to the general foliation; (c) base of the garnet-clinopyroxene amphibolite zone, widely affected by rodingitization witnessing pervasive Ca-rich fluid ingressions; (d) contact between the garnet-clinopyroxene amphibolite (zone 2a) and the underlying plagioclase amphibolite (zone 2b) underlined by a  $\leq 2\text{-}3$  m thick highly sheared biotite-rich amphibolite layer; (e) close up-view on the red-brown weathered biotite-rich amphibolite layer at the contact; (f) thin biotite-bearing amphibolite layer interbedded in the zone 2b; (g-k) heterogeneous structures in the zone 2b with (g, k) alternations from plagioclase-rich to darker amphibole-rich layers and (h-i) crumbly anastomosed-shape amphibole-rich layer where rare clinopyroxene is locally observed; (j) sheared veinlets of plagioclase crosscutting the main foliation of the zone 2b; (l) undeformed  $\sim 40$  cm-thick plagioclase-rich veins including cm-thick amphibole-rich clasts from the surrounding rocks crosscutting the zone 2b.

---

## 3.6 Field observations on the HT metamorphic sole

### 3.6.1 Sumeini

The most complete and preserved section of the Semail metamorphic sole crops out in the Sumeini window, northern Oman (Fig. 3.1; Searle & Malpas, 1982). The typical sequence is composed of a ~80 m thick HT sole overlying a several hm-thick LT sole. The general dip of the foliation is sub-parallel to that of the overlying km-thick banded peridotite (zone 1; Fig. 3.1, 3.2a). In between the sole and the basal peridotite, a  $\leq$  3 m-thick serpentinite layer embeds cm- to dm-scale boudins of amphibolite and peridotite. In the HT sole (zone 2), detailed inspection reveals the existence of two distinct parts (noted 2a and 2b on Fig. 3.1):

i) Zone 2a corresponds to the top of the HT sole and is composed of 20-25 m-thick highly sheared metabasalt with fine-grained garnet + clinopyroxene + plagioclase + amphibole (2a on Fig. 3.1). Foliation is flat-lying or gently dipping to the NE and lacks a macroscopic stretching lineation. The first couple of metres contain 10-15% garnet and 20-30% clinopyroxene. The modal proportion of garnet and clinopyroxene decreases downwards, in favour of an increasing amount of amphibole (from 30 to ~50%) and plagioclase (from 0 to 15%). The grain size of amphibole is overall ~0.5 mm except within the first 2 m from the contact with peridotites where it is  $\leq$  0.3 mm. Garnet is usually rimmed by plagioclase in pressure shadow. From ~25 to 35 m away from the contact, the HT sole is composed of garnet-free and/or clinopyroxene-free metabasalt, and is crosscut by numerous rodingite veins (2a\* on Fig. 3.1, Fig. 3.2b,c). Epidote is present either as boudins within the amphibolite or at the edges of the rodingite veins crosscutting the amphibolite. These rodingites, generally ~10 cm-thick, are made of calcite  $\pm$  garnet  $\pm$  clinopyroxene  $\pm$  tremolite  $\pm$  talc  $\pm$  olivine  $\pm$  serpentine. They are spatially associated with pervasive epidote crystallization in the amphibolite. Two rodingite layers bound the top and the base of this 10 m-thick sequence (Fig. 3.2c). These layers, 2 m-thick and several hm-long, are sub-parallel to the amphibolite foliation and embed cm to dm-scale amphibolite cataclastic breccia.

ii) Zone 2b is located ~40 to 70 m away from the contact. There, the HT sole is made of plagioclase bearing amphibolite with rare, cm-thick intercalations of biotite-plagioclase bearing amphibolite. The transition between 2a and 2b is underlined by a  $\leq$  2-3 m thick highly sheared biotite-rich amphibolite layer (Fig. 3.2d,e), containing quartz + feldspar + garnet in addition to red-brown weathered biotite. This biotite-rich layer is structurally concordant with the main foliation of the HT sole (Fig. 3.1, 3.2d,e). The grain

size of amphibole and plagioclase approximates 1 mm and reach 3-4 mm for post-kinematic crystals.

Throughout zone 2b, coarse-grained amphibole and plagioclase coexist in roughly equal proportions. Alternations from plagioclase-rich to darker amphibole-rich layers are nevertheless observed (Fig. 3.2g-i). Plagioclase-rich amphibolites are usually dm to m-thick cohesive layers extending up to several tens of meters. A component of simple shear deformation is witnessed by discrete shear bands and sheared veinlets of plagioclase (Fig. 3.2j). Lineation, marked by amphibole, is significantly dispersed, ranging between N110 and 150. These plagioclase-rich amphibolites are wrapped by dm to several m-thick amphibole-rich layers characterized by crumbly anastomosing patterns and mm-scale shear structures (Fig. 3.2k). Garnet was observed without clinopyroxene in a plagioclase-rich layer. Conversely, clinopyroxene was found without garnet in the crumbly anastomosed-shape amphibole-rich layer. Interbedded biotite-bearing amphibolite is observed all along zone 2b (Fig. 3.2f).

Near the base of zone 2b, rare, undeformed ~40 cm-thick veins made of large crystals of plagioclase and cm-thick amphibole-rich clasts from the surrounding rocks cut across the plagioclase-bearing amphibolite sole (Fig. 3.1,3.2l), and are commonly accompanied by rodingite and associated epidote within the neighbouring ~10 m. The base of the HT sole is characterized by a 10-20 m-thick fine-grained ( $\leq 0.5$  mm) amphibolite composed of heterogeneously distributed epidote and plagioclase. The amount of epidote increases downward. This zone is structurally located just above the sharp transition between the HT and LT soles (Fig. 3.1).

### 3.6.2 Khubakhib

The Khubakhib section lies within the Asimah area (United Arab Emirates; Fig. 3.4b), where the largest (recumbently thickened) outcrops of metamorphic sole were reported beneath the Semail ophiolite (Gnos, 1992, 1998). The thickest section of HT metamorphic sole is made of ~70 m of garnet-bearing amphibolite. A  $\leq 2$ -3 m thick and highly sheared serpentinite sole separates the metamorphic sole from the overlying banded peridotite (Fig. 3.1). The overall thickness of the HT sole could not be estimated precisely because of late normal fault cross-cutting the garnet-free amphibolite. Although thicker, the sequence of metamorphic sole in Khubakhib is structurally similar to the one observed in Sumeini, and two of the three zones described for Sumeini are found here (Fig. 3.3a):

- i) zone 2a: At the top, the HT sole is composed of ~10% garnet + 15-20% clinopyroxene + plagioclase + amphibole. The orientation of the foliation, outlined by the layering

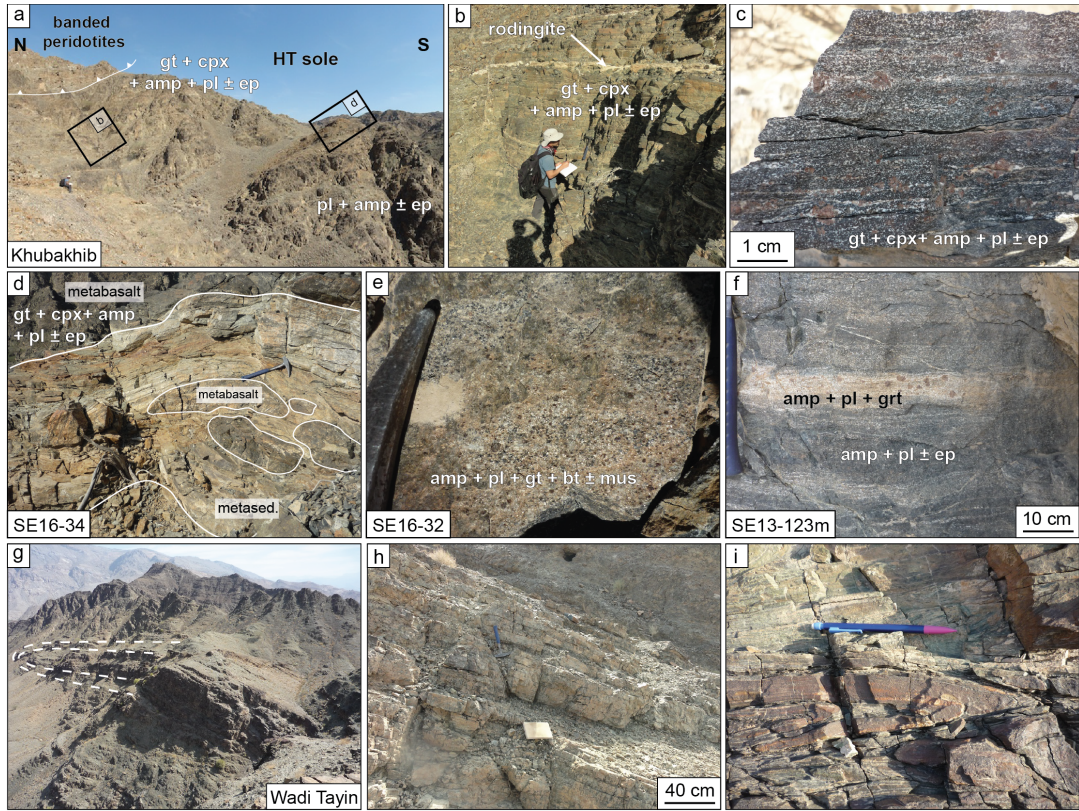


Figure 3.3: Representative structure of the base of the Semail ophiolite outcropping in the area of Khubakhib (a-f) and Wadi Tayin (g-i). (a) Contacts between the banded peridotites (zone 1) and garnet-bearing metamorphic sole (zone 2a), and with the plagioclase amphibolite (zone 2b), with general foliation systematically subparallel to the contact; (b) garnet–clinopyroxene amphibolite (zone 2a) crosscut by rodingite veins subparallel to the general foliation; (c) strongly foliated amphibolite from the zone 2a with (white) plagioclase crystallizing after garnet (red) in pressure shadow; (d-e) zoom-in on the red-brown weathered biotite-rich amphibolite layer imbedded shear amphibolite boudins at the contact between the zones 2a and 2b; (f) rare evidence of garnet in the plagioclase amphibolite (zone 2b) only localized in plagioclase rich-layer; (g) structure of the base of the Wadi Tayin ophiolitic complex with the metamorphic sole affected by a spectacular hm-scale recumbent fold outlying by a 10 m-thick quartzite band; (h) strongly layered plagioclase amphibolite; (i) 10-cm scale isoclinal folding in the zone 2b.

of amphibole and plagioclase throughout the metamorphic sole, is consistent with that observed in the banded peridotite (zone 1; Fig. 3.1, 3.3b). Lineation strikes consistently N080-N090 throughout this part of the sole, with top-to-the-east shear senses on cm-scale garnet pressure shadows. Garnet crystals are up to ~2 cm large and are usually elongated and boudinaged along the stretching lineation defined by amphibole and plagioclase (Fig. 3.3b,c). Clinopyroxene and (numerous) amphibole inclusions in garnet are easily recognized in hand specimen. Tens of cm-thick rodingite layers are found parallel to the main foliation of the HT sole (Fig. 3.3b). Further than 5 m from the contact with the

peridotite, the amount of amphibole and plagioclase steeply increases from  $\leq 50\%$  to  $\geq 80\%$ , and syn-kinematic epidote occurs in places.

ii) zone 2b: from  $\sim 40$  to  $\sim 70$  m away from the contact, the HT sole is made of coarse-grained plagioclase-bearing amphibolite. As for 2a, deformation in zone 2b is characterized by strong flattening (Fig. 3.1). Lineation is more dispersed (N050-100), with evidence of top to the east shear senses. The transition between 2a and 2b is underlined by an anastomosing network of 0.5 to  $\sim 5$  m thick red-brown mica-rich layers, highly sheared and complexly folded, composed of quartz + biotite + muscovite + feldspar + garnet + amphibole. These mica-rich layers extend laterally over several hundreds of meters, embedding m-long amphibolite boudins (Fig. 3.1, 3.3d,e). Garnet was found in one plagioclase-rich layer only, directly below the highly sheared mica-rich layer (Fig. 3.3f). No clinopyroxene was found. Plagioclase and amphibole are generally present in equal proportions. Epidote is restricted to cm to dm-thick epidote-rich layers. Rare dm-thick garnet-biotite bearing quartzites are present, wrapping boudinaged m-thick amphibolite.

### 3.6.3 Wadi Tayin

In the Wadi Tayin section (Fig. 3.3g), the overall thickness of the metamorphic sole is  $\geq 250$  m, yet the thickness of the HT sole is debated, its basal part being either attributed to the greenschist facies LT sole (Ghent & Stout, 1981, Gray & Gregory, 2000) or to the lower amphibolite-facies HT sole overprinted by greenschist facies metamorphism (Hacker & Mosenfelder, 1996). Three zones (2a, 2b and 2c) have been recognized on top of a distinctive LT greenschist facies portion, marked by the appearance of chlorite + actinolite + albite + epidote in metabasalts, and abundant phengite in quartzites.

i) zone 2a: the first  $\sim 15$  m, away from the peridotite, are composed of strongly layered and coarse-grained ( $\sim 1-2$  mm) plagioclase  $\pm$  clinopyroxene  $\pm$  epidote bearing amphibolite (Fig. 3.3h). Fine-grained ( $\leq 0.5$  mm) garnet-clinopyroxene bearing amphibolite lenses were found only in the uppermost few meters, within garnet-free amphibolite (Fig. 3.1). In the first meters, rodingite is observed cross-cutting the metamorphic sole.

ii) zone 2b: between  $\sim 15$  m and  $\sim 40$  m away from the peridotite, the amphibolite made of coarse-grained amphibole + plagioclase is associated with repeated imbrications of  $\sim 50$  cm-thick metacarbonate and quartzite. In this part, the HT sole shows strong flattening, with isoclinal recumbent folding on the scale of tens of cm highlighted by meta-sediments alternations (Fig. 3.3i). The strike and dip of the foliation are  $\sim$ N060 50 SE with a faint lineation striking N080-100. Rodingite veins associated with epidote crystallization intrude locally the base of this zone.

---

iii) zone 2c: beyond  $\sim$ 40-50 m, the HT sole is made of fine-grained ( $\leq$  1 mm) plagioclase-bearing amphibolite, boudinaged in places, alternating with thick quartzite and minor carbonate-rich bands (Fig. 3.1). A spectacular hm-scale recumbent fold is outlined by a 10 m-thick quartzite band (Fig. 3.3g; see also Cowan et al., 2014). A dm-thick layer of garnet-biotite bearing quartzite marks the transition between zones 2b and 2c (Fig. 3.3e).

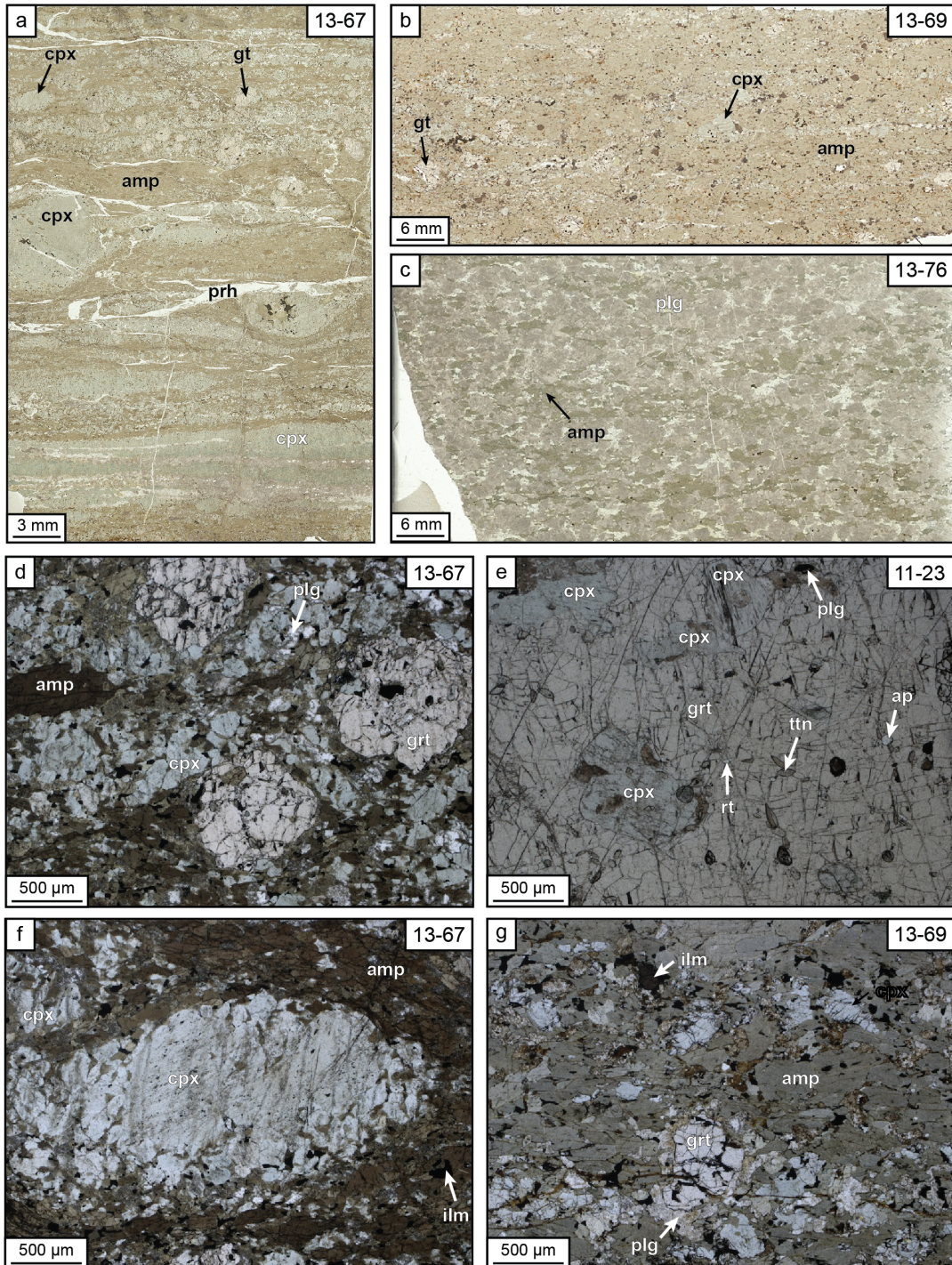
## 3.7 Petrography

The description below follows the division presented in the former section. Mineral occurrences for each sample can be found in Table 1.

### 3.7.1 Sumeini

i) zone 2a: within  $\sim$ 2 m from the contact (SE11-23; SE13-67), the mineral assemblage contains brown amphibole (35-45 vol%), pale blue clinopyroxene (25-35%) + garnet (10-15%) + plagioclase ( $\leq$  10%) + rutile + titanite (Fig. 3.7a). Brown amphibole and clinopyroxene are generally  $\leq$  300  $\mu$ m long. The majority of brown amphibole co-exists in the matrix with clinopyroxene. Garnet shows irregular ovoid contours and forms boudins, with pressure shadows filled with clinopyroxene and amphibole (Fig. 3.7d). In the absence of garnet, clinopyroxene is boudinaged, wrapped by strongly oriented amphibole (Fig. 3.7f). Garnet cores are usually free of inclusions, except for minute rutile and titanite. In contrast, garnet rims show frequent inclusions of globular clinopyroxene, rutile, titanite and less frequently brown amphibole (Fig. 3.7e). Plagioclase rims garnet but is rarely found in the matrix, being replaced by a late, post-kinematic mixture of epidote, albite and muscovite. Ilmenite is only found in the matrix, at grain boundaries by exsolution from titanite. Pumpellyite, pectolite, prehnite and chlorite are found as alteration phases around garnet, amphibole and clinopyroxene. Chlorite is also present in garnet cracks, and prehnite in veins crosscutting the matrix.

Between  $\sim$ 4 m and  $\sim$ 25 m from the contact (from SE13-68 to SE13-71), the metamorphic sole shows a similar mineral assemblage (Fig. 3.7b), yet with a higher proportion of brown amphibole (50-70%) and plagioclase (10-20%) and a slightly coarser grain size (usually  $\leq$  500  $\mu$ m). Plagioclase and most amphiboles in the matrix crystallize after clinopyroxene and garnet, respectively (Fig. 3.7g). No correlation between the distance from the contact and the modal abundance or the grain size has been evidenced. Strong retrogression with abundant epidote is observed approximately 20 m away from the contact,



close to m-thick and hm-long rodingite horizons sub-parallel to the foliation (SE13-74). Two meters below, the metamorphic sole comprises clinopyroxene, amphibole and plagioclase with a grain size  $\leq 500 \mu\text{m}$  (SE13-75; SE16-27). Clinopyroxene and brown amphibole are overgrown by green amphibole, secondary plagioclase and epidote (Fig. 3.4a). Titanite is locally present as inclusion in both clinopyroxene and primary plagioclase, while ilmenite is only found at grain boundaries (Fig. 3.7g). At  $\sim 4$  m beneath the rodingite ( $\sim 25$  m

---

Figure 3.3: Representative mineral assemblages in the garnet-clinopyroxene amphibolite (zone 2a) of the Sumeini metamorphic sole. (a) ~ 2 m away from the contact, well-preserved mineral equilibrium texture and deformation structure; (b) ~ 8 m away from the contact, higher degree of retromorphose characterized with an increase content of plagioclase and brown amphibole; (c) ~ 25 m away from the contact (base of the zone 2a), highly retromorphosed amphibolite associated with the secondary crystallization of coarse grained brown to green amphibole, epidote and plagioclase; (d) boudins of garnet surrounded by a fine-grained matrix of clinopyroxene and brown amphibole with rare plagioclase lying in the foliation; (e) porphyroblast of garnet with inclusions of clinopyroxene, titanite and rutile; (f) shear boudin of clinopyroxene wrapped by fine grained brown amphibole. (g) foliated matrix characterized by coarse grained (sericitized) plagioclase and brown to greenish amphibole growing after garnet and clinopyroxene. Abbreviations after Whitney & Evans (2010).

from the peridotite), garnet and clinopyroxene disappear (SE13-76). Amphibole is brown to greenish-brown amphibole and closely associated with plagioclase, with a coarser grain size, generally between 750  $\mu\text{m}$  and 1000  $\mu\text{m}$ . This assemblage is in places overgrown by late xenomorphic epidote (Fig. 3.4a). Titanite is again found in inclusion in amphibole and plagioclase, whereas ilmenite occurs as interstitial crystals in the matrix.

About 35 m away from the peridotite, the 2-3 m thick mica-rich layers are composed of quartz + biotite + garnet + greenish-brown amphibole + plagioclase + rare orthoclase (Fig. 3.4b; SE14-19). Most garnets are xenomorphic with an ovoid-shape parallel to the foliation plane. The cores of the largest garnets are filled with inclusions showing syn-kinematics textures (mainly quartz, titanite and rutile) while their rims are usually inclusion-free.

ii) zone 2b: Between ~40 m and ~70 m from the contact, the metamorphic sole is composed of coarse-grained greenish-brown amphibole + plagioclase + titanite + apatite. In places, biotite ( $\leq 10\%$ ) is present and appears both including and included in plagioclase and amphibole (Fig. 3.4c). All these minerals make up the foliation. Biotite is retrogressed in chlorite and white mica. Plagioclase is rarely preserved, being often altered in turbid albite + epidote + muscovite. In the strongly anastomosed amphibolite, clinopyroxene is locally present in equilibrium with fine-grained greenish-brown amphibole and subordinate plagioclase (SE16-11; Fig. 6d). Near the top of zone 2b, cm-scale garnets are present with rare biotite in plagioclase-rich amphibolite (SE16-26). They show randomly oriented inclusions of fine-grained rutile + titanite + apatite + zircon surrounded by hematite.

The base of zone 2b sole is composed of fine-grained mafic layers (SE16-21) with green amphibole and poorly preserved plagioclase ( $\pm$  epidote, rare orthoclase and calcite) and quartzite layers (SE16-22) with green amphibole, chlorite and rare white mica.

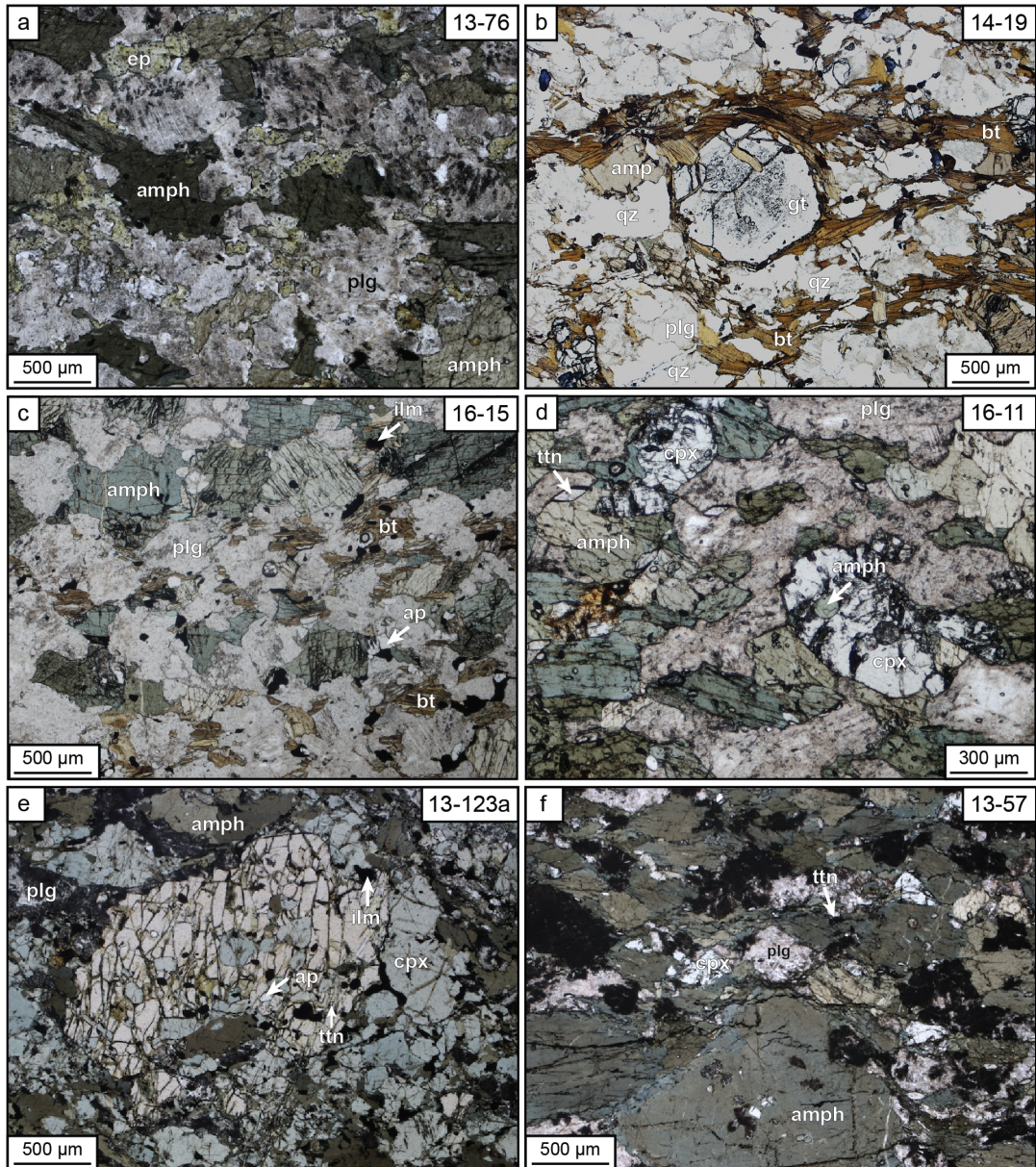


Figure 3.4: Representative mineral assemblages in the Semail metamorphic sole. (a) Epidote growing after secondary brown-greenish amphibole and (sericitized plagioclase) at the base of portion 2a in Sumeini; (b) assemblage of oriented biotite, amphibole, plagioclase, quartz and garnet in the biotite-rich amphibolite layer highlighting the contact between zones 2a and 2b; (c) and (d) assemblage of amphibole and plagioclase  $\pm$  biotite  $\pm$  clinopyroxene in the zone 2b; (e) and (f) garnet-clinopyroxene amphibolite from respectively Khubakhib and Wadi Tayin areas. (f) Pale blue ferric amphibole rimming brown amphibole

### 3.7.2 Khubakhib

In Khubakhib, the metamorphic sole is composed of a  $\sim$ 70 m thick garnet-bearing amphibolite and of a plagioclase  $\pm$  epidote amphibolite below.

---

i) zone 2a: within the first ~4 m (from SE13-123a to SE13-123c), the metamorphic sole is composed of brown amphibole (30-40%) + pale blue clinopyroxene (15-30%) + garnet ( $\leq$  10%) + plagioclase (10-20%) + rutile + titanite. Clinopyroxene is associated with fine grained ( $\leq$  500  $\mu\text{m}$ ) amphibole in the foliated matrix and shows a distinctive globular shape, inter-grown and boudinaged together with garnet (Fig. 3.4e). Garnet hosts inclusions of clinopyroxene, rutile, titanite and rare amphibole. Matrix amphibole contains inclusions of titanite and rare clinopyroxene. Ilmenite is only observed at grain boundaries in the matrix, associated to hematite. Apatite and minute zircon are also present.

Between ~5 m and ~15 m from the contact, epidote can be found with clinopyroxene and amphibole in the core of some garnets (SE13-123d and SE13-123g). Garnet rim is epidote-free and imbricated with globular-shaped clinopyroxene. The matrix is composed of brown-green amphibole + clinopyroxene + plagioclase + titanite + rare rutile and quartz, with late ilmenite, but lacks epidote. Coarser grain size amphibole and poorly preserved plagioclase are present in larger amounts than in the first few meters away from the peridotites. Amphibole and plagioclase destabilize clinopyroxene and garnet, respectively.

Between ~20 m and ~25 m from the contact, clinopyroxene and garnet are absent or appear only sparsely as relicts. Where partly preserved, garnet and clinopyroxene form elongated boudins wrapped and destabilized by a foliated matrix made of coarse-grained brown-green amphibole, epidote, plagioclase, titanite and apatite. Garnet cores host epidote as inclusions, while rims are in textural equilibrium with clinopyroxene (SE13-123j). Late epidote fills garnet cracks together with calcite, pumpellyite and chlorite, suggesting the existence of at least two generations of epidote. A dense network of rodingite veins intrudes this part of the metamorphic sole.

~40 m away from the peridotite, two mica-rich samples were collected. The first one (SE13-123l) is a mylonitic micaceous quartzite composed of quartz (~40%), garnet (~5%) and white mica (~40%). Garnet shows rotating trails of quartz and zircon inclusions. Mica fish and C-S structures are observed with ductily-sheared quartz. The second sample (SE16-34a) is a quartzite with subordinate garnet (~5%), plagioclase, and biotite in the pressure shadows of sheared garnet. Quartz shows strong grain size reduction and elongation along the foliation.

ii) zone 2b: Between ~50 m and ~0 m from the contact, the metamorphic sole (SE13-123k and SE13-123m) is composed of brown-green amphibole (~70%) + plagioclase (~25%)  $\pm$  garnet ( $\leq$  5%)  $\pm$  epidote + titanite + apatite + rare rutile and quartz. Clinopyroxene is no longer observed. Garnet contains small inclusions of plagioclase and

epidote. In the matrix brown-greenish amphibole, epidote and plagioclase are in textural equilibrium with garnet. Greenish amphibole and a second generation of plagioclase are also observed around brown-greenish amphibole and garnet, respectively. Rare imbrications of quartz + garnet + phengite + amphibole wrap several m-scale mafic boudins. Near the base of the HT sole, metabasalt layers are solely composed of coarse-grained and elongated greenish amphibole + plagioclase + epidote. Some organic matter was found in one sample (SE11-17b).

### 3.7.3 Wadi Tayin

Within the first ~2-4 m, the metamorphic sole is composed of mm- to cm-scale garnet (~10%), pale blue clinopyroxene (20%), brown amphibole (50%) and altered plagioclase + rutile + titanite (SE13-56; Table 1). In the garnet-free amphibolite, clinopyroxene is present but largely replaced by secondary brown-green amphibole and plagioclase (SE13-57; Fig. 3.4f). Below, the layered amphibolite becomes clinopyroxene-free and only composed of plagioclase and brown-greenish amphibole. Brown-greenish amphibole is locally rimmed by blue-green xenomorphic amphibole.

## 3.8 Mineral composition

### 3.8.1 Amphibole

The composition of amphibole in metabasalt and mica-rich layers, in the three localities, plot within the pargasite to actinolite fields (Fig. 3.5a,b,c; Leake et al., 1997), with a similar Mg# ( $=\text{Mg}/[\text{Mg}+\text{Fe}]$ ) around  $0.65 \pm 0.15$  (Fig. 7d,e,f). In Khubakhib, amphibole shows a continuously decreasing trend in  $[\text{Na}+\text{K}]^{\text{A}}$  content vs. Si content (all expressed per formula unit; Fig. 3.5a), whereas in Sumeini amphibole is mainly restricted to the pargasite and tschermakite domain (Fig. 3.5b), Wadi Tayin showing an intermediate trend (Fig. 3.5c). In the three localities, no correlation between the Mg# and the distance from the contact is evidenced.

The Ti content of amphibole shows a relatively continuous decrease vs. Si content (Fig. 7g,h,i). It ranges from 0.29 to 0 per formula unit (p.f.u.) with clear textural relations (matrix vs. inclusion) and the distance from the peridotite. Two distinct thresholds in Ti content over the distance from the peridotite are evidenced (Fig. 3.5j,k,l). The change in amphibole composition corresponds to the change in the mineral assemblage.

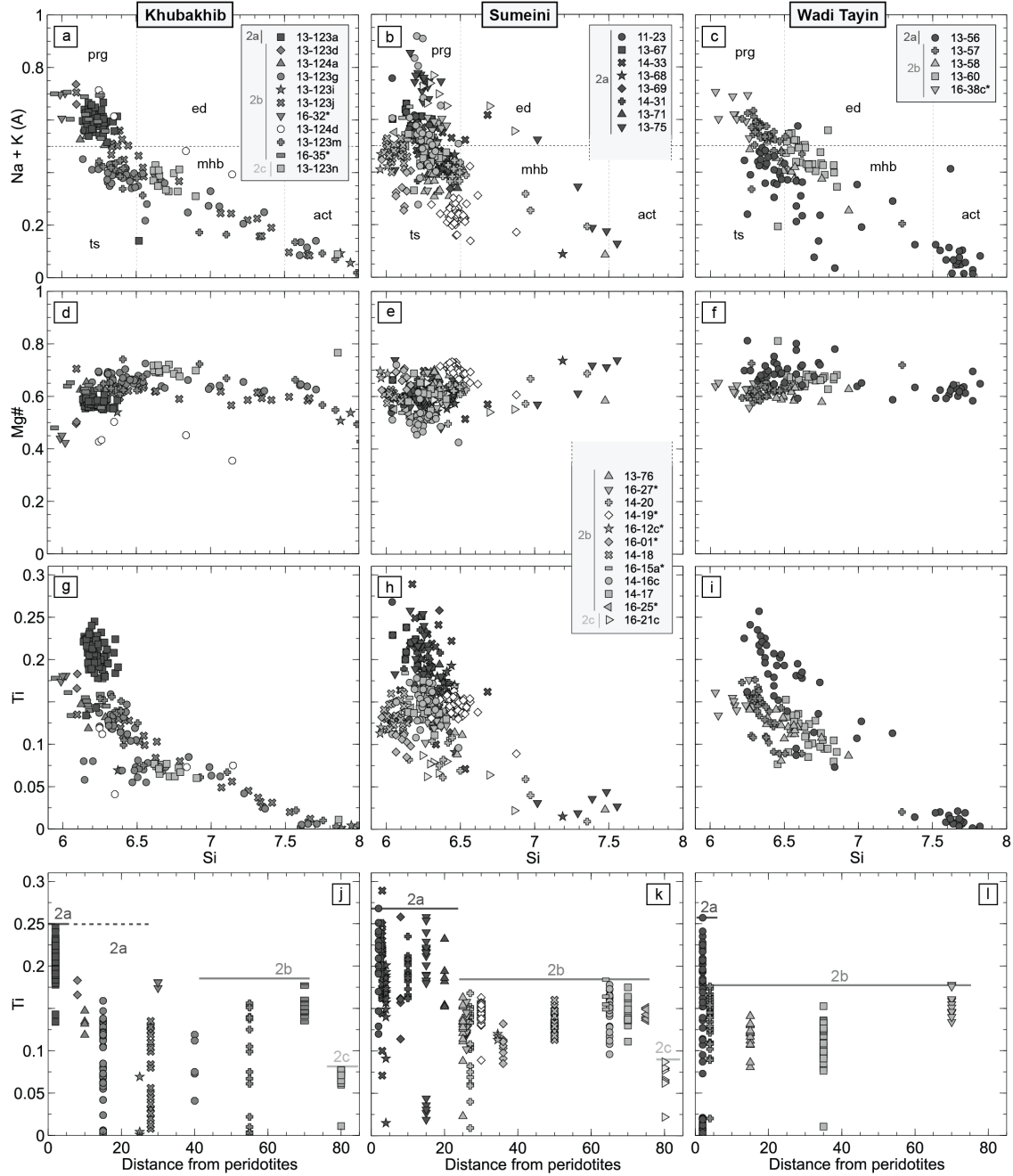


Figure 3.5: Composition of Ca-amphibole in selected samples from Khubakhib, Sumeini and Wadi Tayin (respectively first, second and third columns). All expressed per formula unit (p.f.u.). (a-c) Si vs. (Na+K)<sup>A</sup> after the classification of Leake et al. (1997); (d-f) Si content vs. Mg#; (g-i) Ti content vs. Si content; (j-l) Ti content vs. distance from the contact with the banded peridotites. 2a, 2b and 2c refers to zones defined in the high temperature metamorphic sole.

In Sumeini, with the exception of one crystal included in garnet, amphibole from the garnet-clinopyroxene metamorphic sole show similar composition in Ti with a threshold  $\sim 0.26$  p.f.u. (Fig. 3.5j). Amphibole included in garnet and clinopyroxene shows the

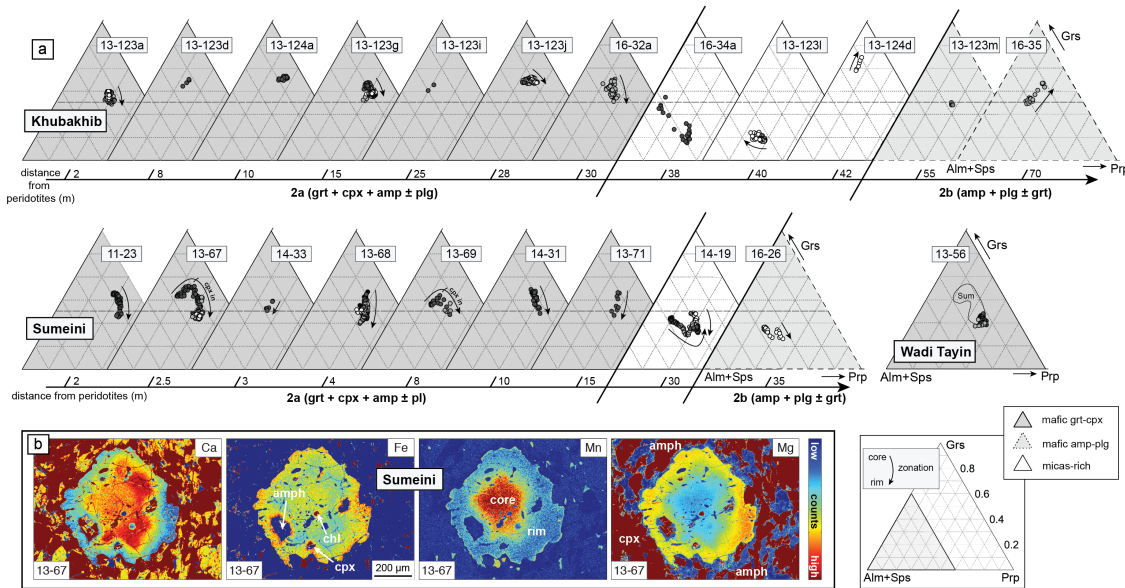


Figure 3.6: (a) Point analyses of garnet in samples from the zones 2a and 2b of Sumeini, Khubakhib and Wadi Tayin metamorphic soles. Samples are reported in respect with the distance from the peridotites (m); (b) Composition maps for Ca, Fe, Mn and Mg showing complex zoning in garnet about 2.5 m away from the contact

highest Ti content, between 0.19 and 0.29 p.f.u. Amphibole destabilising clinopyroxene and garnet shows systematically lower values ( $\leq 0.16$  p.f.u.). Amphibole in the garnet-bearing, clinopyroxene-free amphibolite found at  $\sim 25$  m from the peridotite shows similar maximum Ti values. Green amphibole rimming pargasite, abundant at the base of the sequence 2a, falls in the actinolite and magnesio-hornblende domains with the lowest Ti content ( $\leq 0.10$  p.f.u.). Amphibole in plagioclase-bearing amphibolite systematically shows the same maximum Ti content (0.18 p.f.u.). This threshold is lower than that in garnet-clinopyroxene bearing amphibolite. Amphibole in equilibrium with plagioclase displays a Ti-content  $\geq 0.10$  p.f.u. Amphibole in the micas-rich amphibolite layer (SE14-19) at  $\sim 35$  m from the peridotite, shows a maximum Ti content of 0.14 p.f.u. Late amphibole shows the lowest Ti content ( $\leq 0.10$  p.f.u.).

In Khubakhib and Wadi Tayin, a similar distribution of Ti content in amphibole is observed with respect to the distance from peridotite, to the mineral assemblage and to the texture (Fig. 7k,l). Within the first meters (SE13-123a; SE13-56), amphibole in equilibrium with clinopyroxene and garnet shows a Ti content between 0.19 and 0.25 p.f.u. Below, in garnet-clinopyroxene-epidote bearing amphibolite (Khubakhib; from SE13-123d to SE13-123j) and in clinopyroxene-epidote bearing amphibolite (Wadi Tayin; SE13-57) amphibole shows a variety of Ti contents, with a threshold of ~0.18 p.f.u. Amphibole included in garnet yields again the highest values, whereas amphibole in equilibrium with plagioclase ± epidote ± garnet (SE13-123m) displays a maximum Ti content of 0.16 p.f.u.

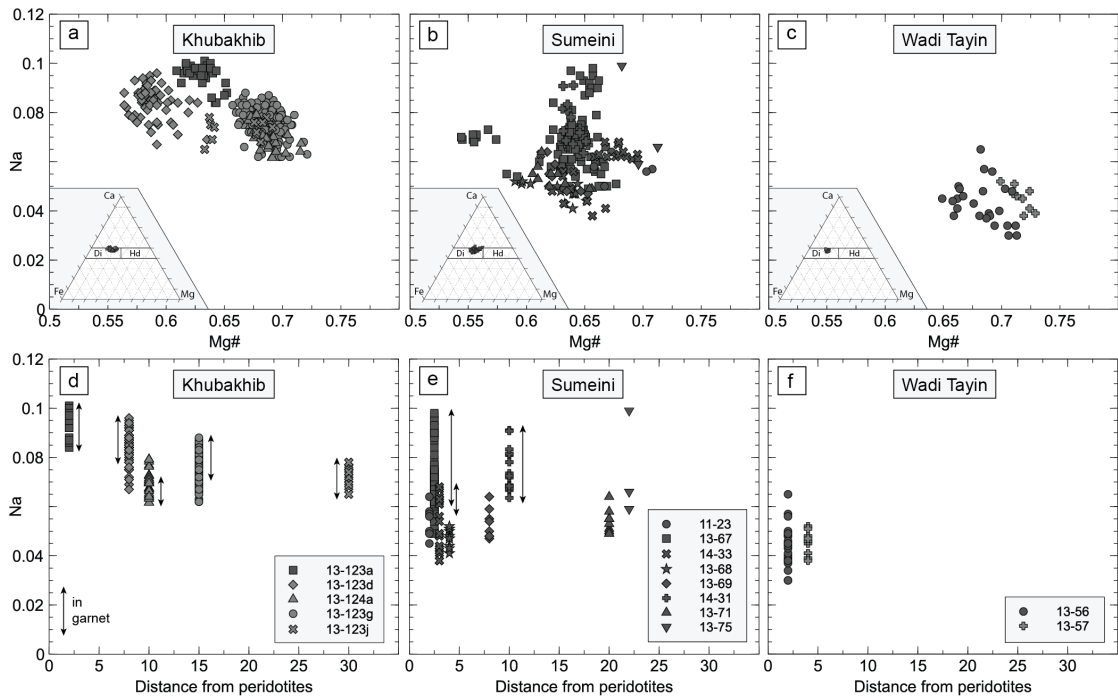


Figure 3.7: Composition of clinopyroxene in samples from the zones 2a and 2b of Sumeini, Khubakhib and Wadi Tayin metamorphic soles. (a-c) Na content (p.f.u.) vs. Mg#; (d-f) Na content vs. distance from the peridotites (m).

Amphibole in the quartzite (SE13-124d) at  $\sim$ 40 m from the peridotite, shows a maximum Ti content of 0.12 p.f.u. At the base of the HT sole of Khubakhib, amphibole co-existing only with plagioclase and epidote shows the lowest Ti content ( $\leq$  0.08 p.f.u.). In Wadi Tayin, amphibole co-existing only with plagioclase has a maximum Ti content ( $\sim$ 0.15 p.f.u.) similar to that in amphibole destabilizing clinopyroxene and early amphibole in the clinopyroxene bearing amphibolite.

A slight difference in the Si/Al<sup>IV</sup> ratio is observed between north and south (Fig. 3.5): pargasite and tschermackite hornblende in the mafic HT sole show a lower minimum Si content in Khubakhib and Sumeini (6.1 p.f.u.) than in Wadi Tayin ( $\geq$  6.2 p.f.u.).

### 3.8.2 Garnet

Garnet consists dominantly of almandine with small proportions of pyrope and grossular (Fig. 3.6a). The largest garnet crystals from the mafic HT sole show significant zoning in the 3 localities, generally characterized by a decrease in grossular and spessartine contents correlated with small variations in pyrope and almandine. In rare garnet grains, the zonation is more complex (Fig. 3.6b), characterized by an increase and then a decrease in grossular content towards the rim. The amount of almandine is generally constant from

core to rim. The smallest garnet grains have the same composition as the rim of the zoned garnets.

In Khubakhib and Sumeini, variations in garnet composition from zone 2a are not correlated with the distance from the contact (Fig. 3.6a). In Sumeini, garnet cores (SE13-67, SE13-69) enriched in grossular only contain titanite and rutile in inclusion (Fig. 3.6b). Homogeneous garnets and zoned garnet with a grossular content decreasing towards the rim include clinopyroxene, titanite, rutile and rare Ti-rich amphibole ( $Ti \leq 1.8$  p.f.u.). In Khubakhib, garnets with a similar decreasing in grossular from the core to the rim (SE13-123a, SE13-123g) show inclusions of clinopyroxene, amphibole, titanite and rutile, without epidote. Garnets enriched in grossular towards the rim (SE13-123d, SE13-124a, SE13-123j) include epidote, clinopyroxene, amphibole, titanite and rutile. Both types of garnet are surrounded by a matrix showing the same assemblage as in inclusions.

Garnet in clinopyroxene-free amphibolite has a different composition in both Khubakhib and Sumeini (Fig. 3.6a). In Sumeini, garnet incorporates a smaller amount of grossular but a similar zoning pattern with a decrease of the grossular content towards the rim. In the 2-3 m thick highly sheared micas-rich amphibolite composed of quartz + biotite + feldspar + garnet + amphibole, two compositions of garnet are observed (Fig. 3.6a; SE14-19). The first one is similar to that observed in the clinopyroxene-free amphibolite. The second one presents a similar grossular content but a higher proportion of almandine. Towards the rim, both grossular and almandine contents decrease. The outer rim shows an increase of both grossular and pyrope. The outer rims of both types of garnets have similar composition.

In Khubakhib, homogenous garnets from clinopyroxene-free amphibolite have a composition close to that of garnets from clinopyroxene bearing amphibolite (Fig. 3.6a). A garnet (in SE16-35) shows zoning where the amounts of grossular and pyrope increase towards the rim. Garnets in micas-rich amphibolite display different composition and evolution. At  $\sim 40$  m from the peridotite, in mylonitic phengite bearing quartzite (SE13-123l), garnets characterized by rotating tails of quartz and zircon inclusions are grossular-poor and almandine-rich. Garnets from the biotite-plagioclase-bearing quartzite (SE16-34a) are highly zoned and characterized by a decrease of grossular and an increase of almandine and pyrope from core to rim.

In Wadi Tayin, garnets from the garnet-clinopyroxene-bearing amphibolite are barely zoned (Fig. 3.6a), with a composition similar to that of the rim of garnets from garnet-clinopyroxene-bearing amphibolite from Khubakhib and Sumeini.

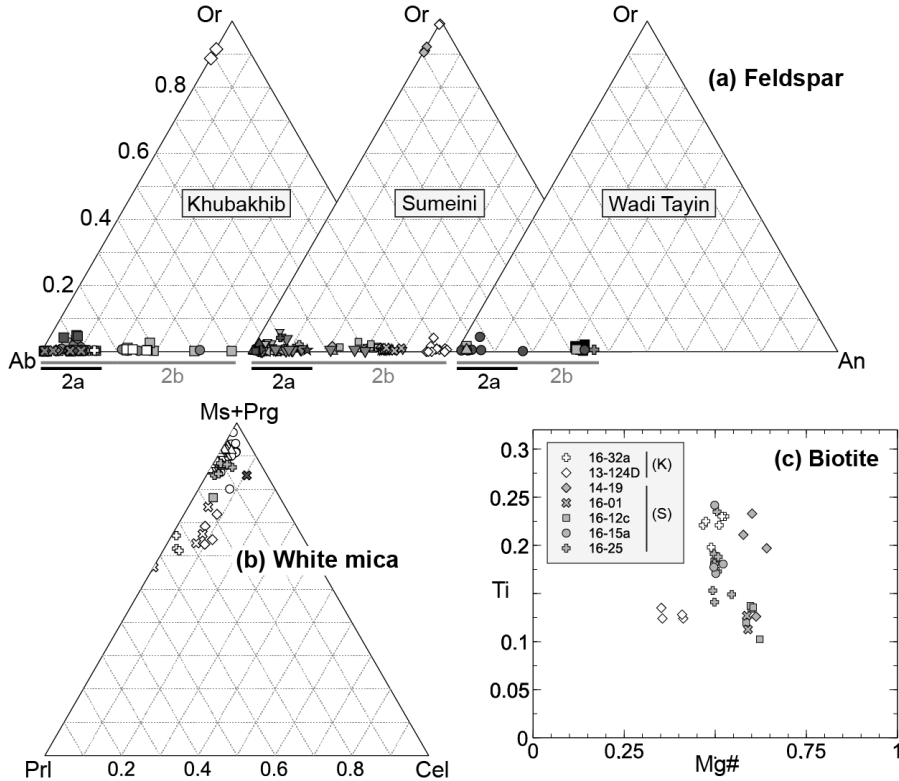


Figure 3.8: Composition of: (a) feldspar; (b) white mica; (c) biotite in the metamorphic sole from three localities (Khubakhib, Sumeini and Wadi Tayin). 2a, 2b and 2c refers to zones defined in the high temperature metamorphic sole. (K) Khubakhib, (S) Sumeini areas.

### 3.8.3 Clinopyroxene

Clinopyroxene is diopside-rich, yet with differences in composition between the three localities. In Khubakhib and Sumeini, the Mg# ranges between 0.55 and 0.72 (Fig. 3.7a,b), whereas in Wadi Tayin, it ranges between 0.65 and 0.73 (Fig. 3.7). The amount of Na, representing the jadeite content, varies up to 0.10 p.f.u. in the north and up to 0.05 p.f.u. in the south (Fig. 3.7d,e,f).

Small differences in Mg# and Na are also observed at the scale of the sample and the transect. These differences are not correlated to the distance from the peridotite, except perhaps for Khubakhib but variability is high within each sample (Fig. 3.7d,e,f). The Mg# shows a variability up to  $\pm 0.05$  and the amount of Na varies up to  $\pm 0.03$  p.f.u. Clinopyroxene with the highest Na content is found both as inclusions in garnet and in the matrix.

### 3.8.4 Feldspar and micas

In the mafic HT sole, feldspar is essentially plagioclase-rich (Fig. 3.8a) and poorly preserved due to sericitization. In garnet-clinopyroxene bearing amphibolite (zone 2a), where the mode of plagioclase is low, their anorthite content ( $\text{Ca}/[\text{Ca}+\text{Na}]$ ) does not exceed 20%. In plagioclase bearing amphibolite (zone 2b), the modal proportion of plagioclase is higher and the anorthite content ranges up to 50% in Khubakhib, 40% in Sumeini and 38% in Wadi Tayin.

In the rare imbricated mica-rich layers, plagioclase and or orthoclase are present together with quartz and garnet (Fig. 3.8a). The composition of white mica fall in between muscovite and pyrophyllite end-members (Fig. 3.8b), which is typical of retrogressive micas (Dubacq et al., 2010). Except one sample (SE16-34a) in Khubakhib, where the Si content reaches 3.44 p.f.u., the Si content is generally low ( $\leq 3.20$  p.f.u.). Biotite has the same composition in the Sumeini and Khubakhib sections (Fig. 3.8c). The Ti content varies between 0.10 and 0.25 p.f.u. Biotite with the highest Ti content has Mg# between 0.47 and 0.60 p.f.u.

## 3.9 P-T Estimates

### 3.9.1 Empirical geothermometry

Several geothermometers were used to estimate the temperature and its evolution along profiles through the metamorphic sole in Khubakhib, Sumeini and Wadi Tayin (Fig. 3.9.1a,b).

Garnet-clinopyroxene Fe-Mg exchange equilibrium was used to estimate the temperature of formation of the garnet-clinopyroxene-bearing amphibolite (zone 2a). For these estimates, the pressure was assumed at 1 GPa (after Gnos, 1998, Cowan et al., 2014), a conservative assumption as garnet-clinopyroxene geothermometry is poorly dependent on pressure (pressure variations of 0.5 GPa lead to a temperature increase  $\leq 15$  °C). The geothermometers of Ellis & Green (1979), Powell (1985), Krogh (1988) gave similar T within the uncertainties of the method (i.e., 25 °C). Other T calculations performed using Krogh (2000) geothermometer, which takes into account the spessartine content, gave T estimates  $\sim 50$  °C lower than the other thermometers. For the sake of comparison, estimates obtained with the geothermometer from Powell (1985) only are used for reference below. T estimates lie in the range of  $875 \pm 50$  °C within zone 2a in Khubakhib and Sumeini

---

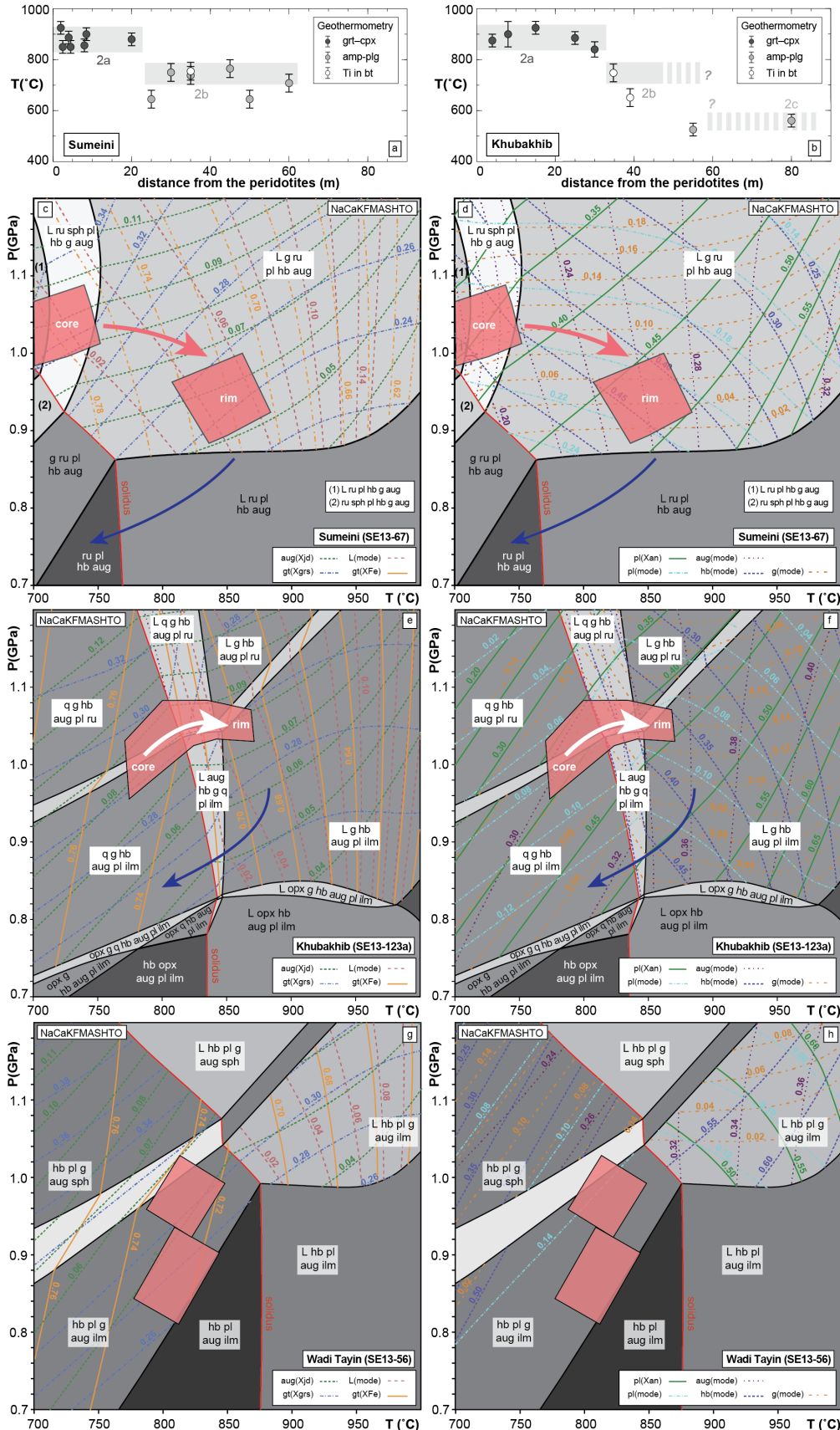
(Fig. 3.9.1a,b) and no trend is observed from top to base (away from the peridotite). In Wadi Tayin, sample SE13-56 gives T estimates around  $825 \pm 25$  °C.

Temperatures of formation of plagioclase-bearing amphibolites (zone 2b) were estimated using the amphibole-plagioclase geothermometer of Holland & Blundy (1994) and the Ti-in-biotite geothermometer of Henry et al. (2005). In Sumeini, amphibole-plagioclase geothermometry gives two T clusters, around  $725 \pm 50$  °C and  $645 \pm 35$  °C (Fig. 3.9.1a). This variation, again, is not correlated with the distance from the peridotite. Since the geothermometer is sensitive to the Ca/Na ratio in plagioclase and samples SE13-76 and SE14-18 have highly-retrogressed plagioclase, the lowest T estimate likely reflects retrogression (with plagioclase compositions getting closer to the albite end-member) rather than peak equilibrium. The Ti in biotite geothermometry for the micas-rich layers at 30 and 64 m from the peridotite (SE14-19 and SE-16-15a) yields T estimates around  $750 \pm 12$  °C and  $740 \pm 12$  °C (Fig. 3.9.1a), similar to the higher T obtained by amphibole-plagioclase geothermometry. In Khubakhib, sample SE13-123m (55 m from peridotite) composed of garnet + amphibole + plagioclase gave T estimates around  $525 \pm 25$  °C and sample SE13-123n (80 m from peridotite) composed of amphibole + plagioclase  $560 \pm 25$  °C (Fig. 3.9.1b). As for Sumeini, these T estimates might be under-estimated due to late plagioclase retrogression. Ti in biotite geothermometry on micas-rich layers located 30 and 40 m away from the peridotite (SE16-32a and SE13-124d) indicates higher T, around  $735 \pm 12$  °C and  $640 \pm 12$  °C (Fig. 3.9.1b). Finally, amphibole-plagioclase thermometry on garnet-free amphibolites from Wadi Tayin (section 2b) indicates similar T around  $710 \pm 20$  °C.

### 3.9.2 Thermodynamic modelling

P-T phase diagrams for fixed bulk rock composition (pseudosections) were calculated in the NaCaKFMASHTO chemical system to constrain the conditions of HT sole formation using the THERMOCALC software (version 3.45; Powell & Holland, 1988, Green et al., 2016) with the updated database version (tc-ds62) of Holland & Powell (2011). The following solution models were used: White et al. (2014) for orthopyroxene, biotite, chlorite and garnet, Green et al. (2016) for mafic melts, augite and hornblende, Holland & Powell (2003) for plagioclase and K-feldspar, and White et al. (2000) for ilmenite-hematite.

The composition used for Sumeini corresponds to the average of all mafic sample compositions across the section (estimated, for each of them, through whole section SEM compositional maps). The composition for Wadi Tayin also corresponds to sample compositions averaged across the section (after Ishikawa et al., 2005). The composition used for Khubakhib was estimated from modal proportions obtained by EBSD mapping on sample



---

Figure 3.8: Estimated P-T conditions for the Semail metamorphic soles. (a-b) T estimates vs. distance from the banded peridotites using empirical geothermometry; (c-h) P-T pseudosections for samples SE13-67 (c-d; Sumeini), SE13-123a (e-f; Khubakhib) and SE13-56 (Wadi Tayin) using the THERMOCALC software (version 3.45; Powell & Holland, 1988, Green et al., 2016) with the updated database version (tc-ds62) of Holland & Powell (2011). The following solution models were used: White et al. (2014) for orthopyroxene, biotite, chlorite and garnet, Green et al. (2016) for mafic melts, augite and hornblende, Holland & Powell (2003) for plagioclase and K-feldspar, and White et al. (2000) for ilmenite-hematite. Bulk compositions are (in mol/ox.): (a,b)  $\text{H}_2\text{O}(3.34)\text{SiO}_2(47.78)\text{Al}_2\text{O}_3(8.79)\text{CaO}(13.41)\text{MgO}(11.42)\text{FeO}(10.47)-\text{K}_2\text{O}(0.33)\text{Na}_2\text{O}(2.44)\text{TiO}_2(1.23)\text{O}(0.79)$ ; (c,d)  $\text{H}_2\text{O}(3.02)\text{SiO}_2(46.36)\text{Al}_2\text{O}_3(7.42)\text{CaO}(14.12)\text{MgO}(13.17)\text{FeO}(11.97)\text{K}_2\text{O}(0.20)\text{Na}_2\text{O}(1.95)\text{TiO}_2(0.89)\text{O}(0.89)$ ; (e,f)  $\text{H}_2\text{O}(3.41)\text{SiO}_2(47.66)\text{Al}_2\text{O}_3(9.60)\text{CaO}(15.75)\text{MgO}(10.75)\text{FeO}(7.84)\text{K}_2\text{O}(0.63)\text{Na}_2\text{O}(2.52)\text{TiO}_2(1.26)\text{O}(0.59)$ . Whole-rock oxidation was estimated at 15%. Arrows highlight the inferred P-T path followed by each unit of garnet-clinopyroxene amphibolite. Abbreviations after Holland & Powell (1998).

SE13-123a. Whole-rock oxidation was estimated at 15%, as in the reference study of Palin et al. (2016).

P-T estimates for zone 2a lie in the fields with garnet, clinopyroxene, amphibole, plagioclase  $\pm$  ru/ilm/sph. Peak conditions were determined based on isopleths for garnet (grossular content and XFe), clinopyroxene (jadeite content), and anorthite content in plagioclase. For Sumeini, maximum P-T conditions yield around  $0.92 \pm 0.03$  GPa -  $850 \pm 30^\circ\text{C}$  (Fig. 3.9.1c,d). For Khubakhib, they are estimated around  $10.04 \pm 0.01$  -  $850 \pm 20^\circ\text{C}$  (Fig. 3.9.1e,f). For Wadi Tayin, P-T estimates are  $0.9 \pm 0.1$  GPa and  $820 \pm 30^\circ\text{C}$  (Fig. 3.9.1g,h).

For Sumeini and Khubakhib estimated modes match those of amphiboles (40-45% against 42% and 31%, respectively, in the samples), clinopyroxene ( $\sim 25$  and 35%, respectively, against 22% and 34% in the samples) and garnet ( $\sim 15\%$  against 12% and 6% and in the samples). For Wadi Tayin, mineral compositions and modes of Ghent & Stout (1981) were considered for reference, as they provide data for more samples than the present study. Ti content in amphibole is somewhat lower than documented (0.1 against 0.15-0.23; Fig. 3.5g-i), but relative variations are correctly reproduced (i.e., higher Ti contents in amphibole for zone 2a than for 2b). Ti-bearing phase relation (rutile, ilmenite, titanite) are complex to reproduce in pseudosection. However, considering their very low calculated modal proportion ( $\leq 0.1\%$ ), change in Ti phases in equilibrium does not change significantly the absolute position of the calculated fields and the chosen mineral isopleths. Modifying the whole-rock oxidation does not affect the Ti phase at equilibrium.

The complex but systematic chemical zonation observed in garnet crystals (Fig. 3.6) allows assessing the shape of the P-T paths for the garnet-clinopyroxene amphibolite (zone 2a). In both Khubakhib and Sumeini, garnet displays a similar core-to-rim zonation with a decrease in Ca and Mn content and an increase in Mg and Fe content. In both areas this zonation is associated with inclusions of clinopyroxene and rare brown amphibole. Rare garnet crystals preserve an inner zonation recording an increase in Ca and Mg contents (Fig. 3.6b). In Sumeini, the zoned core hosts inclusions of rutile + titanite, whereas epidote + clinopyroxene + brown-green amphibole are observed in Khubakhib. This zonation (synchronous with the disappearance of epidote in Khubakhib) is here correlated with an increase of both pyrope and grossular contents toward the rim, and is likely interpreted as the record of increasing T during crystallization. Considering the evolution of the preserved jadeite content in clinopyroxene, P is interpreted to slightly decrease in Sumeini ( $dP \leq 0.1$  GPa) during prograde amphibolite to granulite recrystallization and to slightly increase for Khubakhib (Fig. 3.8c-e). Uncertainties on P estimates are hard to appreciate precisely. They lie likely between 0.03 GPa (considering analytical uncertainties only) and 0.1 GPa (also considering uncertainties on thermodynamic properties as for multi-equilibrium thermobarometry).

Finally, all pseudosections consistently point to small amounts of melt (< 6 vol%). This result is consistent with calculations performed for a MORB-like bulk composition (Palin et al., 2016, i.e., melt amounts < 10 vol% at such T) using the same mafic melt model (Green et al., 2016).

## 3.10 Discussion

### 3.10.1 Stepwise structure of the HT metamorphic sole

Over the three localities, from north to south, the Semail metamorphic sole displays a similar structure marked by a stepwise decrease of the maximum P-T conditions in the HT sole (Fig. 3.9.1; absolute P-T values are discussed below) and a slight but noticeable increase of the proportion of quartz- and mica-rich layers. The metasedimentary fractions remain subordinate, however, compared to the LT sole where they largely dominate over mafic protoliths. Since there are no significant differences in major element composition of the MORB-type protolith across the HT sole (in Wadi Tayin: Ishikawa et al., 2005), differences in mineral composition throughout the HT sole may be interpreted as changes in P and/or T conditions. This "inverted" structure, however, is not gradational and presents sharp changes structure, mineralogy and in mineral composition that can be found in all the studied sections:

---

1. Changes in structure and mineralogy: immediately below the mylonitic peridotite, zone 2a (up to  $\sim$ 40 m in Khubakhib) consists in a strongly foliated, granulitic facies garnet-clinopyroxene-bearing amphibolite (Fig. 3.1, 3.3), with a fine-grained assemblage composed of garnet + blue pale clinopyroxene, together with brown amphibole ( $\leq$  300  $\mu\text{m}$ ) and minor plagioclase (Fig. 3.7a). In Khubakhib and Sumeini, modal proportions do not vary as a function of the distance to the peridotite contact but depend on the degree of retrogression, underlined by the syn-kinematic crystallization of secondary coarse grain size amphibole ( $\geq$  500  $\mu\text{m}$ ) and plagioclase replacing garnet, primary amphibole and clinopyroxene (Fig. 3.7b). Mylonitic textures, with boudinaged clinopyroxene and garnet and grain size reduction at clinopyroxene rims (Fig. 3.7a), are well preserved at the contact with peridotites. This garnet-clinopyroxene amphibolite horizon is much thinner and strongly boudinaged in Wadi Tayin and wrapped by a garnet-free amphibolite (Fig. 3.1).

There is a sharp transition in grain size, deformation patterns and to some extent lithology from zone 2a to zone 2b (Fig. 2) made of plagioclase-bearing amphibolite with brown-greenish amphibole and rare garnet or clinopyroxene. In the three localities, there is an abrupt increase in amphibole (and plagioclase) grain size, varying between 1 and 3 mm, and a higher spatial variability of the mineral assemblage (again, not correlated with the distance from peridotite). Zone 2b is also characterized by the appearance of biotite in small amounts ( $\leq$  10%) in  $\leq$  5 cm-thick imbricated layers. Moreover, a highly sheared zone (red-brown from weathering) coincides structurally, in both Khubakhib and Sumeini, with the lithological and chemical discontinuity observed between zones 2a and 2b (Fig. 3.1): this 2-5 m thick zone made of quartz + biotite + garnet  $\pm$  amphibole  $\pm$  plagioclase  $\pm$  orthoclase is parallel to the main foliation of the HT sole and laterally continuous at the hm-scale. This zone is interpreted as a metagreywacke horizon metamorphosed at high temperature and may have localized deformation during accretion (see below): in Khubakhib, it is folded and embeds sheared amphibolite boudins, suggesting that localized shearing occurred during the structuration and the metamorphism of the HT sole in the amphibolite facies. The 2a/2b transition also coincides with a change in deformation style: the garnet-clinopyroxene-bearing zone 2a mainly displays sub-horizontal flattening, whereas the plagioclase-bearing zone 2b shows shear structures and small-scale folds in addition to strong flattening.

In Sumeini and Khubakhib, zone 2b reaches  $\sim$ 40 m in thickness. Small-scale folds and recumbent folding are observed in Wadi Tayin, essentially marked by imbricated quartzite horizons (Fig. 3.3i). Later retrogression, linked to crosscutting rodingite veins and associated epidote (Fig. 3.2b,c, 3.3b), affects the whole HT sole and leads in places to the

total disappearance of the peak assemblage. Whether in zone 2a or 2b, the degree of retrogression related to these networks of veins increases downwards.

By contrast, the underlying LT sole (zone 3) is characterized by a marked enrichment in quartz and larger heterogeneity in bulk composition, underlined by the presence of ubiquitous m- to hm-scale folds (Fig. 3.1, 3.3g,i). This zone includes metacherts and fine-grained metabasites consisting of acicular actinolite + plagioclase  $\pm$  chlorite  $\pm$  epidote  $\pm$  muscovite and interlayering with calc-silicate rocks. In metacherts, muscovite  $\pm$  chlorite  $\pm$  piemontite  $\pm$  spessartine-rich garnet coexist with quartz.

2. Changes in mineral compositions: garnet, clinopyroxene, amphibole, plagioclase compositions do not show any gradational change in the HT sole (Fig. 7-9), unlike what would be expected in the case of a continuous thermal gradient across the sole. The Fe, Mg and Ca content in garnet, the Ca# in plagioclase, and the Mg# and the jadeite content in clinopyroxene differ only between zones 2a and 2b, confirming the existence of a major discontinuity in structure and mineralogy between these 2 units. The decrease in Ti content of the amphibole away from the peridotites (noted by Ghent & Stout, 1981, Searle & Malpas, 1982, Gnos, 1998, Cowan et al., 2014) is also stepwise (Fig. 3.5). Given the ubiquitous presence of titaniferous phases in the metamorphic sole (titanite, rutile, ilmenite), these thresholds of Ti saturation in amphibole are interpreted as changes in T consistently with the sensitivity of Ti saturation in amphibole to T (Ernst & Liu, 1998). Amphibole has a maximum Ti content  $\leq$  0.23 p.f.u. for brown amphibole in equilibrium with garnet and clinopyroxene in zone 2a (in Sumeini and Wadi Tayin, and in the garnet-clinopyroxene bearing amphibolite closest to the peridotite in Khubakhib) and  $\leq$  0.16 p.f.u. for brown-greenish amphibole in equilibrium with plagioclase  $\pm$  epidote in zone 2b (where garnet and clinopyroxene do not coexist). In zone 2a, coarse-grained brown-greenish amphibole replacing clinopyroxene (and coexisting with plagioclase replacing garnet) also has a Ti-content  $\leq$  0.16 p.f.u. Finally, late green amphibole rimming both brown and brown-greenish amphibole in the HT sole (most pervasively in Wadi Tayin) shows the lowest Ti content ( $\leq$  0.05 p.f.u.), as for green amphibole coexisting with plagioclase and epidote in the peak assemblage of the LT sole.

Although tectonic contacts between zones 1, 2 and 3 (basal peridotites, HT sole and LT sole, respectively) are clear and marked by abrupt changes in lithology and metamorphism (Fig. 3.4c, 3.3a; Searle & Malpas, 1982, Cowan et al., 2014) and even in lineation strike in places (e.g., for Wadi Tayin; Boudier et al., 1985), no tectonic contact had been identified yet within the HT sole. The potential existence of such discrete slices was anticipated by Gray & Gregory (2000) and Cowan et al. (2014). Interestingly, a 40 to 100 m thick biotite- and garnet-rich mylonite zone was also reported by Jamieson & Strong (1981)

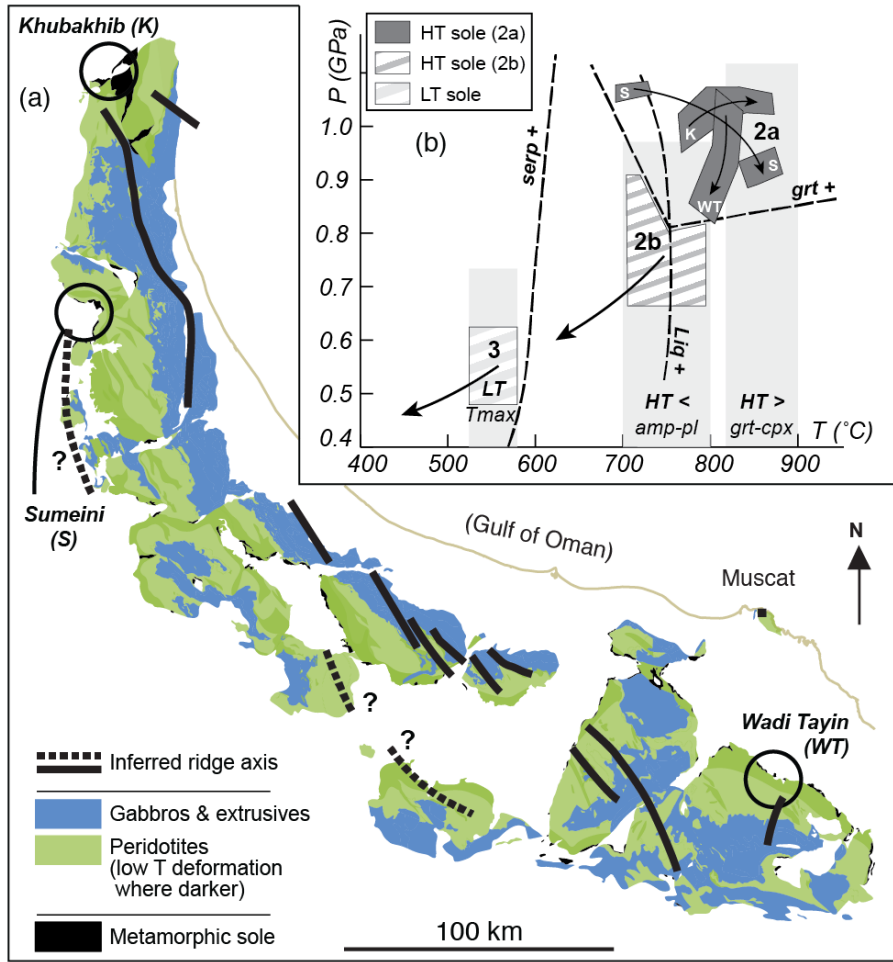


Figure 3.9: (a) Simplified geological map of the Semail ophiolite with the position and orientation of the inferred ophiolitic ridge axis (black lines), after Nicolas et al. (2000); (b) Compilations of P-T estimates and associated P-T paths calculated in this study for each zones, from the garnet-clinopyroxene amphibolite (HT sole 2a), to the plagioclase amphibolite (HT sole 2b) and greenschist facies (HT sole 3) metamorphic sole units. P estimates for the plagioclase amphibolite unit are constrained by the lower limit of stability of garnet + clinopyroxene. P estimates for the LT sole are from Bucher (1991a).

within the metamorphic sole of the St Anthony Complex (Newfoundland, Canada), at a structural and petrological change in the high-grade metamorphic sole. These authors suggested that the mylonite zone formed by localized K-rich metasomatism of the amphibole sole associated with dehydration reactions during the latest stages of the amphibolite-facies metamorphism and deformation. However, in Sumeini, biotite and amphibole are at textural equilibrium, in favour of global equilibration.

### 3.10.2 P-T estimates, P-T paths, along strike variations and implications

Pressure-temperature estimates for the three localities are compared in figure 12. Temperature estimates using garnet-clinopyroxene geothermometry for the HT sole (zone 2a;  $850 \pm 50^\circ\text{C}$ ; Fig. 3.9.1a,b) give systematically  $T \geq 100^\circ\text{C}$  than those estimated by amphibole-plagioclase and Ti in biotite geothermometry for the plagioclase amphibolite (zone 2b;  $725 \pm 50^\circ\text{C}$ ). Maximum T conditions for the garnet-clinopyroxene amphibolites are similar to those previously published for the Semail metamorphic sole (Ghent & Stout, 1981, Searle & Malpas, 1982, Gnos, 1992, 1998, Hacker et al., 1996, Searle & Cox, 2002, Cowan et al., 2014). No continuous T decrease within each of these two zones can be evidenced from garnet-clinopyroxene and plagioclase-amphibole geothermometry (Fig. 3.9.1a,b). Nor does the Mg# in amphibole, which was previously interpreted as a continuous T change through the Semail metamorphic sole (Gnos, 1998), show consistent evolution with the distance from the peridotite. This is in accordance with the uniform distribution of Ti content in amphibole (Fig. 3.5) and with the nature of inclusions and zonation in garnet (Fig. 3.6).

Peak P estimated through pseudosection modelling for Sumeini and Khubakhib range between 0.9 and 1.1 GPa (Fig. 3.9.1c-f, 3.9b), consistently with the presence of kyanite in the HT sole (Gnos, 1992, 1998) and some previous estimates ( $1.1 \pm 0.2$  GPa; Gnos, 1998, Searle & Cox, 2002, Cowan et al., 2014). Pressure estimates for the garnet-clinopyroxene amphibolite are probably less robust than the T estimates due to uncertainties on the re-equilibration of plagioclase. Nevertheless, in the three areas, a systematic gap of  $P \geq 0.2$  GPa is observed between the garnet-clinopyroxene amphibolite (zone 2a) and the plagioclase amphibolite (zone 2b), where garnet and clinopyroxene do not coexist (Fig. 3.9b).

Despite differences in the jadeite content in clinopyroxene (Fig. 3.7) and Si/Al<sup>IV</sup> content in amphibole (Fig. 3.5), no significant difference is observed in the P estimates between the front and the rear of the ophiolite, which is a proxy to the assumed position of the ridge (Fig. 3.9a; Nicolas et al., 2000). No contrast is found between the north and south (Khubakhib and Sumeini vs. Wadi Tayin), except perhaps a slightly lower P in the south. The higher minimum Si content in amphibole from Wadi Tayin ( $\geq 6.2$  p.f.u compared to  $\geq 6.1$  p.f.u. in Khubakhib and Sumeini) would rather be consistent with lower P and/or higher T at peak conditions in the south. Based on observed zonations in garnet, slight differences in P-T path can be inferred (Fig. 3.9.1,3.9b), but are probably to be taken with caution as they lie within the bounds of P-T uncertainties (i.e.,  $\pm 0.1$  GPa  $\pm 30\text{-}50^\circ\text{C}$ ). Considering the fast cation diffusion in garnet at such T (Carlson, 2006,

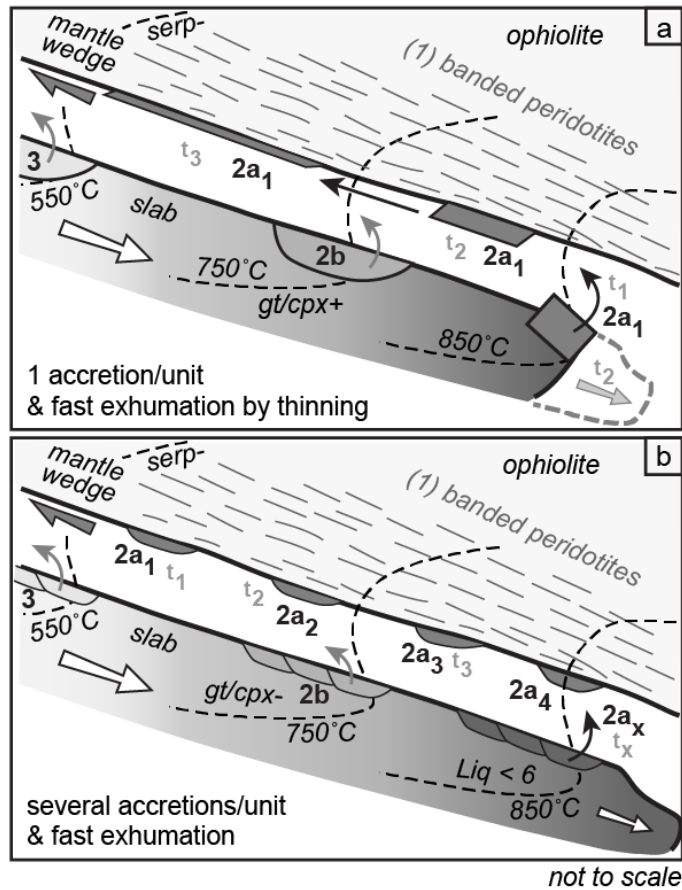


Figure 3.10: Two different *scenarii* proposed for the formation and exhumation of the HT metamorphic soles (and later the LT soles) and its present-day distribution beneath the ophiolite. (a) Accretion of one unique thick sliver at the same location and depth during a short time interval across the ophiolite with a later "redistribution" below the ophiolite by exhumation and/or tectonic thinning together with the basal peridotites; ; (b) Formation by successive and continuous accretion of thin slivers at the same depth across a short time interval ( $\sim 1\text{-}2$  My).

Kohn, 2013), this preservation of zonation hints to a fast formation and/or exhumation. Finally, the thermobarometric estimates presented here argue for a clockwise P-T path, a limited melting in zone 2a ( $< 6$  vol%) and no melting in zone 2b.

All these results contradict the existence of a steep T gradient in the Semail HT metamorphic sole and support instead the structural discontinuity outlined in the previous section. The HT metamorphic sole must be regarded as resulting from the stacking of several homogeneous slivers of oceanic crust formed at different P-T-(t) conditions (zones 2a, 2b and possibly 2c), with discontinuities outlined (and probably mechanically facilitated) by the presence of thin veneers of metasediments (i.e., the micas-rich layers; Fig. 3.1, 3.2d,e, 3.3d). Tectonic and mechanical implications (including those related to the limited amounts of melting) are discussed afterwards.

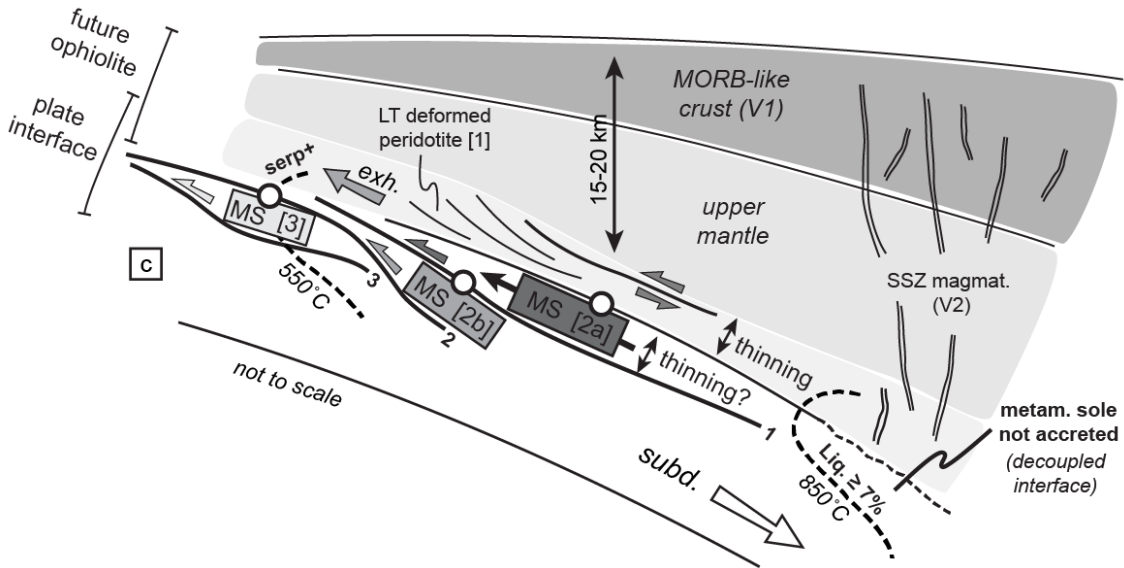


Figure 3.11: Evolutive model for metamorphic sole formation and structuration during the early subduction dynamics by stepwise accretion and exhumation of successive slices from the downgoing slab to the LT deformed base of the ophiolite. The upper and lower limits for allowing interface coupling and metamorphic sole accretion would correspond respectively to the threshold of 7% of partial melting in the slab and the stability field of serpentine in the nascent mantle wedge.

Figures 3.10 and 3.9.1 schematize the successive accretion of several crustal slices to the base of the mantle, now making up the metamorphic sole (with the mostly metasedimentary LT soles from zone 3 systematically underlying the mostly mafic HT soles from zone 2). The present study shows that these thin metamorphic soles, whether now located at the front or rear of the ophiolite thrust, formed at the same approximate P-T conditions and yet got welded along large distances (across 100-150 km). Two explanations can be put forward to account for this puzzling observation: (1) HT metamorphic soles (and later on LT soles) would form at the same location and depth during a short time interval and later be "redistributed" below the ophiolite, together with basal peridotites, by exhumation and/or tectonic thinning (Fig. 3.10a; see below the specific discussion on this point), or (2) HT metamorphic soles (and later on LT soles) would form and get accreted continuously at the same depth across a certain range of time ( $\leq 1$  My given available time constraints; Hacker, 1994, Rioux et al., 2013, 2016) so that their distribution below the ophiolite would result from longer-lived accretion rather than from later deformation (Fig. 3.10b). The similarity in garnet zoning and in the 2a/2b nappe stack (found hundreds of km apart) support the first hypothesis. On the other hand, the absence of compositional trend away from the peridotite advocates for the accretion of thin slices rather than of a thick piece (where a T gradient might have developed) later thinned. In the first hypothesis, the inferred maximum thickness of slices, before thinning, is limited by that of the basalt layer covering the subducting oceanic plate (i.e., since no gabbroic rocks have been reported in

---

the Semail metamorphic sole. In the second hypothesis, the number of slices of a same zone (homogeneous in P-T conditions) is mainly limited by the cooling of the plate interface.

Pressure estimates for zone 2b are slightly lower (0.2-0.4 GPa) than those estimated for zone 2a. This difference can either be explained (Fig. 3.11) by the relative exhumation of the metamorphic sole and basal peridotites (zones 1-3) with respect to the rest of the ophiolite above and/or by the tectonic thinning of basal peridotites and/or metamorphic soles (which, considering the present-day thickness of the mylonitic to ultramylonitic banded peridotites, would imply a  $\gamma$  of  $\sim 4-5$ ), or a combination of both. In the absence of P estimates across the banded, basal peridotites, this remains an open question.

### **3.10.3 Accretion of metamorphic soles and mechanical coupling: extent and role of partial melting and links with the ophiolite**

Metamorphic sole formation may be set back in the broader context of early subduction dynamics (Fig. 3.11; i.e., right after intra-oceanic subduction initiation) and of its joint evolution with the (base of the) ophiolite. The successive formation, detachment and accretion of the mafic HT sole (and of the metasedimentary LT one, later) testifies to an increased mechanical coupling between the downgoing and upper plates (Agard et al., 2016), which is reflected in the coeval high strain mylonitic deformation of the HT sole and the basal/banded peridotites. Right after subduction initiation, as the slab starts penetrating into the upper plate mantle and gets heated up (Fig. 3.4a), it progressively dehydrates and releases fluids into the nascent mantle wedge. This has two consequences (Agard et al., 2016): (1) the slab crust will face increasing resistance from the mantle with depth: at shallow depths it is juxtaposed against a weak, serpentized mantle but progressively encounters downwards a hotter and therefore drier, stiffer mantle; (2) for a given depth, the mantle wedge will progressively weaken over time through hydration and cooling and experiences changes in deformation mechanisms (as noticed in the banded peridotites; Linckens et al., 2011, Herwegen et al., 2016). During slab descent, the strength of the interface material (slab crust and mantle wedge) progressively changes through mineral recrystallization and dehydration/hydration (e.g., formation of clinopyroxene and garnet in the HT soles at T around  $\sim 850 \pm 50^\circ\text{C}$ ) until effective viscosities on either side of the plate interface, as constrained by rock mechanics, become equivalent. This induces transient coupling across the early subduction interface across a restricted P-T-time window ("rheological switch"; Agard et al., 2016) and the welding of metamorphic soles. As the interface gets temporarily clogged, the detachment of the metamorphic soles occurs within the slab on a weaker horizon, probably at the transition between dry mafic granulites and less metamorphosed and/or more hydrated mafic layers, and/or between basalts and sheeted dikes (owing to

the lack of metagabbros in metamorphic soles). (Agard et al., 2016) showed how, during cooling, a second rheological switch between mantle and sediments can account for the accretion of LT soles at  $\sim 550 \pm 50$  °C and  $\sim 0.5$  GPa (Fig. 3.9b).

The present study reveals, at  $750 \pm 100$  °C, via the accretion of the plagioclase-bearing HT sole (zone 2b), another transient coupling (and rheological switch) of the subduction interface. The study of zones 2a and 2b allows better constraining these accretionary processes, in particular as to the role (and extent) of partial melting and of metasediments.

The hardening process associated with increasing amounts of garnet and clinopyroxene (mechanically stronger than amphibole and plagioclase, as shown by Fig. 3.7a) during the prograde evolution of the HT sole, is in competition with partial melting inducing weakening: experimental data on the deformation of partially melted continental crustal rocks reveal a dramatic strength drop when melt fraction  $> 7\%$  (Rosenberg & Handy, 2005), with the formation of interconnected melt channels. This melt fraction threshold could therefore constitute an important upper accretion limit for metamorphic soles to the mantle wedge: with melt fractions larger than  $\sim 7\%$ , the slab interface would become too weak to allow coupling with the mantle wedge peridotites. This weakening would however be counter-balanced by melt extraction, once melt connectivity is allowed in the rock and percolation starts (Maaløe, 1982), which occurs at a 5-10 vol% threshold (Vanderhaeghe, 2009).

In the Semail ophiolite, scattered granitoid intrusions were interpreted to witness transfer of melts from the subducted plate to the nascent mantle wedge (Fig. 3.11) and, together with the liberation of fluids, to contribute to the re-fertilization of the overlying ophiolite (Ishikawa et al., 2005, Python et al., 2008, MacLeod et al., 2013). These granitoid dikes are thought to result from the interaction with the depleted ophiolitic mantle of partial melts derived from either mixed mafic/sedimentary (Rollinson, 2015) or metasedimentary sources only (Haase et al., 2015, 2016). Partial melting would have occurred during the metamorphic sole formation (95-93 Ma; Rioux et al., 2013, 2016, Searle et al., 2014) and at similar P-T conditions ( $\sim 1$  GPa; Rollinson, 2015, Moyen & Stevens, 2013), with melt fractions of  $\sim 20\%$  estimated by Rollinson (2015) to generate the granitoid intrusions.

Partial melting, however, is scarcely observed in the Oman/UAE metamorphic soles and restricted to rare tonalitic to trondhjemite pods, regarded as possible partial melts (Searle & Malpas, 1982, Hacker & Mosenfelder, 1996, Gnos, 1998, Cowan et al., 2014), as supported by U-Pb ages (95-94 Ma; Searle et al., 2014, Rioux et al., 2016) and P-T conditions (770-900 °C and 1.1-1.4 GPa; Cowan et al., 2014) similar to those of the HT

---

sole. Accordingly, thermodynamic modelling of the mafic HT sole shows that only a small melt fraction is expected at these temperature-depth conditions (< 6%; Figs. 3.9.1,3.9; more melting can be predicted deeper down, but corresponding rocks are not exhumed). We therefore conclude that, during the accretion of zone 2a, melting of mafic protoliths likely did not have a strong impact on inter-plate coupling. These amounts may, however, have been sufficient to allow strain localization within the slab and subsequent detachment of the soles (as for the triggering of deep-seated exhumation in the Caledonides; see Labrousse et al., 2011).

Although inferred to be a major melting source for the granitoid intrusions, metasediments are accidental if not absent from the garnet-clinopyroxene amphibolite. The general lack of metasediments in zone 2a (and in most of zone 2b) could be explained by the limited sedimentary supply away from continents (Fig. 3.4a) or, alternatively, by a high degree of melting in these lithologies, such that sediments at the surface of the slab could not have been accreted and/or were removed by magma extraction (thereby contributing to some of the granitoid intrusions). Mafic rocks, more refractory to partial melting, would have been accreted instead.

Extensive sedimentary melting is possible in zone 2a, but very unlikely in zone 2b, given that temperatures are at or below the wet sediment liquidus (i.e., biotite-out reaction, at  $\sim$ 700–750 °C between 1.0 and 1.5 GPa). The m-thick micas-quartz-rich layer located at the boundary between zones 2a and 2b in both Khubakhib and Sumeini may represent the former slab cover, made of interlayered metasediment and metabasalt, or result from fluid circulation and metasomatism during the accretion of the second sliver. In any case, this thin, mechanically weak layer likely contributed to the detachment and accretion of zone 2b (again mainly mafic) to the overlying basal peridotites.

We conclude that the accretion of the higher T portion of the HT soles (zone 2a) took place at the expense of a mainly mafic crustal piece (Fig. 3.11). The strong viscous coupling between the hardened granulite and the basal peridotites of the mantle wedge triggered the process of accretion. Minimal amounts of mafic melts were formed during this process (< 6%), which were partially removed, but may have contributed to strain localization and detachment of this slice. Evidence for metasediments playing a significant role at this stage is still elusive, however 1) limited amounts of melted metasediments may have fed the granitoid intrusions scattered in the Semail ophiolite and 2) metasedimentary veneers documented in zone 2b likely enhanced weakening of the slab crust and strain localization during the detachment of slice 2b.

### 3.11 Conclusion

The comparison of three sections in the Semail ophiolite shows that metamorphic soles formed during subduction infancy are structurally and compositionally discontinuous. Using a combination of structural and petrological data, we show that the metamorphic soles do not record a continuous T gradient, as would be expected from simple heating by the upper plate (i.e., the nascent mantle wedge) or by shear heating. HT soles can be, conversely, subdivided in at least two units (zones 2a and 2b), thereby testifying to the formation and detachment of successive slices from the downgoing slab and accretion/welding to the mylonitic base of the ophiolite.

Detailed petrological work across the three localities tied to thermodynamic modelling allows reappraising the P-T conditions for HT (zone 2a:  $850 \pm 50^\circ\text{C}$ ; zone 2b:  $725 \pm 50^\circ\text{C}$ ) and LT soles (zone 3:  $534^\circ\text{C} \pm 27^\circ\text{C}$ ), each zone being separated by  $\sim 0.2$  GPa. Despite contrasting locations with respect to the ridge axis, no significant along-strike variations are evidenced. Chemical zoning in garnet and jadeite content in clinopyroxene records prograde clockwise P-T path over a  $dT \geq 100^\circ\text{C}$  and a  $dP \geq 0.1$  GPa. Such preservation suggests fast formation and exhumation, in agreement with radiometric data.

The lower T limit for accretion of zone 2a (and its inception) is the appearance of clinopyroxene and garnet (i.e.,  $\sim 800 \pm 50^\circ\text{C}$ ) enhancing the strength of the amphibolite and reducing the rheological contrast with the nascent and strong mantle wedge (Agard et al., 2016). At these peak P-T conditions thermodynamic modelling predicts only limited amounts of partial melting (< 6%), consistently with field observations. During accretion of the garnet-clinopyroxene amphibolite (zone 2a), melting of mafic protoliths likely did not strongly impact interplate viscous coupling (melts remain unconnected for such small fractions) but may have contributed to strain localization and detachment of the zone 2a slice. However, at higher T (i.e., greater depths, as the slab continues its progress into the mantle), accretion of metamorphic soles is probably inhibited once melt connectivity is reached (i.e., for melt fraction > 7%), since the resulting strength drop in the slab crust will favour mechanical decoupling at the plate interface. With time and associated cooling/weakening of the mantle wedge, coupling and accretion is only permitted for weaker, more sediment-rich slices (i.e., zone 2b, with amphibole, plagioclase and biotite). Accretion of the metasediment-rich LT soles (zone 3) marks the end of accretion at  $T \geq$  at the upper stability limit of serpentine, when the mantle wedge transiently reaches a viscosity close to that of metasediments (Agard et al., 2016). Accretion of metamorphic soles becomes inhibited with further cooling, once the nascent mantle wedge becomes serpentized and the viscosity contrast between the slab and the upper plate too high to allow coupling at the plate interface.

---

The new evolutive model proposed to account for the formation of discontinuous metamorphic soles during subduction infancy, via multiple stages of deformation and plate interface coupling, further constrains existing rheological (Agard et al., 2016) and numerical models (Duretz et al., 2016). The existence of successive episodes of slicing of the slab shed light on the thickness, scale and mode of mechanical coupling at the plate interface during early subduction dynamics. Future studies should help elucidate the duration and stress magnitude of these processes.

## Acknowledgment

We thank O. Boudouma (ISTeP– UPMC, France), M. Fialin and N. Rividi (CAMPARIS) and D. Deldicque (ENS Paris, France) for analytical support, and E. Deleris and M. Moroni (ISTeP–UPMC) respectively for the preparation and the scanning of thin-sections. We also thank F. Piccoli, G. Bonnet, A.C Ganzhorn, M. Micatelli and L. Van Unik Hoorn for useful help and interesting discussions. This work was essentially funded through the ONLAP project (ANR blanche, SIMI6; 2010 BLAN 615 01). Additional support was provided by an IUF grant (Institut universitaire de France) to Philippe Agard.

## Supplementary Material

Zones	Dist. (m)	Samples	Mineral occurrences								GPS coordinates	
			Grt	Cpx	Amp	Plg	Ep	Qz	Bt	Other	N (°.')	E (°.')
2a	2	11-23	x	x	x	-					24.41.54.9	56.04.30.6
	2.5	13-67	x	x	x	-	(-)				24.41.51.3	56.03.50.4
	3	14-33	x	x	x	x					24.42.01.9	56.03.41.5
	4	13-68	x	x	x	x					24.41.50.4	56.03.50.2
	8	13-69	x	x	x	x					24.41.50.4	56.03.49.8
	10	14-31	x	x	x	x					24.42.05.2	56.03.37.3
	15	13-71	x	x	x	x					24.41.50.7	56.03.49.6
	20	13-74	-	-	x	x	x				24.41.49.1	56.03.46.7
	22	13-75		x	x	x					24.41.49.1	56.03.46.7
	25	13-76			x	x	x				24.41.49.1	56.03.46.0
2b	26	16-27		x	x	x	x				24.41.47.9	56.03.46.3
	27	14-20			x	x	x				24.41.49.3	56.03.46.1
	30	14-19	x		x	x		x	x	Or	24.41.47.8	56.03.45.7
	34.5	16-12			x	x			x		24.41.45.5	56.03.45.6
	35	16-26	x		x	x			x		24.41.47.0	56.03.45.2
	36	16-01			x	x			x		24.41.46.8	56.03.45.7
	55	16-11		x	x	x	x				24.41.43.8	56.03.44.7
	64	16-15			x	x			x		24.41.41.6	56.03.46.1
	65	14-16			x	x					24.41.45.3	56.03.42.8
	70	14-17			x	x					24.41.45.1	56.03.41.7
	75	16-25			x	x		x			24.41.42.0	56.03.40.3
	80	16-21			x	x	x			Or/Ms	24.41.36.6	56.03.34.3

Table 3.1: Parageneses of metamorphic sole samples analysed and corresponding GPS coordinates from the Sumeini area. Ti phases are ubiquitous (see details in text). x: present; -: rare. Abbreviations after Whitney & Evans (2010).

Khubakhib window			Mineral occurrences								GPS coordinates	
Zones	Dist. (m)	Samples	Grt	Cpx	Amp	Plg	Ep	Qz	Bt	Other	N (°.')	E (°.')
2a	2	13-123a	x	x	-	x					25 26 48.1	56 05 46.6
	8	13-123d	x	x	x	x	-				25 26 48.1	56 05 46.3
	15	13-123g	x	x	x	x	-				25 26 47.2	57 05 46.1
	25	13-123i	x			x	x	x	x	Ms/Chl	25 26 46.3	56 05 46.2
	28	13-123j	x	x	x	x	x				25 26 45.8	56 05 46.2
2b	30	16-32a	x		x	x		x	x	Ms/Chl	25 26 46.2	56 05 45.9
	38	16-34a	x					x		Ms/Chl	25 26 44.9	56 05 45.4
	40	13-124d			x	x			x	Or	25 26 32.9	56 05 32.5
	42	13-123l	x		x		x	x		Ms	25 26 44.3	56 05 46.5
	55	13-123 n	x		x	x	x				25 26 44.3	56 05 46.7
2c	70	16-35	x		x			x		Ms/Chl	25 26 43.1	56 05 45.7
	80	13-123 n			x	x					25 26 41.2	56 05 44.3

Table 3.2: Parageneses of metamorphic sole samples analysed and corresponding GPS coordinates from the Khubakhib area. Ti phases are ubiquitous (see details in text). x: present; -: rare. Abbreviations after Whitney & Evans (2010).

Wadi Tayin window			Mineral occurrences								GPS coordinates	
Zones	Dist. (m)	Samples	Grt	Cpx	Amp	Plg	Ep	Qz	Bt	Other	N (°.')	E (°.')
2a	2	13-56	x	x		x				Ms/Chl	23 03 19.4	58 35 47.4
	4	13-57	x		x	x	x			Ms/Chl	23 03 20.7	58 35 47.1
	15	13-58			x	x	x				23 03 22.2	58 35 48.8
2b	35	13-60a			x	x					23 03 23.4	58 35 50.4
	50	16-38c			x	x	x			Ms	23 03 25.2	58 35 53.4
	80	16-37			x	x					23 03 42.5	58 35 46.7

Table 3.3: Parageneses of metamorphic sole samples analysed and corresponding GPS coordinates from the Wadi Tayin area. Ti phases are ubiquitous (see details in text). x: present; -: rare. Abbreviations after Whitney & Evans (2010).

Table 3.4: Selected representative analyses of amphibole, plagioclase, orthose, clinoptyroxene, biotite and garnet from point analysis and compositional maps. (c): core of zonation. Abbreviations after Whitney & Evans (2010).



---

# 4 Déformation des amphibolites en contexte d'initiation de subduction

## 4.1 Préambule

Ce chapitre correspond à un article en préparation pour la revue *Earth and Planetary Science Letters*.

Nous présentons ici les résultats de l'étude de la déformation et des mécanismes associés des amphibolites de haute température des semelles métamorphique de Semail (Oman, UAE). Cette étude a permis de préciser, par l'apport de nouvelles contraintes mécaniques, le modèle dynamique d'accrétion et d'exhumation de ces unités à l'interface de subduction naissante élaboré à partir de notre étude pétro-structurale.

Ce travail met en évidence l'importante déformation finie des amphibolites des semelles métamorphiques. Cette déformation à hautes températures ( $700\text{--}850\text{ }^{\circ}\text{C}$ ) est essentiellement accommodée par la réorientation rigide dans le plan de foliation des grains d'amphiboles, qui forment la phase principale de ces roches ( $\geq 40\%$ ). Deux grandes étapes de déformation des amphibolites ont été caractérisées et associées à l'évolution continue de la température et du couplage mécanique à l'interface des plaques en cours de refroidissement. Nous mettons en évidence que, si l'amphibole est un minéral résistant, son comportement mécanique est fortement dépendant :

- de la viscosité des phases associées, facilitant ou non la réorientation rigide des grains d'amphibole dans le plan de foliation.
- de la présence de fluides favorisant les processus de précipitation-dissolution.
- du couplage mécanique avec les péridotites de la plaque supérieure.



Mechanical behaviour of the Semail metamorphic sole:  
rheology of amphibolites at lower crustal conditions during  
early subduction

In preparation for *Earth and Planetary Science Letters*

**Mathieu Soret<sup>1</sup>, Philippe Agard<sup>1</sup>, Benoît Dubacq<sup>1</sup>, Benoît Ildefonse<sup>2</sup>, Cécile Prigent<sup>3</sup>**

<sup>1</sup>Sorbonne Universités, UPMC Univ. Paris 06, CNRS, Institut des Sciences de la Terre de Paris (ISTeP), 4 place Jussieu, 75005 Paris, France

<sup>2</sup>Géosciences Montpellier, Universités de Montpellier, CNRS, F-34095 Montpellier, France

<sup>3</sup>Université Grenoble Alpes, CNRS, ISTerre, F-38000 Grenoble, France



## 4.2 Introduction

Amphibolites are commonly found in the middle to lower continental crust (Berger & Stüntz, 1996, Imon et al., 2004, Tatham et al., 2008, Getsinger et al., 2013) and along oceanic transform faults and detachments (Escartín et al., 2003, Boschi et al., 2006). Amphibolites are also the main component of metamorphic soles beneath highly strained peridotites at the base of large-scale ophiolites (as exemplified in Oman; Boudier et al., 1988). Metamorphic soles are crustal slivers stripped from the slab during early subduction and underplated below the upper plate (future ophiolite) mantle when the subduction interface is still young and warm (i.e. during the first million years -My- of intra-oceanic subduction; Malpas, 1979, Jamieson, 1981, Hacker, 1994). Understanding the rheological behaviour of amphibolitic rocks is therefore of major interest to model and quantify deformation and its localisation in varied geodynamical environments.

Amphibolites are chiefly composed of amphibole and plagioclase with varying amounts of clinopyroxene and garnet. While processes of viscous deformation have been well investigated for plagioclase and clinopyroxene (e.g. Rybacki & Dresen, 2000, 2004, Bascou et al., 2002, Dimanov & Dresen, 2005, Dimanov et al., 2007, Hier-Majumder et al., 2005), the mechanical, rheological and physical properties of amphibole and amphibole-bearing polymimetic aggregates are less well known (Ko & Jung, 2015).

Naturally and experimentally deformed amphibolites are commonly strongly foliated. The foliation is usually underlined by the amphibole and plagioclase shape—preferred orientations (SPO). Compared to plagioclase (and clinopyroxene) amphibole displays also a strong crystal—preferred orientation (CPO) over a wide range of pressure—temperature (P-T) conditions. This led authors to consider that the CPO of amphibole accounts for seismic anisotropy of the lower/middle crust (Mainprice & Nicolas, 1989, Lloyd et al., 2011). Although the presence of CPO usually points to dislocation creep as the dominant deformation mechanism (e.g. Wenk & Christie, 1991), amphibole is thought to be one of the strongest silicates (Shelley, 1994) and to have only a limited ability to deform by dislocation creep. Amphibole would rather behave as a rigid particle, rotating and fracturing during deformation (Hacker & Christie, 1990, Ildefonse et al., 1990, Shelley, 1994, Berger & Stüntz, 1996, Imon et al., 2004), as a result of dynamic recrystallization involving dissolution-precipitation processes (Hacker & Christie, 1990, Brodie, 1981, Berger & Stüntz, 1996, Imon et al., 2004). At high temperature ( $T > \sim 650\text{--}700^\circ\text{C}$ ), some studies nevertheless report intracrystalline deformation in amphibole, consistent with dislocation glide along the most favourable slip systems  $\{hk0\}[001]$  (Berger & Stüntz, 1996, Díaz Aspiroz et al., 2007, Cao et al., 2010, Gómez Barreiro et al., 2010). Activation of such deformation mechanisms depends on P-T conditions, water activity, grain size and min-

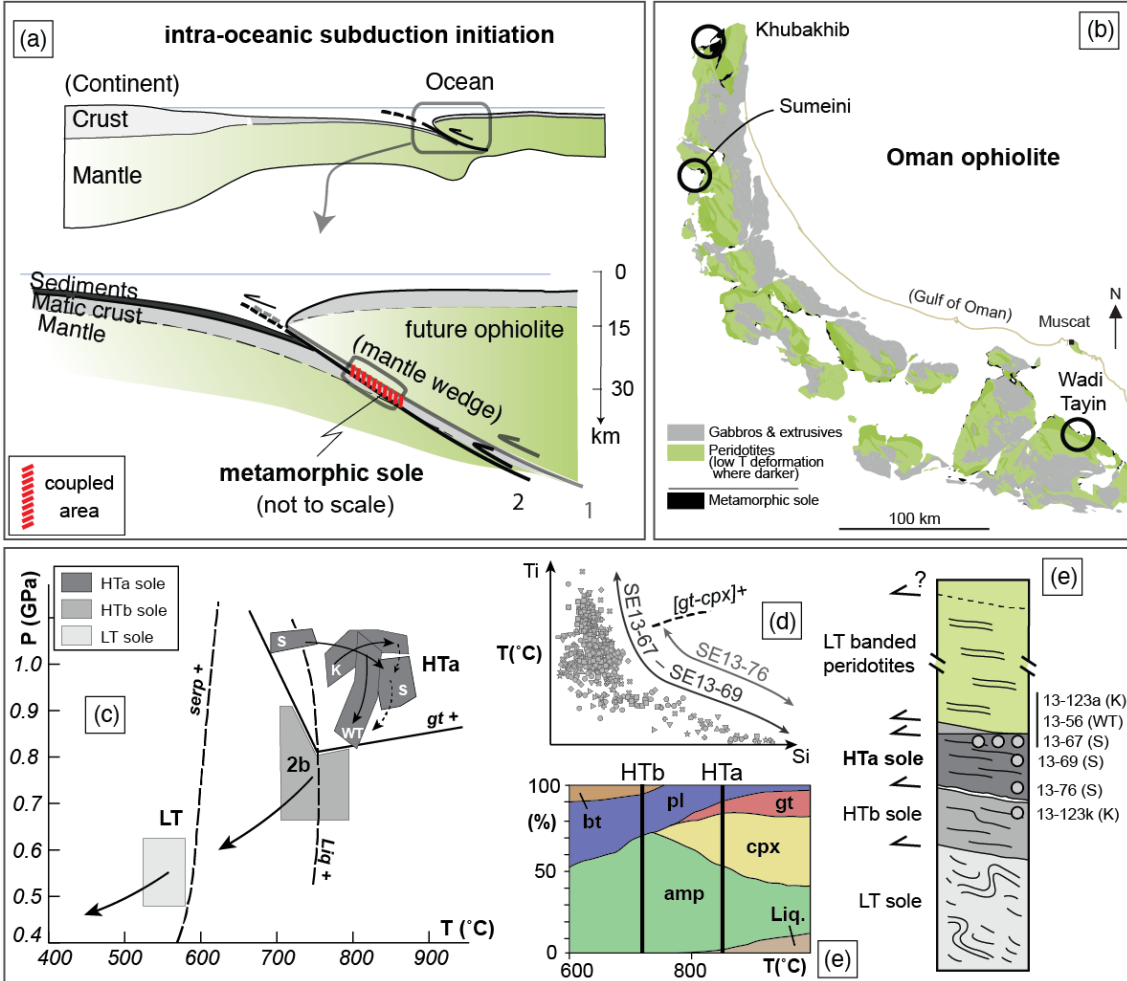


Figure 4.1: (a) Geodynamic setting of metamorphic sole formation during intra-oceanic subduction infancy. The later geodynamic evolution will lead to continental subduction and obduction s.s.; (b) Simplified geological map of the Semail ophiolite, highlighting the systematic outcrops of metamorphic sole beneath the mantle ophiolite (modified after Nicolas et al., 2000); (c) Compilations of P–T estimates and associated P–T paths (Soret et al., subm), from the garnet–clinopyroxene amphibolite (HT2a), to the plagioclase amphibolite (HT2b) and greenschist facies (LT) metamorphic sole units. P estimates for the HTb unit are constrained by the lower limit of stability of garnet + clinopyroxene. P estimates for the LT sole are from Bucher (1991a); (d) Ti content vs. Si content showing the continuous decrease of T conditions during the exhumation of the metamorphic sole; (e) evolution of modal proportion in mafic rocks with PT conditions (computed after pseudosection modeling); (f) schematic structure of the base of the Oman ophiolite showing the structuration of the analyzed samples.

eral assemblage. These parameters, which may explain the disagreement between former studies (e.g. Hacker & Christie, 1990, Berger & Stünitz, 1996, Getsinger et al., 2013), are therefore key parameters in understanding of amphibolite deformation.

This contribution focuses on the deformation mechanisms of amphibole through a microstructural and petrological study of garnet-bearing and garnet-free clinopyroxene-

bearing amphibolites, using EBSD analysis. The first aim is to test the influence of progressive changes in PT conditions during deformation and of the appearance/disappearance of anhydrous minerals (plagioclase, clinopyroxene and garnet) on the mechanical behaviour of mafic amphibolites. The second aim is to track deformation mechanisms during early subduction, through the study of these metamorphosed oceanic rocks, commonly 10-100 m thick, which range from high- to low-grade away from the contact with the peridotites (i.e. from  $800 \pm 100^\circ\text{C}$  -  $0.9 \pm 0.2$  GPa to  $500 \pm 100^\circ\text{C}$  -  $0.5 \pm 0.1$  GPa; and are essentially mafic at the top). The discontinuous structure of metamorphic soles indeed exemplifies step-wise accretion of different slivers as a result of rheological switches between the slab and the upper plate peridotites during the cooling of the plate interface (Agard et al., 2016, Soret et al., subm). However, in contrast to studies on the deformation of basal peridotites (Linckens et al., 2011, Herwegen et al., 2016) progressive changes in the mechanical behaviour of the amphibolites were so far poorly investigated.

### 4.3 The Semail metamorphic sole

Studied samples originate from the base of the Semail ophiolite (Oman and United Arab Emirates), but metamorphic soles worldwide are very similar regardless of the nature of the overlying ophiolite and regional context (see (see Agard et al., 2016, for review)). The Semail ophiolite (Oman, UAE) shows at its base a relatively thin unit (hundreds of meters, to be compared with the 10 km thick ophiolite above) composed of mafic and sedimentary metamorphic rocks (Fig. 4.1e). This unit, designated as a metamorphic sole, results from the juxtaposition of several slices of oceanic crust (Soret et al., subm) that were buried, strained and metamorphosed against the hot overlying mantle wedge, under granulite to greenschist facies conditions. Directly underlying the mylonitic basal peridotite of the Semail ophiolite, the high-temperature (HT) sole crops out onto the low-temperature (LT) sole in scattered places all along the Semail ophiolite (Fig. 4.1e) from Wadi Tayin (Oman) in the south to Sumeini (Oman) and Asimah-Khubakhib (UAE) in the north. The HT sole is composed of two major sub-units (zones 2a and 2b; Fig. 1b), respectively made of garnet-clinopyroxene amphibolite and plagioclase-bearing amphibolite. Contrasting PT conditions are exemplified by the Ti content of amphibole, which shows a large and stepwise decrease from 0.23 to 0.15 p.f.u. and correlates with the increase of the Si content (Fig. 4.1d), suggesting a difference in peak temperature of  $\sim 100^\circ\text{C}$ . Late amphibole recrystallization (remaining part of the trend; Fig. 4.1d) point to an overall decrease of  $\sim 300^\circ\text{C}$  from the accretion to the exhumation during early subduction dynamics (Agard et al., 2016, Soret et al., subm). Peak PT conditions for the HT sole have been estimated for both sub-units ( $850 \pm 50^\circ\text{C}$  -  $0.9 \pm 0.1$  GPa and  $725^\circ\text{C}$  -  $0.8 \pm 0.1$  GPa, respectively)

---

by comparing the results of thermodynamic modelling with preserved compositions (Fig. 4.1; see Soret et al., subm, for details). Changes in modal amounts accompanying (peak to early retrograde) deformation can thus also be inferred, and are shown for garnet, clinopyroxene, amphibole and plagioclase for sub-unit 2a (Fig. 4.1e). The preservation of prograde chemical zoning (over a  $dT \geq 100^\circ\text{C}$  and a  $dP \geq 0.1\text{ GPa}$ ) suggests fast exhumation (as supported by radiometric dating; Hacker, 1994).

The LT sole is mainly composed of greenschist facies quartzite, with imbrications of amphibole-bearing metatuff (Gnos, 1992, Bucher, 1991a), and will not be considered here. Estimated peak pressure-temperature conditions are more loosely constrained and around  $530 \pm 50^\circ\text{C} - 0.5 \pm 0.1\text{ GPa}$  (Searle & Cox, 2002, Cowan et al., 2014, Soret et al., subm).

Structurally, the Semail HT sole changes from a homogeneous, fine-grained garnet, clinopyroxene and plagioclase bearing amphibolite at the top (zone HTa) to a more heterogeneous, coarser-grained plagioclase and/or epidote bearing amphibolite with rare biotite-garnet-rich imbricated layers downwards (zone HTb; Fig. 4.1e). The entire metamorphic sole shows a strong planar fabric with evidence of simple shear deformation. Lineation and lattice preferred orientation of quartz in the inter-bedded quartzite indicate a dominant simple shear regime with a sense of shearing consistent with that of the basal banded peridotites (Boudier et al., 1985, Gray & Gregory, 2000). Deformation is less conspicuous in garnet-bearing HT sole amphibolites than in the garnet-free HT and LT soles where lithological heterogeneities are greater. Complex recumbent folding (cm- to 10 cm-scale) is locally observed in the plagioclase and/or epidote bearing amphibole and broadly observed in the LT sole (m- to 10 m-scale; Hacker et al., 1996, Gray & Gregory, 2000).

#### 4.4 Methods and sampling strategy

A suite of samples was collected from the garnet-clinopyroxene bearing and the garnet-clinopyroxene free amphibolite of the HT sole, from along 3 metamorphic sole localities where the HT sole is the most complete and best preserved (Khubakhib, Sumeini and Wadi Tayin). Six rock samples from the Semail metamorphic sole were analysed with EBSD. For the sake of clarity, only microstructures for the most complete and representative section (Sumeini samples; see Soret et al., subm) are detailed here. Garnet-clinopyroxene bearing samples from Khubakhib (123a) and Wadi Tayin (56) are to be compared with the highest grade sample of Sumeini (67). Khubakhib sample 123k (top of zone HTb) is to be compared with Sumeini sample 76 (base of zone HTa).

EBSD were collected using a CamScan X500FE CrystalProbe scanning electron microscope (SEM) at Géosciences Montpellier (France) by EBSD. Measurements were performed at 25 mm working distance with an accelerating voltage of 15 kV on polished thin sections tilted at 70° from the horizontal within the microscope chamber. Generated diffraction patterns were processed using the Channel 5 software suite (Schmidt & Olesen, 1989). EBSD data were processed using MTEX software, a MATLAB toolbox for textural analysis (Hielscher & Schaeben, 2008, Bachmann et al., 2010).

For each sample, amphibole, plagioclase, clinopyroxene, garnet (together with prehnite and Ti-rich phases such as rutile, titanite and ilmenite) were indexed wherever present. Grains were identified by choosing a 10° threshold, over which the misorientation between two adjacent pixels indexed for the same phase is assumed to correspond to a grain boundary. Grains smaller than 10 pixels were removed. Twins in plagioclase were distinguished from grain boundaries by filtering out the 178° to 180° misorientations during grain boundary identification. Pole figures were calculated using the crystallographic orientation of each pixel and plotted using a subset of 2500 randomly selected points. All plots are represented in lower hemisphere projections contoured with 15° half-width and where contours are multiples of a uniform distribution. MTEX software was also used to characterize the SPO strength by calculating the average orientation of the longest-axis of each phases and the CPO strength with the J index of the orientation distribution function (i.e. from 1 in the case of random orientation distribution to infinity in the case of an ideal single crystal; Mainprice et al., 2014). The modal proportion of each phase, the percentage of indexation and the step-size for each map are listed in Table 1. The aspect ratio (AR) corresponds to the ratio between the two (length/width) principal axes of each grain. The shape-preferred orientation (SPO) is defined by the angle between the long axis of each grain and the foliation plane.

Compositions for major elements and composition maps were measured at CAM-PARIS (UPMC—IPGP, Paris, France) using a CAMECA SX-5 and CAMECA SX-100 electron microprobe. Classical analytical conditions were used for spot analyses (1-2 μm spot size; 15 kV, 10 nA, wavelength-dispersive spectroscopy mode), using Fe<sub>2</sub>O<sub>3</sub> (Fe), MnTiO<sub>3</sub> (Mn, Ti), diopside (Mg, Si), orthoclase (Al, K), anorthite (Ca) and albite (Na) as standards. Representative analyses are given in supplementary material.

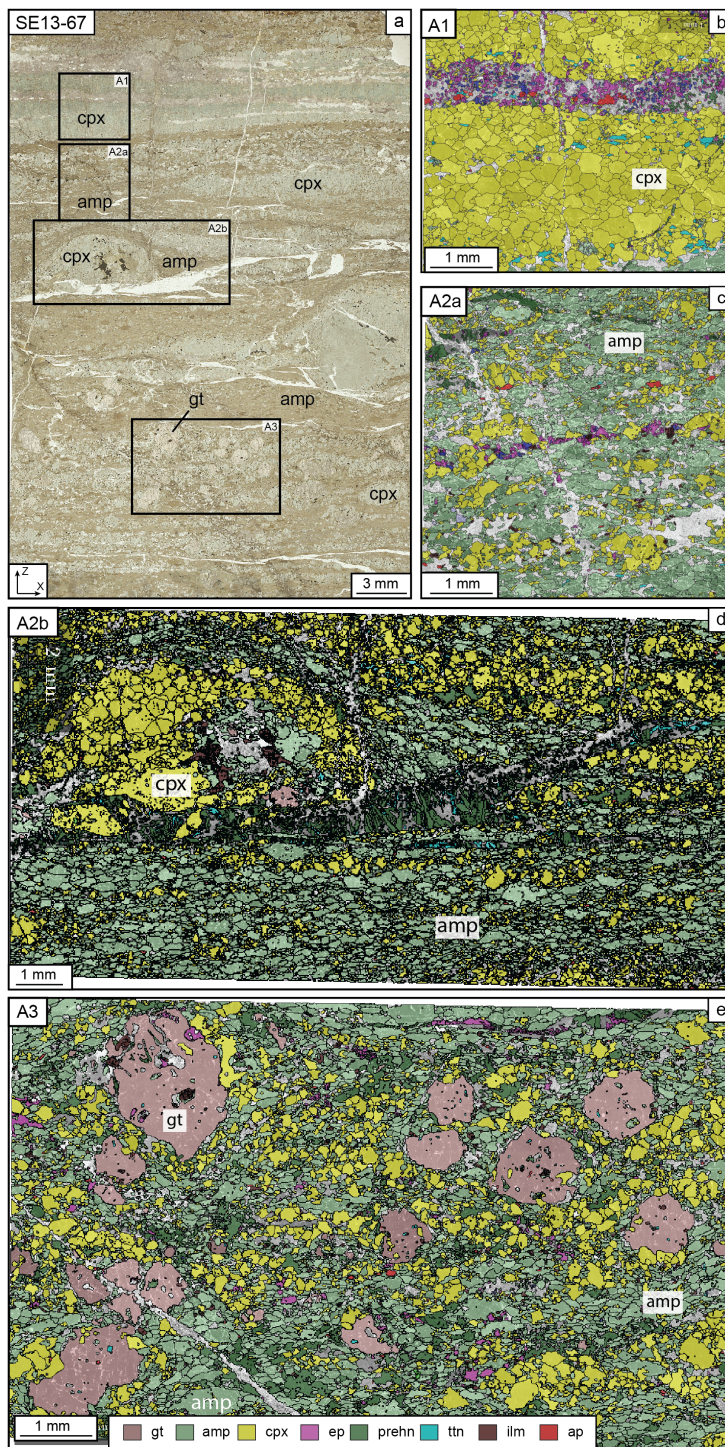


Figure 4.2: Maps of phases from a garnet–clinopyroxene bearing amphibolite sampled at ~2 m from the contact with peridotites and showing the best preserved structures. (b) Area 1 composed essentially of clinopyroxene; (c) and (d) Area 2 composed of amphibole and clinopyroxene. (d) a late prehnite veins crosscut the sample; (e) Area 3 composed of garnet, amphibole and clinopyroxene.

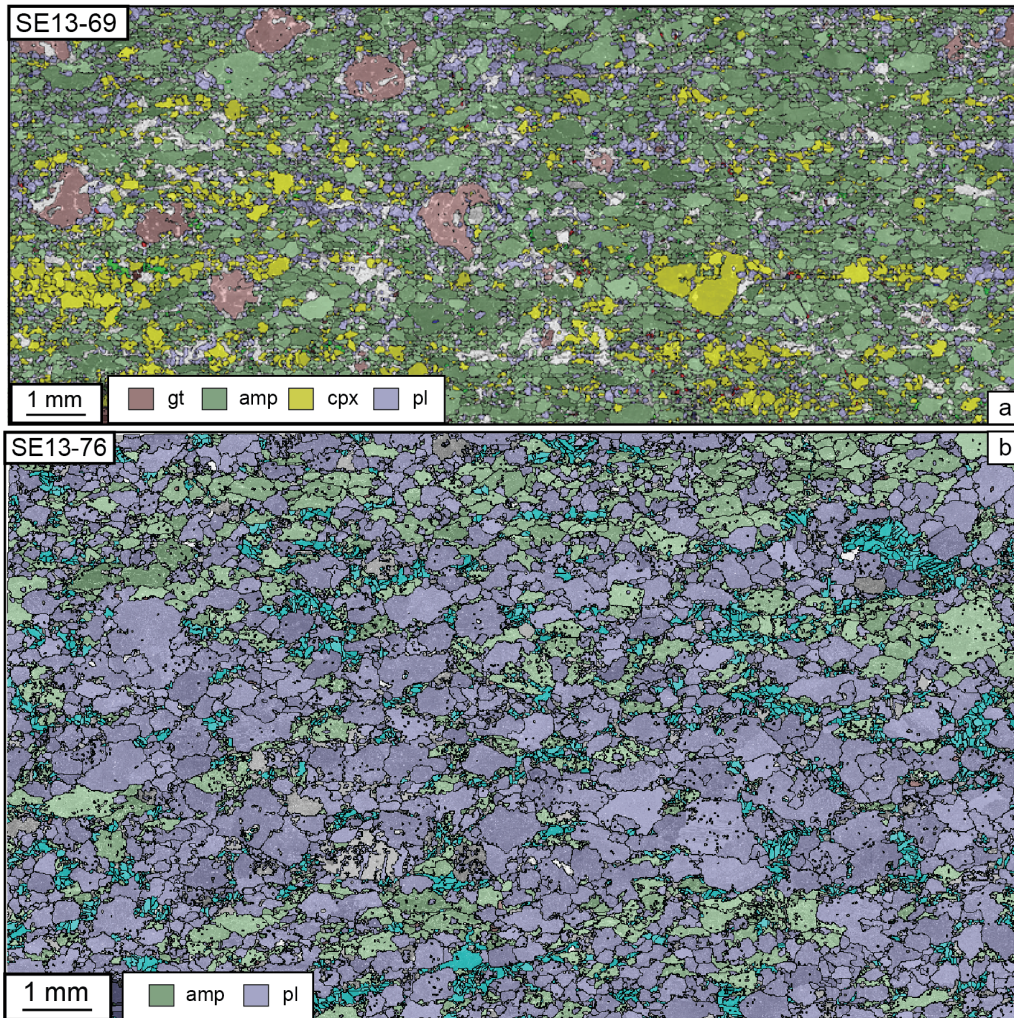


Figure 4.3: Maps of phases from a garnet–clinopyroxene bearing amphibolite sampled at ~8 m from the contact with peridotites, slightly retrogressed at amphibolite facies.

## 4.5 Results

### 4.5.1 Mineralogy

Samples from the Sumeini area are presented from top to bottom, starting from the highest-grade samples collected near the contact with the overlying peridotite to garnet-free samples away from the contact. Within 2 m from the peridotite, the metamorphic sole is typified by garnet-clinopyroxene-bearing amphibolites with the smallest grain size. Garnet and clinopyroxene form in places porphyroclasts, boudinaged and wrapped in a well-foliated amphibole-rich matrix (e.g., sample SE13-67; Fig. 4.2). Textures from the peak metamorphic conditions are particularly well preserved in sample SE13-67, where three layered domains can be recognized in thin section (4.2a):

- 
- Area 1 is dominantly composed of clinopyroxene aligned in the foliation. The small amount of epidote evidences limited retrogression (Fig. 4.2b).
  - Area 2 (a, b) is composed of amphibole (50–65 vol.%) and clinopyroxene (25–35 vol.%). Locally clinopyroxene porphyroclasts form sheared boudins where pressure shadows are filled with amphibole and clinopyroxene (Fig. 4.2c,d).
  - Area 3 is composed of amphibole (42 vol.%), clinopyroxene (22 vol.%) and garnet (12 vol.%; Fig. 4.2e). In the whole sample, most brown amphibole grains are at textural equilibrium with clinopyroxene and garnet (where present). Plagioclase rims garnet and replaces amphibole and clinopyroxene of the matrix. Plagioclase crystals have not been successfully indexed due to pervasive late sericitization, transforming plagioclase into a minute assemblage of albite + zoisite + muscovite. Epidote ( $\leq$  1 vol.%) and prehnite ( $\leq$  5 vol.%) are scattered throughout the matrix or present in sheared veins, sub-parallel to the foliation in places (Fig. 4.3a). These veins indicate a late stage of deformation and fluid circulation at low T conditions.

8 m away from the peridotite (sample SE13-69), the metamorphic sole exhibits a coarser-grained assemblage characterized by a higher proportion of brown amphibole (58 vol.%) and plagioclase grains (14 vol.%), crystallizing after clinopyroxene (12 vol.%) and garnet (3 vol.%; Fig. 4.3a). In 6 m the average grain size of amphibole changes from  $55 \pm 35 \mu\text{m}$  to  $115 \pm 75 \mu\text{m}$ . Meanwhile, the grain size of clinopyroxene remains stable around  $105 \pm 70 \mu\text{m}$ . In sample SE13-69 (Fig. 4.3a), the plagioclase has a comparable grain-size around  $95 \pm 35 \mu\text{m}$ .

25 m away from the peridotite (sample SE13-76, a few meters below the garnet-clinopyroxene-bearing amphibolite), garnet and clinopyroxene are not present (SE13-76; Fig. 4.3b). Amphibole (23 vol.%) has a brown to greenish-brown colour and is closely associated with plagioclase (64 vol.%), both presenting a coarser grain size ( $160 \pm 120 \mu\text{m}$  and  $180 \pm 150 \mu\text{m}$ , respectively). They define a well-developed foliation. This assemblage is strongly affected by the overgrowth of syn-kinematic yellowish xenomorph epidote (12 vol.%) with a grain size of  $90 \pm 35 \mu\text{m}$ .

#### 4.5.2 Microstructures

##### Amphibole

In the studied samples, most amphibole grains have a subhedral shape. Grain size is smaller in the sample closest to the peridotite ( $\leq$  2 m; SE13-67; Fig. 4.4a) and similar on average for amphibole associated with clinopyroxene (Area 2) or to clinopyroxene and garnet (Area 3;  $75 \pm 50 \mu\text{m}$ ,  $65 \pm 68 \mu\text{m}$ , respectively). Away from the peridotite, amphibole increases

in size and variability, from  $115 \pm 75 \mu\text{m}$  (at  $\sim 8 \text{ m}$ ; sample SE13-69) to  $160 \pm 120 \mu\text{m}$  (at  $\sim 25 \text{ m}$ ; SE13-76). Contrary to grain size, the mean aspect ratio of amphibole ( $1.9 \pm 0.6$ ) does not vary with the distance from the peridotite or the mineral assemblage. A small proportion of the grains have a higher aspect ratio, between 3 and 7, but this is not correlated with changes in grain size (Fig. 4.4c).

SPO is very strong in all samples and clusters at  $\sim 90^\circ$  of the normal to the foliation plane (Fig. 4b). The SPO intensity is positively correlated to the grain size and aspect ratio (i.e., the highest grain size and aspect ratio, the lower the variance of orientation degree). However, the SPO of amphibole becomes less clear for grain size  $\leq 75 \mu\text{m}$  or aspect ratio  $\leq 1.5$ , whatever the distance from the peridotite (Fig. 4.4b). Aspect ratio and grain size are not correlated.

In optical microscopy, large amphibole grains display intragranular fractures and irregular boundaries (especially where bounded by -altered- plagioclase or prehnite). Some fractures are along cleavage planes, while others are parallel or perpendicular to the [001] direction (Fig. 4.3a-c). Small grains are devoid of fractures and have straight and sharp boundaries with other amphiboles. Small and large amphibole grains are oriented along C-S structures, evidencing simple shear deformation. This is particularly visible in the amphibolite (SE13-67) directly underlying the peridotite (Fig. 4.5a). Very rare amphibole grains show intragranular microstructures, as undulatory or inhomogeneous extinction and sub-grain formation, indicating crystal plasticity deformation. This deformation is essentially restricted to coarse-grained amphibole boudins wrapped by finer amphibole grains.

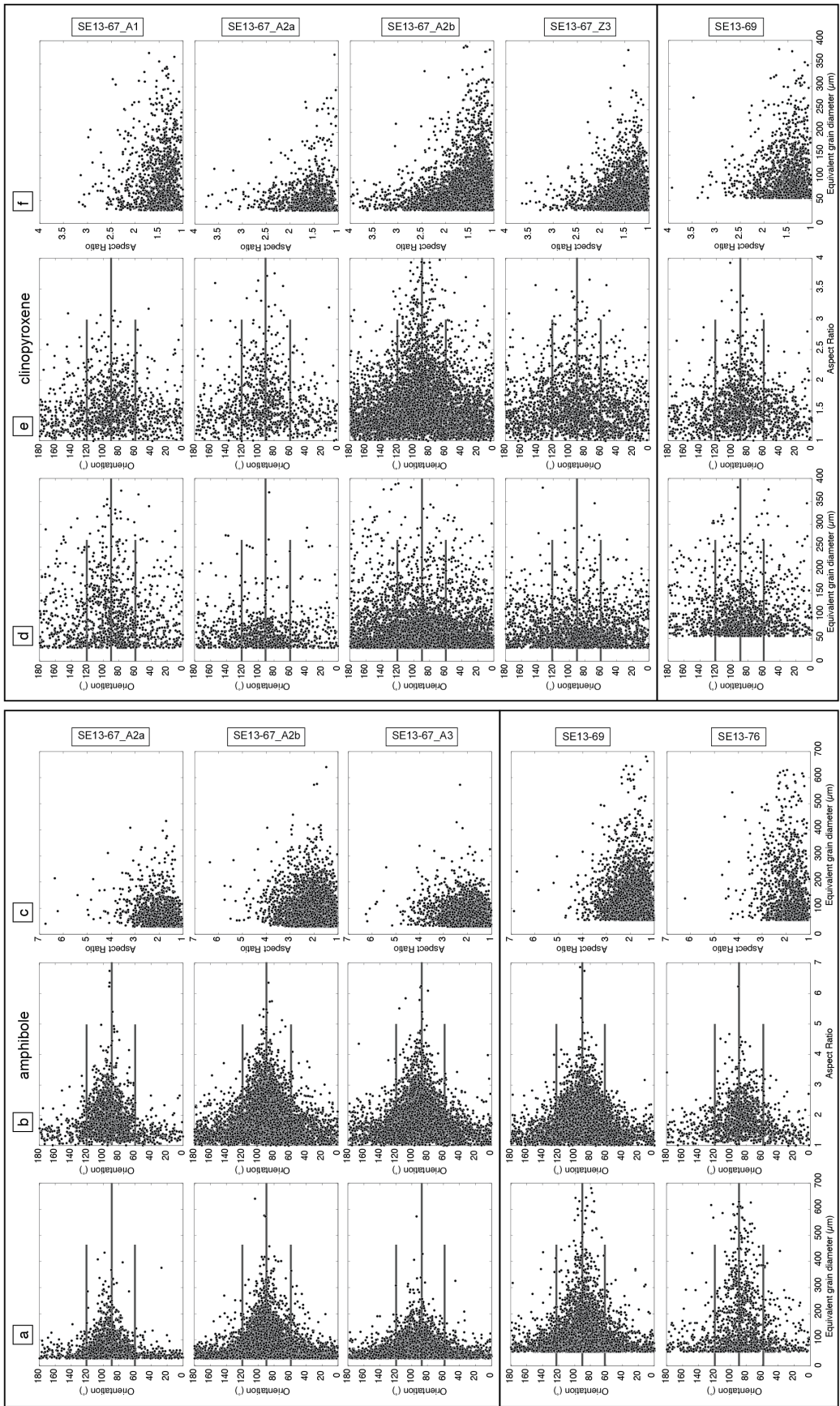


Figure 4.4: Long axis orientation, grain size and aspect ratio of amphibole (a-c) and clinopyroxene (d-f). (a) and (d): Shape-preferred orientation (SPO) vs. grain size; (b) and (e) SPO vs. aspect ratio; (c) and (f) grain size vs. aspect ratio. The longest line represents the foliation plane. The two smaller lines are placed at 60 and 120° and outline the data dispersion.

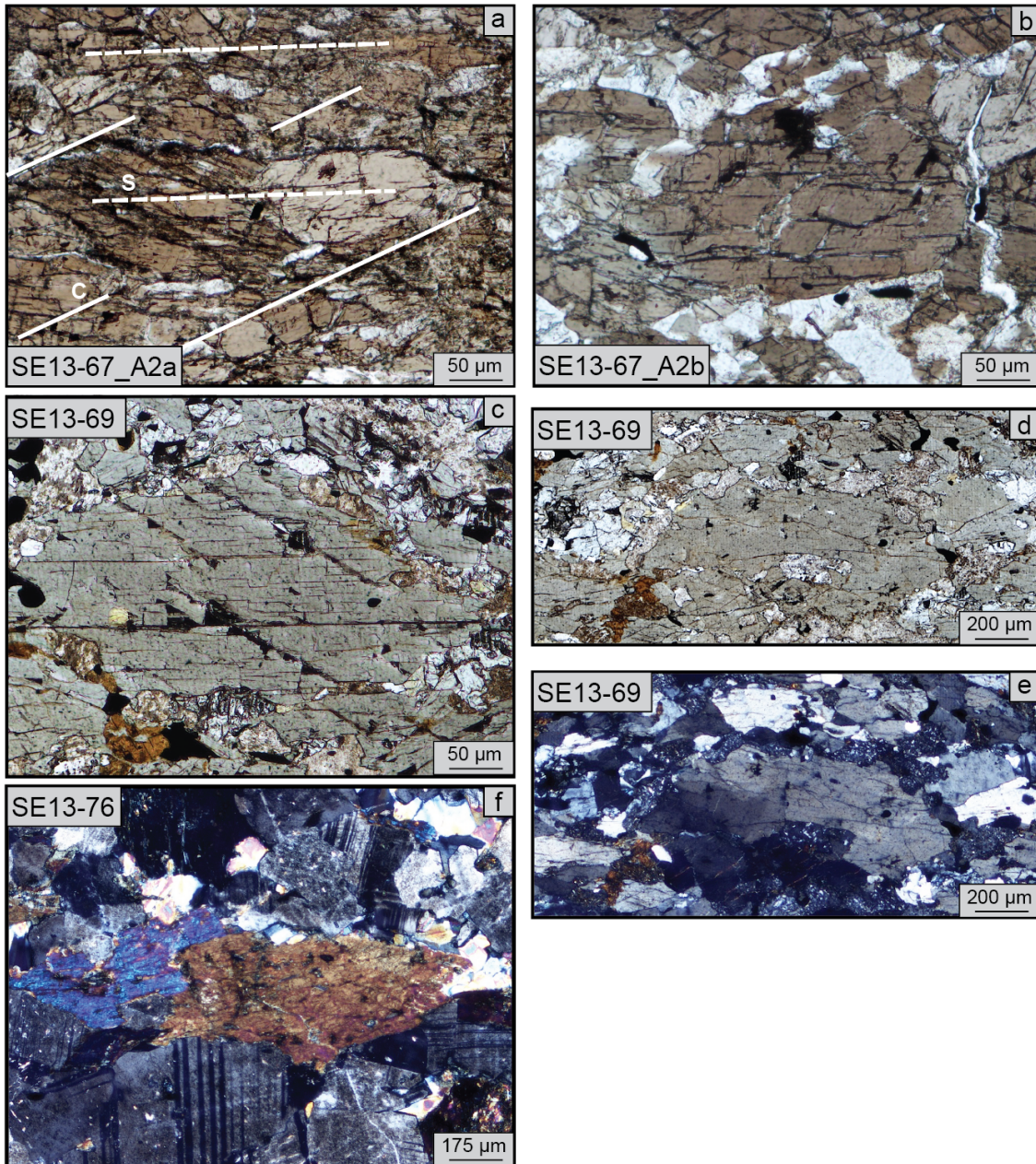


Figure 4.5: Photographs of microstructures in amphibole grains from amphibolite at different distance from the peridotites. (a) Development of S-C structure in amphibole-bearing matrix. Evidence of recrystallization in pressure shadow of elongated grains.; (b) and (c) sets of fracture in coarse grained amphibole; (d) coarse grained amphibole showing irregular boundaries where bounded by -altered- plagioclase or prehnite; (e) inhomogeneous extinction in a coarse grained amphibole; (f) elongated grains wrapped by plagioclase grains and showing bulged boundaries.

### Clinopyroxene

Clinopyroxene porphyroclasts have a rounded shape but little bulging. It is most conspicuous in the mono-phase area (Area 1 in sample SE13-67; Fig. 4.2b). In this area, the average clinopyroxene grain size is  $103 \pm 70 \mu\text{m}$  (Fig. 4.4d). In association with amphi-

---

bole (Area 2 in sample SE13-67; Fig. 4.2c-d), clinopyroxene porphyroclasts form sheared boudins, usually with a tail of fine clinopyroxene grains. Small amphibole grains are also present in the pressure shadows. Where garnet is present (Area 3 in sample SE13-67; Fig. 4.2e), clinopyroxene grains do not form boudins but wrap ellipsoidal garnet crystals. In that case, they are also more scattered in the matrix (i.e. smaller density of clinopyroxene neighbour-pairs). In these 2 areas (A2 and A3), the average grain size ( $\sim 65 \pm 45 \mu\text{m}$ ) is close to that of amphibole and smaller than that found in the monomineralic layer (Fig. 4.4e). Although the mean grain size of clinopyroxene increases down section (but less so than amphibole), its size 8 m away from the peridotite is equivalent to that in the monophasic layer, 2 m away (Area 1; Fig. 4.4e).

The aspect ratio of clinopyroxene is small ( $\sim 1.60 \pm 0.40$  on average) and does not vary with grain size, mineral assemblage or with the distance to the peridotite. Clinopyroxene grains are oriented in the foliation (most lie at  $\sim 90^\circ$  of the normal to the foliation plane), but the SPO is much weaker than that of amphibole. Contrary to amphibole, the correlation with both grain size and aspect ratio is weak (Fig. 4.4f).

No intragranular fracture is visible in clinopyroxene. They rather exhibit undulose extinction, textures indicating grain boundary migration and sub-grain rotation.

Plagioclase is absent in the first meters away from the peridotite, where the metamorphic sole exhibits the best-preserved textures and microstructures. Where present, plagioclase grains are generally poorly preserved due to pervasive sericitization. It is therefore difficult to analyse plagioclase grains and the results shown below are for the best-preserved grains only (and may not be representative of all grains formed at high P-T during the stacking and deformation of the metamorphic sole).

#### 4.5.3 Crystallographic preferred orientation and misorientation

Crystallographic preferred orientation (CPO) has been measured in amphibole in order to quantify changes as a function of the mineralogical assemblage (Figs. 4.6, 4.7). In all samples, amphibole has a very strong CPO. The [001] maxima are subparallel to the direction of the lineation. Poles to (100) are oriented subperpendicular to the foliation and poles to (010) are subperpendicular to the direction of the lineation (Fig. 4.6). Poles to (100) always form the strongest maximum and the [001] maxima is usually stronger than the maxima of poles to (010).

The most pronounced fabric ( $J$  index = 6.83) is found in the sample closest to the peridotite, in a garnet-free layer (Area 2; SE13-67). Fabric intensity is slightly positively

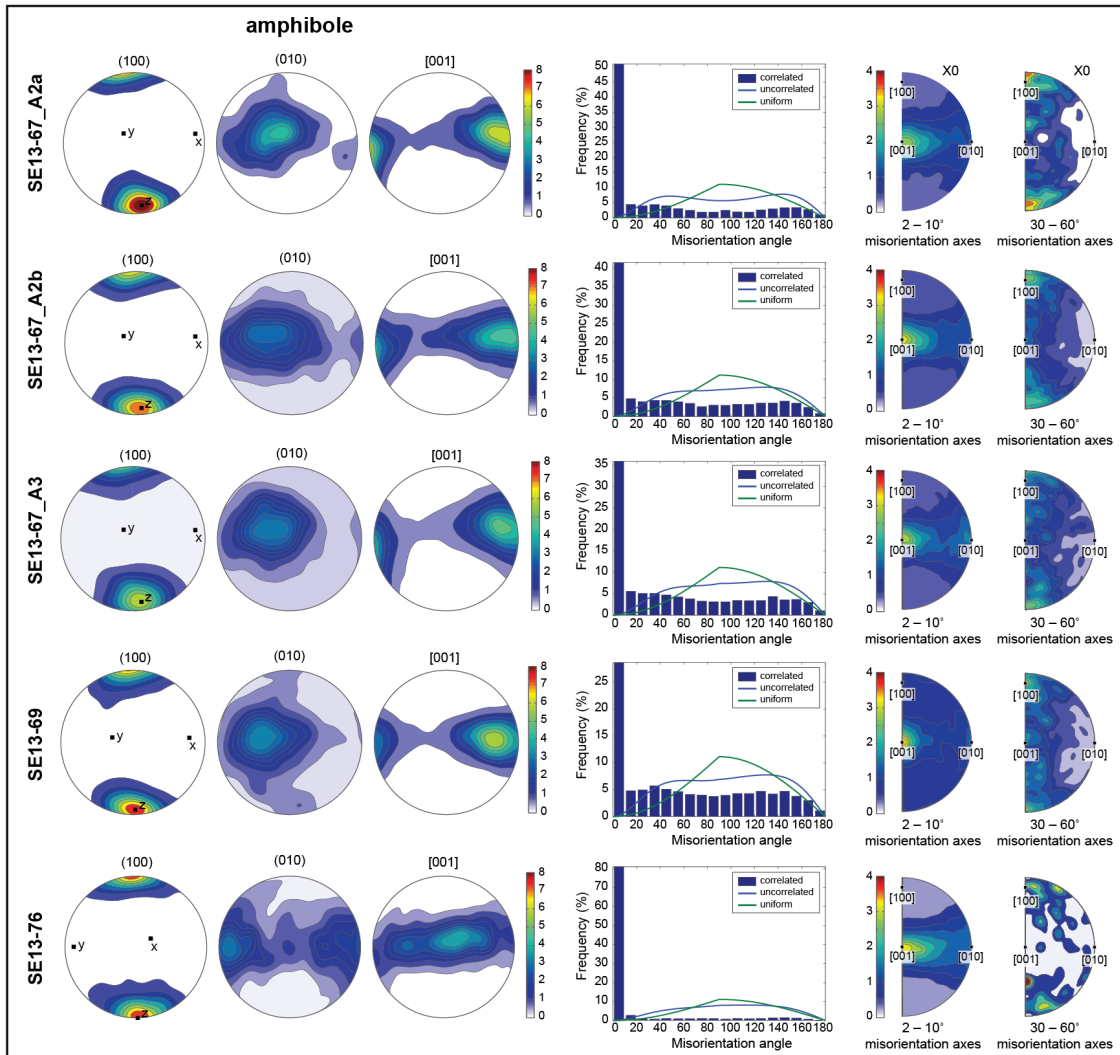


Figure 4.6: (a) Pole figures illustrating crystal lattice orientation (CPO) of amphibole of the analyzed samples (one measurement per grain). Samples are sorted in function of the distance from the peridotites. X, the horizontal line, represents the lineation and Y, the vertical line, is the normal to the general foliation. Contours are multiples of a uniform distribution. Shear sense is sinistral. All plots are lower hemisphere projections contoured with  $15^\circ$  half-width. (c) The low angle intracrystalline ( $2-10^\circ$ ) and high angle misorientation axis for the different phases.

correlated with the modal proportion of amphibole, but no correlation is found with the distance to the peridotite (Fig. 4.6). At  $\sim 8$  m from the contact, where garnet and clinopyroxene coexist, amphibole has a strong fabric too (J-index = 4.98; Fig. 4.8). Away from the contact and in a sample displaying the smallest amphibole modal proportion, the fabric is well developed (J-index = 4.30; SE13-76). Poles to (100) maximum remain strong but poles to (010) and [001] maxima form girdles.

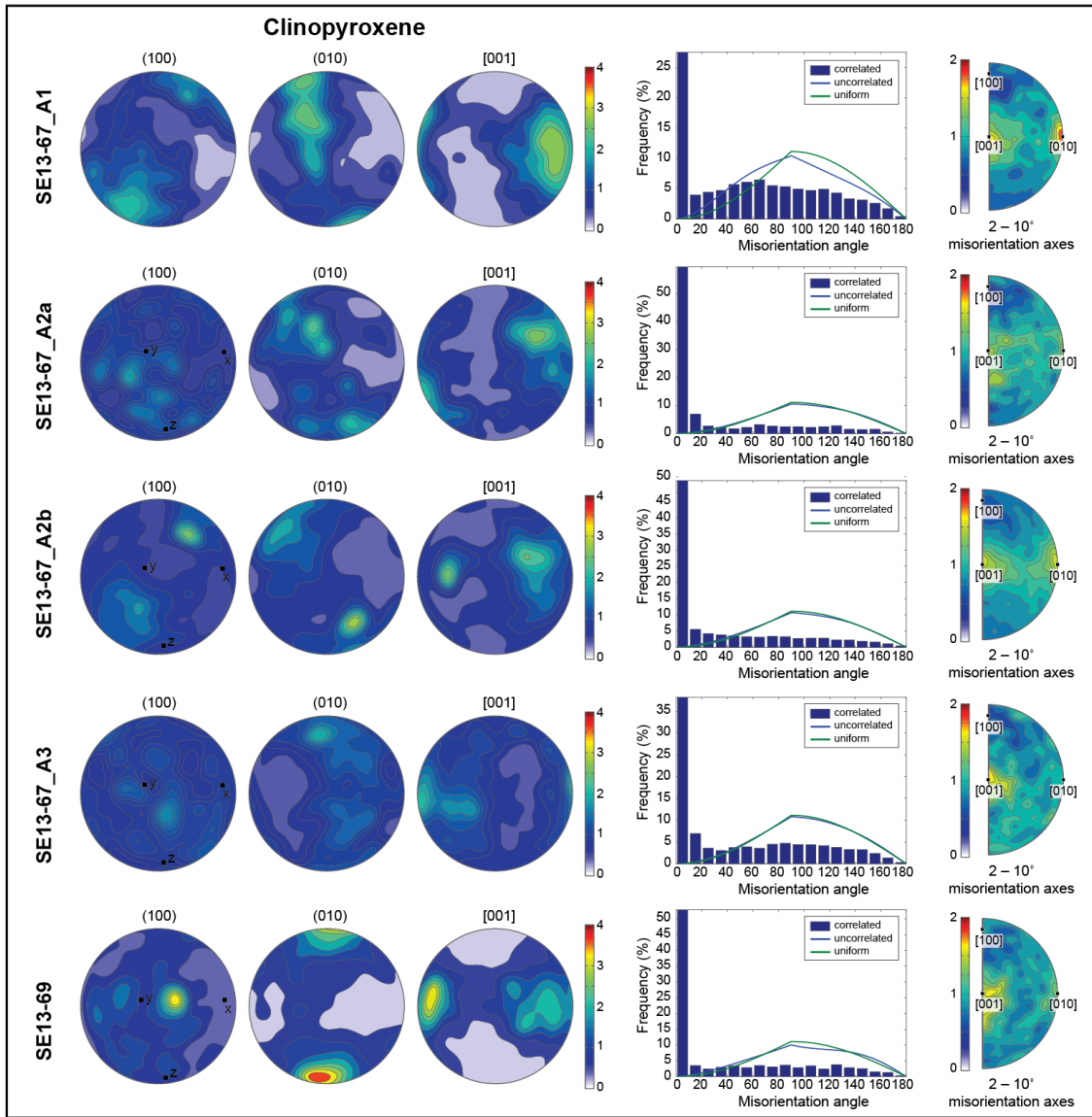


Figure 4.7: Pole figures illustrating crystal lattice orientation (CPO) of clinopyroxene of the analyzed samples (one measurement per grain). Samples are sorted in function of the distance from the peridotites. X, the horizontal line, represents the lineation and Y, the vertical line, is the normal to the general foliation. Contours are multiples of a uniform distribution. Shear sense is sinistral. All plots are lower hemisphere projections contoured with 15° half-width. (c) The low angle intracrystalline (2–10°) and high angle misorientation axis for the different phases.

As highlighted with the SPO, amphibole grains with a grain size  $\leq 75 \mu\text{m}$  or an aspect ratio  $\leq 1.5$  display a similar CPO pattern but significantly smaller in intensity compared to that of larger or more elongated grains (Table 1).

The misorientation angles showed in figure 4.6 are defined by the lowest rotation angle about a common axis that brings two lattices into parallelism (Lloyd et al., 1997, Wheeler et al., 2001). The correlated misorientation angle is calculated between neighbour-

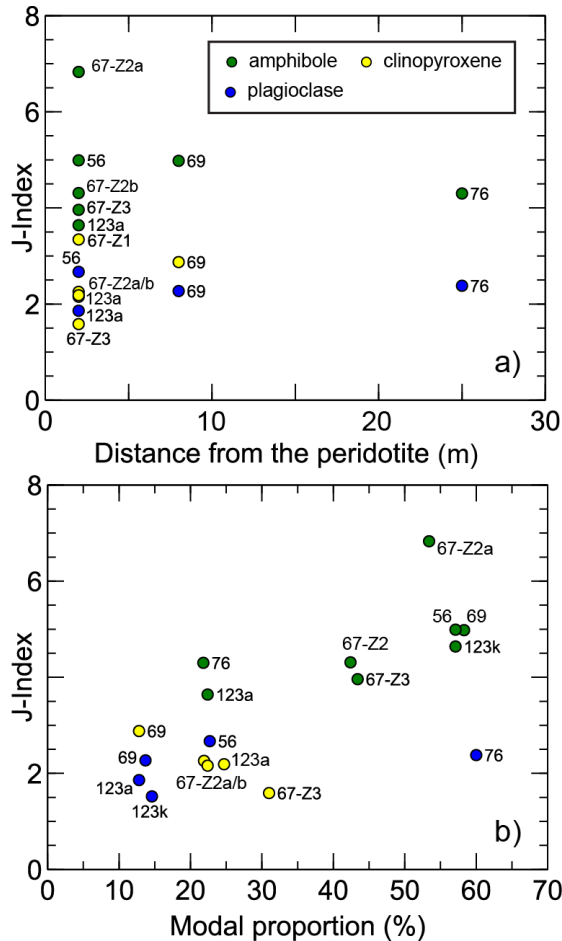


Figure 4.8: Quantified fabric (using the J-index) of amphibole, clinopyroxene and plagioclase vs (a) the distance from the contact with the peridotites and (b) the modal proportion of each phases.

pairs (i.e. adjacent crystals separated by a common boundary). Inversely, the uncorrelated misorientation is calculated between random pair crystals. The misorientation angle distribution of amphibole in all samples highly differs to the theoretical random distribution (i.e., the “uniform” green curve; Fig. 4.6). This is consistent with the strong intensity of the amphibole CPO. Very small misorientation angles (from 2 to 9°) are largely dominant. These intragranular misorientations are correlated with the [001] axis, but little correlated with the [100] axis and even less with the [010] axis. This misorientation pattern does not differ with distance from the contact, the mineral assemblage or the strength of the CPO. Amphibole grains in all samples are also characterized by two clusters of higher misorientation angles at  $\sim 40 \pm 20^\circ$  and  $\sim 150 \pm 20^\circ$ . Contrary to small intragranular misorientations, these misorientations rotate essentially around the [100] axis.

Clinopyroxene has a moderate to weak CPO (Fig. 4.8a). As in amphibole, the [001] maximum is subparallel to the lineation. Poles to (010) have a maximum normal to the

---

foliation. Poles to (100) have a very weak maximum subperpendicular to the lineation. The highest fabric strength is found in the monomineralic layers (zone 1, Fig. 4.2), but remains much smaller than that measured in amphibole. The J-index appears negatively correlated with the modal proportion of amphibole, and decreases from 3.35 to 2.16 with increasing amphibole mode (Fig. 4.8). The distributions of intergranular misorientation angles of amphibole-bearing sites are close to the theoretical random distribution (Fig. 4.7). In contrast, in the monophase layer (Area 1; Fig. 4.2a), clinopyroxene exhibits large frequencies for misorientation angles around  $60 \pm 20^\circ$ . Intragranular misorientations (from 2 to  $9^\circ$ ; Fig. 4.7) rotate essentially around the [010] axis and to a lesser extent around the [001] axis. Neither garnet nor the distance to the peridotite seem to impact the fabric of clinopyroxene. As highlighted for the SPO, and in contrast to amphibole, the CPO of clinopyroxene appears mostly insensitive to grain size and aspect ratio.

Plagioclase has a weak CPO (supplementary material; 4.11). The strength fabric is similar to that of clinopyroxene, with a J-index varying between 2.06 (SE13-69) and 2.38 (SE13-76). Despite a very weak maximum pole figure density, plagioclase grains display patterns analogous to axial-A CPO (Satsukawa et al., 2013). All samples show a concentration of (001) poles normal to the foliation plane and [100] axes subparallel to the lineation. The axial-A CPO is interpreted to evidence a dominantly linear fabric, with the lineation characterized by [001] axes. This fabric occurs preferentially when crystal plastic deformation overprints a strong magmatic foliation with consistent sense of shearing. The inherited orientation from the magmatic stage allows the activation of the [100](010) slip system (Satsukawa et al., 2013). In this study poles to (010) show, however, no preferred alignment and only little intracrystalline misorientation is observed. These misorientations rotate around the [100] axis.

#### 4.5.4 Mineral composition mapping

In order to track recrystallization processes during the deformation of amphibole and amphibolites, composition maps were acquired with electronic microprobe with a  $10\text{-}\mu\text{m}$  spatial resolution.

Amphibole composition plots within the pargasite to actinolite fields (see Soret et al., subm, for detailed compositions). The decreasing Ti content of amphibole is used as a proxy for changing (decreasing) temperatures (Soret et al., subm, see Fig. 4.1;).

$\sim 2$  m away from the peridotite (sample SE13-67), the Ti content of large amphibole grains shows a similar pattern with a Ti zonation and a sharp Ti decrease at the rim (Figs. 9a,b,c). This zonation is truncated by intragranular micro-fractures (compare Figs. 4.9a,b

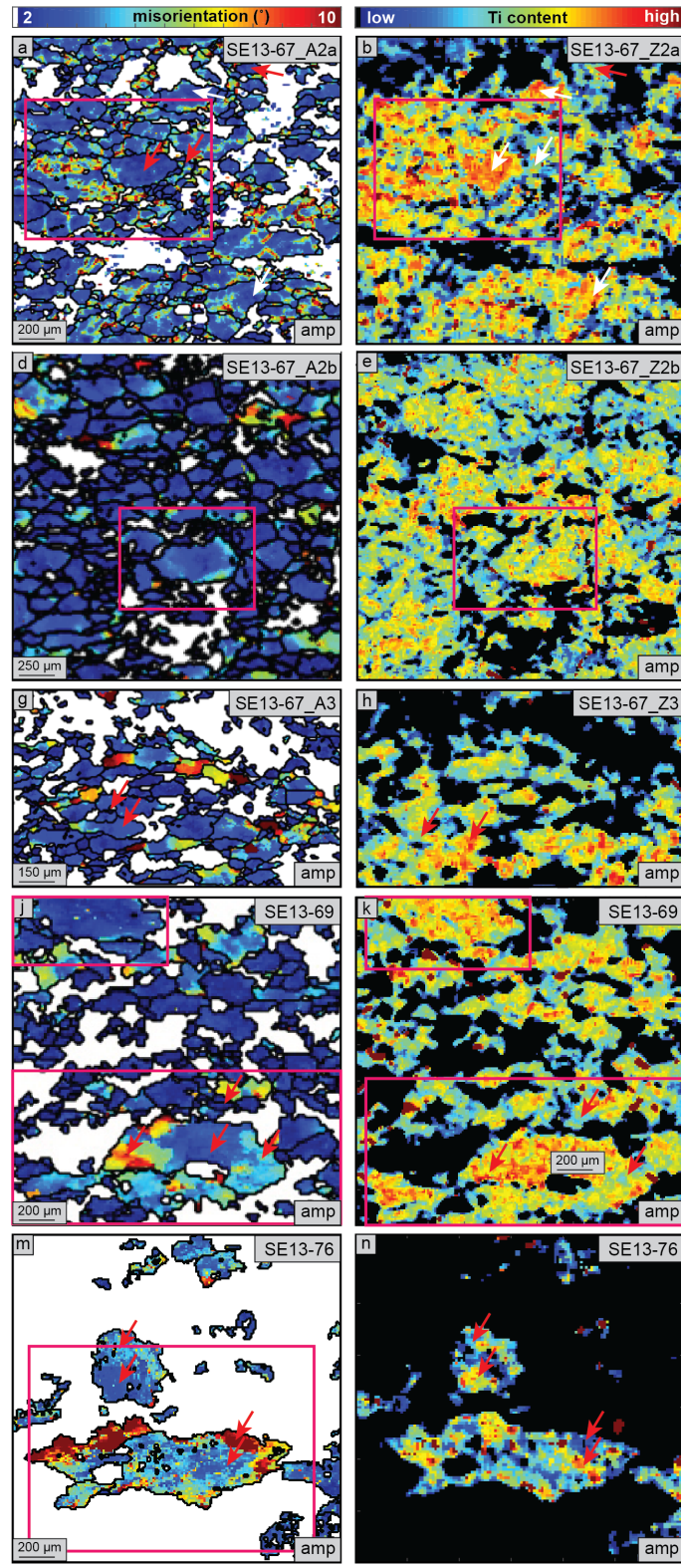


Figure 4.9: Compositional map of Ti (left column) and  $[2-10^\circ]$  intracrystalline misorientation (to the mean; right column) of amphibole in samples sorted in function of the distance from the peridotites.

---

with Figs. 4.5a,b) filled with the crystallization of minute grains of Ti-poor amphibole and/or plagioclase. Grains with the best—preserved and highest Ti content display very low fracture density (Figs. 4.5a,4.9a). If most of small grains record a Ti-rich core with content similar to that of large grains, small anhedral Ti-poor amphibole grains are visible at the tips of large subhedral grains, in low-strain area (Fig. 4.9a). Larger fractures filled by prehnite crosscut amphibole and clinopyroxene without specific orientation.

~8 m away from the peridotite (sample SE13-69), amphibole grains evidence the same zonation (Fig. 4.9d): Ti-poor areas are also located at grain rims and along intragranular micro-fractures. The Ti-poor rim is often truncated by resorption bulges of (altered) plagioclase (Figs. 4.5d,e and Fig. 4.9d). Cores of coarse grains have a similar Ti-content to the one of sample SE13-67 (Figs. 4.9a-d). By contrast, most grains are characterized by a lower Ti-content, suggesting crystallization at lower temperature, and exhibit low fracture densities. This is consistent with the textural evidence indicating that most amphibole grains are not in equilibrium with clinopyroxene and garnet but rather with plagioclase. Interestingly, a coarse grain of amphibole only little fractured and evidencing undulose extinction and subgrain rotation, displays an asymmetrical zonation with Ti content. The subgrains have a lower a Ti content than that of the parent grain.

~25 away from the peridotite (sample SE13-76), where amphibole appears as disjointed large grains surrounded by plagioclase, the longest amphibole grains (with high aspect ratio) show patchy zonation well correlated with the intracrystalline misorientation (Figs. 4.5f, 4.9e). As seen in SE13-69 sample (Fig. 4.9d), the typical zonation is truncated by resorption bulges of sericitized plagioclase and Ti-poor zones are mainly localized in small grains formed at the tips of longer grains (Fig. 4.9e).

## 4.6 Discussion

### 4.6.1 Deformation processes in amphibole

Amphibole grains in the HT metamorphic sole show a very strong fabric, characterized by a J-index up to ~7 (Fig. 4.8). For a J-index of amphibole ~5 in deformed amphibolite with plagioclase and quartz, Tatham et al. (2008) reported shear strain  $\geq 10$ , and Homburg et al. (2010) estimated shear strain in mylonitic gabbro (composed of amphibole, plagioclase and pyroxene) in between 10 and 100 in the Semail ophiolite. The high modal proportion of amphibole in the HT metamorphic soles therefore strongly suggests that HT metamorphic soles underwent high shear strain (even possibly  $\geq 10$ ).

The strong CPO patterns documented here concord with most observations on strained amphibole (Hacker & Christie, 1990, Berger & Stünitz, 1996, Imon et al., 2004, Díaz Aspiroz et al., 2007, Tatham et al., 2008, Cao et al., 2010, Gómez Barreiro et al., 2010, Getsinger et al., 2013). When dislocation creep is the dominant deformation mechanism, the easy slip system is (100)[001]. A large peak of very low angle misorientations, as in figure 4.6, is also expected for dislocation creep (Wheeler et al., 2001).

Amphibole from metamorphic soles, however, shows only rare microfabric evidence for crystal plastic deformation, such as undulose extinction, deformation bands, formation of sub-grains. The correlated [001] axis for intragranular misorientation angles is also inconsistent with dislocation gliding on (100)[001], since the misorientation axis should be perpendicular to the direction of crystal slip (Lloyd et al., 1997). Low angle misorientations around [010] axis would be expected, but are insignificant. Misorientations observed for higher angles, mostly correlated with the [100] axis (Fig. 4.6), correspond to dispersion around the main lineation (Fig. 4.6) and point to a strong flattening component.

Amphibole grains show a strong correlation between CPO and SPO intensities, the long axis being oriented subparallel to the [001] crystallographic axis. This outlines the relationship between grain shape (given by the aspect ratio), grain size and the orientation of amphibole (Fig. 4.4a), suggesting that amphibole grains rather behave as passive marker lines (Ildefonse et al., 1992b). The strong fabric (Fig. 4.6) of amphibole in all samples (with or without garnet, clinopyroxene and plagioclase) would thus testify to rigid grain rotation processes (e.g., Ildefonse et al., 1990, Shelley, 1994, Berger & Stünitz, 1996, Díaz Aspiroz et al., 2007, Tatham et al., 2008). Despite a weaker intensity, the SPO (Fig. 4.4) and CPO (Fig. 4.6) of grains smaller in size and/or aspect ratio are also well defined, indicating that the process of rigid grain rotation must have been very efficient.

In the sample closest to the contact with the peridotite (SE-13-67), where textures at peak conditions are best-preserved, coarse grain brown amphibole shows abundant micro-fractures (Fig. 4.5a-c). Three main sets of micro-fractures are evidenced: parallel (likely along cleavage planes) and normal to the [001] axis (i.e., along the basal plane). Such orientations were previously reported for amphibole (Díaz Aspiroz et al., 2007, Gómez Barreiro et al., 2010) but ascribed to deformation at temperature lower than 700 °C.

Sample SE-13-67 also exhibits a very large number of small grains, compared to that of large grains. Most small grains have no micro-fracture and present a subhedral shape with straight and sharp boundaries (Fig. 4.3a). Micro-fracturing (parallel and perpendicular to the long axis orientation) leading to the formation of smaller grains may explain the similarly small aspect ratios of fine and coarse amphibole grains (essentially  $\leq$  2-3), as suggested by Gómez Barreiro et al. (2010). Furthermore, the Ti contents of both

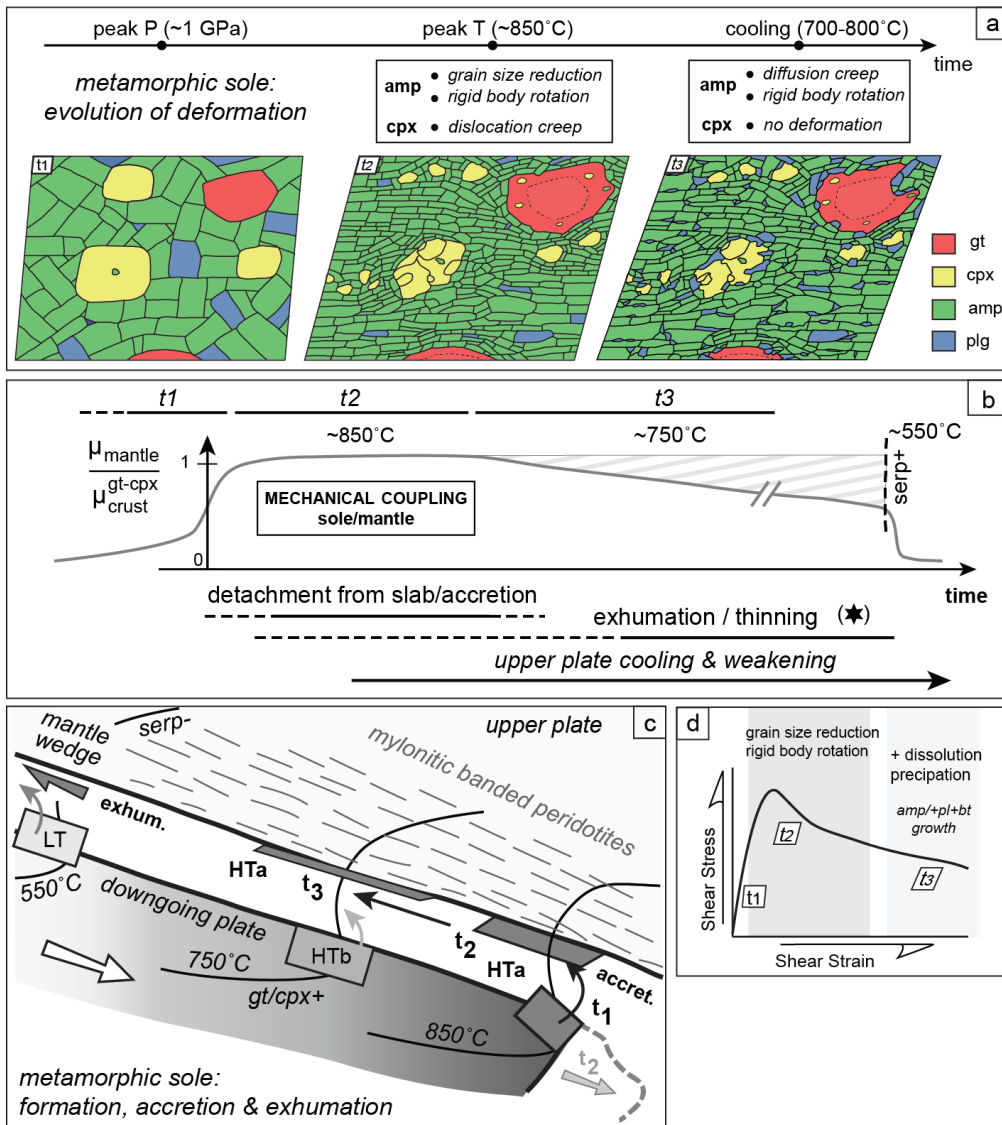


Figure 4.10: (a) Evolutive model of the deformation of the high temperature metamorphic sole of Oman (as a witness of the former slab crust during subduction infancy); (b) Formation and accretion of the high temperature metamorphic sole to the peridotites witnessing mechanical coupling at the slab interface during subduction infancy; (c) Schematic representation of the subduction interface during the early subduction dynamics showing the stepwise formation, accretion and exhumation of slab slivers (partly by thinning together with the overlying peridotites due to strong mechanical coupling). (d) Schematic view of the strain evolution in the amphibolite of the metamorphic sole in function of the stress (the mechanical coupling with the upper plate) at subduction interface.

core and rim are similar for fine-grained brown amphibole and coarser grains, suggesting that grain size reduction appeared at peak conditions (estimated at  $\sim 850^\circ \text{C}$  - 0.9 GPa Soret et al., subm), before retrogression.

These observations (correlation between SPO and aspect ratio, correlation between SPO and CPO, low-angle misorientation axes largely inconsistent with gliding along

(100)[001], set of fractures and composition profiles) suggest that the formation of fine grains chiefly results from a dramatic grain size reduction following cataclastic deformation of coarser parental amphibole grains (e.g. Passchier & Trouw, 1996, p. 25). This brittle deformation is likely related to mechanical interaction between amphibole grains during rigid body rotation. The large modal proportion of coarse and elongate amphibole grains would have temporary blocked the rotation of particles because of intergranular interactions (i.e. true collisions or disturbance of the flow in the matrix due to neighbours; see Ildefonse et al., 1992a). Fracturing and subsequent formation of finer grains would have promoted further slip between particles and rotation. This continuous reorientation of amphibole crystals and reduced grain size increasing the surface energy per unit volume likely produced important softening (Hacker & Christie, 1990).

Most coarse-grained brown amphibole exhibits irregular boundaries associated to resorption bulges of sericitized plagioclase. Some coarse grains present small Ti-poor amphibole at tips in pressure shadows, increasing the aspect ratio (Fig. 4.5).

These features are particularly dominant in samples SE13-69 and SE13-76 ( $\sim 8$  m and  $\sim 25$  m from the peridotite), where retrogression (evidenced by the crystallization of plagioclase and secondary amphibole over clinopyroxene and garnet) is more pervasive. These amphibole grains are characterized by intermediate Ti content in the core, decreasing at the rim. Some of these grains have a coarse grain size and display less fracture density, compared to those in the well-preserved amphibolite SE13-67. The proportion of fine grains with sharp and straight boundaries is also smaller. Nonetheless, both SPO and CPO remain very strong (Fig. 6). During the progressive cooling and exhumation of the metamorphic sole, solution transfer-oriented (over-)growth has therefore likely participated to the SPO development (Shelley, 1994, Berger & Stünitz, 1996) in combination with rigid body rotation. The presence of minute plagioclase with Ti-poor amphibole filling the micro-fractures is consistent with this hypothesis. The concentration of micro-fractures may have enhanced permeability, fluid circulation and retrograde hydration.

#### 4.6.2 Deformation processes in clinopyroxene

Contrary to amphibole, clinopyroxene grains in the metamorphic sole show intra-granular microstructures such as lobate-shape, undulose extinction, small aspect ratio and presence of fine grains around coarse-grained porphyroclasts. These features evidence intracrystalline plastic deformation and grain-boundary migration (Mauler et al., 2000, Bystricky & Mackwell, 2001, Bascou et al., 2002, Kenkmann & Dresen, 2002) indicative of dislocation creep.

---

Clinopyroxene has a moderate CPO. As in amphibole, the [001] maximum is sub-parallel to the lineation. Poles to (010) have a maximum normal to the foliation. Poles to (100) have a very weak maximum sub-perpendicular to the lineation. This pattern corresponds to the (010)-fabric, the most common CPO of omphacite deformed in pure and simple shear (see e.g. Bascou et al., 2002). The orientation of (010) planes parallel to the foliation with [001] axes along the lineation likely reflects the activation of {110} systems (as already reported in omphacite and diopsidite; Ingrin et al., 1991, 1992, Raterron et al., 1994). It was described in diopsidite in naturally sheared gabbro from the Ivrea zone (Barruol & Mainprice, 1993) and in experimentally deformed diopsidite aggregates (Raterron et al., 1994). However, this CPO differs from the one described by Getsinger & Hirth (2014) in very fine-grained clinopyroxene ( $\leq 4 \mu\text{m}$ ) from experimentally deformed amphibolite at P-T conditions similar to those estimated for metamorphic soles. If [001] maximum is similarly oriented, poles to (100) and (010) maxima are reversely oriented. This different pattern may suggest a change in gliding system at very small grain size.

Amphibole appears to control, at least partly, the intensity of the clinopyroxene CPO fabric, which is lower where amphibole is present (Area 2 in SE13-67, and SE13-69). Moreover, coarse-grained clinopyroxene forms boudins and pinch-and-swell structures with smaller grains forming tails. Where amphibole forms a load-bearing framework, clinopyroxene appears to behave as strong and rigid particles due to the high viscosity contrast with amphibole. The small aspect ratio of clinopyroxene grains does not favour the preferential alignment parallel to the stretching direction by promoting rigid grain rotation (Ildefonse et al., 1992b). Since modal proportions of amphibole dramatically increase during retrogression (as evidenced in the sample SE13-69), the deformation of clinopyroxene by rigid grain rotation has most likely occurred during the exhumation of the metamorphic sole.

#### 4.6.3 Implications for metamorphic sole formation

Metamorphic soles are crustal pieces detached from the downgoing slab (as successive slices; Soret et al., subm) and accreted to the mylonitic base of the ophiolite during early subduction. This transient accretion attests to periods of increased mechanical coupling between the two plates, when the effective viscosity of the slab crust and the mantle above become similar across a restricted P-T-time window (i.e. during "rheological switches"; Agard et al., 2016).

The strength of the top of the slab continuously evolves through mineral changes, dehydrates and releases fluids into the nascent mantle wedge, progressively weakening the initially much stronger basal peridotites. With increasing P-T conditions (from amphibolite to granulite facies), constitutive minerals such as Ti-low amphibole and plagioclase

( $\pm$  epidote  $\pm$  biotite; Palin et al., 2016, Soret et al., subm) are progressively replaced by garnet, clinopyroxene and Ti-rich amphibole (Fig. 4.10a).

This study evidences two major deformation episodes and deformation modes:

**Step 1:**

At  $850 \pm 50^\circ\text{C} - 0.9 \pm 0.1 \text{ GPa}$  (Fig. 4.10b): the fact that the garnet–clinopyroxene amphibolite is the first portion of the slab accreted to the upper plate (the future ophiolite) suggests that the strength of the slab crust only then reaches (or is close to) that of the nascent mantle wedge on top (Fig. 4.10b). During this stage of increased mechanical coupling, observations show that the intense deformation of the garnet-clinopyroxene-bearing amphibolite is accommodated by amphibole. This takes place through rigid grain rotation and grain size reduction promoted by brittle deformation, as pointed out earlier by the strong correlation between grain size, aspect ratio, fabric and fracture intensity (Fig. 4.10b). During ongoing deformation, coarse-grain amphibole develops micro-fractures parallel and perpendicular to the long axis, leading to the formation of small grains with straight and sharp boundaries (with a similar aspect ratio to that of inherited granoblastic grains,  $\leq 2\text{-}3$ ). At this stage, the strong fabric of amphibole dominates rock anisotropy, with embedded coarse garnet and clinopyroxene grains (later wrapped in a well-foliated finer-grained amphibole-rich matrix). The inherited, relatively coarse and randomly oriented grains, including some large amphibole grains with high Ti content, indicate growth under relatively low strain and may have crystallized prior to (or at the start of) the slab interface coupling. Clinopyroxene grains crystallized at peak conditions, in equilibrium with Ti-rich amphibole, evidence deformation by dislocation slip parallel to the  $\{110\}$  systems, with the highest CPO in monomineralic layers. Wherever embedded in the amphibole-bearing matrix, clinopyroxene exhibits a weaker CPO, possibly explained by minor contribution of rigid grain rotation, amphibole grains accommodating most of the strain. Finally, where present, garnet acts as boudins modifying locally the orientation of clinopyroxene and amphibole grains in the foliation, leading to weakening of the SPO and CPO in these two phases. The development of boudinage and/or pinch and swell structures of clinopyroxene and garnet indicates that clinopyroxene and garnet are significantly stronger than amphibole but also deform.

**Step 2:**

At  $725 \pm 50^\circ\text{C} - 0.8 \pm 0.1 \text{ GPa}$  (Fig. 4.10c): following detachement from the slab and accretion, a second deformation stage coeval with exhumation (i.e., under decreasing PT conditions; Fig. 4.1c), develops through dissolution–precipitation creep, as evidenced by the Ti zonation and its recurrent truncation in coarse-grained amphibole by plagioclase

---

bulges. The oriented overgrowth of small anhedral Ti-low amphibole grains at the tips of coarser Ti-rich grains also supports the hypothesis that solution mass transfer becomes important during progressive cooling and exhumation of the garnet–clinopyroxene-bearing metamorphic sole. It is exemplified in sample SE13-69, where coarse-grained amphibole replacing clinopyroxene shows little evidence of micro-fractures. The strong S-C fabric associated with finer grains (Fig. 4.5a), lower Ti-content in amphibole and progressive crystallization of plagioclase over clinopyroxene and garnet develops during this stage. This process likely results in significant weakening during cooling, as suggested by the strong impact of amphibole grain-size and SPO on the strength of fine-grained amphibolite (Getsinger & Hirth, 2014). The generation of shear bands also chiefly contributes to the thinning of metamorphic soles. Retrogression of the metamorphic sole also leads to an increase of the plagioclase content (Fig. 4.1d). Under hydrated conditions, plagioclase is known to be mechanically weaker than olivine (Homburg et al., 2010), clinopyroxene (Dimanov & Dresen, 2005) and amphibole(Brodie & Rutter, 1985, Berger & Stünitz, 1996, Díaz Aspiroz et al., 2007, Getsinger et al., 2013). The syn-kinematic growth of plagioclase therefore enhances weakening of the metamorphic sole. It also stops grain size reduction by fracturing of amphibole as these grains rotate in a less viscous medium with progressively increasing viscosity and limited mechanical interactions between rigid particles (Ildefonse et al., 1992a).

#### 4.6.4 Implications for early subduction geodynamics

The finite deformation and the high modal proportion of amphibole in the HT metamorphic sole suggest high shear strain (possibly  $\geq 10$ ). High shearing of amphibolite has important implications in the view of the "metamorphic conundrum" (Hacker and Gnos, 1997) and the spatial distribution of metamorphic soles below large ophiolites (Dewey & Casey, 2013, Plunder et al., 2016, Soret et al., subm). Indeed, Oman metamorphic soles, whether now located at the front or rear of the ophiolite thrust, formed at the same approximate P-T conditions (i.e., at the same depth and thermal regime) and yet got welded along large distances (across 100–150 km) despite being very thin ( $<\sim 50$  m for the HT sole). Two main hypotheses may account for this puzzling observation (see Soret et al., subm): (1) each slice of metamorphic sole forms at the same location and depth during a short time interval and is later "redistributed" below the ophiolite, together with basal peridotites, by exhumation and/or tectonic thinning, or (2) each slice of metamorphic sole forms and gets accreted continuously, at the same depth, across a restricted range of time ( $< 1$  My given available time constraints; Hacker, 1994, Rioux et al., 2013, 2016). In the second hypothesis, distribution of metamorphic soles below the ophiolite results from long-lived accretion rather than from later deformation.

High shearing of the HT metamorphic sole supports the hypothesis of spatial redistribution of metamorphic sole below the ophiolite with an important component of tectonic thinning during the early history of accretion and exhumation. This hypothesis is also supported by structural and petrological evidence (i.e. similarity in mineral zoning and in the HT structure over hundreds of km along and across-strike; Soret et al., subm). The inferred maximum thickness of slices, before thinning, is however limited by that of the basalt layer covering the subducting oceanic plate (i.e., since no gabbroic rocks have been reported in the Semail metamorphic sole) and by the observation that no thermal gradient is recorded with a given slice away from the peridotite (whereas a T gradient might have developed in a thick piece).

## 4.7 Conclusion

Our study points out the existence of two major steps of deformation in the high-temperature amphibolite slices of the metamorphic soles during the early subdduction dynamics.

During the accretion of the first slice of metamorphic sole (the garnet–clinopyroxene amphibolite) to peridotites of the upper plate (at  $850 \pm 50^\circ$ ), strain was essentially accommodated by the orientation of amphibole grains in the foliation plane, promoted by cataclastic deformation (confirming that amphibole is a strong silicate). Clinopyroxene grains were deformed at peak conditions by dislocation creep (resulting in formation and rotation of subgrains) and minor rigid grain rotation where embedded in amphibole-rich matrix.

During the accretion of the second slice of the downgoing plate, at lower P–T conditions, strain was accommodated by amphibole and plagioclase (present in equal modal proportion). Plagioclase grains were deformed by by dislocation creep and formed a less viscous matrix promoting rigid body rotation of amphibole grains in the foliation plane. This step of deformation was assisted by an increase of fluid infiltration leading to the partial dissolution–precipitation of amphibole and plagioclase.

These two steps witness important mechanical coupling and progressive strain localization at plate interface under cooling and hydrated conditions after subduction initiation.

## Supplementary material

	min.	samples	nb grains	mode (%)	J-index	Aspect Ratio	Equi.Diam.	Angle/X
Amphibole	SE13-67_A2a	1817	53	6.83	1.9 (0.6)	73 (51)	91 (28)	
	SE13-67_A2b	7305	43	4.31	1.9 (0.6)	75 (53)	89 (31)	
	SE13-67_A3	4934	42	3.96	1.9 (0.6)	65 (37)	92 (70)	
	SE13-69	5553	58	4.98	1.8 (0.6)	116 (72)	89 (72)	
	SE13-76	1315	21	4.3	1.9 (0.7)	158 (120)	80 (68)	
Clinopyroxene	SE13-67_A1	2495	74	3.35	1.5 (0.4)	103 (69)	91 (45)	
	SE13-67_A2a	987	22	2.26	1.6 (0.5)	63 (40)	92 (41)	
	SE13-67_A2b	5766	31	2.16	1.6 (0.8)	69 (53)	89 (42)	
	SE13-67_A3	2125	22	1.59	1.6 (0.4)	71 (44)	89 (59)	
	SE13-69	1446	13	2.88	1.6 (0.4)	107 (61)	87 (65)	

Table 4.1: Amphibole and clinopyroxene descriptions with number of grains indexed, modal proportion, aspect ratio, equivalent diameter, orientation to the normal of the foliation plane. Number in brackets corresponds to the standard deviation.

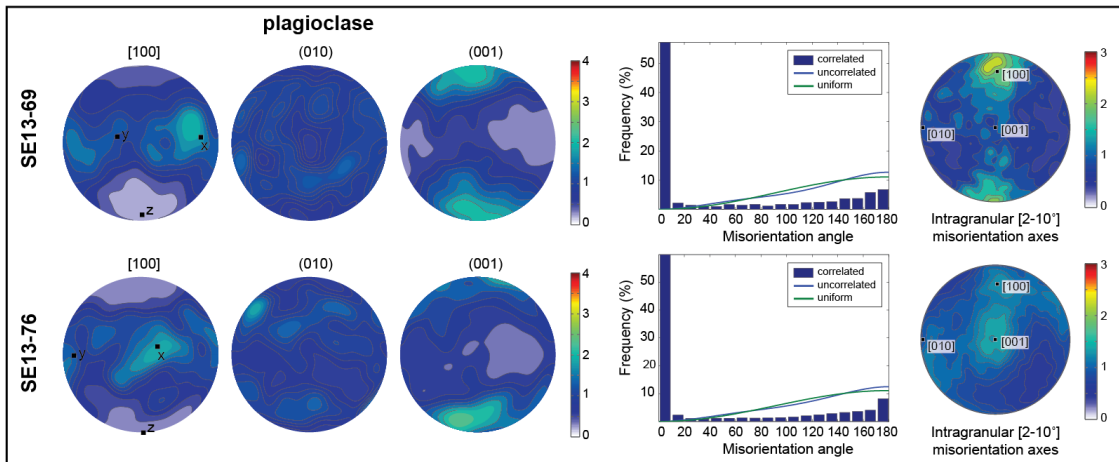


Figure 4.11: (a) Pole figures illustrating crystal lattice orientation (CPO) of plagioclase for the analyzed samples (one measurement per grain). Samples are sorted in function of the distance from the peridotites. X, the horizontal line, represents the lineation and Y, the vertical line, is the normal to the general foliation. Contours are multiples of a uniform distribution. Shear sense is sinistral. All plots are lower hemisphere projections contoured with 15° half-width. c) The low angle intracrystalline (2-10°) and high angle misorientation axis for the different phases.





---

## 5 Déformation expérimentale des amphibolites de haute température

Dans ce chapitre nous nous intéressons au couplage mécanique entre les péridotites et les amphibolites tel qu'il peut exister à l'interface d'une subduction océanique peu de temps après son initiation ( $\leq 2$  Ma ; cf. section 2.3.2) — mais aussi à la base de la croûte continentale. Nous nous intéresserons également à l'influence du grenat dans la rhéologie des amphibolites. Ce travail a en effet pour objectif principal de préciser le comportement mécanique des semelles métamorphiques, composées au pic de métamorphisme d'amphibolites à grenat.

Après avoir été abordée à partir d'une étude structurale sur échantillons naturels, cette problématique est ici traitée à partir d'expériences en laboratoire réalisées à l'aide d'une presse à pression de confinement solide. L'objectif de ces expériences n'était pas d'obtenir des lois rhéologiques mais de reproduire en miniature, à échelle millimétrique, le système géodynamique prévalant lors de la formation des semelles métamorphiques (soit, au premier ordre : manteau sur amphibolites en contexte de cisaillement simple) et de caractériser les déformations résultantes et les modalités du couplage entre les deux compartiments, ou plaques. Ces expériences ont été conduites à l'université de Brown (USA) en collaboration avec Greg Hirh et Keishi Okazaki. Cette étude se trouve par ailleurs être dans la continuité des travaux de thèse d'Amanda Getsinger, qui s'était appliquée à préciser la rhéologie des amphibolites de base de croûte continentale. Seules 5 expériences ont pu être réalisées, au cours d'un séjour d'un peu plus d'un mois. Ces expériences initialement très différentes ont pour objectif de tester un maximum de configurations afin de déterminer celle qui sera la plus appropriée à l'étude des mécanismes de déformation des amphibolites (avec ou sans grenat), ubiquistes en base de croûte continentale et dans les semelles métamorphiques. Le travail présenté ici est donc essentiellement exploratoire. Pour des raisons de commodité, et en vue d'expériences (et de publications) ultérieures, la partie qui suit est rédigée en anglais.



## 5.1 Introduction

Deformed amphibolite is common in the middle to lower continental crust (e.g. Berger & Stüntz, 1996, Imon et al., 2004, Tatham et al., 2008, Homburg et al., 2010, Getsinger et al., 2013) and along oceanic transform faults and detachments (e.g. Escartín et al., 2003, Boschi et al., 2006). Deformed amphibolite is also found beneath highly strained peridotite at the base of large-scale ophiolites (as exemplified in Oman; Boudier et al., 1988, Linckens et al., 2011, Agard et al., 2016). This latter amphibolite, known as metamorphic sole, is thought to result from heat transfer from a young upper plate mantle towards the slab when the subduction interface is still warm. Recent studies reveal that the formation of metamorphic soles record transient rheological switches across the subduction interface during the first My of intra-oceanic subduction (Agard et al., 2016). The viscosity contrast between amphibolite and peridotite may therefore control two major dynamics: 1) the behaviour of lower crust at the Moho; 2) the slab penetration into the mantle (and the formation of metamorphic soles) during subduction infancy.

Despite numerous studies, lower continental crustal rheology and, as a consequence, the viscosity contrast with upper mantle lithologies remain uncertain. Upon analysis of lithospheric elastic thickness estimates (Burov & Watts, 2006), field observations (Homburg et al., 2010) and extrapolation of experimental flow laws (Brace & Kohlstedt, 1980), most models of continental rheology represent the lower crust as a weak layer sandwiched between two stronger layers, the brittle upper crust and the upper mantle. However, some studies focusing on the earthquake depth distributions and the analysis of gravity anomalies (Maggi et al., 2000, Bürgmann & Dresen, 2008, Jackson, 2002) suggest that the lower crust is stronger than the mantle beneath the Moho. To settle the debate, some authors advocate for a strong lithospheric crust except in localized discrete shear zones, much weaker than the host rock (Bürgmann & Dresen, 2008, Jackson, 2002, Mackwell et al., 1998). Indeed, field studies and experimental investigations have demonstrated that deformation mechanisms and rock rheology can strongly vary in function of mineralogy, grain size and fluid activity. Fluid infiltration at high temperatures (650–850 °C) may trigger the crystallization of hydrous phases, such as amphibole, thought to increase the strength contrast between wet and dry lithologies, and therefore to promote strain localization via the formation of these discrete shear zones (Austrheim, 1987, Kenkmann & Dresen, 2002) in the lower continental crust but also at the slab interface.

To investigate the effect of amphibole-forming metamorphism during deformation, most studies have so far focused on lower crust amphibolite, but metamorphic soles may prove a good way to constrain the influence of hydration at high temperature and medium pressure.

---

Amphibolite from the metamorphic sole represents highly strained m to  $\sim$ 500 m thick units of oceanic rocks composed of amphibole, clinopyroxene, garnet and/or plagioclase. The peak of metamorphism is estimated around  $800 \pm 100$  °C and  $0.9 \pm 0.2$  GPa. Structurally above, upper mantle rocks show variable deformation patterns from porphyroclastic to ultramylonitic textures formed in the temperature range of 1100 °C down to  $\sim$ 700 °C (Boudier et al., 1988, Michibayashi & Mainprice, 2004, Linckens et al., 2011) on a m- to hm-scale. From a mechanical point of view, the metamorphic sole should be considered as a threefold stack with, from bottom to top, the LT sole, the HT sole and the base of the ophiolitic mantle sequence. Based on these features and experimentally-derived flow laws for the mantle and mafic crust, Agard et al. (2016) propose the existence of transiently similar rheologies and strong coupling during subduction infancy to explain the metamorphic sole formation and accretion. Metamorphic soles worldwide are therefore a very suitable example to investigate the viscous coupling with upper mantle peridotites, strain localization at amphibolite to granulite-facies conditions and associated deformation mechanisms.

In this work, we investigate strain localization and deformation mechanisms in experimentally deformed amphibolite. Experiments were conducted at a temperature of 800 °C and confining pressure of 1 or 2 GPa using a Griggs solid-medium apparatus apparatus (at Brown University in collaboration with Greg Hirth and Keishi Okazaki). The mantle–crust interface was first simulated under general shear conditions to evaluate the viscous coupling at the slab interface during early subduction dynamics (and the formation of metamorphic soles), or at the Moho. Then, deformation experiments were performed with garnet to analyze the impact of this strong mineral on the deformation of amphibolites.

## 5.2 Experimental procedures

The experiments were conducted using a Griggs solid-medium apparatus apparatus at Brown University (Figure 5.1a, Table 5.1). Hydrostatic annealing and general shear deformation experiments were conducted on fine-grained amphibolite samples (Figure 5.1b). Fine-grained amphibolite samples was synthesized following the procedure used by Getsinger & Hirth (2014). 1 wt% nanopure deionized (DI) water were added to a powdered basalt derived from a mid-ocean ridge basalt (MORB). The basalt comprises  $\sim$ 50% plagioclase,  $\sim$ 30% clinopyroxene,  $\sim$ 10% olivine, and trace amphibole, orthopyroxene and chlorite (see detailed in Getsinger & Hirth, 2014). The basalt was crushed in a tungsten carbide shatterbox, sieved to  $\leq 10$   $\mu\text{m}$ , and settled in DI water to obtain grain sizes of  $\leq 5$   $\mu\text{m}$ . San Carlo wet olivine powder with a grain size  $\leq 10$   $\mu\text{m}$  were also used for two experiments to simulate peridotite behaviour.

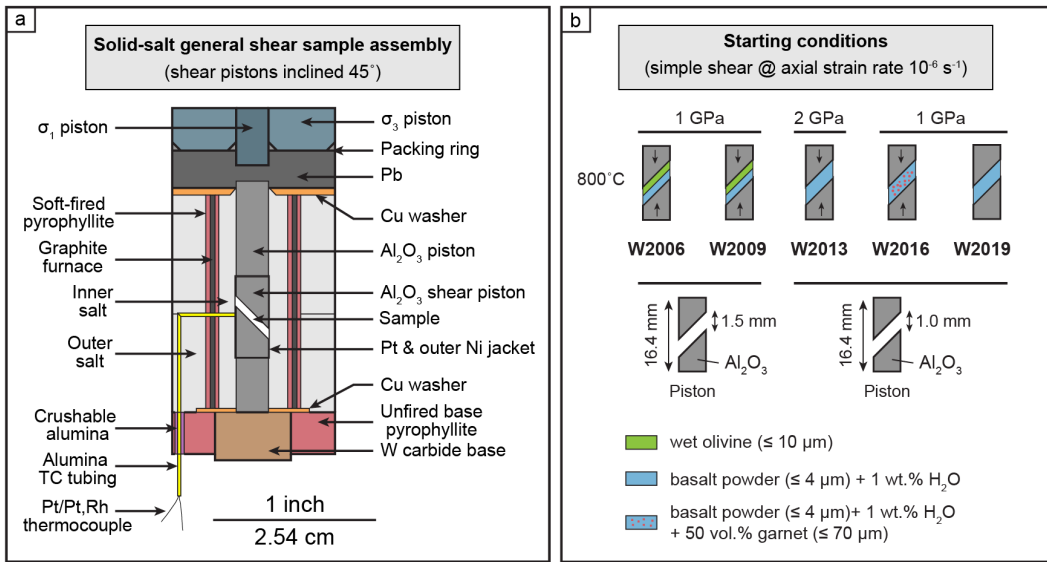


Figure 5.1: (a) Experimental assembly used during general shear strain experiments; (b) schematic representation of the conditions and the starting material used in the 5 experiments conducted in this study.

Expt #	Sample material	Type	T(°C)	Press (GPa)	Gear Rate (s <sup>-1</sup> )	Wt% H <sub>2</sub> O	$\gamma$	Piston	Total time (h)	Time (h) < hit point
W2006	2 layers: olivine & powder basalt	shear	800	1	10-6	1	1.2	Zr <sub>2</sub> O <sub>3</sub>	50	28
W2009	2 layers: olivine & powder basalt	shear	800	1	10-6	1	3.8	Al <sub>2</sub> O <sub>3</sub>	72	27
W2013	powder basalt	shear	800	2	10-6	1	3.6	Al <sub>2</sub> O <sub>3</sub>	61	24
W2016	powder basalt mixed with 50% of garnet	shear	800	1	10-6	1	3.8	Al <sub>2</sub> O <sub>3</sub>	77	38
W2019	powder basalt	hydrostatic	800	2	-	1	-	Al <sub>2</sub> O <sub>3</sub>	50	-

Table 5.1: Experimental conditions and sample descriptions.

Shear deformation was imposed on a thin layer of the sample gouge sandwiched between two alumina or yttria-stabilized zirconia pistons (6.35 mm in diameter) with oblique surfaces oriented 45° from the cylinder's axis (Figure 5.1). Due to a stick-slip event occurring during the first experiment (W2006), other deformation experiments were conducted with grooved pistons. Powdered samples had an initial thickness of ~1 to 1.5 mm. They were enclosed in an inner platinum (Pt) jacket and outer nickel (Ni) jacket. The Pt jacket was folded over two Pt disks placed between Al<sub>2</sub>O<sub>3</sub> shear and axial pistons to seal mechanically the samples. The confining medium was composed of Sodium chloride (NaCl) for both inside and outside the graphite furnace. The temperature was measured using a Pt-Pt10%Rh thermocouple centered on the sample, outside the outer Ni jacket. Based on previous calibrations, variations of ~10 °C may occur along the sample (see Getsinger, 2015, for details). The pressure is accurate to ~100 MPa (e.g. ?).

---

All deformation experiments were performed with a strain rate of  $10^6$  s $^{-1}$  (Figure 5.1b). All experiments were deformed after annealing at run conditions ( $800^\circ\text{C}$ ) for at least 24 hours, during  $\sigma_1$  piston advancement. The shear stress versus shear strain curves were calculated using the initial thickness of the samples and the measured final sample thickness and shear displacement of the pistons. The stress is accurate with a deviation of  $\sim 25$  MPa and corrected for the strain rate dependence of friction (see Getsinger & Hirth, 2014, for details). Mechanical data were processed using a MATLAB script written by Keishi Okazaki.

Two general shear deformation experiments (W2006 and W2009; Figure 5.1b) were conducted at temperature of  $800^\circ\text{C}$  and confining pressure of 1 GPa with two parallel layers composed of fine-grained synthetized amphibolite and wet (San Carlo) olivine in order to reproduce the interface between an upper mantle and the slab (or the lower continental crust). Experiment W2013 (Figure 5.1b) was conducted at the same temperature but higher confining pressure (2 GPa) to evaluate the mechanical behaviour of synthetized fine-grained garnet-bearing amphibolite under general shear conditions. With the similar objective, deformation experiment W2016 (Figure 5.1b) was performed at a confining pressure of 1 GPa with a starting material composed of 50% hydrated powdered basalt and 50 % natural crushed garnet crystals ( $\leq 50\ \mu\text{m}$ ). W2019 experiment was conducted under hydrostatic conditions at  $800^\circ\text{C}$  and 2 GPa for 50 hours at  $800^\circ\text{C}$ , which is equivalent to the duration of the deformation experiment (W2013). Deformation experiments conducted at  $800^\circ\text{C}$  and 1 GPa with hydrated basalt powder are compared to the hydrostatic sample previously produced by A. Getsinger after 63h annealing (W1779; Getsinger & Hirth, 2014).

### 5.3 Mechanical data

At  $800^\circ\text{C}$  and 1 GPa, the first experiment W2006 with 2 layers composed of fine-grained olivine and amphibolite reached a maximum shear stress of 500 MPa at a shear strain ( $\gamma$ )  $\approx 0.6$  (Figure 5.2a). This peak was followed by 3 drastic decreases of the shear stress of  $\sim 60$ ,  $\sim 110$  and  $\sim 200$  MPa. The experiment was closed at  $\gamma \approx 1.2$ , while the rapid weakening was still ongoing. The post-experiment sample descriptions showed that slips occurred between the sample and the olivine layer, causing the slip-stick events.

The same experiment was reproduced with grooved shear pistons to increase the friction with the sample. This experiment W2009 reached a maximum shear stress of 660 MPa at  $\gamma \approx 0.7$ . It was followed by a strong weakening up to  $\gamma \approx 3.8$ , leading to

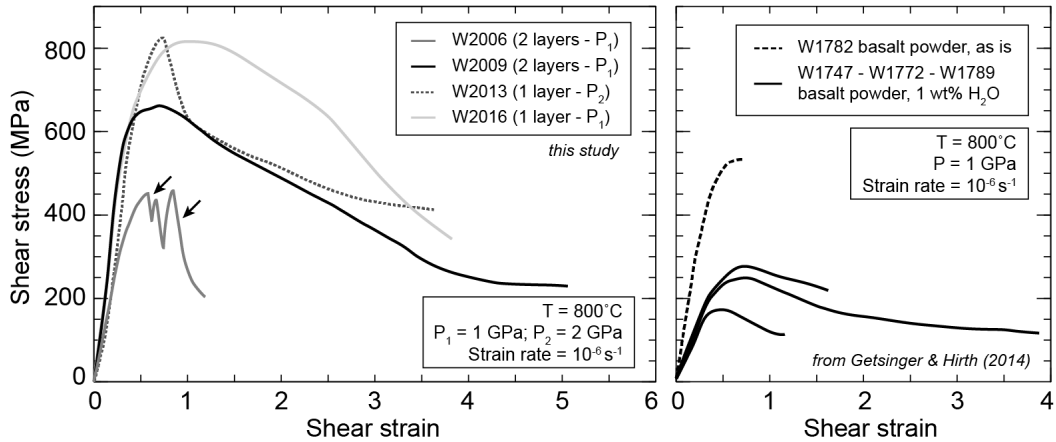


Figure 5.2: (left graphic): Shear stress vs. shear strain curves for each experiments conducted in this study (left graphic) and for representative experiments conducted by (Getsinger & Hirth, 2014) on the same hydrated basalt powder and at similar strain rate and P-T conditions.

~60% strength reduction (Figure 5.2a). At higher strain, the weakening ceased almost completely, probably approaching a steady-state shear stress of 240 MPa.

Monolayer of hydrated basalt powder experiment W2013 at  $800^\circ\text{C}$  and confining pressure of 2 GPa attained a peak stress of ~830 MPa at  $\gamma \approx 0.7$  (Figure 5.2a). Between  $\gamma \approx 0.7$  and  $\approx 1.0$ , the peak was followed by a very strong and quick weakening which led to ~25% strength reduction. Between  $\gamma \approx 1.0$  and  $\approx 2.7$ , the stress-strain curve shows a strong but more moderate strength weakening with a slope comparable to that of experiment W2009. At higher strain, the weakening ceased almost completely. The experiment was closed at  $\gamma \approx 3.6$ . The post-experiment sample descriptions showed that the upper shear piston was decoupled to the sample. Despite grooved pistons, a slip-stick between the shear piston and the sample probably occurred during the experiment, causing the rapid first shear drop at very high axial stress.

Deformation experiment W2016 performed at a confining pressure of 1 GPa and  $800^\circ\text{C}$  with a starting material composed of 50% hydrated powdered basalt and 50% crushed garnet crystals reached a maximum shear stress of 820 MPa at  $\gamma \approx 0.9$  (Figure 5.2a). This maximum stress is characterized by a plateau rather than a peak, and was followed by strong and continuous weakening from  $\gamma \approx 1.3$  to 3.8, marking the end of the experiment.

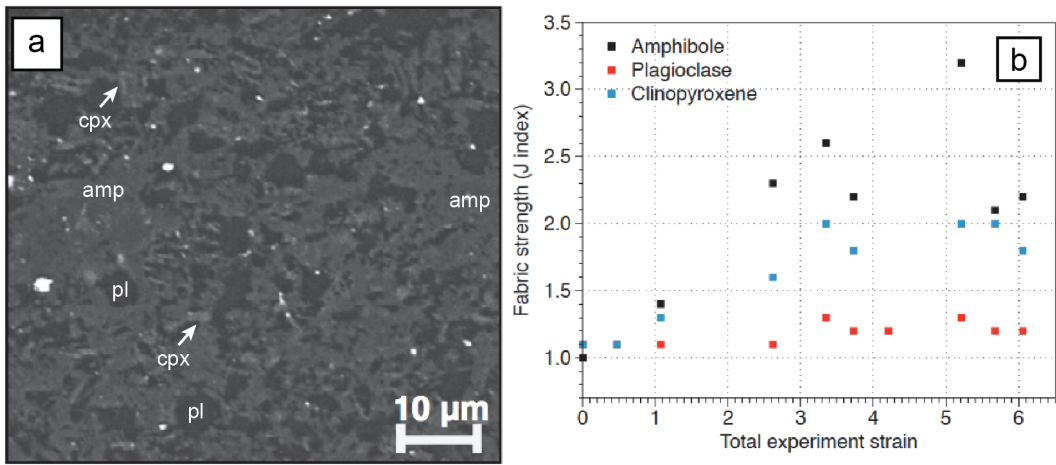


Figure 5.3: (a): Backscattered electron emission image of a fine-grained experimental amphibolite from (Getsinger & Hirth, 2014) synthetized at hydrostatic conditions and characterized by no shape-preferred orientation (SPO); (b): Fabric (quantifying with the J-index) vs. total experiment strain. Plagioclase (red square) fabric does not exhibit any correlation with the strain. Clinopyroxene (light blue square) and amphibole (dark blue square) fabrics show strong positive correlation with the strain.

## 5.4 Analytical methods

The sample descriptions have been conducted using SEM BSE images and EBSD maps. Thin sections were made of a longitudinal slice of each experimental sample (i.e., XZ plane).

The EBSD data have been collected using a CamScan X500FE CrystalProbe scanning electron microscope (SEM) at Géosciences Montpellier (France) by electron backscatter diffraction techniques (EBSD). The EBSD measurements were performed at 25 mm of working distance with an accelerating voltage of 15 kV on carbon coated and polished thin sections tilted at 70° from the horizontal within the microscope chamber. The step size was 0.3  $\mu\text{m}$ , the maximum spatial resolution of the EBSD. Generated diffraction patterns were processed using the Channel 5 software suite (Schmidt & Olesen, 1989). The EBSD data was processed using MTEX software, a MATLAB toolbox for textural analysis (Hielscher & Schaeben, 2008, Bachmann et al., 2010). Contrary to olivine layers, deformed amphibolite layers had very low EBSD indexing. It cannot be used for grain size, mineralogy and fabric analyzes of deformed fine-grained amphibolites.

## 5.5 Mineralogy and Microstructure

### 5.5.1 Previous observations

(Getsinger & Hirth, 2014) performed numerous experiments with the 1 wt% hydrated basalt powder at similar P–T conditions ( $800^{\circ}\text{C}$ –1GPa; (Figure 5.2b), 5.3). Based on a short hydrostatic experiment (W1904), she assessed that ~40% of amphibole were formed after ~15 hours (the minimum duration of the advancement of the  $\sigma_1$  piston). After the experiments, both deformed and hydrostatically annealed samples samples with 1 wt%  $\text{H}_2\text{O}$  added were composed of ~20 to 40% plagioclase, ~40 to 65% amphibole, ~10 to 20% clinopyroxene, and trace olivine, orthopyroxene, chlorite, and mica, homogeneously distributed. During experiments, hydration reactions occurred and amphibole + sodic plagioclase crystallized after anorthitic plagioclase + clinopyroxene + orthopyroxene + olivine.

In the deformed samples, the mean plagioclase and amphibole grain diameters range, respectively, between 4.2 and 4.9  $\mu\text{m}$  and between 3.2 and 4.3  $\mu\text{m}$ . A. Getsinger noticed that their grain sizes slightly increased with increasing shear strain. Conversely, clinopyroxene grain sizes remain approximately constant as a function of strain, between 3.6 to 4.1  $\mu\text{m}$ . Amphibole, plagioclase and clinopyroxene have, therefore, approximatively similar grain size. Moreover, these phases present a mean aspect ratio  $< 2$  in both hydrostatic and deformed samples, the mean aspect ratio of all plagioclase and clinopyroxene grains is 1.4 to 1.6 and amphibole is 1.4 to 1.8.

While in samples held at hydrostatic conditions (Figure 5.3a), amphibole, plagioclase and clinopyroxene developed a moderate to random shape-preferred orientation (SPO) and crystal-preferred orientation (CPO), deformed sample evidenced a S-C fabric defined by the SPO of each phase. Amphibole and clinopyroxene are also characterized by a strong CPO. The J index, quantifying the strength fabric shows that amphibole fabric strength increases with increasing strain (Figure 5.3b). This increasing fabric as a function of strain is also visible in clinopyroxene, although not as significantly. However, plagioclase grains exhibited a weak CPO, even at very high strain (as shown by their J index values; Figure 5.3b).

### 5.5.2 Amphibolite-mantle coupling simulation

The deformation experiment W2006 composed of an upper layer of fine-grained olivine and a lower layer of basalt powder with 1 wt%  $\text{H}_2\text{O}$  added failed at  $\gamma \approx 0.6$  due to

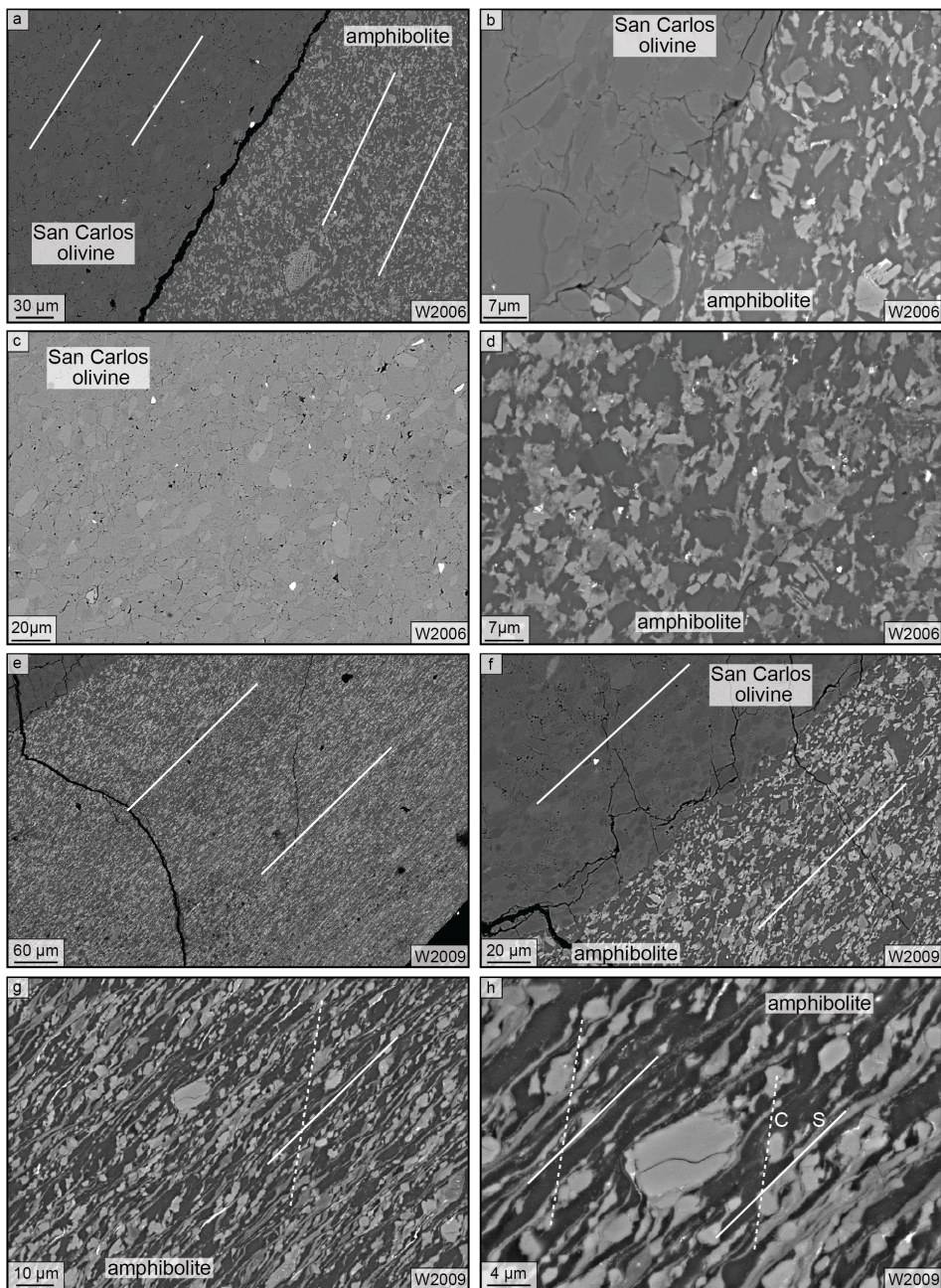


Figure 5.4: Post experimental back-scattered images of finite microstructures in the two-layers samples W2006 (a-d) and W2009 (e-h) deformed during shear strain experiments. White lines highlight the foliation plane and dashed white lines indicate shear band direction (sub-parallel to the  $\sigma_1$  direction). (a-b, e-f) Zoom into the contact between the two layers simulating the mechanical coupling at plate interface during subduction initiation. In both experiments, plagioclase grains are present in higher proportion in the amphibolite, compared to clinopyroxene and amphibole. Conversely of sample W2006, sample W2009, deformed at higher total strain, displays a strong and similar foliation in the two layers. In the amphibolite layer, a pervasive deformation is localized at the center of the layer along S-C structures (g-h). Clinopyroxene grains form sheared boudins. Plagioclase and amphibole grains are aligned along the shear direction and the shear bands.

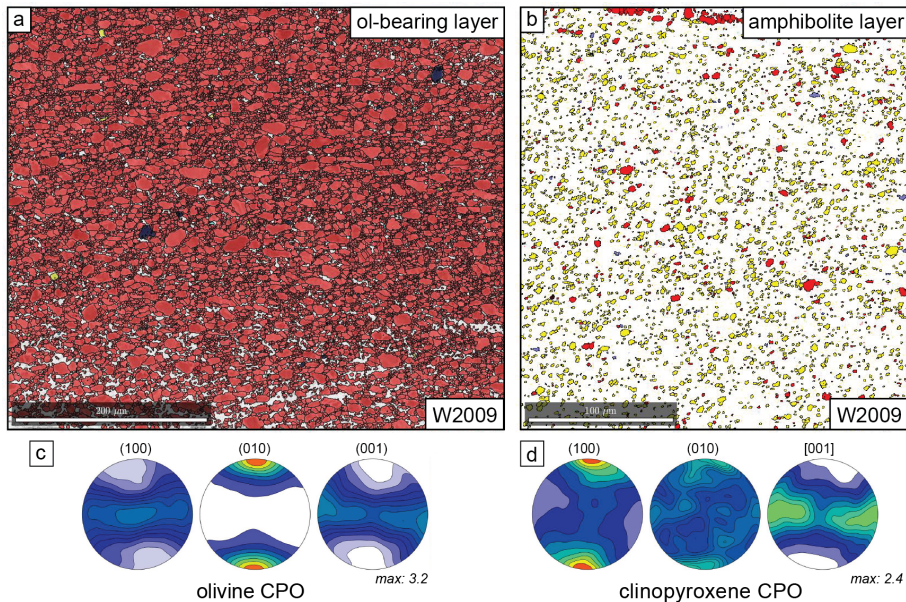


Figure 5.5: EBSD maps of sample W2009 showing the quality of the indexation in each layer (a-b) and pole figures of (c) olivine and (d) clinopyroxene. In the amphibolite latter layer, the general grain size is too small to allow correct indexation. Only clinopyroxene was well-analyzed.

a slip-stick occurrence between the piston and the olivine layer. However, this experiment can still be analyzed as a low strain sample and compared to the experiment W2009 characterized by the same starting material and deformed at a higher strain, up to  $\gamma \approx 5$ .

In both experiments, it can first be noticed that the two layers present a sub-parallel foliation separated by a straight and sharp boundary correctly oriented at  $45^\circ$  C tp the  $\sigma_1$  piston direction (Figure 5.4). EBSD map performed on the low strain sample has a relatively high indexing for olivine, plagioclase and clinopyroxene. However, very few amphibole grains were indexed (< 5%). Their number is not sufficient to be used for analyzes. In the high strain experiment sample, only olivine and clinopyroxene were correctly indexed (Figure 5.5a,b). Plagioclase and amphibole exhibit a very low indexing. In very high strain experiment, (Getsinger & Hirth, 2014) interprets that low indexing percentage of plagioclase grains in very high strain experiment as a probable result of very high dislocation densities.

In both experiments, olivine grains in the upper layer (modeling the upper mantle peridotites) exhibit a nearly similar fine-grained size between 2 and 5  $\mu\text{m}$  and a small aspect ratio ( $\sim 1.5 \pm 0.3$  at  $\gamma \approx 0.6$  and  $\sim 1.4 \pm 0.3$  at  $\gamma \approx 5$ ; Figure 5.4c). However, the highest strain sample (W2009) olivine grains show a planar fabric, defining the foliation plane. In the low strain sample W2006, olivine exhibits a moderate SPO and CPO. The J index, quantifying the strength fabric, is 1.68. In the high strain sample W2009, olivine

---

exhibits a slight stronger fabric, ( $J$  index = 1.92) associated with a higher proportion of olivine subgrains around coarser grains with high density of misorientation. In both experiments, the olivine CPO is characterized by essentially the [010] axes perpendicular to the foliation plane, and both [100] and [001] axes are more dispersed, lying in the foliation plane (Figure 5.5a). The [001] axes are slightly subparallel to the shear direction and the (100) plane subparallel to the shear plane. This fabric pattern is consistent with the type-B reported by Jung & Karato (2001) for San Carlos olivine for water-rich and/or high-stress conditions ( $\geq 350$  MPa) at  $T \leq 1000$  °C. It is reported in the peridotites from the mantle wedge (Michibayashi et al., 2006) deformed in transpression regimes directly above the slab (Tommasi & Vauchez, 2015). Usually, these olivine grains have a weaker fabric compared to that of the other types and do not exhibit well-developed subgrain structure. This pattern suggests the preferential activation of the (010)[001] slip system.

In both experiments, the amphibolite layer developed a S-C fabric defined by the SPO of amphibole, clinopyroxene, and plagioclase grains. In the low strain sample, these phases show a moderate SPO subparallel to the shear direction. With increasing strain, the SPO strength remains relatively constant for clinopyroxene and plagioclase but largely increases for amphibole, although it is difficult to define with precision the grain boundaries due to the very fine grain size and the very low EBSD indexing. In the high strain sample, some amphiboles grains are subhedral with a grain size  $\geq 2$   $\mu\text{m}$ . Most of grains appear as narrow tails crystallizing after subhedral amphibole, anorthitic plagioclase and clinopyroxene porphyroclasts. These tails form subparallel lines lying in the foliation plane and reoriented locally along shear bands.

In both experiments, clinopyroxene was correctly indexed, allowing texture analyzes (Figure 5.4b). In the lower layer, clinopyroxene has a fine grain size, mostly ranging between 1.5 and 4  $\mu\text{m}$ . They also show a similar aspect ratio around  $1.4 \pm$  and weak strength fabric ( $J$  index = 1.31 and 1.44). Pole figures are equivalent to those reported by (Getsinger & Hirth, 2014, Getsinger, 2015). As for olivine, the (100) plane is subparallel to the shear plane and the [001] axis orientation clusters subparallel to the shear direction (Figure 5.4b). At temperature of 800 °C and laboratory strain rates, this pattern is thought to reflect the activation of the (100)[001] slip system (Ingrin et al., 1992). This orientation gliding is also consistent with the [010] rotation axis observed for small angle misorientations (2–10°). Bascou et al. (2002) proposed that this fabric could also result from the activation of {110}[001] glide systems.

Plagioclase grains were only successfully indexed in the low strain sample. Their size, aspect ratio and strength fabric ( $J$  index = 2.01) are equivalent to those of clinopyroxene. With a weak clustering of the (010) plane subparallel to the foliation and the [100]

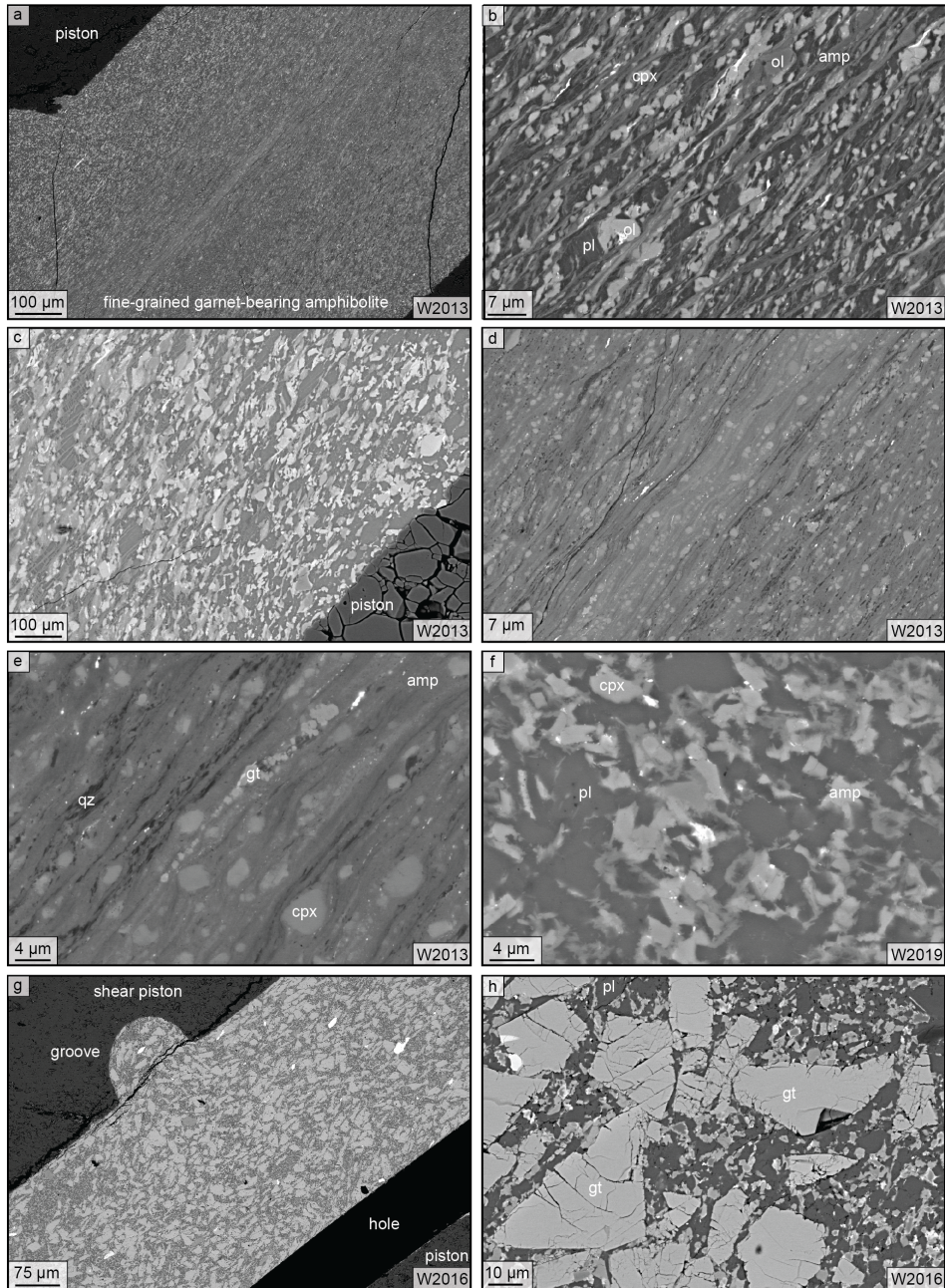


Figure 5.6: Post experimental back-scattered images of finite microstructures in garnet-bearing amphibolite. (a-b) Microstructures of the same W2013 with an important strain gradient towards the center of the sample (c-d). The proportion of amphibole increases with strain. At the maximum strained area (d-e), newly formed garnet is observed with amphibole and quartz, and plagioclase is rare. It could indicate that reaction albite = jadeite + quartz occurred in the sample where fluids were localized; (f) Low shape-preferred orientation in the sample W2019 held at hydrostatic conditions. No garnet and quartz are observed. (g-h) Images of the sample W2016, with fractured garnet porphyroclasts wrapped by a low strain amphibolite matrix.

axis subparallel to the shear direction, pole figures indicate a potential activation of the (010)[100] slip system.

---

Amphibole grains were not sufficiently indexed to allow any textural quantification. However, the comparison with the deformation experiments conducted by (Getsinger & Hirth, 2014) with the same basalt powder and amount of water indicates that the modal proportion of amphibole is likely lower in our experiments. This might be explained by the fact that, considering the configuration of our double layer experiments, the water was added onto the olivine layer and not on the underlying basalt powder. During the pre-hit period, corresponding to  $\sigma_1$  piston advancement, the water circulation was not enough efficient to permit any homogeneous distribution of reactions phases. This could also explain why in the low strain sample the proportion of amphibole seems to be lower than at higher strain. Increasing strain have probably enhanced fluid circulation throughout the sample allowing a better spatial distribution of hydration reactions.

### 5.5.3 Garnet-bearing amphibolite

The same basalt powder with 1 wt% of water added was deformed at higher confining pressure (2 GPa) with the aim to synthetize garnet crystals (Figure 5.6). The experiment W2013 reached a  $\gamma \approx 3.6$ . The sample exhibits an increase of the deformation from the shear pistons toward the core of the sample (Figure 5.6a). The edges of the sample remain rich in plagioclase and clinopyroxene (Figure 5.6c). These phases are destabilized by the crystallization of elongated amphibole grains which form lines parallel to either the shear direction (as clinopyroxene and plagioclase) or the shear bands (Figure 5.6b). Modal proportion of amphibole progressively increases as a function of strain localization throughout the sample (Figure 5.6d).

In the highest strain area, small euhedral garnet crystals crystallized after plagioclase and in equilibrium with amphibole (Figure 5.6d,e). Plagioclase and clinopyroxene appear only as rare relicts embedded in a matrix of very fine-grained amphibole (Figure 5.6d,e). Garnet is not observed in lower strain regions (Figure 5.6c), nor is it present in the sample W2019 held at hydrostatic conditions (Figure 5.6f). In this sample, plagioclase, amphibole and clinopyroxene exhibit a grain size  $< 5 \mu\text{m}$  with a moderate SPO and grain elongation sub-parallel to the shear direction developed during hot pressing (Figure 5.6f).

The basalt powder with 1 wt% of water added was deformed up to  $\gamma \approx 3.8$  with 50% of crushed garnet crystals at confining pressure of 1 GPa (Figure 5.6i,j). The analysis of the sample W2016 indicate that garnet grains are  $\leq 50 \mu\text{m}$ . They have very different shapes, from low to high aspect ratio (Figure 5.6i,j). Most of grains lie in the foliation plane, with the longest shape axis parallel to the shear direction. They exhibit numerous cracks, usually subperpendicular to the foliation plane. Between garnet grains, fine-grained plagioclase, clinopyroxene and amphibole appears as little deformed pockets (Figure 5.6j).

These phases are much less elongated and oriented than those in our previous experiments, or those conducted by (Getsinger & Hirth, 2014) at similar  $\gamma$ .

## 5.6 Interpretation and discussion

Mechanical data indicate that two-layer experiments W2006 and W2009 are stronger than synthetized amphibolite deformed at similar conditions (Getsinger & Hirth, 2014). This sample hardening is likely the combination of:

- the resistance of olivine; mechanically stronger than plagioclase and amphibole as suggested in the amphibolite layer by the presence of olivine boudins.
- the lower modal proportion of amphibole, indicating a lower hydration of the powder basalt during the experiment despite a similar amount of water added (due to the sample structure, the water was added onto the olivine layer, and not directly onto the basalt).

The olivine-bearing and amphibolite layers show both important deformation, highlighting the existence of mechanical coupling at their interface. Interestingly, the highest strain area is the interface but within the amphibolite layer. It would indicate that amphibolite viscosity were not high enough to reach that of olivine and allowing more distributed deformation. Future experiments should also attempt to further weaken the olivine layer (e.g., by addition of more water or of second phases such as clinopyroxene or amphibole).

The amphibolite layer accommodated strain by the development of localized S-C structure, allowing an important thinning of the sample. Clinopyroxene and olivine form sheared boudins in a less viscous matrix composed of well elongated amphibole and plagioclase. It suggests that clinopyroxene is mechanically much stronger than plagioclase and amphibole, as in natural samples from metamorphic soles (see chapter 4 of this thesis). The CPO pattern indicates that clinopyroxene mainly deformed by gliding along the  $\{hk0\}[001]$  slip systems. Although amphibole grains evidence growth along shear bands, it is difficult to define any high viscosity contrast between plagioclase and amphibole in the presence of water (despite the fact that plagioclase is usually thought to be weaker than amphibole). Phase indexation, unfortunately, was too low to allow structure analyses for these two phases.

The olivine-bearing layer does not exhibit S-C structures. Finite deformation indicates that olivine grains are oriented along the shear direction and developed plastic structures (subgrain formation and rotation), as a probable result of the activation slip on the (010) plane in dislocation creep. This deformation mechanism is commonly observed

---

in peridotites deformed in transpression regime in the presence of water, as in the mantle wedge.

To summarize, below are the main conclusions which can be drawn from both deformed experiments simulating the crust–mantle interface at amphibolite facies and general shear strain conditions, in our attempt to replicate at mm-scale the conditions of the plate interface contact:

W2006: it is the mechanically stronger experiment, due to olivine and insufficient water. Although viscous coupling is important, the maximum of strain is not localized at the interface between the two layers but rather within the amphibolite, which underwent the highest thinning and developed S-C structures. Both amphibole and plagioclase appear weaker than clinopyroxene, but it is difficult to ascertain which of the two is the weakest: amphibole form really narrow lines parallel to both the shear direction and shear bands at high angle from the shear direction, while plagioclase are both strongly sheared and wrapped around in places by amphibole.

W2013: This experiment shows, contrary to the common inference that plagioclase is weaker than amphibole under wet conditions, that this is not obvious in our experiments — nor in natural samples from the metamorphic sole. No structure unambiguously testifies to a clear viscous difference between the two (such as boudins or pinch and swell structures). Amphibole seem more elongated but this could also result from the activation of different deformation mechanisms. Again, however, both minerals are clearly much weaker than clinopyroxene.

More experiments and a better indexation are needed to get further insights into metamorphic sole deformation and viscous coupling at the plate interface during subduction infancy.

## Supplementary material

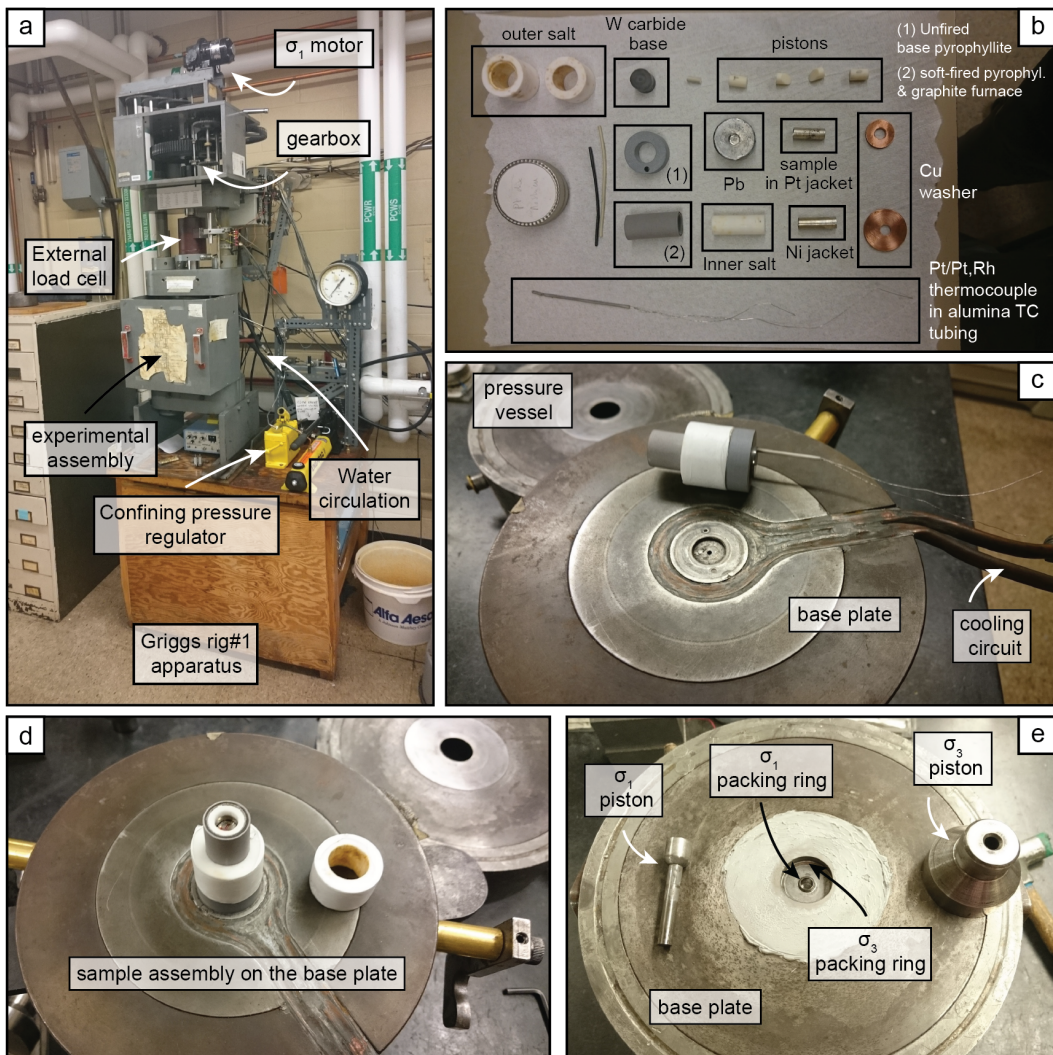


Figure 5.7: (a) Photographs of (a) the press Griggs apparatus during an experiment; (b) the pieces forming the sample assembly; (c-d) the base plate with its water cooling circuit; (e) the base plate with the axial and shear pistons



---

# 6 Discussion générale

Dans ce chapitre, nous présenterons les principaux résultats des différents axes de travail de cette thèse. Nous discuterons ensuite de leurs implications dans la dynamique de (dé)formation, d'accrétion et d'exhumation des semelles métamorphiques en lien avec la base de l'ophiolite sus-jacente à travers la présentation d'un nouveau modèle évolutif intégré de mise en place d'une zone de subduction océanique. La dernière partie s'attachera à discuter des implications de notre modèle sur la géodynamique régionale du système subduction-obduction omanais au moment de son initiation.

## 6.1 Synthèse des résultats pétrologiques et structuraux

### 6.1.1 Nouvelles structure et conditions P–T des semelles métamorphiques de haute température

Sur la base des observations structurales, de l'existence de contrastes marqués dans la composition et dans les assemblages minéralogiques et de nouvelles estimations P–T, nous avons mis en évidence trois grandes discontinuités au sein des semelles métamorphiques situées sous l'ophiolite de Semail (Oman, UAE). Ces grandes discontinuités définissent les contours d'unités métamorphiques dont les conditions P–T ont été estimées respectivement à  $850^{\circ}\text{C} - 1\text{ GPa}$  et  $725^{\circ}\text{C} - 0.8\text{ GPa}$ . pour les unités supérieures (HTa) et intermédiaires (HTb). L'unité basale (BT), essentiellement composée de métasédiments, a été peu étudiée dans le cadre de ce travail de thèse. Toutefois, la mesure d'une température de  $535 \pm 25^{\circ}\text{C}$  par thermométrie Raman sur matière carbonée a permis de confirmer le métamorphisme subi dans le faciès des schistes verts représente bien un maximum de P-T et non un épisode rétrograde. Par ailleurs, de par sa structure extrêmement replissée et sa minéralogie relativement pauvre, il est difficile de déterminer si cette unité résulte, comme l'unité HT, de l'empilement successif de sous-unités avec des conditions P–T différentes. L'analyse thermométrique systématique de la matière organique le long de cette unité pourrait permettre d'apporter une première réponse.

---

Nous avons ainsi apporté significativement précisé la structure thermique des semelles métamorphiques, qui était un des premiers enjeux de ce travail de thèse. **Les résultats de notre étude pétro-structurale montrent que le gradient thermique apparent très élevé calculé dans les semelles métamorphiques ( $\leq 1000$  °C/km; Hacker & Mosenfelder, 1996) n'est probablement pas continu mais plutôt la conséquence de l'accrétion et l'exhumation de multiples unités homogènes en P-T.** Dans cette hypothèse, les semelles métamorphiques ne résultent donc pas d'un unique et simple épisode de réchauffement par transfert de chaleur depuis les péridotites de la plaque supérieure, comme proposé précédemment (Ghent & Stout, 1981, Boudier et al., 1988, Hacker & Mosenfelder, 1996).

D'autre part, la construction de pseudosections à l'aide d'un nouveau modèle de fusion partielle dans le système des métabasites (Green et al., 2016) nous a permis d'affiner les estimations barométriques pour les unités de plus haut grade métamorphique (à grenat + clinopyroxene). Les conditions calculées (autour de 1 GPa) sont cohérentes avec les estimations obtenues avec des méthodes thermo-barométriques multi-équilibres (Searle & Cox, 2002, Cowan et al., 2014) et la présence de disthène à Khubakhib (Gnos, 1992, 1998). **Les zonations chimiques observées dans les grenats nous ont également permis de définir pour la première fois un chemin P-T prograde pour les unités de plus haute température des localités de Sumeini et Khubakhib.** Ces zonations confirment une formation et une exhumation suffisamment rapides pour empêcher l'homogénéisation chimique des cristaux par diffusion, en dépit de températures élevées (i.e.,  $\geq 800$  °C). L'hypothèse d'une **exhumation rapide** des semelles métamorphiques avait déjà été avancée dans la littérature afin d'expliquer la conservation du gradient thermique calculé.

Compte tenu de l'importante déformation associée aux nombreux changements de phases (et donc de volume) enregistrés par les semelles métamorphiques, et de la mise en évidence d'unités distinctes, marquées par des conditions P-T homogènes, les pressions calculées ne résultent probablement pas d'une surpression tectonique. La présence sous d'autres ophiolites de semelles métamorphiques clairement affectées par une rétromorphose dans le faciès des schistes bleus, comme en Turquie ( $\sim 1.2$  GPa –  $425$  °C ; Plunder et al., 2016) est une confirmation supplémentaire de l'enfouissement à des profondeurs significatives des semelles métamorphiques.

Nos estimations barométriques montrent que les semelles métamorphiques de plus haut grade métamorphique de l'ophiolite de Semail se forment vraisemblablement toutes à une profondeur équivalente (soit environ 30–35 km, en régime lithostatique), et ceci indépendamment de leur position structurale sous l'ophiolite. En effet, si les unités de

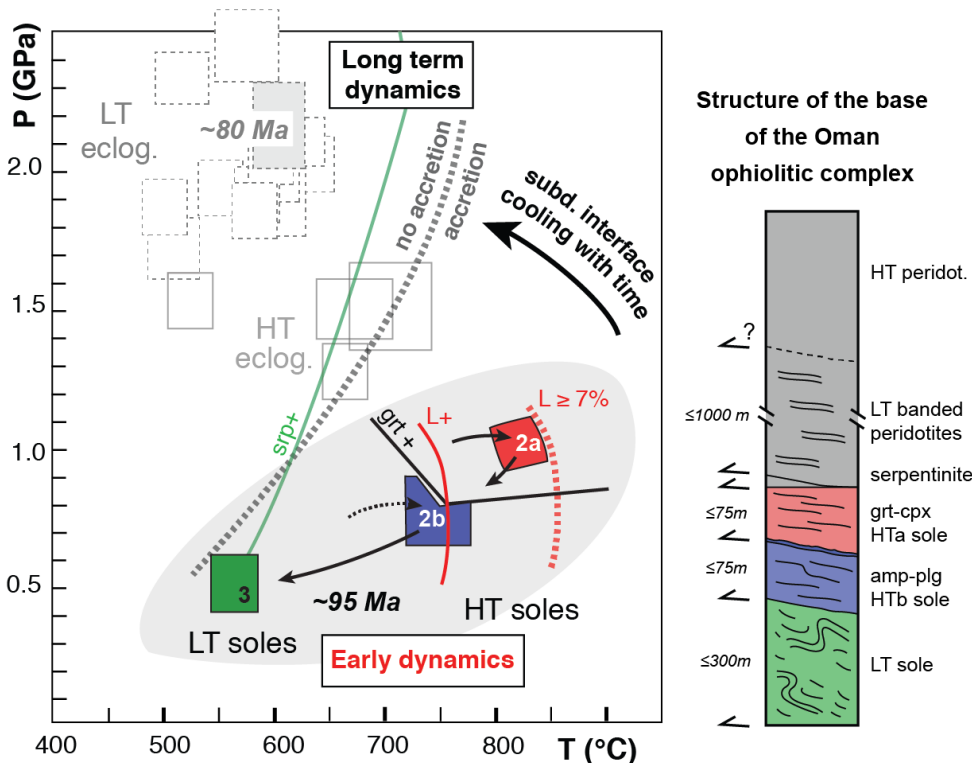


Figure 6.1: Compilation des conditions P–T des semelles métamorphiques de haute et basse températures estimées au cours de cette étude. L'enveloppe grisée représente les estimation P–T des semelles métamorphiques à l'échelle mondiale, telles que recensées dans ce travail (voir aussi Agard et al., 2016, en annexes). Ces conditions sont comparées aux conditions P–T des roches de HP–BT (ici les éclogites) formées plus tardivement dans l'histoire des subductions.

Khubakhib et de Sumeini situées au nord sont positionnées au front de propagation de l'ophiolite, celle de Wadi Tayin affleure au sud en arrière de ce front. Combinés aux estimations de température, ces résultats suggèrent l'existence d'un régime thermique (donc potentiellement d'un environnement géodynamique) initial très similaire entre le nord et le sud de l'ophiolite : aux mêmes pressions, en effet, les températures sont équivalentes latéralement, soit de part et d'autre de la région du Semail gap. Ces résultats renforcent l'hypothèse d'une exhumation rapide et précoce des semelles métamorphiques de haute température, qui n'ont pas été affectées par le refroidissement du régime thermique de la subduction.

Par ailleurs, au moyen des pseudosections (calculées dans un système dépourvu d'eau libre), nous avons pu modéliser pour la première fois le volume de fusion partielle attendu au maximum de température atteint par les unités de plus haut grade métamorphique. Celui-ci demeure inférieur à 6% dans les trois localités étudiées. Ce résultat est cohérent avec les estimations (entre 5 et 10%; Searle & Malpas, 1982, Boudier et al., 1988, Hacker & Gnos, 1997, Searle & Cox, 1999) préalablement réalisées à partir d'observations de

---

terrain. Il est également cohérent avec la faible proportion de liquide silicaté reporté dans les bandes mylonitiques des péridotites sus-jacentes, contemporaines de l'accrétion des semelles métamorphiques. On estime en effet que l'extraction de liquide silicaté est activée lorsque celui-ci devient interconnecté (Maaløe, 1982), au-delà d'un seuil de 5 à 10 vol% (Vanderhaeghe, 2009).

### 6.1.2 Mécanismes de déformation des amphibolites et couplage mécanique à l'interface des plaques

L'étude micro-structurale des unités de haute température a permis de quantifier l'importante déformation subie par les semelles métamorphiques lors de leur mise en place. Nous avons identifié deux étapes majeures de déformation dans la dynamique d'accrétion et d'exhumation des amphibolites des unités de haute température. Ces deux étapes correspondent à différents mécanismes de (dé)formation, qu'il est possible d'associer à une évolution continue de la thermicité et du couplage mécanique à l'interface des plaques en cours de refroidissement après l'initiation de la subduction. Ce travail apporte donc de nouvelles contraintes sur la mécanique précoce des zones de subduction océanique à l'interface des plaques.

**Étape 1 :** à  $850 \pm 50^\circ\text{C}$  –  $0.9 \pm 0.1 \text{ GPa}$ , les amphibolites à grenat-clinopyroxène (HTa) sont accrétées aux péridotites de la plaque supérieure. Les roches de cette unité sont essentiellement composées d'amphibole ( $\geq 40\text{-}50\%$ ). Le plagioclase est quant à lui présent en faible proportion ( $\leq 10\%$ ). Les grains de grenat et de clinopyroxène sont boudinés, indiquant que ces deux phases sont plus résistantes que l'amphibole, et que celle-ci contrôle probablement l'essentiel de la déformation. Les grains d'amphiboles montrent à la fois un rapport de forme élevé, une forte réduction de taille des grains et une orientation préférentielle très importante dans le plan de foliation. Au travers de l'étude micro-structurale nous avons mis en évidence que cette fabrique résulte de la combinaison polycyclique d'une déformation cassante et d'un alignement rigide des grains parallèlement à la direction de cisaillement principal. Nous suggérons donc que les grains d'amphibole sont encore rigides et cassants à haute température. Cependant ils restent moins résistants que les clinopyroxènes et les grenats. Entre les grains d'amphiboles les grains de clinopyroxène boudinés se déforment essentiellement par fluage dislocation et le développement de sous-grains. Les grains de grenats présentent souvent une forme ellipsoïdale, témoin de leur cristallisation syn-cinématique. Ils forment également des boudins, parfois fracturés, avec des évidences de rotation rigide.

**Étape 2 :** à  $725 \pm 50$  °C –  $0.8 \pm 0.1$  GPa, l'unité amphibolitique à plagioclase (grenat et clinopyroxène absents; HTb) est accrétée à la plaque supérieure alors que l'amphibolite à grenat-clinopyroxène est en cours d'exhumation et de refroidissement. Cette dernière est affectée par une forte rétromorphose (notamment à sa base) caractérisée par la cristallisation de plagioclase et d'amphibole secondaires. Nous avons mis en évidence que ces deux phases cristallisent essentiellement par processus de précipitation-dissolution. Avec l'augmentation de la proportion de plagioclase dans la matrice, les amphiboles sont de plus grande taille et moins fracturées : elles peuvent désormais s'orienter plus facilement dans une matrice devenue moins visqueuse. L'analyse des mécanismes de déformation du plagioclase a été plus difficile à réaliser en raison de leur forte altération par séricitisation. Ils sont caractérisés par une faible fabrique (Satsukawa et al., 2013, de type *Axial-A*;) qui semble être le résultat d'une déformation par fluage dislocation suivant les systèmes de glissement (001)[100].

Berger & Stüntz (1996) ont montré que l'alignement des amphiboles parallèlement à la direction de cisaillement principale entraîne un affaiblissement considérable de la roche encaissante. De plus, l'augmentation modale du plagioclase, au dépend de phases beaucoup plus résistantes que sont le clinopyroxène et le grenat, a probablement pour effet d'accentuer cet affaiblissement à plus faible température (dans l'amphibolite à grenat-clinopyroxène lors de son exhumation et dans l'amphibolite à plagioclase lors de son accrétion). Par ailleurs, la fabrique très forte des amphiboles (quantifiée par la mesure du J index) suggère un amincissement important des unités amphibolitiques à grenat et clinopyroxene lors de leur accrétion à la plaque supérieure. La comparaison avec des études précédentes sur des amphibolites expérimentales et naturelles (Tatham et al., 2008, Homburg et al., 2010, Getsinger et al., 2013) suggère des facteurs d'amincissement supérieurs à 5, voire 10.

Les périclases mylonitisées de la base de l'ophiolite sus-jacente présentent une évolution continue et localisante de la déformation (Boudier et al., 1988, Michibayashi & Mainprice, 2004, Linckens et al., 2011, Herwegen et al., 2016) depuis des stades protomylonitiques ( $\sim 900$  °C) à ultramylonitiques ( $\leq 700$  °C; Linckens et al., 2011, Herwegen et al., 2016). Cette localisation progressive de la déformation est associée à une augmentation graduelle des infiltrations de fluides dans un système en refroidissement. L'évolution continue et les températures associées aux déformations à la base des périclases sont donc analogues à celles que nous avons décrites dans les amphibolites de la semelle métamorphique.

Il faut pourtant souligner ici à quel point les modalités précises d'accrétion (et *pro parte* d'exhumation) des semelles métamorphiques ont été jusqu'à présent peu étudiées et restent imprécises.

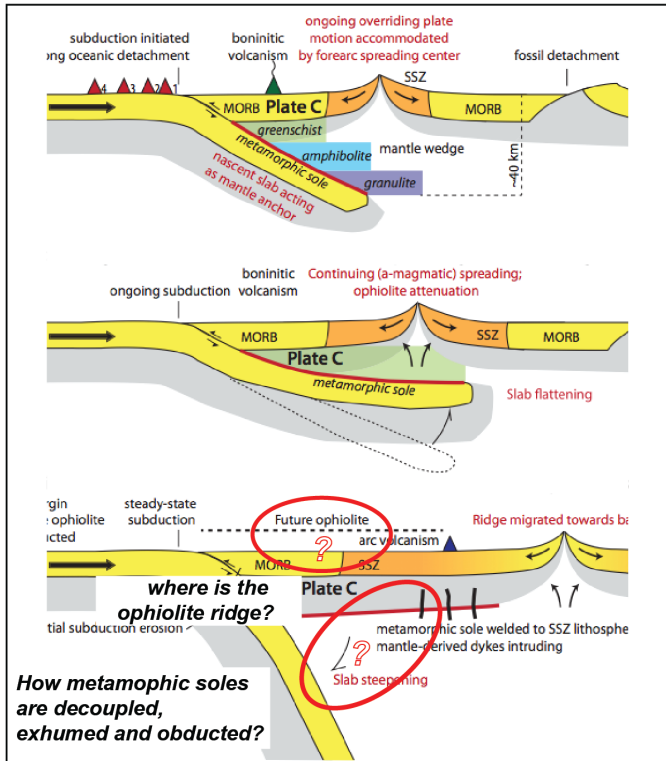


Figure 6.2: Modèle de subduction intra-océanique avec une initiation sur un détachement proche d'une ride de type MOR, (Figure modifiée d'après Van Hinsbergen et al., 2015)

Ceci peut être illustré par un des plus récents modèles d'initiation d'un système subduction-obduction, proposé par Van Hinsbergen et al. (2015). Si ce modèle intègre la formation des semelles métamorphiques et leurs conditions P-T approximatives pour contraindre l'environnement thermique de la zone de subduction lors de son initiation (i.e., sur un détachement océanique situé à proximité de la ride ; Figure 6.2), l'évolution de l'ophiolite est ensuite déterminée au travers de l'interprétation de signatures géochimique des laves de sa partie crustale... et les semelles semblent se déplacer mystérieusement d'une étape à l'autre. Rappelons que la seule explication avancée jusque-là est celle d'un réchauffement des semelles par le manteau sus-jacent, "jeune" et chaud : aucune explication dynamique n'existe quant au détachement, à l'accrétion de ces écailles, et leur empilement systématique en semelles (HT sur LT), de surcroît à des conditions quasiment invariantes. Leur exhumation rapide dans l'histoire de la subduction, l'écart qui existe entre les pressions estimées pour les unités de plus haute température et les épaisseurs actuelles des ophiolites restent également énigmatiques, tout comme les modalités de l'obduction finale qui doivent être caractérisées par un important niveau de décollement à la base des semelles métamorphiques.

## 6.2 Un modèle conceptuel d'évolution : accrétion et exhumation des semelles métamorphiques

Nous proposons ici un modèle d'évolution pétrologique et structurale intégré des modalités de formation des semelles métamorphiques, en lien avec l'évolution thermo-mécanique des péridotites basales de l'ophiolite sus-jacente (Figure 6.4).

La compilation pétro-structurale réalisée sur les semelles métamorphiques mondiales montre des disparités systématiques à l'échelle mondiale entre les unités de haute température (de faciès amphibolitique à granulitique, et principalement métabasiques) et de basse température (de faciès schistes verts et principalement métasédimentaires; Figure 6.1). De plus, l'ensemble des résultats de notre étude intégrée montre que la structuration séquentielle des semelles métamorphiques peut être plus complexe, avec l'existence de sous-unités dans la semelle de haute température présentant une lithologie et des conditions P-T différentes. L'étude micro-structurale a également montré que les étapes d'accrétion et d'exhumation de ces unités sont accompagnées d'une importante déformation, compatible avec un fort facteur d'amincissement et cohérente avec celle des péridotites mylonitiques sus-jacentes (Linckens et al., 2011, Herwegh et al., 2016).

Ces résultats, combinés aux lois rhéologiques existantes pour les différents matériaux mis en jeu (cf. chapitre 2.3.2; Figure 6.3b), fournissent des contraintes essentielles pour élaborer ci-dessous un modèle général de formation des semelles métamorphiques, en lien avec l'évolution des péridotites basales de l'ophiolite sus-jacente. Ce modèle apporte un éclairage nouveau sur les modalités d'accrétion et d'exhumation des roches à l'interface des plaques, et permet de préciser les processus thermo-mécaniques accompagnant le développement des zones de subduction intra-océanique.

### 6.2.1 Accrétion de la semelle amphibolitique à grenat-clinopyroxène : première "*inversion rhéologique*" à l'interface de la subduction

La formation des semelles métamorphiques résulte de l'initiation d'une subduction océanique (Boudier et al., 1988, Hacker, 1994, Maffione et al., 2015), dans un régime thermique élevé (puisque la plaque plongeante atteint environ 800 °C vers 30 km de profondeur), relativement loin d'une marge continentale et de ses apports terrigènes. Au moment de l'initiation de la subduction, le sommet de la plaque plongeante est donc essentiellement composé de basaltes, la couverture sédimentaire étant réduite sinon absente. La rhéologie de l'interface de subduction naissante est donc alors contrôlée par celles des basaltes et celles des péridotites de la plaque supérieure.

---

Dans les toutes premières étapes de la subduction, la partie crustale de la plaque plongeante est initialement froide et rigide. Elle pénètre facilement dans un manteau froid et serpentiniisé (donc mécaniquement faible; Figure 6.3a,b). Puis, au cours de son enfouissement, la croûte se réchauffe et s'affaiblit mécaniquement. Dans le même temps, elle se heurte à un manteau de plus en plus rigide (car plus chaud et anhydre; Figure 6.3a), qui constitue donc un butoir de plus en plus efficace. Le contraste de viscosité à l'interface de subduction, initialement très important, diminue progressivement jusqu'à s'inverser (Figure 6.3b). À une certaine profondeur (et température), la croûte de la plaque plongeante rencontre alors **momentanément** un manteau de même rigidité : cette résistance, qui se traduit par un fort couplage mécanique à l'interface des plaques, détermine la formation d'écaillles.

La première portion de la plaque plongeante accrétée aux péridotites de la plaque supérieure est composée de basaltes métamorphisés à amphibole + grenat + clinopyroxène ± rare plagioclase (Figure 6.4a). L'analyse micro-structurale de cette unité et de nos échantillons expérimentaux a mis en évidence que le grenat et le clinopyroxène sont des phases mécaniquement très résistantes, bien plus que le plagioclase et l'amphibole. L'augmentation croissante du mode de clinopyroxène et de grenat, combinée à la diminution de celle du plagioclase, au sommet de la plaque plongeante entraîne son durcissement et donc une modification de la pente de sa courbe de viscosité (courbe rouge; Figure 6.3b). **La première "inversion rhéologique" à l'interface des plaques apparaît alors probablement à légèrement plus haute température, autour de 850 °C et ~ 1 GPa comme le suggèrent nos estimations pour la semelle amphibolitique à grenat-clinopyroxène.**

Ce cadre interprétatif, s'il est correct, comporte deux conséquences importantes pour l'avenir du couplage à cette profondeur de 30 km, sachant qu'en refroidissant le manteau va devenir mécaniquement plus faible avec le temps :

- aucun couplage avec des portions de croûte aussi rigides n'est possible à plus faible profondeur, où l'on peut prévoir que seules des portions mécaniquement plus faibles pourront être accrétées;
- on peut imaginer que le slab, en poursuivant sa course plus profondément (à plus haute température), rencontrera un manteau plus dur, et pourrait être écaillé. Pourquoi n'en est-il rien (puisque on ne retrouve pas de semelles plus "chaudes") ?

Nous proposons que l'accrétion de cette première sous-unité de semelle métamorphique est en réalité limitée à plus haute température par une réaction importante : la fusion partielle des métabasaltes. Les résultats de notre étude pétro-structurale montrent en effet que les semelles métamorphiques accrétées et exhumées contiennent une fraction de

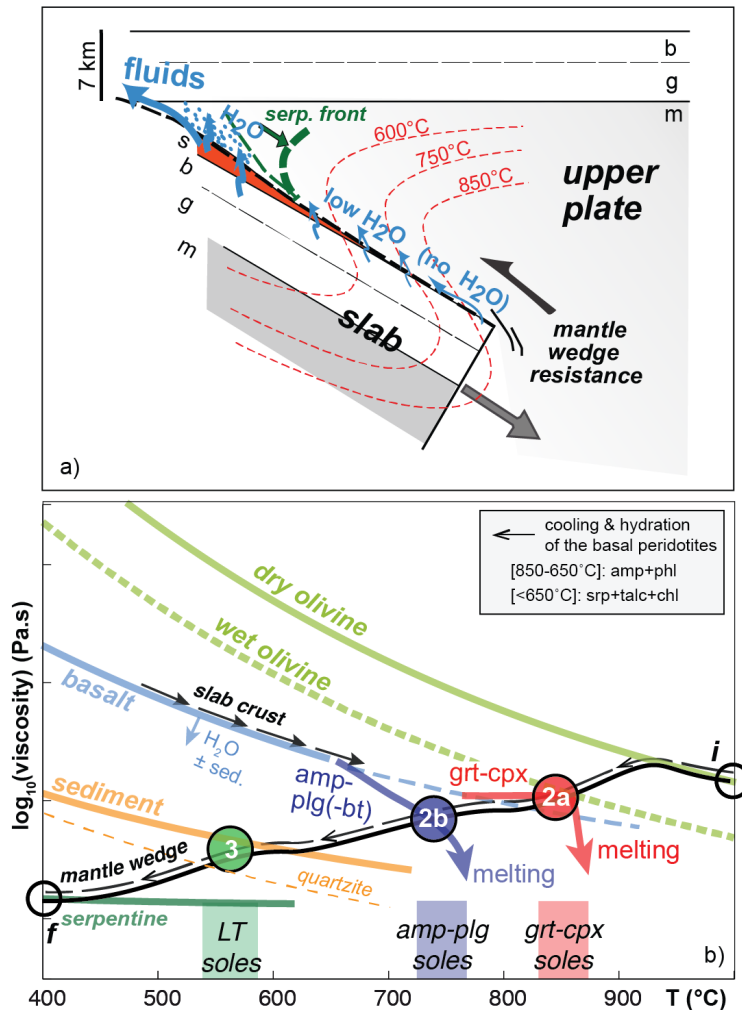


Figure 6.3: a) Schéma en deux dimensions illustrant la déshydratation importante de la plaque plongeante peu de temps après l'initiation de la subduction. La ligne verte en pointillés représente la limite de stabilité de la serpentine. Les points bleus représentent le domaine affecté significativement par la serpentisation. L'hydratation du coin de manteau diminue avec la profondeur (et la température); s : sédiment; b : basalte; g : gabbro; m : péridotite mantellique. b) schéma illustrant les sauts de viscosité à l'interface de subduction responsables des accrétions des différentes unités structurant les semelles métamorphique. L'évolution des viscosités de la croûte basaltique métamorphisée à haute température (à grenat-clinopyroxène en rouge, ou à amphibole-plagioclase en bleu) est donnée qualitativement.

liquide silicaté toujours inférieure à 6%. Il a été démontré qu'au delà de cette fraction, la viscosité de la roche encaissante chute dramatiquement (flèche rouge; Figure 6.3b; Rosenberg & Handy, 2005). Nous proposons donc que ce seuil de 7% de fusion partielle au sommet de la croûte subductée correspond au seuil limitant l'accrétion des semelles métamorphiques de haute température.

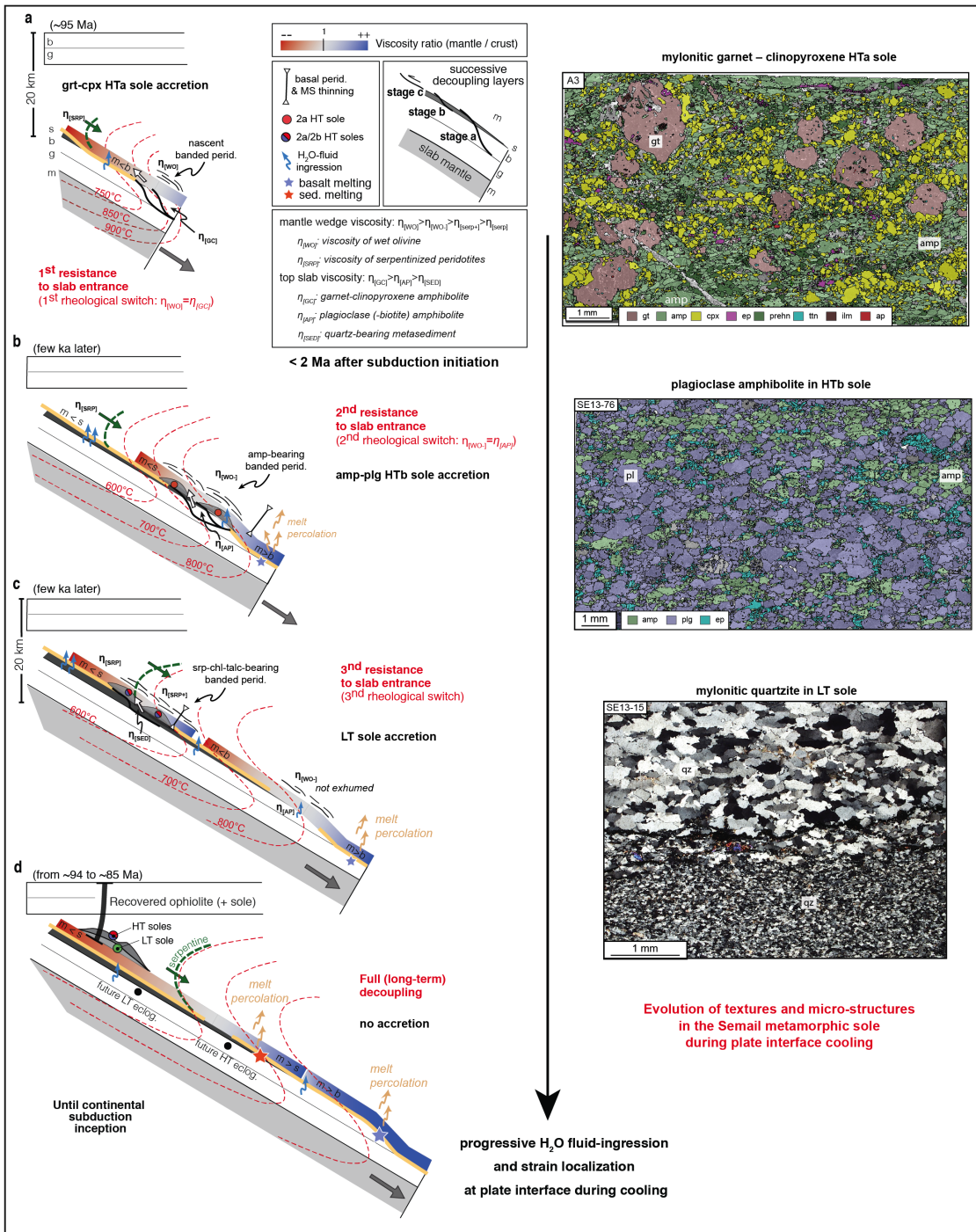


Figure 6.4: Modèle évolutif de formation des semelles métamorphiques par les accréations successives de différentes portions écaillées de la plaque pongoante issues de changements rhéologiques majeurs à l'interface des plaques dans un régime thermique en cours de rééquilibrage. En parallèle sont représentées des textures de déformation minérales caractéristiques de chaque unités de semelles métamorphiques dé(formées) à différentes conditions P-T et avec une viscosité différente.

Au delà de ce seuil, la plaque plongeante est découpée totalement des péridotites de la plaque supérieure. Le liquide silicaté, tonalitique à dioritique, serait interconnecté et

pourrait percoler (assisté par la déformation) au travers de la plaque supérieure, refertilisant les péridotites de la plaque supérieure.

### 6.2.2 Accrétion de la semelle amphibolitique à plagioclase ± biotite : seconde "*inversion rhéologique*" à l'interface de subduction

Alors qu'initialement la plaque plongeante est relativement peu hydratée, l'arrivée en subduction d'une proportion plus importante de sédiments a pour conséquence de favoriser les réactions hydratées à l'interface des plaques. Les champs de stabilité de l'amphibole, du plagioclase et des micas augmentent. L'augmentation modale de ces phases entraîne un affaiblissement de la plaque plongeante à l'interface des plaques. Dans le même temps, les péridotites de la plaque supérieure se refroidissent et des phases hydratées (essentiellement amphibole et phlogopite) cristallisent. **À une profondeur donnée, la viscosité du manteau diminue progressivement avec la ré-équilibration thermique de la subduction.** L'écaillage n'est donc que transitoire, pour une lithologie donnée. **L'accrétion de la semelle amphibolitique à plagioclase (HTb) suggère qu'un nouvel épisode de convergence des viscosités des péridotites refertilisées et de la croûte amphibolitisée à l'interface des plaques** (Figure 6.4b), vers  $725 \pm 50^\circ\text{C}$  et  $\sim 7\text{-}8 \text{ GPa}$ , comme illustré sur la figure 6.3b.

Par ailleurs, à la fois à Khubakhib et Sumeini, la semelle amphibolitique à plagioclase est limitée à son sommet par un niveau très déformé et dont la nature, riche en quartz et micas, diffère totalement des métabasaltes sous-jacents. S'il peut être expliqué par des circulations de fluides alcalins importants à l'interface entre les deux sous-unités de haute température (comme interprétés par Jamieson & Strong, 1981, à Terre Neuve), il pourrait également représenter l'ancienne couverture sédimentaire de la plaque plongeante (compte-tenu de sa nature et de sa position structurale). Dans cette deuxième hypothèse, la présence de ces métasédiments peut avoir été un facteur déterminant dans la localisation de la déformation et l'accrétion de la seconde sous-unité (principalement d'affinité crustale). En effet, une augmentation de la proportion de sédiment, comme celle de l'activité d'eau, a pour séquence de diminuer la viscosité générale des roches encaissantes, principalement d'affinité crustale (courbe bleue vs. courbe orange; Figure 6.3b).

Enfin, dans cette unité plus riche en métasédiments (moins réfractaires à la fusion que les roches crustales), le volume de fusion partielle est probablement un facteur limitant d'accrétion à haute température, comme nous l'avons déjà évoqué pour l'unité de plus haute température. Comme montré précédemment, au-delà d'un seuil de 7% de liquide silicaté

---

dans la roche encaissante, la viscosité de cette dernière chute dramatiquement, empêchant tout couplage mécanique avec la plaque supérieure (cf. flèche bleue; Figure 6.3b).

### 6.2.3 Accrétion de la semelle de faciès des schistes verts : troisième (et dernière ?) "*inversion rhéologique*" à l'interface de subduction

Au cours de la subduction, l'interface de subduction continue de se refroidir et de s'hydrater, ce qui entraîne peu à peu les péridotites de la plaque supérieure vers la serpentinitisation. La viscosité de cette dernière devient inférieure à celles des basaltes (Figure 6.3b) et converge vers celle des métasédiments. L'accrétion de la semelle métamorphique de basse température, essentiellement composée de métasédiments, suggère que la résistance du manteau a diminué suffisamment pour devenir similaire à celle des sédiments de la couverture de la plaque plongeante. La limite de haute température du champ de stabilité de la serpentine semble donc bien être un paramètre essentiel à la troisième "*inversion rhéologique*" à l'interface des plaques (Figure 6.4c).

L'accrétion de cette unité principalement composée de métasédiment indique également que le couplage mécanique et la déformation associée à l'interface de subduction sont plus localisés. L'écaillage est désormais plus superficiel, restreint à la couverture de la plaque plongeante, la viscosité de la partie crustale étant devenue bien plus importante que celles du coin de manteau à cette profondeur (Figure 6.3b).

~ 1-2 Ma après l'initiation, le régime thermique de la subduction atteint finalement un état d'équilibre, le long d'un gradient de HP-BT. Les péridotites serpentinitisées de la plaque supérieure forment désormais un coin de manteau hydraté bien plus faible mécaniquement que les sédiments entrant en subduction (Escartín et al., 2001). L'interface des plaques est durablement découpée. Ceci pourrait aussi expliquer pourquoi les roches de haute pression basse température qui se développent à l'interface de subduction dans le champ de stabilité de la serpentine sont finalement rarement accrétées et exhumées (Figure 6.4d).

### 6.2.4 Accrétion, amincissement et exhumation : une distribution ubiquiste sous l'ophiolite

Dans le modèle que nous proposons, les accrétions successives résultent de changements de viscosité entre le sommet de la plaque plongeante (composé de métabasalte puis de métasédiment) et la base de la plaque supérieure (composée de péridotites). Si chaque unité de semelles métamorphiques (haute comme basse températures) peut se trouver di-

rectement en contact avec les périclases (Gnos, 1992), aucune étude ne rapporte l'existence de périclases entre les différentes unités des semelles métamorphiques. De plus, lorsque la séquence est complète, les semelles métamorphiques de haute température sont toujours au-dessus des semelles de basse température. Pour répondre à cette problématique, deux situations de couplage mécanique sont proposées :

- entre la base du manteau et la plaque inférieure. Le manteau situé au-dessus de la nouvelle unité accrétée est tectoniquement découpé de celle-ci lors de l'exhumation de l'unité précédemment accrétée.
- le couplage peut également avoir lieu directement entre la plaque inférieure et les unités précédemment accrétées et exhumées (qui forment alors la nouvelle base de la plaque supérieure). Cette hypothèse plaide en faveur d'une exhumation précoce et conjointe des semelles métamorphiques de haute température avec les périclases rubannées de la base de l'ophiolite sus-jacente. Ce couplage peut être alors expliqué par l'importante rétromorphose affectant la base de ces dernières qui entraîne la diminution progressive de leur viscosité. Cette situation est notamment compatible avec l'hypothèse d'une exhumation par amincissement progressif de l'ensemble de la base de la plaque supérieure.

Nous proposons également que **la distribution quasiment ubiquiste des semelles métamorphiques sur plusieurs dizaines de kilomètres sous l'ophiolite de Semail (Figure 6.5) résulte de son amincissement (et donc de l'étalement) précoce et important à l'interface de subduction**. Celui-ci, d'un facteur potentiellement supérieur à 5 voire à 10, a débuté lors de leur accrétion aux périclases (de la future ophiolite obductée) et s'est développé jusqu'à leur exhumation finale. Les amphiboles se déformant de manière cassante à haute température, nous pouvons également imaginer que lors de l'épisode d'amincissement et d'étalement sous l'ophiolite, des unités de semelles métamorphiques continues peuvent avoir été morcellées. Ceci pourrait notamment expliquer la présence discontinue des affleurements de chacune des unités sous l'ophiolite obductée (Figure 6.5).

Le modèle que nous proposons pourrait être affiné en contraignant mieux les points ou aspects suivants :

- la quantité d'amincissement de la semelle métamorphique, qui reste à ce stade encore inconnue. L'absence de gradient thermique continu à l'intérieur de chaque unité favorise plutôt l'hypothèse d'accrétion d'écaillles d'épaisseur réduite. De même, la quasi-absence de gabbros dans la semelle métamorphique limite l'épaisseur maximale de chaque unité à celle de la paléo-couverture basaltique de la croûte océanique subductée.

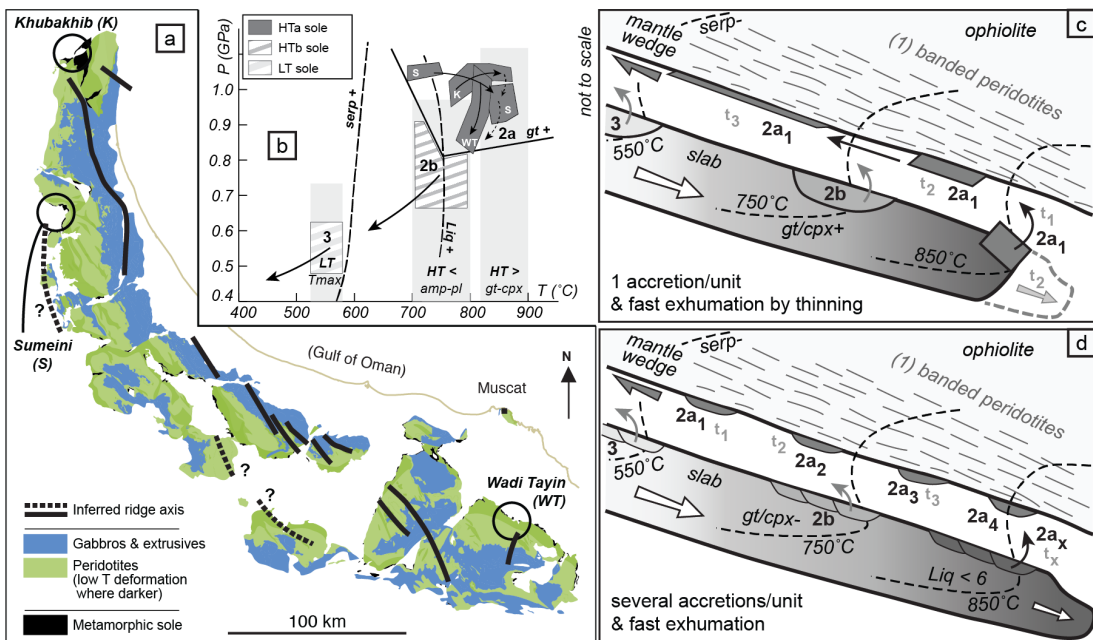


Figure 6.5: (a) Carte géologique simplifiée de l'ophiolite de Semail (Oman, UAE) avec la position de sa ride et de sa semelle métamorphique sous-jacente ubiquiste. (b) Compilation des conditions P–T estimées dans notre étude pour chaque écaille de semelle métamorphique dans les localités de Khubakhib (K), Sumeini (S) et Wadi Tayin (WT). (c) et (d) modèles évolutifs opposés de (dé)formation et d'exhumation des semelles métamorphiques expliquant leur distribution ubiquiste sous l'ophiolite : (c) une seule écaille par unité est accrétée qui est ensuite ultra amincie lors de son exhumation; (d) plusieurs écailles par unités sont accrétées et exhumées rapidement sans grande déformation.

- le rôle des nombreuses hétérogénéités de la séquence crustale subductée (par exemple: basalte en coussins vs. complexe filonien vs. gabbro), qui représentent des zones de faiblesse mécanique pouvant limiter l'accrétion d'unités très épaisses.
- la vitesse de diffusion de la chaleur et/ou le shear heating, qui reste un phénomène relativement lent pouvant introduire par les réactions métamorphiques associées des zones de faiblesses à la surface de la plaque subductée.

Puisque le saut de pression entre les semelles amphibolitique à grenat-clinopyroxène et plagioclase est d'environ 0.2 à 0.4 GPa, soit une différence 5 et 10 km de profondeur de formation, on peut envisager qu'il résulte de l'un des deux processus suivants:

- **une exhumation relative de l'ensemble de la base de l'ophiolite sus-jacente** (semelle amphibolitique à grenat-clinopyroxène ET périclases mylonitisées) par rapport au reste de la séquence ophiolitique ;
- **un amincissement progressif de la base des périclases.** Considérant l'épaisseur actuelle totale de l'ophiolite (15-20 km) et celle kilométrique des périclases mylonitisées, un amincissement d'un facteur ~ 4-5 est proposé. Il est intéressant d'observer que l'expérience en laboratoire simulant l'interface de sub-

duction reproduit au premier ordre le différentiel d'amincissement proposé ici entre les péridotites et les amphibolites (Figure 6.6).

En l'absence d'estimation de pression à travers les péridotites de l'ophiolite, il est cependant, à ce stade, difficile d'estimer la part de ces deux processus dans l'exhumation du complexe basale de l'ophiolite de Semail.

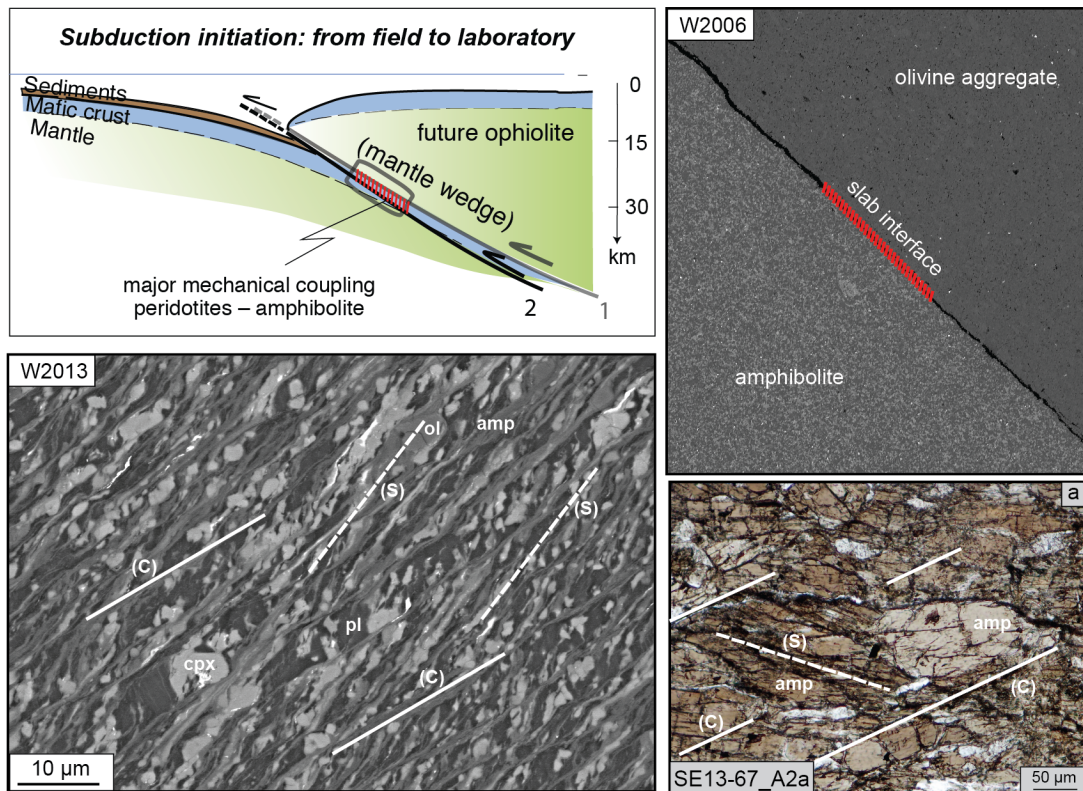


Figure 6.6: Illustration du couplage mécanique et des déformations associées à l'interface croûte-manteau lors de l'initiation de la subduction : du terrain (avec la semelle métamorphique) au laboratoire (avec des exemples d'expérience que nous avons menées).

### 6.3 Implications pour la genèse des ophiolites

Le modèle que nous proposons apporte de nombreuses précisions sur les modalités d'accrétion et d'exhumation des semelles métamorphiques. En premier lieu, il suggère que les semelles métamorphiques ne se forment pas sous l'effet d'un "coup de chaud" (type fer à repasser) par transfert de chaleur depuis des périclases jeunes et chaudes de la plaque supérieure (ce qui serait analogue à un métamorphisme de contact). La plaque plongeante se réchauffe progressivement au cours de son enfouissement, certes au contact de périclases plus chaudes (car situées à plus grande profondeur) mais en refroidissement.

**Les semelles métamorphiques témoignent en réalité d'accrétions successives issues de changements rhéologiques majeurs à l'interface des plaques dans un régime thermique en cours de ré-équilibration.** La plaque plongeante doit surtout vaincre, dans son enfance ("infancy"; Agard et al., 2016), la résistance transitoire d'un manteau (ou butoir) qui lui arrache des lambeaux tout d'abord très visqueux (les semelles de haute température, principalement métabasiques), puis moins (les semelles de basse température, à métasédiments essentiellement) et enfin n'offre plus aucune résistance, puisque plus aucune unité n'est accrétée (sinon de rares roches de haute pression (voir pour ces aspects la discussion dans notre article ; Agard et al., 2016, en annexes)). Ce modèle apporte donc une nouvelle vision et des contraintes sur la formation des semelles métamorphique mais aussi, à plus grande échelle, sur la nature des ophiolites sus-jacentes.

Or, il existe un grand débat sur la nature et l'origine exactes de l'ophiolite de Semail (Oman, UAE), comme des autres grandes ophiolites obductées. Deux grands modèles géodynamiques s'affrontent pour expliquer les âges et la signature géochimique (controversée) de la partie crustale de l'ophiolite. Leur principale différence réside dans la chronologie relative entre l'accrétion de la lithosphère océanique (la future ophiolite) et l'initiation de la subduction permettant l'obduction de l'ophiolite dans ses stades terminaux.

1. soit la formation de l'ophiolite précède l'initiation de la subduction océanique (Boudier et al., 1985, Nicolas et al., 2000). Dans ce modèle, la subduction est initié proche de la ride, potentiellement sur un détachement d'échelle lithosphérique (Maffione et al., 2015), afin de répondre aux contraintes thermiques imposées par les semelles métamorphiques. L'eau nécessaire pour expliquer la composition des laves (V1) provient alors de circulation de fluides hydrothermaux dans la chambre magmatique (Benoit et al., 1999).

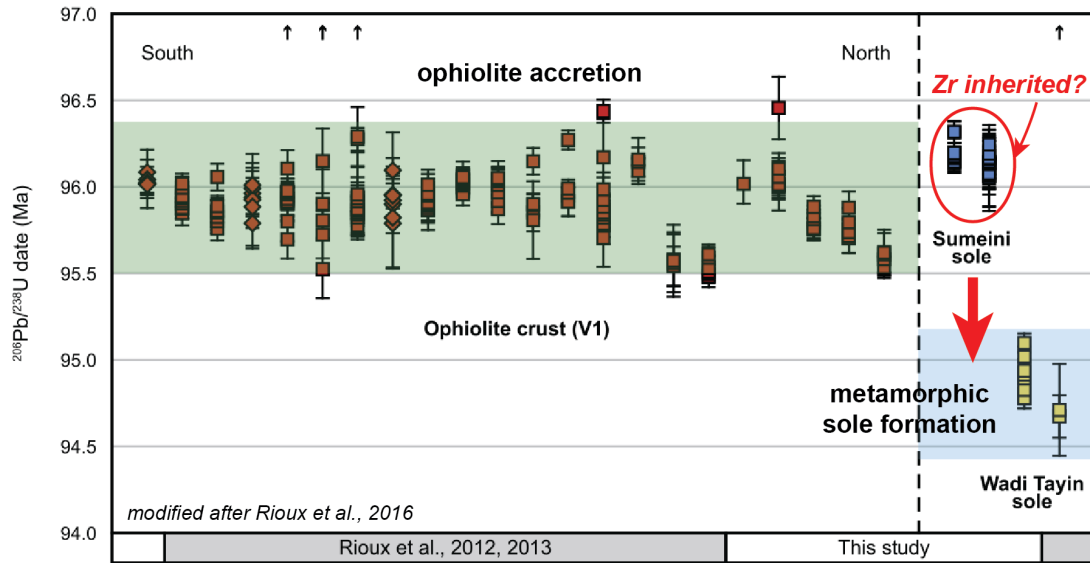


Figure 6.7: Compilation d'âges obtenues par méthode  $^{206}\text{Pb}/^{238}\text{U}$  sur zircons dans la croûte ophiolitique et dans la semelle métamorphique du complexe ophiolitique de Semail (Rioux et al., 2012, 2013, 2016). Le bandeau vert représente la fenêtre moyenne du magmatisme V1 omanais. Le bandeau bleu représente la grande majorité des âges obtenus pour la semelle métamorphique (Hacker et al., 1996, Hacker & Gnos, 1997, Warren et al., 2003).

2. soit la formation de l'ophiolite est la conséquence de l'initiation de la subduction, cette dernière précédant alors la genèse de l'ophiolite (Searle & Cox, 1999, Stern, 2004, Dilek & Furnes, 2009, Whattam & Stern, 2011, MacLeod et al., 2013). C'est le modèle de la subduction spontanée (Stern, 2004, Rioux et al., 2013), dans lequel l'accrétion ophiolitique résulte du retrait de la plaque plongeante. La signature aqueuse du magmatisme (V1; Benoit et al., 1999) est expliquée par la déshydratation de cette plaque plongeante (MacLeod et al., 2013). Ce n'est qu'ensuite, lors de son refroidissement, que la semelle métamorphique est formée. Ni accrétion aux périclites basales, ni son exhumation ne sont toutefois expliquées.

Notre modèle, par les contraintes thermo-mécaniques qu'elles impliquent sur l'évolution de l'interface de subduction, est difficilement compatible avec l'hypothèse d'une accrétion ophiolitique synchrone ou postérieure à la formation des semelles métamorphiques :

- notre étude est compatible avec l'existence d'un couplage mécanique précoce, important et durable (jusqu'à l'obduction) entre les différentes unités de semelles métamorphiques et la base des périclites.
- les accrétions polyphasées des semelles métamorphiques se produisent le long d'une interface en cours de refroidissement, avec une cohérence structurale remarquable (toujours les semelles HT sur BT, pas de manteau entre, et sans indice d'épisode de recuit postérieur à leur formation et exhumation).

- 
- les semelles métamorphiques et la base des périclites déformées et refertilisées de manière synchrone sont composées de phases relativement peu réfractaires à la fusion. Celles-ci auraient probablement fondu dans le cas d'un épisode magmatique suffisamment important pour former une nouvelle lithosphère.

De plus, aucun modèle numérique n'a pu reproduire à ce jour la formation et l'exhumation des semelles métamorphiques dans le cas d'une accrétion synchrone à postérieure de l'ophiolite sus-jacente (voir Duretz et al., 2016). Cette dernière est trop faible mécaniquement et/ou trop chaude pour créer les conditions de couplage mécanique à l'interface des plaques et créer ce saut de l'interface de subduction afin de permettre l'exhumation précoce de la base des ophiolites.

L'hypothèse d'une subduction initiée avant la genèse de l'ophiolite sus-jacente, probablement à proximité d'une ride d'accrétion océanique au vu des températures enregistrées (impliquant donc une lithosphère océanique jeune; Hacker & Gnos, 1997) est donc beaucoup plus cohérente avec notre modèle de formation des semelles métamorphiques et de ses implications. **La plupart des datations effectuées sur les semelles métamorphiques indiquent que leur formation est légèrement postérieure ( $\sim$  1-2 Ma) à la première phase de magmatisme (V1) de l'ophiolite de Semail.** Ces datations plaident donc également en faveur du premier modèle proposé.

Cependant, la plupart d'entre elles présentent une incertitude de mesure suffisamment importante pour ne pas pouvoir trancher définitivement le débat. D'autant plus que récemment, Rioux et al. (2016) ont mesuré à travers des analyses U/Pb sur zircons des âges dans la semelle de haute température de Sumeini antérieurs à la mise en place du magmatisme V1 ( $\sim$ 96  $\pm$  0.5 Ma ; Figure 6.7; Rioux et al., 2013, 2016), ce qui serait plus en faveur du second modèle proposé. Toutefois, ces nouvelles datations doivent être prises avec précaution. Les zircons sont des minéraux extrêmement réfractaires, ils peuvent avoir donné des âges hérités de l'étape d'accrétion océanique. De plus, la température de fermeture des zircons est estimée au-delà de 900 °C (Lee et al., 1997), soit des températures supérieures à celles estimées pour les unités de plus haut grade métamorphiques. La mesure d'âges à 96.5 Ma dans des dykes interprétés comme tardifs de la semelle métamorphique de Sumeini, et d'âges à  $\sim$  95.5 Ma dans la semelle métamorphique de Wadi Tayin sont d'autres indices compatibles avec une hypothèse d'âges pour partie hérités.

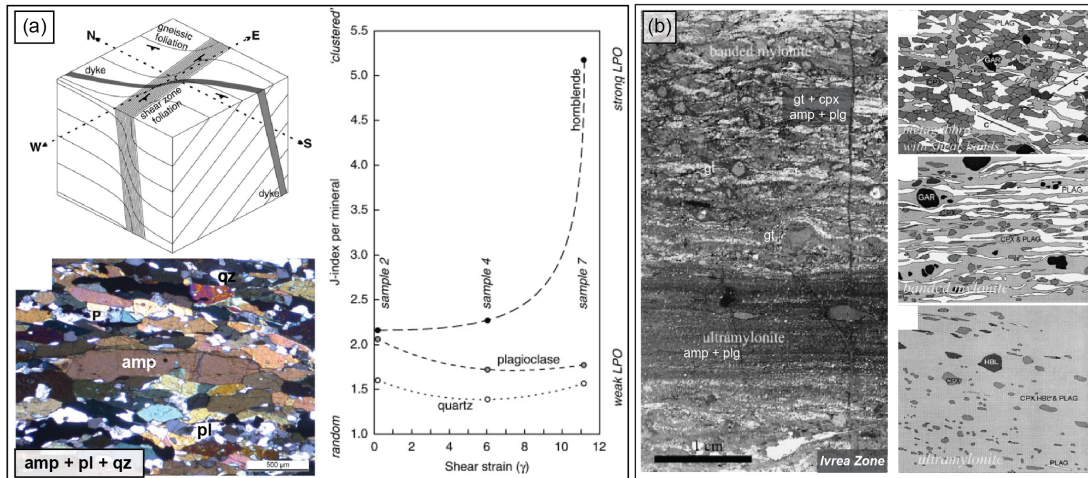


Figure 6.8: (a) Bande de cisaillement amphibolitique (à (60%) amphibole + (30%) plagioclase + (10%) quartz) localisée sur des intrusions basiques en base de croûte continentale (bloc central du Lewisian , NO Ecosse). Une relation directe entre la fabrique des grains amphiboles (Le J index) et la déformation finie est présentée (Tatham et al., 2008). (b) bande de cisaillement mylonitique à ultramylonitique localisée dans dans des métagabbros à amphibole + plagioclase (en blanc) ± clinopyroxène ± grenat (en noir) de base de croûte continentale (Zone d’Ivrée, Italie; Kenkmann & Dresen, 2002). À droite, schématique évolution de la fabrique minérale dans les métagabbros au cours de l’ultra mylonitisation dans un système en cours de refroidissement (de 650 à 500 °C à 0.5 ± 0.1 GPa).

## 6.4 Les implications pour la base de croûte continentale

Le comportement mécanique de la croûte continentale inférieure est encore mal contraint, et particulièrement l'état du couplage mécanique avec les péridotites du manteau sous-jacentes (Homburg et al., 2010). De nombreuses études suggèrent que la croûte inférieure a une viscosité faible, à l'inverse de la croûte supérieure et du manteau sous-jacent qui se comportent de manière cassante — le modèle du "jelly sandwich" (Burov & Watts, 2006). Cependant, ce contraste de viscosité important en base de croûte est remis en question par d'autres études géophysiques qui évoquent la possibilité d'une croûte inférieure plus résistante, avec des viscosités proches voire supérieures à celles de la croûte supérieure, comme dans une "crème brûlée" (Maggi et al., 2000, Jackson, 2002, McKenzie & Jackson, 2002, Burov & Watts, 2006).

Ce débat n'est pas tranché, notamment en raison de l'effet encore méconnu des grandes bandes de cisaillement qui structurent la croûte continentale inférieure (Kirby, 1985, Jackson, 2002). Ces bandes de cisaillement d'échelle métrique à pluri-kilométrique (Figure 6.8 Kenkmann & Dresen, 2002, Tatham et al., 2008) témoignent de fortes rétroactions positives entre localisation de la déformation et circulation de fluides, avec précisément la cristallisation syn-cinématique d'amphibole, de plagioclase, de clinopyroxène et/ou

---

de grenat (Figure 6.8; Kenkmann & Dresen, 2002, Tatham et al., 2008). De plus, de récentes études ont montré que les anisotropies sismiques dans la croûte continentale inférieure sont compatibles avec une anisotropie dominée par les amphiboles (voir références dans Ko & Jung, 2015). **Les amphibolites peuvent donc avoir un rôle crucial dans l'accommodation de la déformation au sein de la base de croûte continentale, en plus de celle évoquée ici à l'interface des plaques en zone de subduction naissante, ou de subduction chaude.**

Or, les amphibolites de la semelle métamorphique présentent des minéralogies, des dimensions, des conditions P-T et des déformations finies similaires aux amphibolites de la croûte continentale inférieure. **Étudier le comportement mécanique des amphibolites des semelles métamorphique peut permettre de préciser la rhéologie de la base de croûte continentale, par exemple à différentes conditions P-T ou différentes conditions de fugacité d'eau.** L'étude des amphibolites des semelles métamorphique peut également apporter des contraintes sur l'évolution du couplage mécanique au niveau du Moho, qui dépasse le cadre de la présente étude. Ne resterait-il alors plus qu'à appliquer une simple rotation pour retrouver les péridotites sous les amphibolites ?...





---

## 7 Conclusion

Ce travail de thèse a porté sur l'étude des amphibolites des semelles métamorphiques, comme seuls témoins de l'initiation des zones de subduction. L'intégration des études structurale, pétrologique et mécanique a permis la construction d'un nouveau modèle évolutif de formation et d'accrétion des semelles métamorphiques apportant des contraintes fortes et essentielles pour la dynamique précoce des zones de subduction.

Ce modèle propose notamment que les semelles métamorphiques ne résultent pas tant d'un "coup de chaud" (par transfert de chaleur depuis des péridotites jeunes et chaudes de la plaque supérieure) que d'un processus d'écaillage lié à la résistance rencontrée par la surface de la plaque plongeante lors de son début de descente dans le manteau, face à un butoir mantellique dont les propriétés rhéologiques varient au cours du temps. Le gradient thermique apparent très élevé ( $\leq 1000^\circ\text{C/km}$ ; Hacker & Mosenfelder, 1996) calculé dans les semelles métamorphiques n'est en effet probablement pas continu mais plutôt le résultat de l'écaillage successif de portions de la plaque plongeante accrétées à la plaque supérieure lors de changements rhéologiques majeurs à l'interface des plaques. Ces "*inversions rhéologiques*" interviennent dans un régime thermique en cours de ré-équilibration et refroidissement.

Sur la base d'observations structurales, de changements brusques dans la composition et dans les assemblages minéralogiques et de nouvelles estimations P-T, nous avons mis en évidence trois grandes discontinuités au sein des semelles métamorphiques situées sous l'ophiolite de Semail (Oman, UAE). Ces grandes discontinuités définissent les contours d'unités métamorphiques dont les conditions P-T ont été estimées respectivement à  $850 \pm 50^\circ\text{C} - 0.9 \pm 0.1 \text{ GPa}$  pour l'unité supérieure,  $725 \pm 50^\circ\text{C} \text{ et } 0.7 \pm 0.1 \text{ GPa}$  et  $535 \pm 25^\circ\text{C}$ , pour les unités intermédiaires et inférieures. Au moyen des pseudosections, nous avons également pu modéliser pour la première fois le volume de fusion partielle attendu pour les unités de plus haut grade métamorphique (< 6% dans les trois localités étudiées). Par analogie avec des études expérimentales portant sur l'impact de la fusion dans la rhéologie des roches encaissantes, nous proposons que cette fraction de liquide silicaté représente un seuil au-delà duquel la viscosité des amphibolites chute dramatiquement, empêchant tout couplage (et tout écaillage) à l'interface des plaques.

---

A l'échelle micro-structurale, nous mettons en évidence deux étapes majeures de déformation dans la dynamique d'accrétion et d'exhumation des amphibolites des unités de haute température (que nous associons aux pics de couplage ("*inversion rhéologique*") à l'interface des plaques : (1) lors de l'accrétion de l'unité supérieure à grenat-clinopyroxène, la déformation est essentiellement accommodée par cataclase et ré-orientation rigide des grains d'amphibole dans le plan de foliation. Cette première étape correspondrait à la mylonitisation des périclases rubanées estimées autour de  $850 \pm 50$  °C; (2) lors de l'accrétion de l'unité intermédiaire, la déformation est accommodée par les amphiboles et les plagioclases, en proportion modale équivalente : les grains de plagioclase se déforment par fluage dislocation et forment une matrice moins visqueuse permettant aux grains d'amphibole de se ré-orienter de manière passive parallèlement à la direction de cisaillement principale sans se fracturer. Cette seconde étape correspondrait à l'ultra-mylonitisation des périclases rubanées estimées autour de 700 °C. Cette localisation de la déformation s'accompagne d'une augmentation des infiltrations de fluides venues de la plaque plongeante. Ces deux étapes témoignent d'un couplage mécanique et d'une localisation progressive de la déformation à l'interface des plaques en cours de refroidissement et d'hydratation après l'initiation de la subduction. Afin de préciser les conditions de (dé)formation des semelles métamorphiques, des expériences en laboratoire simulant l'interface des plaques en subduction ont été conduites dans des conditions P-T équivalentes. Bien qu'exploratoires, ces expériences ont permis d'observer et de reproduire au premier ordre (1) le couplage mécanique important entre les deux matériaux et (2) la déformation drastique localisée préférentiellement dans l'amphibolite permettant son très fort amincissement.

Compte tenu de la déformation importante observée dans les périclases rubanées et dans la semelle métamorphique, nous proposons que le saut de pression entre les unités supérieures et intermédiaires résulte, dans des proportions qu'il est difficile de quantifier en l'absence d'estimations de pression tirées des périclases, d'une (1) exhumation conjointe (par rapport au reste de l'ophiolite) des périclases basales et de la semelle amphibolitique à grenat-clinopyroxène et (2) d'un amincissement progressif de la base des périclases. Le facteur d'amincissement pourrait atteindre  $\sim 4\text{--}5$  pour la base des périclases, et  $\geq 5$  à 10 pour les amphibolites des semelles métamorphiques. Nous proposons que ce fort amincissement soit à l'origine de la distribution ubiquiste, sur une centaine de kilomètres sous l'ophiolite de Semail, de semelles métamorphiques formées à des conditions P-T similaires.

Enfin, les expériences en laboratoire que nous avons menées nous ont également permis de mettre en évidence la rétroaction positive entre la formation d'amphibole par réaction d'hydratation et la localisation progressive de la déformation. Cette rétroaction est probablement un des facteurs importants permettant le décollement des unités amphibolitiques des semelles métamorphiques lors de leur accrétion avec la plaque supérieure.





---

# Bibliographie

- Agard, P., Jolivet, L., Vrielynck, B., Burov, E., & Monié, P. (2007). Plate acceleration : The obduction trigger ? *Earth Planet. Sci. Lett.*, 258(3-4), 428–441.
- Agard, P., Searle, M. P., Alsop, G. I., & Dubacq, B. (2010). Crustal stacking and expulsion tectonics during continental subduction : P-T deformation constraints from Oman. *Tectonics*, 29(5), 1–19.
- Agard, P., Yamato, P., Jolivet, L., & Burov, E. (2009). Exhumation of oceanic blueschists and eclogites in subduction zones : Timing and mechanisms. *Earth-Science Rev.*, 92(1-2), 53–79.
- Agard, P., Yamato, P., Soret, M., Prigent, C., Guillot, S., Plunder, A., Dubacq, B., Monié, P., & Chauvet, A. (2016). Plate interface rheological switches during subduction infancy : control on slab penetration and metamorphic sole formation. *Earth Planet. Sci. Lett.*
- Al-Riyami, K., Robertson, A., Dixon, J., & Xenophontos, C. (2002). Origin and emplacement of the Late Cretaceous Baer–Bassit ophiolite and its metamorphic sole in NW Syria. *Lithos*, 65, 225–260.
- Alabaster, T., Pearce, J., & Malpas, J. (1982). The volcanic stratigraphy and petrogenesis of the Oman ophiolite complex. *Contrib. to Mineral. Petrol.*, 81, 168–183.
- Allemann, F. & Peters, T. (1972). The ophiolite-radiolarite belt of the North-Oman Mountains. *Eclogae Geol. Helv.*, 65(3), 657–697.
- Amstutz, A. (1951). Sur l'évolution des structures alpines. *Arch. Sci.*, 4(5), 323–329.
- Arculus, R. J., Ishizuka, O., Bogus, K. a., Gurnis, M., Hickey-Vargas, R., Aljahdali, M. H., Bandini-Maeder, A. N., Barth, A. P., Brandl, P. a., Drab, L., do Monte Guerra, R., Hamada, M., Jiang, F., Kanayama, K., Kender, S., Kusano, Y., Li, H., Loudin, L. C., Maffione, M., Marsaglia, K. M., McCarthy, A., Meffre, S., Morris, A., Neuhaus, M., Savov, I. P., Sena, C., Tepley III, F. J., van der Land, C., Yogodzinski, G. M., & Zhang, Z. (2015). A record of spontaneous subduction initiation in the Izu–Bonin–Mariana arc. *Nat. Geosci.*, 8(9), 728–733.

- 
- Aubouin, J. (1965). *Geosynclines*. Amsterdam : Elsevier.
- Austrheim, H. (1987). Eclogitization of lower crustal granulites by fluid migration through shear zones. *Earth Planet. Sci. Lett.*, 81(2-3), 221–232.
- Bachmann, F., Hielscher, R., & Schaeben, H. (2010). Texture Analysis with MTEX – Free and Open Source Software Toolbox. *Solid State Phenom.*, 160, 63–68.
- Barruol, G. & Mainprice, D. (1993). 3-D Seismic Velocities Calculated from Lattice-Preferred Orientation and Reflectivity of a Lower Crustal Section - Examples of the Val Sesia Section (Ivrea Zone, Northern Italy). *Geophys. J. Int.*, 115(3), 1169–1188.
- Bascou, J., Tommasi, A., & Mainprice, D. (2002). Plastic deformation and development of clinopyroxene lattice preferred orientations in eclogites. *J. Struct. Geol.*, 24(8), 1357–1368.
- Bébien, J., Shallo, M., Manika, K., & Gega, D. (1998). The Shebenik Massif (Albania) : a link between MOR-and SSZ-type ophiolites ? *Ophioliti*, 23(1), 7–15.
- Beccaluva, L., Coltorti, M., Giunta, G., & Siena, F. (2004). Tethyan vs. Cordilleran ophiolites : a reappraisal of distinctive tectono-magmatic features of supra-subduction complexes in relation to the subduction mode. *Tectonophysics*, 393(1-4), 163–174.
- Beccaluva, L., Coltorti, M., Premti, I., Saccani, E., Siena, F. t., & Zeda, O. (1994). Mid-ocean ridge and supra-subduction affinities in the ophiolitic belts from Albania. *Ophioliti*, 19(1), 77–96.
- Benoit, M., Ceuleneer, G., & Polvé, M. (1999). The remelting of hydrothermally altered peridotite at mid-ocean ridges by intruding mantle diapirs. *Nature*, 402(December), 514–518.
- Benson, W. N. (1926). *The tectonic conditions accompanying the intrusion of basic and ultrabasic igneous rocks*. US Government Printing Office.
- Berger, A. & Stünitz, H. (1996). Deformation mechanisms and reaction of hornblende : examples from the Bergell tonalite (Central Alps). *Tectonophysics*, 257, 149–174.
- Beyssac, O., Goffé, B., Chopin, C., & Rouzaud, J. N. (2002). Raman spectra of carbonaceous material in metasediments : A new geothermometer. *J. Metamorph. Geol.*, 20(9), 859–871.
- Bortolotti, V., Marroni, M., Pandolfi, L., Principi, G. T., & Saccani, E. (2002). Interaction between mid-ocean ridge and subduction magmatism in Albanian ophiolites. *J. Geol.*, 110(5), 561–576.

- 
- Boschi, C., Früh-Green, G. L., Delacour, A., Karson, J. A., & Kelley, D. S. (2006). Mass transfer and fluid flow during detachment faulting and development of an oceanic core complex, Atlantis Massif (MAR 30°N). *Geochemistry, Geophys. Geosystems*, 7, Q01004.
- Boudier, F., Bouchez, J. L., Nicolas, A., Cannat, M., Ceuleneer, G., Misseri, M., & Montigny, R. (1985). Kinematics of oceanic thrusting in the Oman ophiolite : model of plate convergence. *Earth Planet. Sci. Lett.*, 75(2-3), 215–222.
- Boudier, F., Ceuleneer, G., & Nicolas, A. (1988). Shear zones, thrusts and related magmatism in the Oman ophiolite : Initiation of thrusting on an oceanic ridge. *Tectonophysics*, 151(1-4), 275–296.
- Boudier, F., Godard, M., & Armbruster, C. (2000). Significance of gabbronorite occurrence in the crustal section of the Semail ophiolite. *Mar. Geophys. Res.*, 21(3-4), 307–326.
- Bowen, N. L. (1927). The Origin of ultra-basic and related rocks. *Am. J. Sci.*, 14(80), 89–108.
- Bowen, N. L. & Tuttle, O. F. (1949). The system MgO - SIO<sub>2</sub> - H<sub>2</sub>O. *Bull. Geol. Soc. Am.*, 60, 439–460.
- Brace, W. F. & Kohlstedt, D. L. (1980). Limits on lithospheric stress imposed by laboratory experiments. *J. Geophys. Res. Solid Earth*, 85(B11), 6248–6252.
- Brodie, K. H. (1981). Variation in amphibole and plagioclase composition with deformation. *Tectonophysics*, 78(1-4), 385–402.
- Brodie, K. H. & Rutter, E. H. (1985). On the relationship between rock deformation and metamorphism with special reference to the behaviour of basic rocks. *Metamorph. React.*, 4, 138–179.
- Brongniart, A. (1813). Essai d'une classification minéralogique des roche mélangées. *J. des Mines*, 34(199), 5–48.
- Brongniart, A. (1827). *Classification et caractères minéralogiques des roches homogènes et hétérogènes*. Harvard University Mineralogical Library.
- Brunn, J. H. (1960). Mise en place et différenciation de l'association pluto-volcanique du cortège ophiolitique. *Rev. Géographie Phys. Géologie Dyn.*, 3, 115–132.
- Bucher, M. (1991a). Mineral equilibria in metagabbros : evidence for polymetamorphic evolution of the Asimah Window, northern Oman Mountains, United Arab Emirates. In *Ophiolite Genes. Evol. Ocean. Lithosph.* (pp. 543–571). Springer.

- 
- Bucher, M. (1991b). *The metamorphic series associated with the Semail Ophiolite nappe of the Oman Mountains in the United Arab Emirates*. PhD thesis, University of Berne.
- Bürgmann, R. & Dresen, G. (2008). Rheology of the Lower Crust and Upper Mantle : Evidence from Rock Mechanics, Geodesy, and Field Observations. *Annu. Rev. Earth Planet. Sci.*, 36(1), 531–567.
- Burov, E. & Yamato, P. (2008). Continental plate collision, P-T-t-z conditions and unstable vs. stable plate dynamics : Insights from thermo-mechanical modelling. *Lithos*, 103(1-2), 178–204.
- Burov, E. B. & Watts, A. B. (2006). The long-term strength of continental lithosphere : "jelly sandwich" or "creme brûlée" ? *GSA Today*, 16(1), 4–10.
- Bystricky, M. & Mackwell, S. (2001). Creep of dry clinopyroxene aggregates. *J. Geophys. Res.*, 106(B7), 13443.
- Cao, S., Liu, J., & Leiss, B. (2010). Orientation-related deformation mechanisms of naturally deformed amphibole in amphibolite mylonites from the Diancang Shan, SW Yunnan, China. *J. Struct. Geol.*, 32(5), 606–622.
- Capedri, S., Venturelli, G., Bocchi, G., Dostal, J., Garuti, G., & Rossi, A. (1980). The geochemistry and petrogenesis of an ophiolitic sequence from Pindos, Greece. *Contrib. to Mineral. Petrol.*, 74(2), 189–200.
- Carlson, W. D. (2006). Rates of Fe, Mg, Mn, and Ca diffusion in garnet. *Am. Mineral.*, 91(1), 1–11.
- Casey, J. F. & Dewey, J. F. (1984). Initiation of subduction zones along transform and accreting plate boundaries, triple-junction evolution, and forearc spreading centres - implications for ophiolitic geology and obduction. *Geol. Soc. London, Spec. Publ.*, 13, 269–290.
- Çelik, Ö. F. & Delaloye, M. F. (2006). Characteristics of ophiolite-related metamorphic rocks in the Beysehir ophiolitic mélange (Central Taurides, Turkey), deduced from whole rock and mineral chemistry. *J. Asian Earth Sci.*, 26(5), 461–476.
- Ceuleneer, G., Nicolas, A., & Boudier, F. (1988). Mantle flow patterns at an oceanic spreading The Oman peridotites record. *Tectonophysics*, 151, 1–26.
- Clague, D., Rubin, J., & Brackett, R. (1981). The age and origin of the garnet amphibolite underlying the Thetford Mines ophiolite, Quebec. *Can. J. Earth Sci.*, 18(3), 469–486.

- 
- Cluzel, D., Jourdan, F., Meffre, S., Maurizot, P., & Lesimple, S. (2012). The metamorphic sole of New Caledonia ophiolite :  $^{40}\text{Ar}/^{39}\text{Ar}$ , U-Pb, and geochemical evidence for subduction inception at a spreading ridge. *Tectonics*, 31(3), TC3016.
- Coleman, R. (1971). Tectonic Emplacement Upper Mantle Peridotites along Continental Edges. *J. Geophys. Res.*, 76(5), 1212–1222.
- Coleman, R. G. (1977). *Ophiolites : ancient oceanic lithosphere ?*, volume 12. Springer-Verlag.
- Coleman, R. G. R. (1981). Tectonic setting for ophiolite obduction in Oman. *J. Geophys. Res. Solid Earth*, 86(B4), 2497–2508.
- Cowan, R. J., Searle, M. P., & Waters, D. J. (2014). Structure of the metamorphic sole to the Oman Ophiolite , Sumeini Window and Wadi Tayyin : implications for ophiolite obduction processes Structure of the metamorphic sole to the Oman Ophiolite , Sumeini Window and Wadi Tayyin : implications for ophiolite. *Geol. Soc. London, Spec. Publ.*, 392, 155–175.
- Dewey, J. F. (1976). Ophiolite obduction. *Tectonophysics*, 31, 93–120.
- Dewey, J. F. & Bird, J. M. (1971). Origin and Emplacement of the Ophiolite Suite : Appalachian Ophiolites in Newfoundland. *J. Geophys. Res.*, 76(14).
- Dewey, J. F. & Casey, J. F. (2013). The sole of an ophiolite : the Ordovician Bay of Islands Complex, Newfoundland. *J. Geol. Soc. London.*, 170(5), 715–722.
- Díaz Aspiroz, M., Lloyd, G. E., & Fernández, C. (2007). Development of lattice preferred orientation in clinoamphiboles deformed under low-pressure metamorphic conditions. A SEM/EBSD study of metabasites from the Aracena metamorphic belt (SW Spain). *J. Struct. Geol.*, 29(4), 629–645.
- Dilek, Y. & Furnes, H. (2009). Structure and geochemistry of Tethyan ophiolites and their petrogenesis in subduction rollback systems. *Lithos*, 113(1-2), 1–20.
- Dilek, Y. & Furnes, H. (2011). Ophiolite genesis and global tectonics : Geochemical and tectonic fingerprinting of ancient oceanic lithosphere. *Geol. Soc. Am. Bull.*, 123(3-4), 387–411.
- Dilek, Y., Furnes, H., & Shallo, M. (2007). Suprasubduction zone ophiolite formation along the periphery of Mesozoic Gondwana. *Gondwana Res.*, 11(4), 453–475.
- Dilek, Y., Furnes, H., & Shallo, M. (2008). Geochemistry of the Jurassic Mirdita Ophiolite (Albania) and the MORB to SSZ evolution of a marginal basin oceanic crust. *Lithos*, 100(1-4), 174–209.

- 
- Dilek, Y., Thy, P., Moores, E. M., & Ramsden, T. W. (1990). Tectonic evolution of the Troodos Ophiolite within the Tethyan Framework. *Tectonics*, 9(4), 811–823.
- Dilek, Y. & Whitney, D. L. (1997). Counterclockwise P-T-t trajectory from the metamorphic sole of a Neo-Tethyan ophiolite (Turkey). *Tectonophysics*, 280, 295–310.
- Dimanov, A. & Dresen, G. (2005). Rheology of synthetic anorthite-diopside aggregates : Implications for ductile shear zones. *J. Geophys. Res. Solid Earth*, 110(7), 1–24.
- Dimanov, A., Rybacki, E., Wirth, R., & Dresen, G. (2007). Creep and strain-dependent microstructures of synthetic anorthite-diopside aggregates. *J. Struct. Geol.*, 29(6), 1049–1069.
- Dimo-Lahitte, A., Monié, P., & Vergély, P. (2001). Metamorphic soles from the Albanian ophiolites : Petrology,  $^{40}\text{Ar}/^{39}\text{Ar}$  geochronology, and geodynamic evolution. *Tectonics*, 20(1), 78–96.
- Dubacq, B., Vidal, O., & de Andrade, V. (2010). Dehydration of dioctahedral aluminous phyllosilicates : Thermodynamic modelling and implications for thermobarometric estimates. *Contrib. to Mineral. Petrol.*, 159(2), 159–174.
- Duretz, T., Agard, P., Yamato, P., Ducassou, C., Burov, E. B., & Gerya, T. V. (2016). Thermo-mechanical modeling of the obduction process based on the Oman Ophiolite case. *Gondwana Res.*, 32, 1–10.
- Dymkova, D. & Gerya, T. (2013). Porous fluid flow enables oceanic subduction initiation on Earth. *Geophys. Res. Lett.*, 40(21), 5671–5676.
- El-Naby, H. A., Frisch, W., & Hegner, E. (2000). Evolution of the Pan-African Wadi Haimur metamorphic sole, Eastern Desert, Egypt. *J. Metamorph. Geol.*, 18, 639–651.
- El-Shazly, A. K., Brocker, M., Hacker, B. R., & Calvert, A. (2001). Formation and exhumation of blueschists and eclogites from NE Oman : new perspectives from Rb–Sr and  $^{40}\text{Ar}/^{39}\text{Ar}$  dating. *J. Metamorph. Geol.*, 19, 233–248.
- Ellis, D. J. & Green, D. H. (1979). Contributions to Mineralogy and An Experimental Study of the Effect of Ca Upon Garnet-Clinopyroxene Fe–Mg Exchange Equilibria. *Contrib. to Mineral. Petrol.*, 71, 13–22.
- Encarnacion, J. P., Essene, E. J., Mukasa, S. B., & Hall, C. H. (1995). High-Pressure and -Temperature Subophiolitic Kyanite - Garnet Amphibolites Generated during Initiation of Mid-Tertiary Subduction, Palawan,. *J. Petrol.*, 36(6), 1481–1503.

- 
- Ernwein, M., Pflumio, C., & Whitechurch, H. (1988). The death of an accretion zone as evidenced by the magmatic history of the Sumail ophiolite (Oman). *Tectonophysics*, 151, 247–274.
- Ernst, W. & Liu, J. (1998). Experimental phase-equilibrium study of Al-and Ti-contents of calcic amphibole in MORB-A semiquantitative thermobarometer. *Am. Mineral.*, 83, 952–969.
- Escartín, J., Hirth, G., & Evans, B. (2001). Strength of slightly serpentinitized peridotites : Implications for the tectonics of oceanic lithosphere. *Geology*, 29(11), 1023–1026.
- Escartín, J., Mével, C., MacLeod, C. J., & McCaig, A. M. (2003). Constraints on deformation conditions and the origin of oceanic detachments : The Mid-Atlantic Ridge core complex at 15°45' N. *Geochemistry, Geophys. Geosystems*, 4(8).
- Faccenna, C., Giardini, D., Davy, P., & Argentieri, A. (1999). Initiation of subduction at Atlantic-type margins' Insights from laboratory experiments. *J. Geophys. Res.*, 104(1999), 2749–2766.
- Facenna, C. & Becker, T. W. (2001). History of subdcution and and back arc extension in the central Mediterranean. *Geophys. J. Inter.*, 145, 809–820.
- Farahat, E. (2011). Geotectonic significance of Neoproterozoic amphibolites from the Central Eastern Desert of Egypt : A possible dismembered sub-ophiolitic metamorphic sole. *Lithos*, 125(1-2), 781–794.
- Gaggero, L., Marroni, M., Pandolfi, L., & Buzzi, L. (2009). Modeling the oceanic lithosphere obduction : Constraints from the metamorphic sole of Mirdita ophiolites (Northern Albania). *Ophioliti*, 34(1), 17–42.
- Ganguly, J. (1979). Garnet and clinopyroxene solid solutions, and geothermometry based on Fe-Mg distribution coefficient. *Geochim. Cosmochim. Acta*, 43, 1021–1029.
- Gartzos, E., Dietrich, V., Migiros, G., Serelis, K., & Lymeropoulou, T. (2009). The origin of amphibolites from metamorphic soles beneath the ultramafic ophiolites in Evia and Lesvos (Greece) and their geotectonic implication. *Lithos*, 108(1-4), 224–242.
- Gerya, T. (2011). Future directions in subduction modeling. *J. Geodyn.*, 52(5), 344–378.
- Gerya, T. V., Stockhert, B., & Perchuk, A. L. (2002). Exhumation of high-pressure metamorphic rocks in a subduction channel : A numerical simulation. *Tectonics*, 21(6), 6–1–6–19.
- Getsinger, A. J. (2015). *The Rheology of Amphibolite*. PhD thesis, Brown University.

- 
- Getsinger, A. J. & Hirth, G. (2014). Amphibole fabric formation during diffusion creep and the rheology of shear zones. *Geology*, 42(6), 535–538.
- Getsinger, A. J., Hirth, G., Stünitz, H., & Goergen, E. T. (2013). Influence of water on rheology and strain localization in the lower continental crust. *Geochemistry, Geophys. Geosystems*, 14(7), 2247–2264.
- Ghent, E. D. & Stout, M. Z. (1981). Metamorphism at the Base of the Samail Ophiolite, Southeastern Oman Mountains. *J. Geophys. Res.*, 86(B4), 2557–2571.
- Girardeau, J. & Nicolas, A. (1981). The structures of two ophiolite massifs, Bay-of-Islands, Newfoundland : a model for the oceanic crust and upper mantle. *Tectonophysics*, 77, 1–34.
- Glennie, K. W., Boeuf, M. G., Hughes Clarke, M. W., Moody-Stuart, M., Pilaar, W. F. H., & Reinhardt, B. M. (1974). Geology of the Oman Mountains, parts 1 and 2. *R. Dutch Geol. Min. Soc. (KNGMG)*, Utrecht, Netherlands, (pp. 423).
- Gnos, E. (1992). *The metamorphic rocks associated with the Semail Ophiolite (Sultanate of Oman and United Arab Emirates)*. PhD thesis, Université de Bern, Suisse.
- Gnos, E. (1998). Peak Metamorphic Conditions of Garnet Amphibolites Beneath the Semail Ophiolite : Implications for an Inverted Pressure Gradient. *Int. Geol. Rev.*, 40(4), 281–304.
- Gnos, E. & Kurz, D. (1994). Sapphirine-quartz and sapphirine-corundum assemblages in metamorphic rocks associated with the Semail Ophiolite (United Arab Emirates). *Contrib. to Mineral. Petrol.*, 116, 398–410.
- Godard, M., Bosch, D., & Einaudi, F. (2006). A MORB source for low-Ti magmatism in the Semail ophiolite. *Chem. Geol.*, 234(1-2), 58–78.
- Godard, M., Dautria, J.-M., & Perrin, M. (2003). Geochemical variability of the Oman ophiolite lavas : Relationship with spatial distribution and paleomagnetic directions. *Geochemistry, Geophys. Geosystems*, 4(6).
- Godard, M., Jousselin, D., & Bodinier, J. (2000). Relationships between geochemistry and structure beneath a palaeo-spreading centre : a study of the mantle section in the Oman ophiolite. *Earth Planet. Sci. Lett.*, 180(1-2), 133–148.
- Gómez Barreiro, J., Martínez Catalán, J. R., Prior, D., Wenk, H., Vogel, S., Díaz García, F., Arenas, R., Sánchez Martínez, S., & Lonardelli, I. (2010). Fabric Development in a Middle Devonian Intraoceanic Subduction Regime : The Careón Ophiolite (Northwest Spain). *J. Geol.*, 118(2), 163–186.

- 
- Goodenough, K. M., Styles, M. T., Schofield, D., Thomas, R. J., Crowley, Q. C., Lilly, R. M., McKervey, J., Stephenson, D., & Carney, J. N. (2010). Architecture of the Oman-UAE ophiolite : Evidence for a multi-phase magmatic history. *Arab. J. Geosci.*, 3, 439–458.
- Gray, D. R. & Gregory, R. T. (2000). Implications of the structure of the Wadi Tayin metamorphic sole, the Ibra-Dasir block of the Samail ophiolite, and the Saih Hatah window for late stage extensional ophiolite emplacement, Oman. *Mar. Geophys. Res.*, 21(3-4), 211–227.
- Green, D. & Ringwood, A. (1967). The genesis of basaltic magmas. *Contrib. to Mineral. Petrol.*, 15, 103–190.
- Green, E. C. R., White, R. W., Diener, J. F. A., Powell, R., Holland, T. J. B., & Palin, R. M. (2016). Activity–composition relations for the calculation of partial melting equilibria in metabasic rocks. *J. Metamorph. Geol.*
- Guilmette, C., Hébert, R., Dostal, J., Indares, A., Ullrich, T., Bédard, É., & Wang, C. (2012). Discovery of a dismembered metamorphic sole in the Saga ophiolitic mélange, South Tibet : Assessing an Early Cretaceous disruption of the Neo-Tethyan supra-subduction zone and consequences on basin closing. *Gondwana Res.*, 22(2), 398–414.
- Gurnis, M., Hall, C., & Lavier, L. (2004). Evolving force balance during incipient subduction. *Geochemistry, Geophys. Geosystems*, 5(7), Q07001.
- Haase, K. M., Freund, S., Beier, C., Koepke, J., Erdmann, M., & Hauff, F. (2016). Constraints on the magmatic evolution of the oceanic crust from plagiogranite intrusions in the Oman ophiolite. *Contrib. to Mineral. Petrol.*, 171(5), 46.
- Haase, K. M., Freund, S., Koepke, J., Hauff, F., & Erdmann, M. (2015). Melts of sediments in the mantle wedge of the Oman ophiolite. *Geology*, 43(4), 275–278.
- Hacker, B. & Mosenfelder, J. (1996). Metamorphism and deformation along the emplacement thrust of the Samail ophiolite, Oman. *Earth Planet. Sci. Lett.*, 144(3-4), 435–451.
- Hacker, B. R. (1990). Simulation of the metamorphic and deformational history of the metamorphic sole of the Oman ophiolite. *J. Geophys. Res. Earth*, 95(B4), 4895–4907.
- Hacker, B. R. (1991). The role of deformation in the formation of metamorphic gradients : Ridge subduction beneath the Oman Ophiolite. *Tectonics*, 10(2), 455–473.
- Hacker, B. R. (1994). Rapid emplacement of young oceanic lithosphere : argon geochronology of the Oman ophiolite. *Science*, 265, 1563–1565.

- 
- Hacker, B. R. & Christie, J. M. (1990). Brittle/Ductile and Plastic/Cataclastic Transitions in Experimentally Deformed and Metamorphosed Amphibolite. *Geophys. Monogr. Ser.*, 56, 127–148.
- Hacker, B. R. & Gnos, E. (1997). The conundrum of samail : explaining the metamorphic history. *Tectonophysics*, 279, 215–226.
- Hacker, B. R., Mosenfelder, J. L., & Gnos, E. (1996). Rapid emplacement of the Oman ophiolite : Thermal and geochronologic constraints. *Tectonics*, 15(6), 1230–1247.
- Hall, C. E., Gurnis, M., Sdrolias, M., Lavier, L. L., & Muller, R. D. (2003). Catastrophic initiation of subduction following forced convergence across fracture zones. *Earth Planet. Sci. Lett.*, 212(1-2), 15–30.
- Harris, R. A. (1998). Origin and tectonic evolution of the metamorphic sole beneath the Brooks Range ophiolite, Alaska. *Geol. Soc. Am. Spec. Pap.*, 324, 293–312.
- Harrison, M. T. (1982). Diffusion of  $^{40}\text{Ar}$  in hornblende. *Contrib. to Mineral. Petrol.*, 78(3), 324–331.
- Harrison, T. M., Célérier, J., Aikman, A. B., Hermann, J., & Heizler, M. T. (2009). Diffusion of  $^{40}\text{Ar}$  in muscovite. *Geochim. Cosmochim. Acta*, 73(4), 1039–1051.
- Hässig, M. (2014). *The obduction process : what extent, what timing, what cause(s) ? The study of the northern branch of Neotethys in Anatolia and the Lesser Caucasus (Turkey and Armenia)*. Thesis, Université Nice Sophia Antipolis.
- Hässig, M., Duretz, T., Rolland, Y., & Sosson, M. (2016a). Obduction of old oceanic lithosphere due to reheating and plate reorganization : Insights from numerical modelling and the NE Anatolia – Lesser Caucasus case example. *J. Geodyn.*
- Hässig, M., Rolland, Y., Duretz, T., & Sosson, M. (2016b). Obduction triggered by regional heating during plate reorganization. *Terra Nov.*, 28(1), 76–82.
- Hassig, M., Rolland, Y., Sahakyan, L., Sosson, M., Galoyan, G., Avagyan, A., Bosch, D., & Müller, C. (2015). Multi-stage metamorphism in the South Armenian Block during the Late Jurassic to Early Cretaceous : Tectonics over south-dipping subduction of Northern branch of Neotethys. *J. Asian Earth Sci.*, 102, 4–23.
- Henry, D. J., Guidotti, C. V., & Thomson, J. A. (2005). The Ti-saturation surface for low-to-medium pressure metapelitic biotites : Implications for geothermometry and Ti-substitution mechanisms. *Am. Mineral.*, 90(2-3), 316–328.
- Herwegh, M., Mercolli, I., Linckens, J., & Müntener, O. (2016). Mechanical anisotropy controls strain localization in upper mantle shear zones. *Tectonics*, 35, 1177–1204.

- 
- Hess, H. H. (1938). A primary peridotite magma. *Am. J. Sci.*, 35(209), 321–344.
- Hess, H. H. (1955). Serpentines, orogeny, and epeirogeny. *Geol. Soc. Am. Spec. Pap.*, 62, 391–408.
- Hielscher, R. & Schaeben, H. (2008). A novel pole figure inversion method : Specification of the MTEX algorithm. *J. Appl. Crystallogr.*, 41(6), 1024–1037.
- Hier-Majumder, S., Mei, S., & Kohlstedt, D. L. (2005). Water weakening of clinopyroxenite in diffusion creep. *J. Geophys. Res. Solid Earth*, 110(7), 1–12.
- Hirth, G. & Kohlstedt, D. (2003). Rheology of the upper mantle and the mantle wedge : A view from the experimentalists. *Geophys. Monogr. Ser.*, 138, 83–105.
- Hirth, G. & Kohlstedt, D. L. (2015). The stress dependence of olivine creep rate : Implications for extrapolation of lab data and interpretation of recrystallized grain size. *Earth Planet. Sci. Lett.*, 418, 20–26.
- Holland, T. & Blundy, J. (1994). Non-ideal interactions in calcic amphiboles and their bearing on amphibole-plagioclase thermometry. *Contrib. to Mineral. Petrol.*, 116(4), 433–447.
- Holland, T. & Powell, R. (2003). Activity-compositions relations for phases in petrological calculations : An asymmetric multicomponent formulation. *Contrib. to Mineral. Petrol.*, 145(4), 492–501.
- Holland, T. J. B. & Powell, R. (1998). An internally consistent thermodynamic data set for phases of petrological interest. *J. Metamorph. Geol.*, 16(3), 309–343.
- Holland, T. J. B. & Powell, R. (2011). An improved and extended internally consistent thermodynamic dataset for phases of petrological interest, involving a new equation of state for solids. *J. Metamorph. Geol.*, 29(3), 333–383.
- Homburg, J. M., Hirth, G., & Kelemen, P. B. (2010). Investigation of the strength contrast at the Moho : A case study from the Oman Ophiolite. *Geology*, 38(8), 679–682.
- ichiro Karato, S. (2010). Rheology of the deep upper mantle and its implications for the preservation of the continental roots : A review. *Tectonophysics*, 481(1-4), 82–98.
- Ildefonse, B., Lardeaux, J. M., & Caron, J. M. (1990). The behavior of shape preferred orientations in metamorphic rocks : amphiboles and jadeites from the Monte Mucrone area (Sesia-Lanzo zone, Italian Western Alps). *J. Struct. Geol.*, 12(8), 1005–1011.
- Ildefonse, B., Launeau, P., Bouchez, J. L., & Fernandez, A. (1992a). Effect of Mechanical Interactions on the Development of Shape Preferred Orientations - a 2-Dimensional Experimental Approach. *J. Struct. Geol.*, 14(1), 73–83.

- 
- Ildefonse, B., Sokoutis, D., & Mancktelow, N. S. (1992b). Mechanical interactions between rigid particles in a deforming ductile matrix. Analogue experiments in simple shear flow. *J. Struct. Geol.*, 14(10), 1253–1266.
- Imon, R., Okudaira, T., & Kanagawa, K. (2004). Development of shape- and lattice-preferred orientations of amphibole grains during initial cataclastic deformation and subsequent deformation by dissolution-precipitation creep in amphibolites from the Ryoke metamorphic belt, SW Japan. *J. Struct. Geol.*, 26(5), 793–805.
- Ingrin, J., Doukhan, N., & Doukhan, J. C. (1991). High-Temperature Deformation of Diopside Single-Crystal .2. Transmission Electron-Microscopy Investigation Of The Defect Microstructures. *J. Geophys. Res. Earth Planets*, 96(B9), 14287–14297.
- Ingrin, J., Doukhan, N., & Doukhan, J.-C. (1992). Dislocation glide systems in diopside single crystals deformed at 800–900C. *Eur. J. Mineral.*, 4(6), 1291–1302.
- Ishikawa, T., Fujisawa, S., Nagaishi, K., & Masuda, T. (2005). Trace element characteristics of the fluid liberated from amphibolite-facies slab : Inference from the metamorphic sole beneath the Oman ophiolite and implication for boninite genesis. *Earth Planet. Sci. Lett.*, 240(2), 355–377.
- Jackson, J. (2002). Faulting, Flow, and the Strength of the Continental Lithosphere. *Int. Geol. Rev.*, 44(1), 39–61.
- Jamieson, R. A. (1981). Metamorphism during Ophiolite Emplacement-the Petrology of the St. Anthony Complex. *J. Petrol.*, 22(3), 397–449.
- Jamieson, R. A. (1986). P-T paths from high temperature shear zones beneath ophiolites. *J. Metamorph. Geol.*, 4, 3–22.
- Jamieson, R. A. & Strong, D. F. (1981). A metasomatic mylonite zone within the ophiolite aureole, St. Anthony complex, Newfoundland. *Am. J. Sci.*, 281, 264–281.
- Jung, H. & Karato, S.-i. (2001). Water-Induced Fabric Transitions in Olivine. *Science*, 293(5534), 1460–1463.
- Kenkmann, T. & Dresen, G. (2002). Dislocation microstructure and phase distribution in a lower crustal shear zone - An example from the Ivrea-Zone, Italy. *Int. J. Earth Sci.*, 91(3), 445–458.
- Kirby, S. H. (1985). Rock mechanics observations pertinent to the rheology of the continental lithosphere and the localization of strain along shear zones. *Tectonophysics*, 119(1-4), 1–27.

- 
- Ko, B. & Jung, H. (2015). Crystal preferred orientation of an amphibole experimentally deformed by simple shear. *Nat. Commun.*, 6, 6586.
- Kohn, M. J. (2013). Geochemical Zoning in Metamorphic Minerals. *Treatise Geochemistry Second Ed.*, 4, 249–280.
- Krogh, E. J. (1988). The garnet-clinopyroxene Fe-Mg geothermometer - a reinterpretation of existing experimental data. *Contrib. to Mineral. Petrol.*, 99(1), 44–48.
- Krogh, E. J. (2000). The garnet – clinopyroxene Fe<sup>2+</sup> – Mg geothermometer : an updated calibration. *J. Metamorph. Geol.*, 18(2), 211–219.
- Labrousse, L., Prouteau, G., & Ganzhorn, A. C. (2011). Continental exhumation triggered by partial melting at ultrahigh pressure. *Geology*, 39(12), 1171–1174.
- Lagabrielle, Y., Chauvet, A., Ulrich, M., & Guillot, S. (2013). Passive obduction and gravity-driven emplacement of large ophiolitic sheets : The New Caledonia ophiolite (SW Pacific) as a case study ? *Bull. la Soc. Geol. Fr.*, 184(6), 545–556.
- Lallemand, S. (1999). La subduction océanique. *Pour Sci.*, 259, 108.
- Lázaro, C., Blanco-Quintero, I., Rojas-Agramonte, Y., Proenza, J., Núñez-Cabra, K., & García-Casco, A. (2013). First description of a metamorphic sole related to ophiolite obduction in the northern Caribbean : Geochemistry and petrology of the Güira de Jauco Amphibolite complex (eastern Cuba) and tectonic implications. *Lithos*, 179, 193–210.
- Le Mée, L., Girardeau, J., & Monnier, C. (2004). Mantle segmentation along the Oman ophiolite fossil mid-ocean ridge. *Nature*, 432(7014), 167–72.
- Leake, B. E., Woolley, A. R., Arps, C. E. S., Gilbert, M. C., Grice, J. D., Hawthorne, F. C., Kisch, H. J., Krivovichev, V. G., Canada, J. A. M., Maresch, W. V., Schumacher, J. C., France, D. C. S., Stephenson, N. C. N., & Whittaker, E. J. W. (1997). Nomenclature of amphiboles. *Can. Mineral.*, 35, 219–246.
- Lee, J. K. W., Williams, I. S., & Ellis, D. J. (1997). Pb, U and Th diffusion in natural zircon. *Nature*, 390(November), 159–162.
- Linckens, J., Herwegh, M., & Muntener, O. (2011). Linking temperature estimates and microstructures in deformed polymimetic mantle rocks. *Geochemistry, Geophys. Geosystems*, 12(8), 1–19.
- Lippard, S. J. (1986). The ophiolite of northern Oman. *Geol. Soc. Mem.*
- Lloyd, G. E., Butler, R. W. H., Casey, M., Tatham, D. J., & Mainprice, D. (2011). Constraints on the seismic properties of the middle and lower continental crust. *Geol. Soc. London, Spec. Publ.*, 360(1), 7–32.

- 
- Lloyd, G. E., Farmer, A. B., & Mainprice, D. (1997). Misorientation analysis and the formation and orientation of subgrain and grain boundaries. *Tectonophysics*, 279(1-4), 55–78.
- Lus, W. Y., McDougall, I., & Davies, H. L. (2004). Age of the metamorphic sole of the Papuan Ultramafic Belt ophiolite, Papua New Guinea. *Tectonophysics*, 392(1-4), 85–101.
- Maaløe, S. (1982). Geochemical aspects of permeability controlled partial melting and fractional crystallization. *Geochim. Cosmochim. Acta*, 46(1), 43–57.
- Mackwell, S. J., Zimmerman, M. E., & Kohlstedt, D. L. (1998). High-temperature deformation of dry diabase with application to tectonics on Venus. *J. Geophys. Res. Solid Earth*, 103(B1), 975–984.
- MacLeod, C., Lissenberg, C., & Bibby, L. (2013). “Moist MORB” axial magmatism in the Oman ophiolite : The evidence against a mid-ocean ridge origin. *Geology*, 41(4), 459–462.
- Maffione, M., Thieulot, C., Van Hinsbergen, D. J., Morris, A., Plümper, O., & Spakman, W. (2015). Dynamics of intraoceanic subduction initiation : 1. Oceanic detachment fault inversion and the formation of supra-subduction zone ophiolites. *Geochemistry, Geophys. Geosystems*, 16, 1753–1770.
- Maggi, A., Jackson, J. A., McKenzie, D., & Priestley, K. (2000). Earthquake focal depths, effective elastic thickness, and the strength of the continental lithosphere. *Geology*, 28(1990), 495–498.
- Mainprice, D., Bachmann, F., Hielscher, R., & Schaeben, H. (2014). Descriptive tools for the analysis of texture projects with large datasets using MTEX : strength, symmetry and components. *Geol. Soc. London, Spec. Publ.*, 409(1), 251–271.
- Mainprice, D. & Nicolas, A. (1989). Development of shape and lattice preferred orientations : application to the seismic anisotropy of the lower crust. *J. Struct. Geol.*, 11(1-2), 175–189.
- Malo, M., Ruffet, G., Pinciv, A., & Tremblay, A. (2008). A  $^{40}\text{Ar}/^{39}\text{Ar}$  study of oceanic and continental deformation processes during an oblique collision : Taconian orogeny in the Quebec reentrant of the Canadian Appalachians. *Tectonics*, 27(4).
- Malpas, J. (1979). The dynamothermal aureole of the Bay of Islands ophiolite suite. *Can. J. Earth Sci.*, 16, 2086–2010.
- Marchesi, C., Garrido, C. J., Godard, M., Belley, F., & Ferré, E. (2009). Migration and accumulation of ultra-depleted subduction-related melts in the Massif du Sud ophiolite (New Caledonia). *Chem. Geol.*, 266(3-4), 171–186.

- 
- Mauler, A., Bystricky, M., Kunze, K., & Mackwell, S. (2000). Microstructures and lattice preferred orientations in experimentally deformed clinopyroxene aggregates. *J. Struct. Geol.*, 22(11-12), 1633–1648.
- McCaig, A. M. (1983). P-T conditions during emplacement of the Bay of Islands ophiolite complex. *Earth Planet. Sci. Lett.*, 63(3), 459–473.
- McKenzie, D. & Jackson, J. (2002). Conditions for flow in the continental crust. *Tectonics*, 21(6), 1055.
- Meffre, S., Falloon, T. J., Crawford, T. J., Hoernle, K., Hauff, F., Duncan, R. A., Bloomer, S. H., & Wright, D. J. (2012). Basalts erupted along the Tongan fore arc during subduction initiation : Evidence from geochronology of dredged rocks from the Tonga fore arc and trench. *Geochemistry, Geophys. Geosystems*, 13(12), 1–17.
- Mehl, L. & Hirth, G. (2008). Plagioclase preferred orientation in layered mylonites : Evaluation of flow laws for the lower crust. *J. Geophys. Res. Solid Earth*, 113(5), 1–19.
- Michibayashi, K., Abe, N., Okamoto, A., Satsukawa, T., & Michikura, K. (2006). Seismic anisotropy in the uppermost mantle, back-arc region of the northeast Japan arc : Petrophysical analyses of Ichinomegata peridotite xenoliths. *Geophys. Res. Lett.*, 33(10), 2–5.
- Michibayashi, K. & Mainprice, D. (2004). The Role of Pre-existing Mechanical Anisotropy on Shear Zone Development within Oceanic Mantle Lithosphere : an Example from the Oman Ophiolite. *J. Petrol.*, 45(2), 405–414.
- Minear, J. W. & Toksöz, M. N. (1970). Thermal Regime of a Downgoing Slab and New Global Tectonics. *J. Geophys. Res.*, 75(8), 1397–1419.
- Monnier, C., Girardeau, J., Maury, R. C., & Cotten, J. (1995). Back-arc basin origin for the East Sulawesi ophiolite (eastern Indonesia). *Geology*, 23(9), 851–854.
- Moores, E. M., Kellogg, L. H., & Dilek, Y. (2000). Tethyan ophiolites, mantle convection, and tectonic "historical contingency" : A resolution of the "ophiolite conundrum". *Geol. Soc. Am. Spec. Pap.*, 349(3-12).
- Moret, L. (1951). La structure de l'île d'Elbe. *Compte rendu la réunion la société géologique Ital.*
- Moyen, J. F. & Stevens, G. (2013). Experimental Constraints on TTG Petrogenesis : Implications for Archean Geodynamics. *Archean Geodyn. Environ.*, 164, 149–175.
- Mubroto, B., Briden, J. C., McClelland, E., & Hall, R. (1994). Palaeomagnetism of the Balantak ophiolite, Sulawesi. *Earth Planet. Sci. Lett.*, 125, 193–209.

- 
- Mulder, J. A., Berry, R. F., Meffre, S., & Halpin, J. A. (2016). The metamorphic sole of the western Tasmanian ophiolite : New insights into the Cambrian tectonic setting of the Gondwana Pacific margin. *Gondwana Res.*, 38, 351–369.
- Newton, R. C. & Smith, J. V. (1967). Investigations concerning the breakdown of albite at depth in the earth. *J. Geol.*, 75, 268–286.
- Nicolas, A. (1981). *Structures of Ophiolites and Dynamics of Oceanic Lithosphere*. Kluwer aca edition.
- Nicolas, A., Boudier, F., Ildefonse, B., & Ball, E. (2000). Accretion of Oman and United Arab Emirates ophiolite – Discussion of a new structural map. *Mar. Geophysical Res.*, 21, 147–179.
- Nicolas, A., Ceuleneer, G., Boudier, F., & Misseri, M. (1988). Structural mapping in the Oman ophiolites : Mantle diapirism along an oceanic ridge. *Tectonophysics*, 151(1-4), 27–56.
- O’Beirne-Ryan, A. M., Jamieson, R. A., & Gagnon, Y. D. (1989). Petrology of garnet-clinopyroxene amphibolites from Mont Albert, Gaspé, Quebec. *Can. J. Earth Sci.*, 27, 72–86.
- Okay, A. I., Harris, N. B. W., & Kelley, S. P. (1998). Exhumation of blueschists along a Tethyan suture in northwest Turkey. *Tectonophysics*, 285(3–4), 275–299.
- Önen, A. P. (2003). Neotethyan ophiolitic rocks of the anatolides of NW Turkey and comparison with Tauride ophiolites. *J. Geol. Soc. London.*, 160(6), 947–962.
- Önen, A. P. & Hall, R. (1993). Ophiolites and related metamorphic rocks from the Küütahya region, north-west Turkey. *Geol. J.*, 28(3-4), 399–412.
- Önen, A. P. & Hall, R. (2000). Sub-ophiolite metamorphic rocks from NW Anatolia, Turkey. *J. Metamorph. Geol.*, 18(5), 483–495.
- Pagé, P., Bédard, J. H., Schroetter, J.-M., & Tremblay, A. (2008). Mantle petrology and mineralogy of the Thetford Mines Ophiolite Complex. *Lithos*, 100(1-4), 255–292.
- Palin, R. M., White, R. W., Green, E. C. R., Diener, J. F. a., Powell, R., & Holland, T. J. B. (2016). High-grade metamorphism and partial melting of mafic and intermediate rocks. *J. Metamorph. Geol.*
- Pamić, J., Tomljenović, B., & Balen, D. (2002). Geodynamic and petrogenetic evolution of Alpine ophiolites from the central and NW Dinarides : an overview. *Lithos*, 65, 113–142.

- 
- Paris, J. P. (1981). Géologie de la Nouvelle-Calédonie. Un essai de synthèse. *Mem. BRGM*, 113, 278.
- Parkinson, C. (1998). Emplacement of the East Sulawesi ophiolite : evidence from subophiolite metamorphic rocks. *J. Asian Earth Sci.*, 16(1), 13–28.
- Parlak, O., Bozkurt, E., & Delaloye, M. (1996). The Obduction Direction of the Mersin Ophiolite : Structural Evidence from Subophiolitic Metamorphics in the Central Tauride Belt, Southern Turkey. *Int. Geol. Rev.*, 38(8), 778–786.
- Parlak, O. & Delaloye, M. (1999). Precise  $^{40}\text{Ar}/^{39}\text{Ar}$  ages from the metamorphic sole of the Mersin ophiolite (southern Turkey). *Tectonophysics*, 301(1-2), 145–158.
- Passchier, C. W. & Trouw, R. A. J. (1996). *Microtectonics*, volume 256. Springer.
- Peacock, S. M. (1987). Inverted Metamorphic Gradients of New England. *J. Geophys. Res.*, 92(B12), 12763–12781.
- Peacock, S. M., van Keken, P. E., Holloway, S. D., Hacker, B. R., Abers, G. A., & Fergason, R. L. (2005). Thermal structure of the Costa Rica - Nicaragua subduction zone. *Phys. Earth Planet. Inter.*, 149(1-2 SPEC. ISS.), 187–200.
- Peacock, S. M. S. & Wang, K. (1999). Seismic consequences of warm versus cool subduction metamorphism : examples from southwest and northeast Japan. *Science (80-)*, 286(5441), 937–939.
- Pearce, J. A. (2003). Supra-subduction zone ophiolites : the search for modern analogues. *Spec. Pap. Soc. Am.*, (pp. 269–294).
- Pearce, J. A. & Alabaster, T. (1981). The Oman ophiolite as a Cretaceous arc-basin complex : evidence and implications. *R. Soc. Publ.*, 300(1454), 299–317.
- Pearce, J. A., Lippard, S. J., & Roberts, S. (1984). Characteristics and tectonic significance of supra-subduction zone ophiolites. *Geol. Soc. London, Spec. Publ.*, 16(1), 77–94.
- Petrini, K. & Podladchikov, Y. (2000). Lithospheric pressure-depth relationship in compressive regions of thickened crust. *J. Metamorph. Geol.*, 18(1), 67–77.
- Pirard, C. (2012). Transfer of melts in the sub-arc mantle : Insights from high-pressure experiments and from the New Caledonia ophiolite. *Coll. Phys. Math. Sci.*
- Plunder, A., Agard, P., Chopin, C., Pourteau, A., & Okay, A. I. (2015). Accretion, underplating and exhumation along a subduction interface : From subduction initiation to continental subduction (Tavşanlı zone, W. Turkey). *Lithos*, 226(1), 233–254.

- 
- Plunder, A., Agard, P., Chopin, C., Soret, M., & Okay, A. (2016). Metamorphic sole formation, emplacement and blueschist overprint : early obduction dynamics witnessed by western Turkey ophiolites. *Terra Nov.*
- Powell, R. (1985). Regression diagnostics and robust regression in geothermometer/geobarometer calibration : the garnet-clinopyroxene geothermometer revisited. *J. Metamorph. Geol.*, 3(3), 231–243.
- Powell, R. & Holland, T. (1994). Optimal geothermometry and geobarometry. *Am. Mineral.*, 79(1-2), 120–133.
- Powell, R. & Holland, T. J. B. (1988). An internally consistent dataset with uncertainties and correlations : 3. Applications to geobarometry, worked examples and a computer program. *J. Metamorph. Geol.*, 6(2), 173–204.
- Prinzhofer, A. (1981). *Structure et pétrologie d'un cortège ophiolitique : le Massif du Sud (Nouvelle Calédonie) : la transition manteau-croûte en milieu océanique*. Ecole nati edition.
- Prinzhofer, A., Nicolas, A., Cassard, D., Moutte, J., Leblanc, M., Paris, J.-P., & Rabino-vitch, M. (1980). Structures in the new caledonia peridotites-gabbros : implications for oceanic mantle and crust. *Tectonophysics*, 69, 85–112.
- Python, M., Ceuleneer, G., & Arai, S. (2008). Chromian spinels in mafic–ultramafic mantle dykes : Evidence for a two-stage melt production during the evolution of the Oman ophiolite. *Lithos*, 106(1-2), 137–154.
- Rabu, D. (1987). Géologie de l'autochtone des Montagnes d'Oman : la fenêtre du Jabal Akhdar. *Univ. Pierre Marie Curie – Paris VI*.
- Råheim, A. & Green, D. (1974). Experimental determination of the temperature and pressure dependence of the Fe-Mg partition coefficient for coexisting garnet and clinopyroxene. *Contrib. to Mineral. Petrol.*, 48, 179–203.
- Ranalli, G. & Murphy, D. C. (1987). Rheological stratification of the lithosphere. *Tectonophysics*, 132, 281–295.
- Raterron, P., Doukhan, N., Jaoul, O., & Doukhan, J. C. (1994). High temperature deformation of diopside IV : predominance of {110} glide above 1000C. *Phys. Earth Planet. Inter.*, 82(3-4), 209–222.
- Rioux, M., Bowring, S., Kelemen, P., Gordon, S., Dudás, F., & Miller, R. (2012). Rapid crustal accretion and magma assimilation in the Oman-U.A.E. ophiolite : High precision U-Pb zircon geochronology of the gabbroic crust. *J. Geophys. Res.*, 117(B7), B07201.

- 
- Rioux, M., Bowring, S., Kelemen, P., Gordon, S., Miller, R., & Dudás, F. (2013). Tectonic development of the Samail ophiolite : High-precision U-Pb zircon geochronology and Sm-Nd isotopic constraints on crustal growth and emplacement. *J. Geophys. Res. Solid Earth*, 118, 2085–2101.
- Rioux, M., Garber, J., Bauer, A., Bowring, S., Searle, M., Kelemen, P., & Hacker, B. (2016). Synchronous formation of the metamorphic sole and igneous crust of the Semail ophiolite : New constraints on the tectonic evolution during ophiolite formation from high-precision U-Pb zircon geochronology. *Earth Planet. Sci. Lett.*, 451, 185–195.
- Roberts, N. M. W., Thomas, R. J., & Jacobs, J. (2015). Geochronological constraints on the metamorphic sole of the Semail ophiolite in the United Arab Emirates. *Geosci. Front.*, (pp. 1–11).
- Rolland, Y., Billo, S., Corsini, M., Sosson, M., & Galoyan, G. (2009a). Blueschists of the amassia-stepanavan suture zone (Armenia) : Linking tethys subduction history from E-Turkey to W-Iran. *Int. J. Earth Sci.*, 98(3), 533–550.
- Rolland, Y., Galoyan, G., Bosch, D., Sosson, M., Corsini, M., Fornari, M., & Verati, C. (2009b). Jurassic back-arc and Cretaceous hot-spot series In the Armenian ophiolites - Implications for the obduction process. *Lithos*, 112(3-4), 163–187.
- Rollinson, H. (2015). Slab and sediment melting during subduction initiation : granitoid dykes from the mantle section of the Oman ophiolite. *Contrib. to Mineral. Petrol.*, 170(3), 32.
- Rosenberg, C. L. & Handy, M. R. (2005). Experimental deformation of partially melted granite revisited : implications for the continental crust. *J. Metamorph. Geol.*, 23, 19–28.
- Ross, J. & Sharp, W. (1988). The effects of sub-blocking temperature metamorphism on the K/Ar systematics of hornblendes : 40Ar/39Ar dating of polymetamorphic garnet amphibolite from the Franciscan Complex, California. *Contrib. to Mineral. Petrol.*, 100, 213–221.
- Rybacki, E. & Dresen, G. (2000). Dislocation and diffusion creep of synthetic anorthite aggregates. *J. Geophys. Res.*, 105(B11), 26017.
- Rybacki, E. & Dresen, G. (2004). Deformation mechanism maps for feldspar rocks. *Tectonophysics*, 382(3-4), 173–187.
- Rybacki, E., Gottschalk, M., Wirth, R., & Dresen, G. (2006). Influence of water fugacity and activation volume on the flow properties of fine-grained anorthite aggregates. *J. Geophys. Res. Solid Earth*, 111(3).

- 
- Saccani, E. & Photiades, A. (2004). Mid-ocean ridge and supra-subduction affinities in the Pindos ophiolites (Greece) : implications for magma genesis in a forearc setting. *Lithos*, 73(3-4), 229–253.
- Satsukawa, T., Ildefonse, B., Mainprice, D., Morales, L. F. G., Michibayashi, K., & Barou, F. (2013). A database of plagioclase crystal preferred orientations (CPO) and microstructures-implications for CPO origin, strength, symmetry and seismic anisotropy in gabbroic rocks. *Solid Earth*, 4(2), 511–542.
- Savic, G. (1988). *Structural and metamorphic geology of the subophiolitic dynamothermal metamorphic sole and peridotite tec-tonites, Blow Me Down massif, Newfoundland-Canada : Tectonic implications for subduction and obduction*. PhD thesis, University of Houston, Texas.
- Schmidt, N.-H. & Olesen, N. (1989). Computer-aided determination of crystal-lattice orientation from electron-channeling patterns inthe SEM. *Can. Mineral.*, 27, 15–22.
- Searle, M., Cherry, A. G., Ali, M. Y., & Cooper, D. J. W. (2014). Tectonics of the Musandam Peninsula and northern Oman Mountains : From ophiolite obduction to continental collision. *GeoArabia*, 19(2), 135–174.
- Searle, M. P. (1980). *The metamorphic sheet and underlying volcanic rocks beneath the Semail ophiolite in the Northern Oman mountains of Arabia*. PhD thesis, University College of Wales, Aberystwyth.
- Searle, M. P. & Cox, J. (1999). Tectonic setting, origin, and obduction of the Oman ophiolite. *Geol. Soc. Am. Bull.*, 111(1), 0104.
- Searle, M. P. & Cox, J. (2002). Subduction zone metamorphism during formation and emplacement of the Semail ophiolite in the Oman Mountains. *Geol. Mag.*, 139(03), 241–255.
- Searle, M. P. & Malpas, J. (1982). Petrochemistry and origin of sub-ophiolitic metamorphic and related rocks in the Oman Mountains. *J. Geol. Soc. London.*, 139(3), 235–248.
- Shelley, D. (1994). Spider texture and amphibole preferred orientations. *J. Struct. Geol.*, 16(5), 709–717.
- Shervais, J. W. (2001). Birth, death, and resurrection : The life cycle of suprasubduction zone ophiolites. *Geochemistry, Geophys. Geosystems*, 2(2000), 2000G000080.
- Soret, M., Agard, P., Dubacq, B., Plunder, A., Yamato, P., & Prigent, C. (subm). Petrological and tectonic reappraisal of Oman metamorphic soles : the record of plate interface deformation during incipient subduction.

- 
- Soret, M., Agard, P., Dubacq, B., Vitale-Brovarone, A., Monié, P., Chauvet, A., Whitechurch, H., & Villemant, B. (2016). Strain localization and fluid infiltration in the mantle wedge during subduction initiation : Evidence from the base of the New Caledonia ophiolite. *Lithos*, 244, 1–19.
- Sosson, M. & Rolland, Y. (2010). Subductions, obduction and collision in the Lesser Caucasus (Armenia, Azerbaijan, Georgia), new insights. *Geol. Soc. . . .*, 340, 329–352.
- Spray, J. G., Bebien, J., Rex, D. C., & Roddick, J. C. (1984). Age constraints on the igneous and metamorphic evolution of the Hellenic-Dinaric ophiolites. *Geol. Soc. London, Spec. Publ.*, 17(1), 619–627.
- Steinmann, G. (1927). Die ophiolithischen Zonen in dem mediterranen Kettengebirge. *14th Intern. Geol. Congr. Madrid*, 2, 638–667.
- Stern, R. & Bloomer, S. H. (1992). Subduction zone infancy : Examples from the Eocene Izu-Bonin-Marinana and Jurassic California arcs. *Bull. Geol. Soc. Am.*, 104(12), 1621–1636.
- Stern, R. J. (2002). Subduction zones. *Rev. Geophys.*, 40(4).
- Stern, R. J. (2004). Subduction initiation : spontaneous and induced. *Earth Planet. Sci. Lett.*, 226(3-4), 275–292.
- Stünitz, H., Fitz Gerald, J. D., & Tullis, J. (2003). Dislocation generation, slip systems, and dynamic recrystallization in experimentally deformed plagioclase single crystals. *Tectonophysics*, 372(3-4), 215–233.
- Stünitz, H. & Tullis, J. (2001). Weakening and strain localization produced by syn-deformational reaction of plagioclase. *Int. J. Earth Sci.*, 90(1), 136–148.
- Sun, S.-s. & McDonough, W. F. (1989). Chemical and isotopic systematics of oceanic basalts : implications for mantle composition and processes. *Geol. Soc. London, Spec. Publ.*, 42(1), 313–345.
- Syracuse, E. M., van Keken, P. E., Abbers, G. A., Suetsugu, D., Bina, C., Inoue, T., Wiens, D., & Jellinek, M. (2010). The global range of subduction zone thermal models. *Phys. Earth Planet. Inter.*, 183(1-2), 73–90.
- Takazawa, E., Okayasu, T., & Satoh, K. (2003). Geochemistry and origin of the basal lherzolites from the northern Oman ophiolite (northern Fizh block). *Geochemistry, Geophys. Geosystems*, 4(2), 1021.
- Tatham, D. J., Lloyd, G. E., Butler, R. W. H., & Casey, M. (2008). Amphibole and lower crustal seismic properties. *Earth Planet. Sci. Lett.*, 267(1-2), 118–128.

- 
- Tilton, G. R., Hopson, C. A., & Wright, J. E. (1981). Uranium-lead isotopic ages of the Samail Ophiolite, Oman, with applications to Tethyan ocean ridge tectonics. *J. Geophys. Res. Solid Earth*, 86(B4), 2763–2775.
- Tommasi, A. & Vauchez, A. (2015). Heterogeneity and anisotropy in the lithospheric mantle. *Tectonophysics*, 661, 11–37.
- Trzcienski, W. E. J. (1988). Retrograde eclogite from Mont Albert, Gaspé, Quebec. *Can. J. Earth Sci.*, 25, 30–37.
- Ulrich, M., Picard, C., Guillot, S., Chauvel, C., Cluzel, D., & Meffre, S. (2010). Multiple melting stages and refertilization as indicators for ridge to subduction formation : The New Caledonia ophiolite. *Lithos*, 115(1–4), 223–236.
- Van Hinsbergen, D. J., Peters, K., Maffione, M., Spakman, W., Guilmette, C., Thieulot, C., Plümper, O., Gürer, D., Brouwer, F. M., Aldanmaz, E., & Kaymakci, N. (2015). Dynamics of intraoceanic subduction initiation : 2. Suprasubduction zone ophiolite formation and metamorphic sole exhumation in context of absolute plate motions. *Geochemistry, Geophys. Geosystems*, 16, 1771–1785.
- Vanderhaeghe, O. (2009). Migmatites, granites and orogeny : Flow modes of partially-molten rocks and magmas associated with melt/solid segregation in orogenic belts. *Tectonophysics*, 477(3-4), 119–134.
- Vaughan, A. P. & Scarrow, J. H. (2003). Ophiolite obduction pulses as a proxy indicator of superplume events ? *Earth Planet. Sci. Lett.*, 213(3-4), 407–416.
- Vergely, P., Dimo, A., & Monié, P. (1998). Datation des semelles métamorphiques ophiolitiques d'Albanie par la méthode  $^{40}\text{Ar}/^{39}\text{Ar}$  : conséquences sur le mécanisme de leur mise en place. *Académie des Sci.*, 326, 717–722.
- Wakabayashi, J. (1990). Counterclockwise P-T-t paths from amphibolites, Franciscan complex, California : relics from the early stages of subduction zone metamorphism. *J. Geol.*, 98(5), 657–680.
- Wakabayashi, J. & Dilek, Y. (2000). Spatial and temporal relationships between ophiolites and their metamorphic soles : A test of models of forearc ophiolite genesis. *Geol. Soc. Am. Spec. Pap.*, 349, 53–64.
- Warren, C. J., Parrish, R. R., Searle, M. P., & Waters, D. J. (2003). Dating the subduction of the Arabian continental margin beneath the Semail ophiolite, Oman. *Geology*, 31(10), 889–892.

- 
- Wenk, H. R. & Christie, J. M. (1991). Comments on the interpretation of deformation textures in rocks. *J. Struct. Geol.*, 13(10), 1091–1110.
- Whattam, S. A. & Stern, R. J. (2011). The ‘subduction initiation rule’ : a key for linking ophiolites, intra-oceanic forearcs, and subduction initiation. *Contrib. to Mineral. Petrol.*, 162(5), 1031–1045.
- Wheeler, J., Prior, D., Jiang, Z., Spiess, R., & Trimby, P. (2001). The petrological significance of misorientations between grains. *Contrib. to Mineral. Petrol.*, 141(1), 109–124.
- White, R. W., Powell, R., Holland, T. J. B., Johnson, T. E., & Green, E. C. R. (2014). New mineral activity-composition relations for thermodynamic calculations in metapelitic systems. *J. Metamorph. Geol.*, 32(3), 261–286.
- White, R. W., Powell, R., Holland, T. J. B., & Worley, B. a. (2000). The effect of TiO<sub>2</sub> and Fe<sub>2</sub>O<sub>3</sub> on metapelitic assemblages at greenschist and amphibolite facies conditions : mineral equilibria calculations in the system K<sub>2</sub>O–FeO–MgO–Al<sub>2</sub>O<sub>3</sub>–SiO<sub>2</sub>–H<sub>2</sub>O–TiO<sub>2</sub>–FeO<sub>3</sub>. *J. Metamorph. Geol.*, 18, 497–511.
- Whitney, D. L. & Evans, B. W. (2010). Abbreviations for names of rock-forming minerals. *Am. Mineral.*, 95(1), 185–187.
- Williams, H. & Smyth, W. R. (1973). Metamorphic aureoles beneath ophiolite suites and alpine peridotites ; tectonic implications with west Newfoundland examples. *Am. J. Sci.*, 273, 594–621.
- Wyllie, P. J. (1967). *Ultramafic and related rocks*. Wiley New York.
- Yamato, P., Agard, P., Goffé, B., De Andrade, V., Vidal, O., & Jolivet, L. (2007). New, high-precision P-T estimates for Oman blueschists : implications for obduction, nappe stacking and exhumation processes. *J. Metamorph. Geol.*, 25(6), 657–682.
- Yoshikawa, M., Python, M., Tamura, A., Arai, S., Takazawa, E., Shibata, T., Ueda, A., & Sato, T. (2015). Melt extraction and metasomatism recorded in basal peridotites above the metamorphic sole of the northern Fizh massif, Oman ophiolite. *Tectonophysics*, 650, 53–64.



---

## 7 Annexes

7.1 Agard et al. (2016) : *Plate interface rheological switches during subduction infancy : Control on slab penetration and metamorphic sole formation*





Contents lists available at ScienceDirect

## Earth and Planetary Science Letters

[www.elsevier.com/locate/epsl](http://www.elsevier.com/locate/epsl)

## Plate interface rheological switches during subduction infancy: Control on slab penetration and metamorphic sole formation

P. Agard<sup>a,b,\*</sup>, P. Yamato<sup>c</sup>, M. Soret<sup>a</sup>, C. Prigent<sup>d</sup>, S. Guillot<sup>d</sup>, A. Plunder<sup>a</sup>, B. Dubacq<sup>a</sup>, A. Chauvet<sup>e</sup>, P. Monié<sup>e</sup>

<sup>a</sup> Sorbonne Universités, UPMC Univ Paris 06, CNRS, Institut des Sciences de la Terre de Paris (iSTEPI), 4 place Jussieu 75005 Paris, France

<sup>b</sup> Institut Universitaire de France, F-75005 Paris, France

<sup>c</sup> Géosciences Rennes, Université de Rennes 1, CNRS UMR 6118, F-35042 Rennes Cedex, France

<sup>d</sup> Univ. Grenoble Alpes, CNRS, ISTerre, F-38000 Grenoble, France

<sup>e</sup> Géosciences Montpellier, Univ Montpellier 2, CNRS, F-34095 Montpellier, France



## ARTICLE INFO

## Article history:

Received 17 March 2016

Received in revised form 28 June 2016

Accepted 30 June 2016

Available online xxxx

Editor: M. Bickle

## Keywords:

subduction  
metamorphic sole  
rheology  
plate interface  
slab dehydration  
mechanical coupling

## ABSTRACT

Subduction infancy corresponds to the first few million years following subduction initiation, when slabs start their descent into the mantle. It coincides with the transient (yet systematic) transfer of material from the top of the slab to the upper plate, as witnessed by metamorphic soles welded beneath obducted ophiolites. Combining structure–lithology–pressure–temperature–time data from metamorphic soles with flow laws derived from experimental rock mechanics, this study highlights two main successive rheological switches across the subduction interface (mantle wedge vs. basalts, then mantle wedge vs. sediments; at ~800 °C and ~600 °C, respectively), during which interplate mechanical coupling is maximized by the existence of transiently similar rheologies across the plate contact. We propose that these rheological switches hinder slab penetration and are responsible for slicing the top of the slab and welding crustal pieces (high- then low-temperature metamorphic soles) to the base of the mantle wedge during subduction infancy. This mechanism has implications for the rheological properties of the crust and mantle (and for transient episodes of accretion/exhumation of HP-LT rocks in mature subduction systems) and highlights the role of fluids in enabling subduction to overcome the early resistance to slab penetration.

© 2016 Elsevier B.V. All rights reserved.

## 1. Introduction

Understanding subduction initiation, in both space and time, has been a challenge since the advent of plate tectonics (Dewey, 1976; Regenauer-Lieb et al., 2001; Gurnis et al., 2004). What is referred to as “subduction initiation” in the literature encompasses two different concepts and periods: (i) how and where subduction nucleates (i.e., what triggers the beginning of subduction; e.g., Regenauer-Lieb et al., 2001; Stern, 2004), and (ii) how subduction proceeds over the first few million years of its history (“subduction infancy”; Stern and Bloomer, 1992).

This study focuses on subduction infancy, when a newly born slab starts its descent into the mantle and when the thermal regime of the subduction zone progressively cools down be-

fore reaching steady-state (e.g., Syracuse et al., 2010; Plunder et al., 2015; Figs. 1a, b). The only rock remnants of this elusive geodynamic step are thin (~10–500 m) metamorphosed slivers of oceanic crust (metamorphic soles; Williams and Smyth, 1973; Wakabayashi and Dilek, 2000) found beneath pristine, 100–1000 km long, ≤10–15 km thick fragments of oceanic lithosphere emplaced on top of continents as ophiolites (Coleman, 1981; Nicolas, 1989; Fig. 1c).

Metamorphic soles correspond to upper crustal material from the downgoing slab (with variable proportions of basalts and pelagic sediments; Spray 1984; Boudier et al., 1988) and have long been recognized as formed during the first few My of intra-oceanic subduction (Fig. 1b; Dewey, 1976; Spray, 1984; Dewey and Casey, 2013). Their formation would result from heat transfer from the upper plate mantle and/or shear heating when the slab enters the mantle and heats up (Dewey, 1976; Hacker, 1990). Explaining how such thin metamorphosed tectonic slivers of oceanic crust get welded (“underplated”) to the upper plate along hundreds of km (e.g., Oman, Turkey: Hacker and Gnos, 1997; Çelik et al., 2011)

\* Corresponding author at: Sorbonne Universités, UPMC Univ Paris 06, CNRS, Institut des Sciences de la Terre de Paris (iSTEPI), 4 place Jussieu 75005 Paris, France.

E-mail address: [philippe.agard@upmc.fr](mailto:philippe.agard@upmc.fr) (P. Agard).

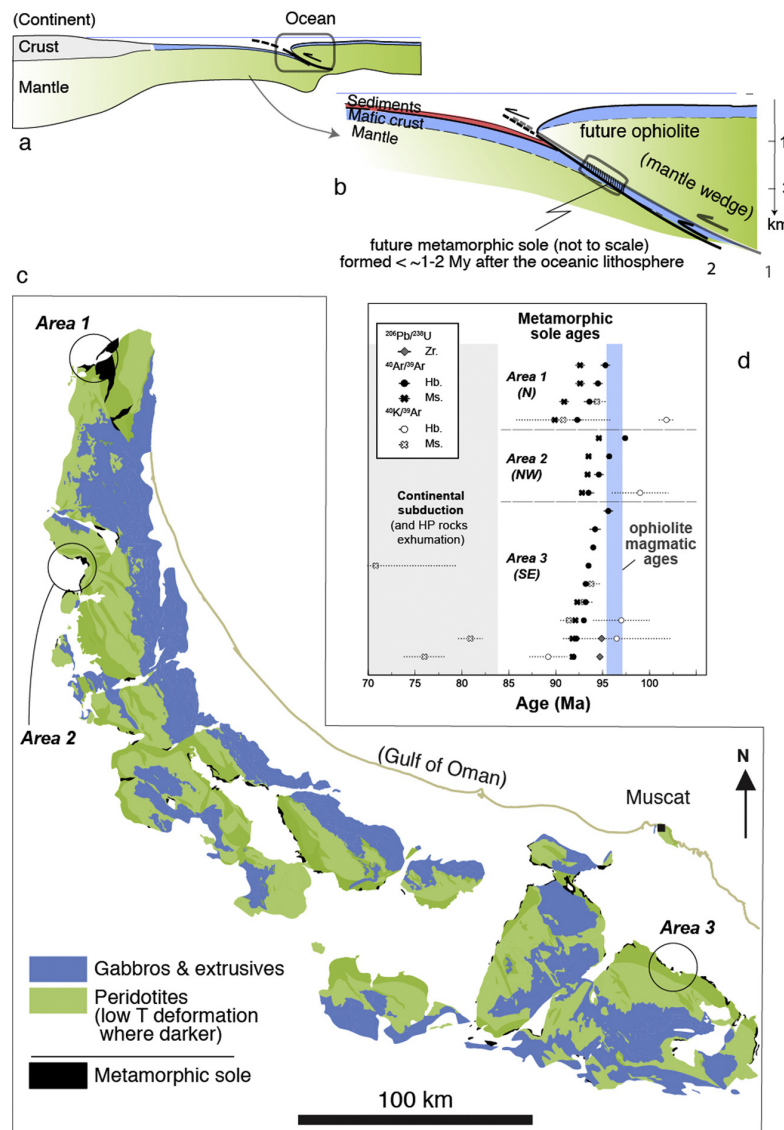


**Fig. 1.** (a) Geodynamic setting of metamorphic sole formation during subduction infancy, following intra-oceanic subduction initiation. The later geodynamic evolution will lead to continental subduction and obduction s.s. (i.e., emplacement of the oceanic lithosphere onto continental lithosphere; after Agard et al., 2007); (b) Close-up view of Fig. 1a: the formation and accretion of metamorphic soles imply a shift of the subduction interface during subduction initiation (from thrust 1 to thrust 2); (c) simplified geological map highlighting the striking continuity of the metamorphic sole beneath the mantle of the Oman ophiolite (modified after Nicolas et al., 2000); (d) age constraints for metamorphic sole formation along the Oman ophiolite (Hb: hornblende; Ms: white mica; Zr: zircon; see Table 1 for references). Radiometric ages for the ophiolite are shown for comparison (after Rioux et al., 2013; see discussion in Section 5.2).

is essential for understanding mechanical coupling during subduction infancy (and possibly during later subduction), but has so far remained enigmatic (Jamieson, 1981; Dewey and Casey, 2013).

This problem is herein addressed by (i) compiling worldwide characteristics of metamorphic soles (i.e., lithologies, internal organization, thicknesses, thermobarometric constraints), augmented by refined estimates for their pressure-temperature ( $P-T$ ) conditions of formation using thermodynamic modeling and by (ii) calculating effective viscosities of materials present along the plate interface from known rheological properties for the crust and mantle (i.e., peridotite, basalt, sediment, serpentinite).

This study reveals the existence of rheological switches across the subduction interface, and proposes that these changes in rheological properties control slab penetration into the mantle and the formation of metamorphic soles during subduction infancy. This

mechanism has implications for effective rheologies of the crust and mantle and for the general understanding of accretion processes and early slab dynamics.

## 2. Metamorphic soles: the record of subduction infancy

### 2.1. Metamorphic sole constitution

The main characteristics (i.e., structural position, lithologies, constitution) and  $P-T$  conditions of metamorphic soles worldwide are reviewed in Fig. 2 and Table 1. This synthesis shows that metamorphic soles are ubiquitous beneath non-metamorphosed ophiolites (e.g., Oman, Turkey, Papua, Newfoundland) and share similar characteristics regardless of the ophiolite or the detailed geological/geodynamical setting (Spray, 1984; Wakabayashi and Dilek, 2003). Radiometric ages of metamorphic soles and ophiolites gen-

**Table 1**

Worldwide compilation of data on metamorphic soles (temperature, pressure, metamorphic ages and thicknesses).

#	Reference location	Authors	Thickness (m)		High temperature conditions					Low temperature conditions <sup>a</sup>			
			HT	LT	P (GPa)	dP (GPa)	T (°C)	dT (°C)	t (Ma)	P (GPa)	dP (GPa)	T (°C)	dT (°C)
1	Oman	Gnos, 1998	≤70		1.1	0.2	800	100	95				
		Gnos and Kurz, 1994	2000		0.77	0.12	825	25		0.5	0.05		
		Ghent and Stout, 1981	30–40	80–85	0.5	0.2	810	55					
		Hacker and Mosenfelder, 1996					825		92.6–95.7				
		Hacker and Gnos, 1997					825	50					
		Searle and Cox, 2002			1.16	0.16	840	70					
		Searle and Malpas, 1980			0.5?		825	50					
		Bucher, 1980								0.4	0.1	500	50
		Hacker et al., 1997							93.7 ± 0.8				
		Hacker et al., 1996	≤500						92.6–95.7				
		Hacker, 1994							92.4–95.7				
		Warren et al., 2003							94.5 ± 0.23				
2	Turkey	Cowan et al., 2014	80	150	1.2	0.1	840	60					
		Okay et al., 1998			0.85	0.35	700	50					
		Plunder et al., 2015			1.1	0.2	800	60					
		Dilek and Whitney, 1997	10–150				≥560		92–90				
		Önen and Hall, 1993	35	122	0.3	0.1	750	50	93–90				
3	Caucasus	Önen, 2003							92–90				
		Parlak and Delaloye, 1999							92.6 ± 0.2				
		Celik and Delaloye, 2006	≤500						91.2 ± 2.3	0.55	0.05	575	25
4	Dinarides	Hassig et al., 2013			0.65	0.05	≥630		91–94				
		Hassig et al., 2015			0.83	0.1	710	40	90.8 ± 3				
5	Cyclades Greece	Pamic et al., 2002	≤600		0.7		730	110	136 ± 15	0.6	0.1	624	9
		Gaggero et al., 2009	600						162.4–172.6				
6	Syria	Gartzos et al., 2009	≤250						150–155				
		Saccani and Photiades, 2004							163 ± 3–172 ± 5				
7	Egypt	Al-Ryami et al., 2002	200–300				≥600		93.4 ± 2				
		Parlak et al., 1996			0.75	0.15	700	50	630–590	0.62	0.15	550	80
8	Newfoundland	El-Naby et al., 2000			0.6	0.15	670	50					
		Farahat, 2011											
		Malpas, 1979	70				750	50		0.6	2	625	75
		Jamieson, 1981		80	0.85	0.15	875	25	480 ± 5	0.42	0.07	600	50
9	Québec	McCaig, 1983	70		0.9	0.2	800	50	477 ± 5				
		Jamieson, 1986			0.8	0.25	900	50		0.4	0.1	575	75
		Savic, 1988	100		0.75	0.15	750	100					
		O'Beirne-Ryan et al., 1990			0.85	0.05	800	50					
10	Brooks Range	Trzcienski, 1988	50	450	1.2		840						
		Clague et al., 1981			0.65	0.15	775	35					
		Malo et al., 2008							465.2 ± 2				
		Harris, 1998	500		0.5		≥650		164–169				
11	California	Wakabayashi, 1990			0.95	0.05	645	15	160–163				
		Lazarro et al., 2013			0.86	0.01	655	10	70				
13	Tibet	Guilmette et al., 2015			1.2	0.25	850	100	132–127				
		Encarnacion et al., 1995	80–250		0.95		730	30	34 ± 0.6				
14	Philippines	Parkinson, 1998	300	300			700	60	30	0.5	0.1	555	15
15	Sulawesi	Meffre et al., 2012			0.85	0.15	725	25	511 ± 4				
		Cluzel et al., 2012			0.6	0.3	800	100	55 ± 2				
17	New Caledonia	Lus et al., 2004	40	160	0.4		900		58.3 ± 0.4				
		THIS STUDY											
18	Papua	Oman (Kh)	This study	100	200	0.95	0.1	850	30				
		Oman (Sum)	–	35	300	0.75	0.1	810	25				
16	Australia	Turkey (Yes)	–	10	100	1.05	0.15	790	35				
		Turkey (Küt)	–	5	20	1.0	0.15	800	40				

<sup>a</sup> Estimates from amphibole-plagioclase thermometry, amphibole barometry or other methods. See supplementary material for references. Abbreviations: Kh: Khubakhib; Küt: Kütahya; Sum: Sumeini; Yes: Yesilova.

erally fall within 1–2 My (e.g., Fig. 1d for Oman; Hacker et al., 1996; Rioux et al., 2013), suggesting the existence of a still warm (i.e., >1000 °C) upper plate mantle near the subduction interface.

Metamorphic soles comprise ~10 to ~500 m thick (Figs. 2b–c) highly strained and metamorphosed crustal rocks where amphibolitized metabasalt dominates, together with increasing proportions of pelagic metasediment structurally downwards (mainly

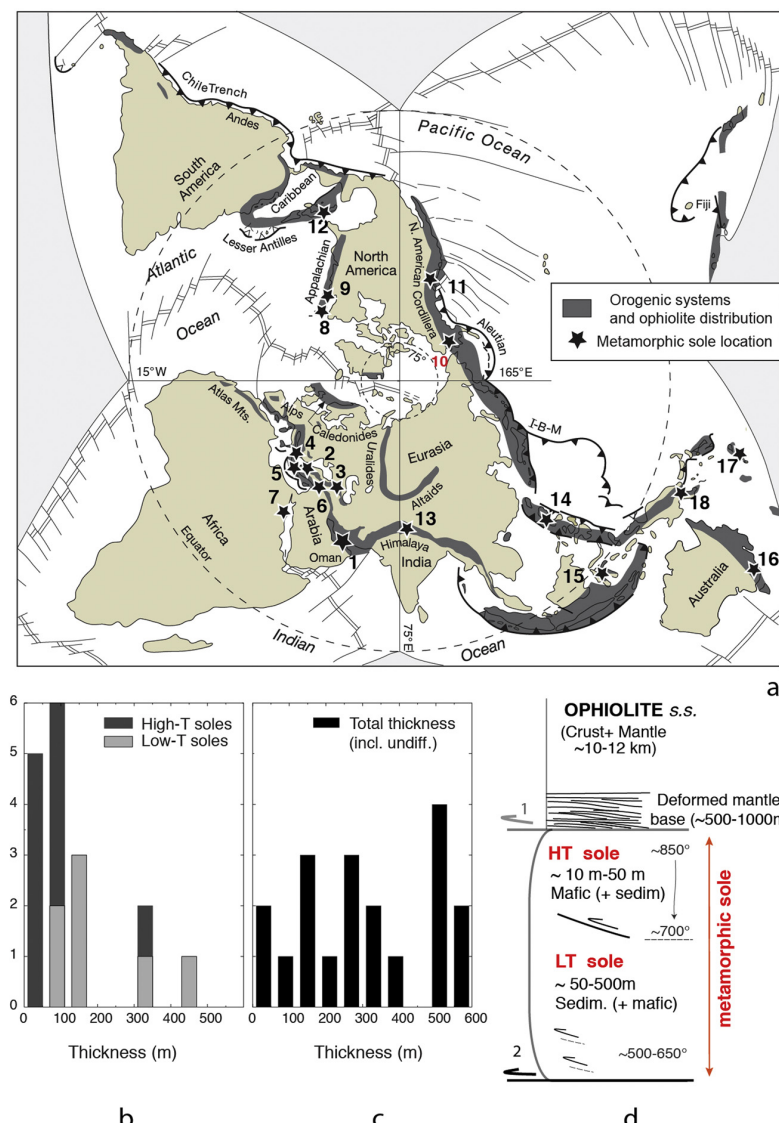


**Fig. 2.** (a) Location of metamorphic soles and of the main large-scale obducted ophiolites worldwide (spanning late Proterozoic to Phanerozoic times); (b) and (c): histograms of thicknesses for metamorphic soles (after Table 1); (d) general structure of ophiolite soles (not to scale), emphasizing differences between the HT and LT sections (temperature indications after Fig. 3a). Note the strongly deformed mantle section at the base of the ophiolite. Thrusts 1 and 2 as in Fig. 1b.

metaradiolarite, with intercalations of metatuff and metapelitic downwards). Vertically, metamorphic soles exhibit an inverted metamorphic sequence with isograds subparallel to the basal peridotite foliation (Spray, 1984). They grade steeply from thin high temperature (HT) granulite/amphibolite facies lithologies adjacent to the overlying peridotites (>700–850 °C; Fig. 2d; e.g., McCaig, 1983; Jamieson, 1986) to thicker amphibolite/greenschist facies low temperature soles (LT; ~550–650 °C; Table 1). This temperature trend is not continuous, however, since the structurally and thermally lower LT sole is arguably formed later, and at lower pressure than the HT sole, by successive stacking of increasing amounts of metasediment (e.g., Malpas, 1979; Casey and Dewey, 1984; Jamieson, 1986; Fig. 2d). Whenever radiometric constraints are available, HT soles are coeval or slightly older than LT soles, yet within ~2 My (e.g., for Oman: Fig. 1d; Hacker et al., 1996; Roberts et al., in press). HT soles and/or LT soles may be missing in places but wherever both are observed, and not disturbed by obvious later tectonics, HT soles are overlying LT soles.

High deformation in the HT and LT soles is marked by mylonites and complex recumbent folding. This deformation, however, is commonly less conspicuous in HT sole mafic amphibolites than in the LT soles (Jamieson, 1981; this study), due to the extent of recrystallization (e.g., Oman) and/or to the lack of lithological heterogeneities. Wherever (rarely) preserved, stretching lineations in the HT soles and LT soles strike differently (e.g., Newfoundland; Dewey and Casey, 2013), suggesting that boundary conditions and/or accretion dynamics may have been modified during sequential underplating.

Some earlier workers, on the basis of rare gabbroic occurrences (associated with dunite and locally intercalated between the mantle and the HT metamorphic amphibolite; Jamieson, 1981), suggested that the whole metamorphic sole could represent a metamorphosed, overturned limb of ophiolite crust (with sediments, basalts and gabbros from bottom to top; see also Wakabayashi and Dilek, 2003). This interpretation is however unlikely: (i) in contrast with the ophiolite crust, gabbros are extremely rare in the soles

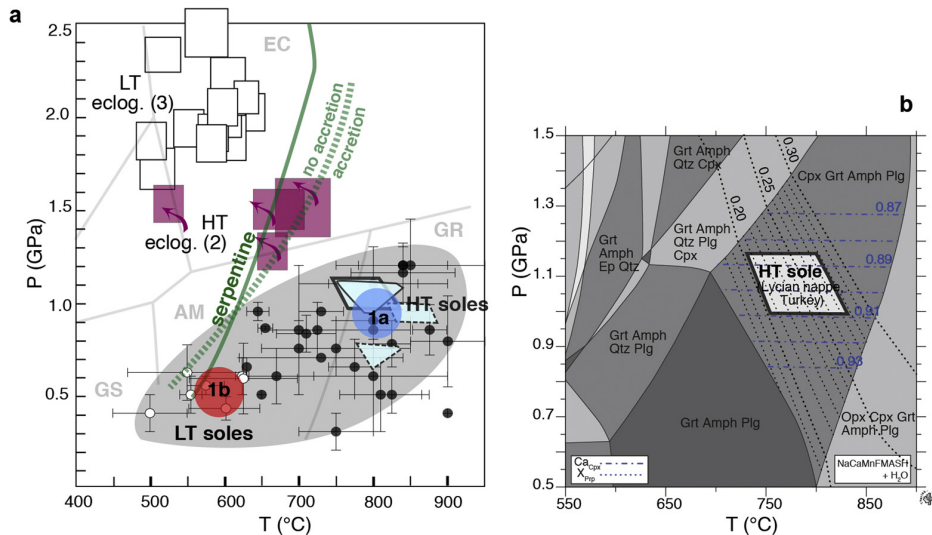


**Fig. 3.** (a) Compilation of pressure–temperature data for HT (black) and LT (white) metamorphic soles (see Table 1; all are enclosed in the grey shaded area).  $P$ – $T$  conditions for representative eclogites (HT: purple; LT: white) are also given for comparison (after Agard et al., 2009). Arrows outline counterclockwise  $P$ – $T$  paths for HT eclogites. Boxes in the HT sole domain correspond to phase diagram calculations in this study. Plain boxes: results for two sample locations in Turkey (Kütahya and Yesilova); dashed boxes: results for two locations in Oman (Sumeini and Khubakhib). The diamond-shaped box with a thicker contour corresponds to the estimate for the HT sole sample from Yesilova described in the text and in Fig. 3b. Samples have the following molar proportions (%): Kütahya: Si (46.92), Al (16.14), Fe (9.98), Mg (10.08), Ca (10.49), Na (6.39)/Yesilova: Si (44.29), Al (16.77), Fe (7.68), Mn (0.45), Mg (15.52), Ca (10.37), Na (4.14)/Sumeini: Si (43.24) Al (15.66) Fe (10.46) Mg (11.37) Ca (16.81) Na (2.46)/Khubakhib: Si (44.85) Al (15.67) Fe (8.82) Mg (11.51) Ca (14.36) Na (4.79). (b) Phase diagram calculated in the Na<sub>2</sub>O–CaO–MnO–FeO–MgO–Al<sub>2</sub>O<sub>3</sub>–SiO<sub>2</sub>–H<sub>2</sub>O chemical system for a MORB-type HT metamorphic sole (YE1302b; Lycian ophiolite, W. Turkey). The studied equilibrium peak assemblage (i.e. garnet–clinopyroxene–amphibole–plagioclase) is stable within a  $P$ – $T$  field refined using mineral isopleths (e.g., pyrope content in garnet:  $X_{\text{Py}}$ ; Calcic component in clinopyroxene:  $\text{Ca}_{\text{Cpx}}$ ) to  $1.08 \pm 0.1$  GPa and  $780 \pm 40^\circ\text{C}$ . Abbreviations for minerals with solid solutions: Amph: amphibole; Cpx: clinopyroxene; Ep: epidote; Grt: garnet; Opx: orthopyroxene; Plg: plagioclase; Qtz: quartz. (For interpretation of the references to color in this figure legend, the reader is referred to the web version of this article.)

(and may represent small-scale intrusions in the mantle), (ii) HT mafic amphibolites tend to have a distinctive nature/geochemical signature (i.e., MORB transitional to OIB or E-MORB; Dewey and Casey, 2013) and (iii) the overturned limb hypothesis fails to explain why pressure conditions in the metasedimentary LT sole are lower than in the HT sole located above (Gnos, 1998; Section 2.2).

The mantle rocks immediately above the metamorphic sole are also highly deformed (Fig. 2d), showing m- to hm-scale deformation patterns consistent with those observed in the underlying HT sole (Boudier et al., 1988), pressure estimates equivalent to those of HT sole peak metamorphism (Jamieson, 1981; McCaig, 1983) and porphyroclastic to ultramylonitic textures formed in the temperature range of 1100 °C down to ~700 °C (Boudier et al., 1988; Michibayashi and Mainprice, 2004; Linckens et al., 2011b). This suggests that the base of the ophiolite mantle deformed and cooled during subduction infancy and that, from a mechanical point of view, the metamorphic sole should be considered as a threefold stack with, from bottom to top, the LT sole, the HT sole and the base of the ophiolitic mantle sequence (hereafter noted as: LTsole\HTsole\basal peridotites).

## 2.2. $P$ – $T$ conditions of metamorphic soles

Published  $P$ – $T$  estimates for metamorphic sole formation (Fig. 3a; Table 1) spread along a high to medium T/P gradient, which partly arises from the diversity and variable precision of thermobarometric methods used. New  $P$ – $T$  estimates for HT soles are provided here using thermodynamic modeling.  $P$ – $T$  phase diagrams for fixed bulk rock composition (pseudosections) were calculated to constrain the conditions of HT sole formation using the Gibbs-free-energy minimization software THERIAK/DOMINO (de Capitani and Petrikakis, 2010; with the updated database of Holland and Powell (1998); tcdb55cc2d.ds) with the following solution models: Diener et al. (2007) for amphibole, Green et al. (2007) for clinopyroxene, White et al. (2007) for orthopyroxene,

Holland et al. (1998) for chlorite, Baldwin et al. (2005) for plagioclase and Holland and Powell (1998) for garnet.  $P$ – $T$  conditions for LT soles are difficult to assess, unfortunately, owing to the high variance of the assemblages and uncertainties in thermodynamic models.

A representative pseudosection (Fig. 3b) was calculated within the chemical system Na<sub>2</sub>O–CaO–FeO–MnO–MgO–Al<sub>2</sub>O<sub>3</sub>–SiO<sub>2</sub>–H<sub>2</sub>O for a typical mafic amphibolite (YE1302b; Lycian ophiolite, W. Turkey) with garnet, clinopyroxene, plagioclase and amphibole. The corresponding sample comes from the region of Salda (South Western Turkey; N037°46'44" E029°56'21"), where garnet–clinopyroxene amphibolites are passing downwards, away from the contact with the overlying peridotite, to amphibolites and then to greenschist facies rocks. Spinel is replaced by plagioclase in the nearby peridotite, suggesting former equilibration of the rock at pressures >0.8–1 GPa. At the thin section scale, garnet and clinopyroxene are intimately intergrown (with globular shape inclusions of clinopyroxene in garnet). Amphibole and plagioclase are found both in the matrix and as inclusions in garnet and clinopyroxene, and therefore formed during peak conditions. Clinopyroxene has diopside compositions with Mg# ~0.80 and a Ca content of 0.88–0.91 per formula unit (p.f.u.). The pyrope content in garnet ranges between 0.20–0.28 p.f.u. and plagioclase (when preserved) has an anorthite fraction of 0.2–0.3.

$P$ – $T$  conditions for the garnet–clinopyroxene–amphibole–plagioclase peak assemblage of sample YE1302b, using mineral isopleths, are  $1.08 \pm 0.1$  GPa and  $780 \pm 40^\circ\text{C}$ . Water amounts were set to match amphibole modes (50–60 vol%). TiO<sub>2</sub> was neglected in the calculation as it enters mainly accessory minerals (rutile, titanite) and amphibole, in which titanium is not accounted for (Diener et al., 2007). The MnO content reproduces the observed garnet chemistry and ensures consistent garnet and clinopyroxene Fe–Mg exchange.

A similar range of estimates was obtained with phase diagrams for metamorphic soles from Turkey (in Kütahya; boxes in Fig. 3a;

**Table 1**) and Oman (in Sumeini and Khubakhib; dashed boxes, Fig. 3a), pointing to definitely high  $P$  values for the upper HT soles when compared to the spread of published estimates (i.e., black dots in Fig. 3a). This conclusion is strengthened by the similarity of available mineral assemblages and compositions worldwide. These estimates are consistent with the presence of only subordinate amounts of melts in the HT soles (Gnos, 1998), suggesting that temperatures do not significantly exceed amphibolite dehydration melting (in agreement with predicted melt fractions <5–10 vol% at 850 °C, depending on pressure; Green et al., in press).

### 2.3. Significance of metamorphic soles within thermal subduction regimes

The above compilation shows that conditions for metamorphic sole formation are remarkably similar worldwide and characterized by the accretion of HT soles that are thinner, more mafic, accreted earlier, at greater depths, at almost invariant  $P$ - $T$  conditions ( $800 \pm 50$  °C at  $1.0 \pm 0.2$  GPa) and always on top of LT soles (equilibrated at  $\sim 600 \pm 50$  °C at  $0.5 \pm 0.1$  GPa).

These estimates are compared to peak conditions reached by oceanic rocks during later subduction, namely those for HT and LT eclogites (Fig. 3a; see Agard et al., 2009 for a review). Their contrasting  $P$ - $T$  conditions exemplify the change in the subduction thermal gradient through time, from warm to cold, from peak burial conditions of  $\sim 800$  °C and 1.0 GPa to  $\sim 550$  °C and 2.5 GPa. Fig. 3a shows that during subduction infancy and subsequent cooling, three rock types successively form from the upper crust of the down-going slab: (1) metamorphic soles within the first 1–2 My, along the hotter gradient, (2) HT oceanic eclogites postdating initiation by  $\sim 5$  My, commonly exhumed in serpentinite mélanges with counter-clockwise  $P$ - $T$  paths (arrows in Fig. 3a; e.g., Wakabayashi, 1990; Garcia-Casco et al., 2006), (3) LT oceanic eclogites formed after 5–10 My and, whenever exhumed, mostly as continuous tectonic slices.

Contrary to metamorphic soles, the fraction of eclogites exhumed worldwide is only rarely accreted to an upper plate ophiolite mantle. Fig. 3a also shows that accretion largely overlaps the domain where serpentine is not stable.

Most HT metamorphic soles do not show later HP-LT metamorphism overprint, such as would be expected from progressive cooling if these rocks had remained at their depth of formation. The implication is that the HT soles formed at  $\sim 1$  GPa must have been accreted and partly exhumed (together with the deformed base of the ophiolite mantle) during subduction infancy (i.e., before significant cooling of the subduction thermal regime), and later underplated below the undeformed ophiolite mantle.

### 3. Rheology of the plate interface and mechanical coupling during subduction infancy

A generic mechanical process is needed to explain how slices of crustal material from the slab get accreted to the mantle wedge (i) only during subduction infancy and (ii) in such a uniform manner. Accretion (or “underplating”) of any tectonic slice across the subduction interface requires the combination of:

- (i) an increase in mechanical coupling across the plate contact beyond some threshold, in order to preferentially localize strain and relative displacement elsewhere within the slab, along some other physical discontinuity (e.g., basalt vs. sediment, or basalt vs. sheeted dykes; Kimura and Ludden, 1995; Dewey and Casey, 2013),
- (ii) some deformation mechanisms allowing for effective slicing within the slab. Whether slicing takes place through slow creep, fluid-mediated slip (such as slow slip events) or re-

peated regular earthquakes is unknown to date and beyond the scope of the present study.

Noteworthily, mechanical coupling is maximum when rheologies on both sides of the plate interface are similar: strain is otherwise localized and the interface is decoupled.

### 3.1. Effective viscosities of plate interface material constrained by rock mechanics

Flow laws derived from experimental rock mechanics (Table 2) are used to estimate the effective viscosity ( $\eta$ ) of plate interface materials as a function of temperature ( $T$ ). Fig. 4a shows this dependency for rocks expected to lie at the base of the upper plate (peridotite, serpentinite) and at the top of the slab (basalt, sediment), using a strain rate ( $\dot{\varepsilon}$ ) derived from natural constraints ( $10^{-13} \text{ s}^{-1}$  for Oman; Linckens et al., 2011b) and the following formula:

$$\eta = \frac{1}{2} A^{-\frac{1}{n}} \dot{\varepsilon}^{\frac{1-n}{n}} \exp\left(\frac{Q}{nRT}\right)$$

where  $n$ ,  $A$ ,  $Q$  and  $R$  correspond to the power-law exponent, the material constant, the activation energy and the gas constant, respectively.

The reader is referred to Karato (2010) and Hirth and Kohlstedt (2015) for reviews of flow laws of relevance for the mantle. These were derived from experiments on dry or wet olivine for dislocation creep (e.g., Hirth and Kohlstedt, 2003) and for grain size dependent deformation mechanisms such as diffusion creep (Hirth and Kohlstedt, 2003; Faul and Jackson, 2007) and dislocation-accommodated grain boundary sliding (disGBS; Hirth and Kohlstedt, 2003; Hansen et al., 2011). Important independent constraints on mantle deformation along the plate interface come from natural data on basal peridotites and mantle shear zones rooting in the deformed mantle base of the ophiolite (Boudier et al., 1988; Linckens et al., 2011a, 2011b). The evolution from 1100 °C in porphyroclastic peridotites to  $\sim 700$  °C in ultramylonites shows that (i) olivine grain size decreases from  $\sim 2$  mm to 10–50  $\mu\text{m}$  and (ii) deformation mechanisms evolve at  $\sim 800$ –850 °C from dislocation creep to grain size sensitive creep, diffusion creep being the most likely dominant mechanism in localized shear bands (the boundary between diffusion creep and disGBS is not well known however; Linckens et al., 2011b).

Flow laws for metamorphic sole mafic rocks are scarce in comparison and can be approached by using wet/dry diabase and mafic granulite. Flow laws are even scarcer for metasediments (Table 2). Given the abundance of metaradiolarites in the LT soles, the flow law of quartz is considered here as representative. Felsic granulite (dashed purple curve; Fig. 4a) may represent an equivalent to a strongly metamorphosed metasediment.

Importantly, at any given temperature and (at least as a first order approximation) regardless of which flow law is used, the mechanical strength of peridotite (i.e., dry or wet olivine: thick green curves and green overlay, respectively; Fig. 4a) is greater than that of mafic oceanic crust (blue overlay in Fig. 4b). Sediments are weaker than basalt, yet stronger than serpentinite. This is emphasized in Fig. 4b, where averages of flow laws are shown for the mantle (i.e., dislocation creep for dry and wet olivine and diffusion creep or disGBS with a grain size of 30  $\mu\text{m}$ ), for the mafic crust (“basalt”) and for serpentinite. It is emphasized that changing the strain rate modifies the absolute value of  $\eta$  but does not affect the relative position of these curves (see supplementary Fig. S1). The strength contrasts existing between these different materials therefore seem independent of strain rate.

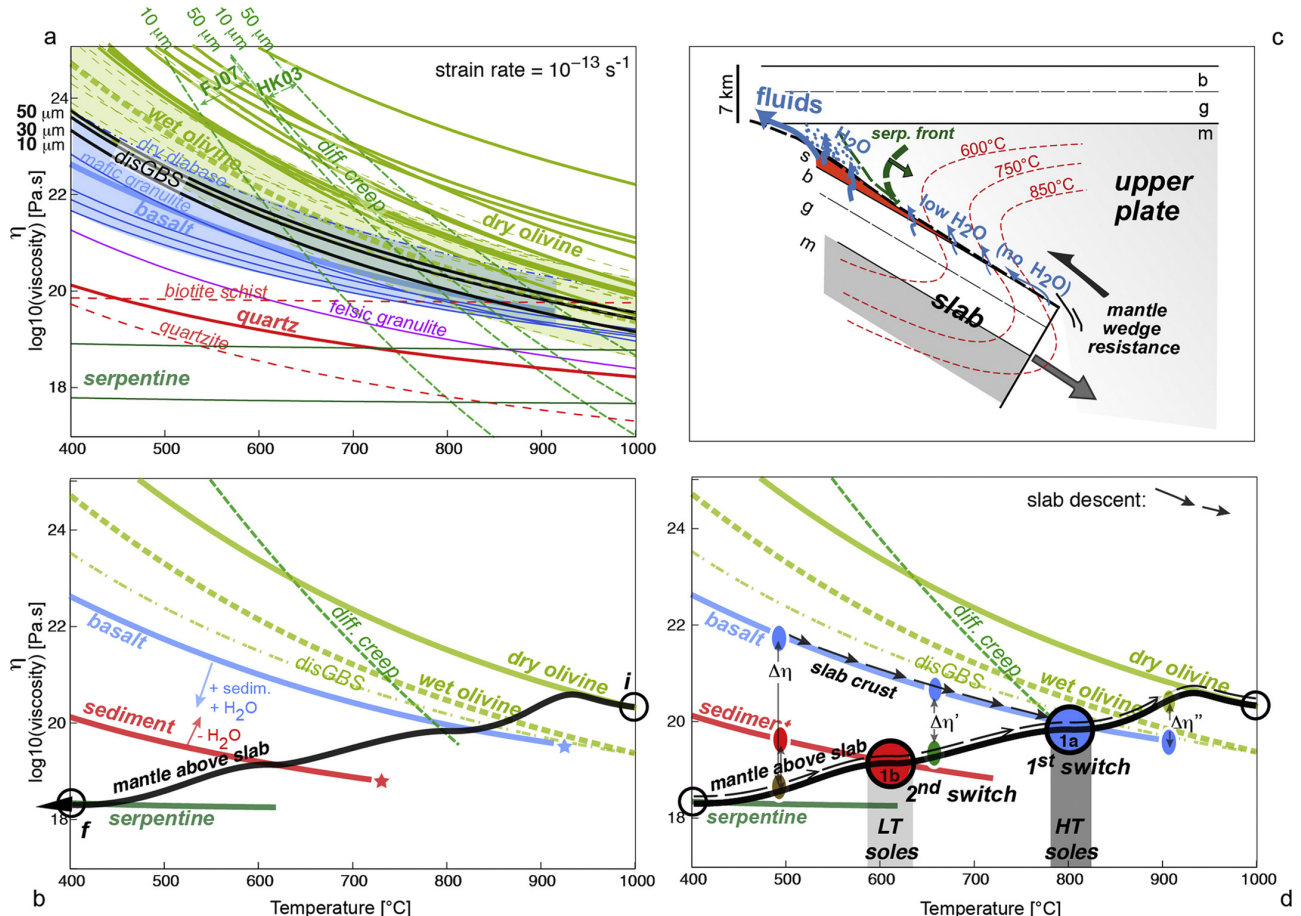


**Fig. 4.** (a) Calculated temperature dependency of effective viscosities ( $\eta$ ) for key plate interface lithologies (peridotite, basalt, sediments and serpentinite; see Table 2 and Section 3.1 for details) for an average strain rate of  $10^{-13} \text{ s}^{-1}$  (after the Oman example; Linckens et al., 2011b). Note the systematic location of the dry and wet olivine dislocation creep flow laws above those for mafic rocks (i.e., basalt, blue overlay). Abbreviations: disGBS: dislocation-accommodated grain boundary sliding; diff creep: diffusion creep; FJ07: Faul and Jackson, 2007; HK03: Hirth and Kohlstedt, 2003. Diffusion creep flow laws have been calculated for two different olivine aggregate grain sizes (10 and 50  $\mu\text{m}$ ) corresponding to the extreme values estimated by Linckens et al. (2011b) in Oman mantle ultramylonites. (b) Plot of averages of published flow laws (after Fig. 4a) showing the qualitative viscosity decrease of a cooling and hydrating mantle wedge, from i to f (see text). Note that the viscosity of incoming crust will tend to decrease (from basalt to sediment) with increasing amounts of sediments and/or with addition of water released from progressive sediment dehydration. Stars mark the inception of melting of basalt and sediments (after Kessel et al., 2005 and White et al., 2007, respectively). (c) 2D sketch of slab penetration during subduction infancy, emphasizing the importance of fluid liberation from the slab. The dashed green line bounds the stability field of serpentine ("serp. front"; blue dots suggest that only part of this domain may be effectively hydrated). Fluid storage capacity of the mantle wedge decreases downwards (see Section 3.2). Background isotherms are taken after 1 My from thermo-kinematic modeling (see supplementary material). Abbreviations: s: sediments (shown here in red, as in Fig. 1b), b: basaltic layer, g: gabbroic layer, m: mantle, serp.: serpentinite; (d) Black arrows outline evolving rheologies of the crust on top of the slab (basalt, then sediment) and of the mantle immediately above the slab (Fig. 4c) when the slab descends during subduction infancy. The rheological contrast across the plate interface between the basaltic crust and mantle wedge evolves from  $\Delta\eta$  to  $\Delta\eta'$  and  $\Delta\eta''$ . Evolution along the black arrows shows the existence of two rheological switches during subduction infancy, when slab crustal rocks reach viscosities comparable to that of the mantle wedge (dots 1a and 1b; see also Fig. 3a). The temperature range for the formation of HT and LT soles is indicated. (For interpretation of the references to color in this figure legend, the reader is referred to the web version of this article.)

### 3.2. Rheological switches across the plate interface

Slab dehydration (see Faccenda, 2014 for a review) can be anticipated to be critical for mechanical coupling during subduction infancy. Fluids released into the nascent mantle wedge (Fig. 4c) will induce serpentinization of the mantle below  $\sim 550$ – $650$  °C (depending on pressure; Fig. 3a; Ulmer and Trommsdorff, 1995). These fluids will be stored in progressively lesser amounts deeper down, first as hydrous phases such as chlorite  $\pm$  amphibole  $\pm$  phlogopite  $\pm$  talc, then at  $T > \sim 850$ – $900$  °C as fluid inclusions or point defects in nominally anhydrous minerals such as olivine or pyroxene (Hirth and Kohlstedt, 2015).

Contrary to the general increase of material strength with cooling (Fig. 4b), cooling of hydrated mantle wedge peridotites will therefore progressively weaken the mantle wedge towards serpen-

tine rheology (from point i to f; Fig. 4b) by (i) absorption of OH in olivine ("wet" olivine) at 1000–900 °C and changes in deformation mechanisms from dislocation creep to grain size sensitive creep at  $T < \sim 850$ – $900$  °C (i.e., diffusion creep and disGBS), (ii) formation of weaker hydrated minerals and eventually (iii) serpentinization. Noteworthily, the viscosity of an even mildly serpentinised peridotite (>15%) approaches that of pure serpentinite (Escartin et al., 2001).

Although the exact rheological path from peridotite to serpentinite cannot be precisely quantified presently, an important conclusion is that mantle wedge viscosities will cross over the curves for metabasalt and then metasediment (Fig. 4b): these two "rheological switches" (i.e., when the mantle wedge first becomes weaker than basalts, then than sediments) most probably occur at  $T \sim 800$  °C (where deformation by diffusion creep and disGBS have

**Table 2**

Published flow laws and material creep parameters used to compute the curves of Fig. 4b.  $n$ ,  $A$ ,  $Q$  and  $m$  correspond to the stress exponent, pre-exponential factor activation energy and grain size exponent, respectively.

Lithology	Authors	$n$	$A$ (MPa $^{-n}$ ) <sup>a</sup> (s $^{-1}$ )	$Q$ (kJ/mol)	$m$
<b>Slab crust</b>					
<b>Sediments</b>					
Quartz	Ranalli and Murphy, 1987	3	6.80E−06	156	
Wet quartzite	Kirby and Kronenberg, 1987	2.3	3.20E−04	154	
Biotite schist	Kronenberg et al., 1990	18	1.20E−30	51	
Schists	Shea and Kronenberg, 1993	31	1.30E−67	98	
Felsic granulite	Wilks and Carter, 1990	3.1	8.00E−03	243	
<b>Mafic crust</b>					
Basalt	Shelton and Tullis, 1981 and Hacker and Christie, 1990	3.5	1.00E−04	250	
Wet diabase	Shelton and Tullis, 1981	3.4	2.00E+04	260	
Dry diabase	Mackwell et al., 1998	4.7	8.00E+00	485	
Diabase	Van Hunen and Van den Berg, 2008	3.4	2.21E−04	260	
Microgabbro	Wilks and Carter, 1990	3.5	4.85E+04	535	
Mafic granulite	Wilks and Carter, 1990	4.2	1.40E+04	445	
<b>Mantle wedge</b>					
Dry olivine	Chopra and Paterson, 1981	3.6	4.50E+00	535	
–	Chopra and Paterson, 1984	3	1.00E+04	520	
–	Chopra and Paterson, 1984	3.5	2.50E−04	532	
–	Karato et al., 1986	3.5	5.40E+00	540	
–	Karato and Wu, 1993	3.5	2.42E+05	554	
–	Karato and Rubie, 1997	3	2.40E+05	554	
–	Bussod et al., 1993	3.5	1.12E+05	545	
–	Hirth and Kohlstedt, 2003	3.5	1.10E+05	548	
–	Karato and Jung, 2003	3	1.26E+06	524	
–	Li et al., 2006	3	4.57E+03	554	
–	Kawazoe et al., 2009	3.5	1.10E+05	550	
Diffusion creep	Hirth and Kohlstedt, 2003	1	1.5E+09	375	3
Diffusion creep	Faul and Jackson, 2007	1.4	2E+10	484	2
DisGBS	Hirth and Kohlstedt, 2003	3.5	6.5E+03	400	2
Wet olivine	Chopra and Paterson, 1981	4.4	2.76E+02	498	
–	Chopra and Paterson, 1981	4	2.00E+03	471	
–	Karato et al., 1986	3	1.50E+06	250	
–	Evans and Kohlstedt, 1995	4.5	2.60E+00	498	
–	Hirth and Kohlstedt, 1996	3.5	4.88E+06	515	
–	Mei and Kohlstedt, 2000	3	4.57E+03	470	
–	Mei and Kohlstedt, 2000	3	5.01E+02	508	
–	Karato and Jung, 2003	3	3.63E+00	421	
–	Karato and Jung, 2003	3	7.94E+02	470	
–	Hirth and Kohlstedt, 2003	3.5	9.00E+01	491	
–	Hirth and Kohlstedt, 2003	3.5	1.60E+03	520	
–	McDonnell et al., 1999 <sup>a</sup>	2.14	9.10E+03	302	
Serpentinite	Hilairet et al., 2007	5.8	2.51E−13	20.8	
–	Hilairet et al., 2007	3.8	2.51E−09	12.1	

<sup>a</sup> Calculated with  $X_{\text{H}_2\text{O}} = 0.05 \text{ wt\%}$ . DisGBS: dislocation-accommodated grain boundary sliding. See supplementary material for references.

similar effective viscosities; Fig. 4a, b) and  $\sim 600^\circ\text{C}$ , respectively. The temperature and viscosity values for the HT rheological switch (Fig. 4d) both match the temperature ( $T \sim 800\text{--}850^\circ\text{C}$ ; Boudier et al., 1988; Linckens et al., 2011a) and viscosity ( $\eta \sim 10^{20\text{--}21} \text{ Pas}$ ; Linckens et al., 2011b; Tasaka et al., 2014) inferred from the high strain mylonitic to ultramylonitic deformation of adjacent banded peridotites from the base of the ophiolite.

#### 4. Model for slab penetration into the mantle and metamorphic sole formation

##### 4.1. Evolution of rheological contrasts across the plate interface during subduction infancy

Fig. 4d shows the evolution of the rheological contrast across the plate interface during incipient slab penetration, as the top of the slab progressively heats up, weakens and dehydrates. The top of the slab is first considered as essentially made of mafic crust (i.e., basalt; Fig. 4c), sediments being probably scarce at the start of intra-oceanic subduction, far away from the continent (Fig. 1a). At shallow depths and for temperatures below  $\sim 550\text{--}600^\circ\text{C}$ , the subducting oceanic (basaltic) crust is juxtaposed against an incipiently serpentinised mantle on top (as schematized in Fig. 4c).

A sharp viscosity contrast ( $\Delta\eta$ ) exists on either side of the subduction plane (strong basalt vs. weak mantle wedge; Fig. 4d).

As depth and temperature increase, the subducting crust weakens and progressively encounters a warmer, stronger, unserpentised and less hydrated mantle wedge ( $\Delta\eta'$  in Fig. 4d), where grain size sensitive deformation mechanisms take over (Linckens et al., 2011a; Hirth and Kohlstedt, 2015). The viscosity contrast across the interface reverses (weak basalt vs. stronger mantle wedge) at  $T > \sim 800^\circ\text{C}$ , once the subducting crust is juxtaposed against an almost dry peridotite rheology ( $\Delta\eta''$  in Fig. 4d).

A similar evolution can be envisioned if sediments are present on top of the slab, with a viscosity reversal (sediment vs. mantle wedge) taking place at  $\sim 600^\circ\text{C}$  ("second rheological switch"; Fig. 4d). Although the extent to which basalts and sediments harden as a result of prograde mineral transformations is unknown, flow laws indicate that these rheological switches exist, even considering the change from basalt to mafic granulite or from sediment/quartzite to felsic granulite (Fig. 4a). They will also take place regardless of the age of the overriding lithosphere, although at different depths (the warmer the lithosphere, the shallower the rheological switches).

Rheological switches bear major consequences on mechanical coupling during early slab penetration:

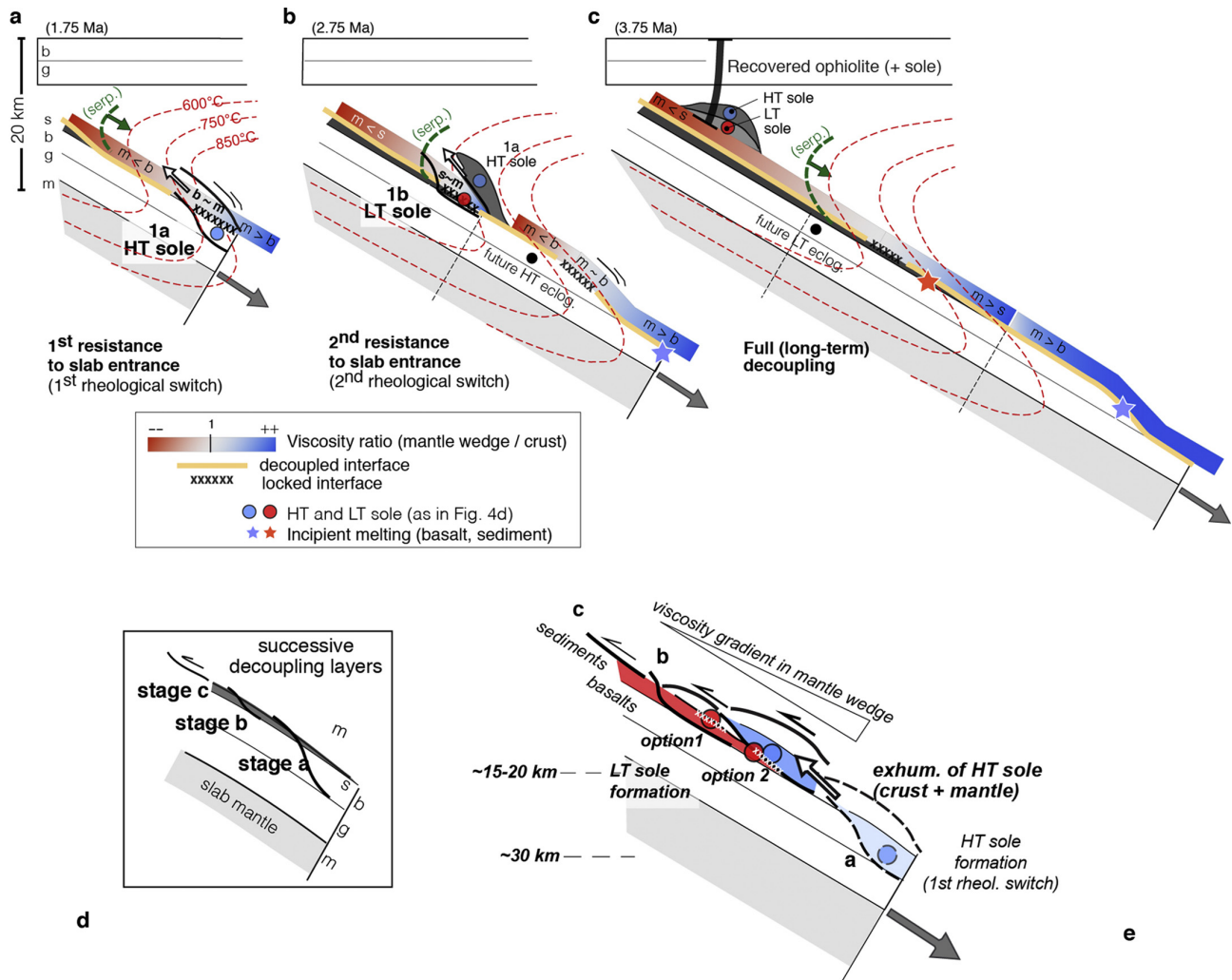


**Fig. 5.** Model evolution for slab penetration and metamorphic sole formation during subduction infancy (2D sketches and abbreviations as in Fig. 4c; the dashed green line marks the downdip limit of the stability of serpentine, “serp.”; the white arrow indicates exhumation): (a) strong interplate mechanical coupling due to the first rheological switch (i.e., when mantle wedge viscosity  $\sim$  slab basal viscosity). Resistance of the mantle wedge to slab penetration triggers the peeling of the slab and HT sole formation. Isotherms and depths are from thermo-kinematic modeling (see supplementary material). Stars indicate incipient melting of basalts and sediments (and plagiogranite formation; Rioux et al., 2013); (b) second rheological switch and LT sole formation. HT metabasalts metamorphosed deeper down in the locked zone are not returned as HT soles (see Section 5.2.1). Some HT eclogites may get embedded in a softer mantle wedge and exhumed early in the subduction process; (c) the plate interface progressively ‘unzips’ by the downward extension of serpentinization until full decoupling.  $P$ - $T$ -rheological conditions are such that LT eclogites form along the subduction zone but are only rarely exhumed (see Section 5.2.1); (d) close-up view on the tectonic configuration along the plate interface during LT sole accretion, when partial exhumation of the HT sole (shown by the white arrow) juxtaposes it onto the LT sole. Accretion of the LT sole may correspond to the mechanical coupling of the sediments with the mantle above (second rheological switch; option 1) or to the mechanical coupling of the sediments with a progressively weakened mafic HT sole (option 2). See text for details. (e) Progressive strain localization results in more superficial decoupling over time within the slab, so that accretion becomes restricted after a few My to shallow near-trench infill. (For interpretation of the references to color in this figure legend, the reader is referred to the web version of this article.)

- (i) at any given time the strength of the mantle wedge will increase downwards (Fig. 4c), so that the slab can be expected to face greater resistance to penetration with depth (at least until mantle melting occurs);
- (ii) as the thermal regime cools with time, the domain where serpentine is stable (above “serp. front” in Fig. 4c) will expand continuously downwards.

#### 4.2. Metamorphic sole formation linked to strong interplate mechanical coupling

Effective viscosities of the lower plate crust and upper plate mantle therefore converge and switch, during subduction infancy, across restricted  $T$  windows (Fig. 4d; with  $P$  and time generally  $\sim 1$  GPa and  $< 2$  Myr, these are restricted  $P$ - $T$ - $t$  windows too). We

propose that the detachment and accretion of metamorphic soles is triggered by peaks of interplate mechanical coupling associated with rheological switches, that distribute deformation over large, km-scale bands across the subduction interface (e.g., Yuen et al., 1978) and localize strain further into the slab where/if a sharper viscosity contrast exists (e.g., Kimura and Ludden, 1995).

Slab penetration and metamorphic sole formation are tentatively reconstructed in Fig. 5 in three major steps (isotherms and depth-time trajectories are from thermo-kinematic models detailed in supplementary material; Figs. S2–S4):

(1) Plate interface mechanical strength peaks during the first rheological switch (metamorphosed basalt vs. metasomatized upper mantle; Fig. 5a) at  $T \sim 750$ – $850^\circ\text{C}$ , leading to the formation of essentially mafic HT metamorphic soles (dot 1a, Fig. 4d). Detachment on a weaker horizon within the slab probably takes place

at the transition between hydrothermalized/weakened basaltic layers and drier basalts below, and/or between basalts and sheeted dykes (if present), accounting for the general lack of metagabbros in metamorphic soles.

(2) Accretion of the metasedimentary-rich LT soles takes place at lower  $T$  (and  $P$ ) conditions at  $\sim 550\text{--}650^\circ\text{C}$  and  $\sim 0.5\text{ GPa}$ , after the partial exhumation of the HT sole (Fig. 5b). This corresponds to the second rheological switch (dot 1b, Fig. 4d). Two different scenarios of mechanical coupling can however be envisioned: (i) between the sediments and the incipiently serpentined, weakening upper mantle (option 1; Fig. 5d) or (ii) between the sediments and the base of the HT sole (option 2; Fig. 5d), whose viscosity will be shifted from basalt to sediment as the sedimentary column increases (blue arrow, Fig. 4b; a similar shift is expected if strain rate increases or if basalt from the HT sole get hydrated by water released from sediments below). Option 2 is supported by the general lack of (serpentined) mantle between the LT and HT sole (see Section 2). Option 1 implies that the mantle above the LT sole is tectonically removed by the exhumation of the (more resistant) HT sole and basal peridotites (Fig. 5d). Option 1 would nevertheless explain the occurrence of LT soles directly beneath the mantle. Accretion of the LT sole indicates, in any case, that the detachment horizon within the slab is located within the sedimentary pile.

The fact that HT soles are thinner than LT soles could result from larger amounts of accumulated strain and later ductile thinning, from the peeling of thinner slices during the first rheological switch and/or from longer duration of accretion during the LT episode.

(3) As the thermal regime of the subduction continues to decrease (Fig. 5c), incoming sediment and basalt remain stronger than the increasingly serpentined mantle wedge (Fig. 4d): the plate interface progressively ‘unzips’ downwards. LT eclogites, which start forming within the refrigerated subduction zone (Fig. 5c), are less likely to get mechanically coupled to the weakened upper plate. This can be the reason why they are rarely exhumed (Agard et al., 2009), in agreement with their location in the serpentine stability field (“no accretion” domain in Fig. 3a).

#### 4.3. Impact of subduction cooling on interplate mechanical coupling

Fig. 5 highlights how cooling dramatically impacts slab penetration during subduction infancy:

- (i) The mantle wedge acts as a buttress which progressively softens with time: it only transiently peels off the slab crust during the first My, thereby forming metamorphic soles, then progressively loses strength with cooling/serpentization until full decoupling;
- (ii) Strain localizes with time in shallower decoupling horizons within the slab (Fig. 5e): accretion affects the top of the mafic crust (stage a), then only the sediments on top (stage b) and, when the plate interface becomes decoupled after a few My (stage c), accretion is restricted to shallow, near-trench infill (e.g., unmetamorphosed Hawasina units found in Oman beneath the metamorphic sole and the ophiolite; Searle and Malpas, 1980; Searle and Cox, 2002), as in present-day accretionary wedges (e.g., Nankai prism). The width of the plate interface shear zone may therefore decrease with time.

## 5. Discussion

The proposed mechanism for metamorphic sole formation and slab penetration (Fig. 5) explains why, through two main steps of accretion, metamorphic soles form and get accreted at remarkably similar  $P\text{--}T$ -time conditions worldwide (Section 2.3) and across a

transient period of subduction lifetime only (i.e., when rheological switches take place).

### 5.1. Uncertainties on $P\text{--}T$ -time conditions, viscosity estimates and strain rate

#### 5.1.1. $P\text{--}T$ -time constraints

$P\text{--}T$  estimates ( $800 \pm 50^\circ\text{C}$  at  $1.0 \pm 0.1\text{ GPa}$  for the early thin HT sole and  $600 \pm 50^\circ\text{C}$  at  $\sim 0.5 \pm 0.1\text{ GPa}$  for the late, thicker LT sole; Fig. 3) depend on the accuracy of thermodynamic models for pyroxene and amphibole. These models were considerably refined but Ti- and  $\text{Fe}^{3+}$ -substitutions in amphiboles are complex and mafic melts are notoriously difficult to model (Diener and Powell, 2012 and references therein; Green et al., in press). Larger uncertainties on pressure conditions for LT soles arise from lesser constraints in the high-variance greenschist to epidote amphibolite fields. The major uncertainty therefore lies in the exact pressure gap between the HT and LT soles, and whether there might be a continuum in between.

Age constraints for HT and LT metamorphic soles tightly cluster within 1–2 My (Table 1; Fig. 1d). The short duration of the process and/or apparent synchronicity might be exaggerated by the fact that  $^{40}\text{Ar}/^{39}\text{Ar}$  ages on amphibole may represent cooling ages for the HT soles (i.e., below  $550^\circ\text{C}$ ), whereas age constraints for the LT sole could represent crystallization ages. But the fact that the LT soles are found below the HT ones (whom underlie the mantle base of the ophiolite) leaves little doubt that they were accreted afterwards. Thermo-mechanical modeling of a cooling subduction zone also shows that cooling lasts no more than a few My (Duretz et al., 2015).

#### 5.1.2. Viscosities and strain rates

One of the largest uncertainties with experimental flow laws is that they are performed at (and extrapolated from) conditions orders of magnitude faster than nature (typically  $10^{-4}\text{--}10^{-6}\text{ s}^{-1}$  versus  $10^{-12}\text{--}10^{-15}\text{ s}^{-1}$  in nature; Burov, 2007; Hirth and Kohlstedt, 2015). Field evidence, however, suggests that mafic, clinopyroxene and plagioclase bearing lithologies are  $\sim 2$  orders of magnitude weaker than dry peridotite at  $\sim 700\text{--}800^\circ\text{C}$  (e.g., Homburg et al., 2010), in agreement with the respective position of calculated flow laws (Fig. 4b, c). Viscosity estimates for the first, HT rheological switch ( $\sim 10^{20}\text{--}21\text{ Pas}$ ; Fig. 4d) are also in remarkable agreement with values deduced from natural observations on strained peridotites from the (ultra)mylonitic base of the ophiolite mantle ( $10^{20}\text{--}21\text{ Pas}$ ; Linckens et al., 2011b; Tasaka et al., 2014).

Another uncertainty comes from the simplifying assumption of considering similar strain rates for estimating the viscosities of all lithologies (Fig. 4b), whereas faster strain rates can be expected where strain localization takes place. Regardless of strain rate, however, “rheological switches” and converging mechanical behavior between the mantle and basalt/sediment will take place across the interface: as the mantle wedge evolves progressively from dry to serpentined, its viscosity curve is bound to cross that of basalt then of sediment (Fig. 4b, d), and this order is independent of strain rate (e.g., from  $10^{12}$  to  $10^{14}\text{ s}^{-1}$ ; Fig. S1). This conclusion is not modified by shear heating either, which only changes the temperature field and shifts the  $T$  window of metamorphic sole formation to shallower depths, but not the characteristic “S-shape” of the isotherms (Fig. S5; so does the thermal state of the upper plate: Fig. S2b, c).

Complex feedbacks may nevertheless exist, since similar viscosities on each side will increase interplate mechanical coupling, which will in turn decrease strain rates, hence probably decrease shear heating (also depending on the width onto which deformation is distributed). Further testing of this scenario using self-

consistent fully coupled thermomechanical models is therefore needed, but there are major challenges:

- (i) refined rheologies for sediments, variably hydrated basalts and gabbros, taking into account the influence of hydrothermal alteration, progressive metamorphic recrystallization, water loss or plagioclase content on crustal rocks are unknown (e.g., Getsinger and Hirth, 2014). The same holds true for the rheology of the mantle wedge (as yet unconstrained, as is fluid migration inside; Faccenda, 2014), for polyphase lithologies that also probably exist along the plate interface, for the impact of subordinate amounts of melt in the HT soles (<~10%), or for assessing the influence of pressure or the extent to which frictional energy is converted into heat (which also depends on rheological laws).
- (ii) appropriate spatial resolution (i.e., down to ~10 m) is required in self-consistent visco-elasto-plastic geodynamic models in order to localize strain and (progressively) slice and detach pieces from the slab, in addition to reaching sufficient temporal resolution (e.g., van Dinther et al., 2013).

Further modeling will help constrain the depth and duration of these processes. The simple thermo-kinematic models used to derive the isotherms of Fig. 5 (see supplementary material) suggest that for a set of realistic velocities, initial thermal age and slab dip, incoming crustal rocks may cross the temperature range of HT sole formation (~750–850 °C) at depths of ~25–35 km and that accretion of individual slices may last on the order of 0.3–0.4 My (Fig. S3). Although inferred from simplified models, these constraints point to the possible formation of metamorphic soles across a range of depths, possibly accounting for some of the scatter observed in the *P-T* estimates for metamorphic soles worldwide (Fig. 3a).

## 5.2. Accretion and exhumation during subduction infancy

### 5.2.1. Accretion of HT soles and incorporation of HT eclogites in serpentinite mélanges

Accretion of mafic HT soles will last less than shown in the reconstruction and probably stop (or decrease) once a significant amount of sediments reaches the trench and becomes involved in the plate interface (Fig. 5b): since incoming sediments reach their rheological switch with the mantle wedge at lower *T* than basalts (Figs. 4c, d), their arrival along the plate interface will indeed localize strain and thus deactivate basalt accretion.

As a result of progressive cooling of the subduction zone, potential accretion of HT soles further downdip can be predicted for a few more My after subduction initiation (Fig. 5b). Such rocks, however, are not accreted below ophiolites and/or not exhumed, which could be due to rock densities exceeding mantle values (thermodynamic modeling shows that this will be the case for basalt at 800 °C for *P* > 1.2 GPa), to dynamics associated with melting at depth (Faccenda, 2014) and/or to the resumption of full coupling between the plates (Syracuse et al., 2010) dragging down these rocks irreversibly.

In contrast, later and further downdip, the mantle wedge will get colder, more hydrated and therefore more buoyant while transiently remaining fairly strong (i.e., still mechanically strongly coupled). HT eclogites and the heterogeneously hydrated/weakened mantle wedge may thus reach broadly equivalent viscosities towards the end of subduction infancy, thereby favoring mechanical coupling, rock mixing and fast (buoyant) joint exhumation. This could explain the anticlockwise, short-lived exhumation of HT eclogites in serpentinite mélanges at depths of 50–60 km and ~5 My after subduction nucleation (Figs. 3a, 5c; e.g., Francis-

can complex or Serpentinite mélange of Cuba; Garcia-Casco et al., 2006).

### 5.2.2. Exhumation of HT soles and basal peridotites: the depth conundrum

This study highlights the contrast between the juxtaposition of HT soles and basal peridotites at ~25–35 km (assuming purely lithostatic *P* estimates) and the final ophiolite thickness (~10–15 km). Whether this can be explained by mantle thinning (Casey and Dewey, 1984; Dewey and Casey, 2013) or relative exhumation (or both) has been a matter of speculation (e.g., the “conundrum of Samail”; Hacker and Gnos, 1997). Mantle thinning would have to be concentrated within the basal peridotites (500–1000 m thick at present) as the rest of the mantle section is mostly undeformed (Ceuleneer et al., 1988; Nicolas et al., 2000), and does not explain how metamorphic soles get accreted.

Based on the pressure difference between the HT and LT soles and on the similar *P-T* conditions retrieved from HT soles and basal peridotites (e.g., Jamieson, 1981; McCaig, 1983; this study), the reconstruction of Fig. 5 depicts their relative exhumation with respect to the rest of the overlying oceanic lithosphere, thanks to buoyancy/rheology contrasts (and through successive stacks: HTsole\peridotite, then LTsole\HTsole\peridotite). The lower density of the slices would account for their exhumation with respect to the overlying mantle, while the rheology (viscosity) contrasts above and below the slices would favor strain localization. Relative exhumation is also supported by the existence of rare blueschist facies overprints on HT soles underlain by blueschist facies rocks (e.g., Turkey; Plunder et al., 2015, *in press*), indicating that, in some cases, the HT sole is not immediately exhumed and stagnates at depth (which would not be the case if the mantle was systematically thinned).

An alternative explanation to the depth conundrum could be that the ~1 GPa pressure estimate for the HT soles corresponds to overpressure arising from strongly coupled lithologies (i.e., dry mantle against basalt; McCaig, 1983). Depths attributed to the deformation of HT soles and basal peridotites could then be reduced by up to a factor of 2 (Petrini and Podladchikov, 2000), matching both the depths/pressures of LT soles and final ophiolite thickness (~10–15 km). Whether such rocks, affected by strong ductile deformation, may sustain excess dynamic pressure is unclear and could be tested with numerical models (with limitations discussed in Section 5.1.2). Overpressure would not, however, affect the conclusions of this study regarding mechanical coupling, accretion or the existence of rheological switches.

### 5.2.3. Are metamorphic soles formed beneath supra-subduction ophiolites?

While the proposed mechanism emphasizes the importance of rheology during subduction infancy, the nature and genesis of ophiolites is still a matter of debate (see Rioux et al., 2013 for a recent discussion), with authors in favor of a MORB-type pre-existing lithosphere (Nicolas, 1989; Nicolas et al., 2000) and others supporting an entirely supra-subduction origin (Stern and Bloomer, 1992). In the first hypothesis, formation of oceanic lithosphere shortly predates intra-oceanic subduction (via near-ridge, detachment or transform fault inversion; Boudier et al., 1988), while in the second hypothesis intra-oceanic spontaneous subduction (often assumed to take place at transform faults) triggers the formation of supra-subduction lithosphere by mantle upwelling (e.g., Stern and Bloomer, 1992). The interplay between lithology/rheology, *T* (and *P*) and mechanical coupling of our proposed mechanism could in principle operate through either inversion of small oceanic basins or mantle upwelling following spontaneous subduction initiation. The second scenario, however, less easily explains the systematic

juxtaposition of HT soles onto LT soles (and the sharp lithological divide between them), as well as the slightly younger and more dispersed ages of the metamorphic soles when compared to those of the ophiolite crust (Fig. 1d; Wakabayashi and Dilek, 2000, 2003). Metamorphic sole formation may thus question the popular spontaneous subduction initiation model (Stern and Bloomer, 1992).

### 5.3. Rheological implications

An important inference from this model is that the effective rheologies of the mantle and crust are similar at  $\sim 800^\circ\text{C}$  and  $\sim 1 \text{ GPa}$  in the presence of fluids. This is an important anchor point for experimental rock mechanics, supporting the validity of extrapolations from laboratory experiments performed orders of magnitude faster than in nature. Although the viscosity–temperature path of the mantle wedge (from i to f; Fig. 4b) or location of the first rheological switch are not determined with precision yet, their location (at  $\pm 50^\circ\text{C}$  and  $\sim 1$  order of magnitude in viscosity) further supports the convergence of the experimental grain size dependent flow laws at  $\sim 800^\circ\text{C}$  (i.e., at the temperature of HT sole formation; Fig. 4d).

Fig. 5 also highlights the importance, for strain localization during subduction infancy, of lubrication by hydrous phases (Regenauer-Lieb et al., 2001; Dymkova and Gerya, 2013) and grain size reduction (Lincikens et al., 2011b; Hirth and Kohlstedt, 2015). Viscosity estimates for sole formation (Fig. 4d) match those inferred for the nucleation of throughgoing low viscosity shear zones ( $\sim 10^{20} \text{ Pa}\cdot\text{s}$ ; Regenauer-Lieb et al., 2001). Although mantle wedge rheology likely depends on the extent of serpentinization and higher  $T$  ductile deformation, the similarity of ophiolite soles worldwide suggests that regional variations (e.g., incoming material, convergence rates, effective fluid release) are averaged out.

The presence of a warm oceanic lithosphere (i.e.,  $<\sim 3 \text{ My}$  and/or rejuvenated; Hacker, 1990; Duretz et al., 2015; supplementary material) appears to be an important requirement for metamorphic sole formation. Their formation is probably inhibited for older lithospheres, not because they are too cold (warm conditions will be met deeper down) but because the plate interface will be too decoupled. On the other hand, previous studies suggested that one-sided intraoceanic subduction initiation requires significant mantle cooling and subsequent weakening (Crameri et al., 2012). Too strong mechanical coupling, during subduction infancy, would favor double-sided subduction as in the Archean (Sizova et al., 2010 and references therein). This potentially explains why ophiolite soles older than the Neo-proterozoic are missing.

These findings also bear important implications for mechanisms of sediment or seamount underplating (i.e., transient episodes of strong coupling may control, in long-lived subduction systems, the potential accretion/exhumation of HP–LT rocks, including eclogites; Kimura and Ludden, 1995; Agard et al., 2007), variably hydrated mantle wedge rheologies (Faccenda, 2014) and for geochemical budgets of volatile fluxing during (hot) subduction (Ishikawa et al., 2005; Sizova et al., 2010).

## 6. Conclusions

Combining structure–lithology– $P$ – $T$ –time data from metamorphic soles with flow laws derived from experimental rock mechanics, we herein (i) outline the existence of two major, systematic rheological switches across the subduction interface (mantle wedge vs. basalts, then mantle wedge vs. sediments), (ii) propose that they control slab penetration and the successive formation of HT then LT metamorphic soles and (iii) provide a tentative reconstruction of metamorphic sole accretion during subduction infancy.

This reconstruction provides a generic explanation for the ubiquitous formation of metamorphic soles and emphasizes how slab

progression is hindered, during subduction infancy, by progressive changes in the mechanical properties of the cooling plate interface, until the interface becomes fully decoupled. Metamorphic sole formation and accretion would not so much result from a transient HT event (i.e., an ‘ironing’ effect), but from the existence of transiently similar rheologies and strong coupling during subduction infancy.

This study sheds light on early slab dynamics and on the role of transient mechanical coupling along the plate interface (i.e., such transient episodes may also control accretion/exhumation of HP–LT rocks in mature subduction systems) and provides a testable hypothesis for thermo-mechanical models. The proposed mechanism also strengthens the applicability of experimentally-derived flow laws for the mantle and mafic crust: although calibrated at much higher strain rates, they appear to be in remarkable agreement with natural data at  $\sim 800^\circ\text{C}$  (and  $\sim 1 \text{ GPa}$ ).

## Acknowledgements

This work was funded through the Agence nationale de la recherche (ANR-10-BLAN-0615) and through Institut Universitaire de France (grant to P.A.). We are grateful to colleagues from the O:NLAP ANR project for fruitful and enthusiastic discussions. An earlier version of this manuscript benefited from the constructive remarks of our friend and colleague E. Burov, who sadly passed away, and A. Schubnel. This work also benefited from discussions with scientists from the ZIP project (REA grant agreement no. 604713 (ZIP “Zooming In between Plates”) from the People Programme (Marie Curie Actions) of the European Union’s Seventh Framework Programme FP7/2007–2013).

## Appendix A. Supplementary material

Supplementary material related to this article can be found online at <http://dx.doi.org/10.1016/j.epsl.2016.06.054>.

## References

- Agard, P., Jolivet, L., Vrielynck, B., Burov, E., Monie, P., 2007. Plate acceleration: the obduction trigger? *Earth Planet. Sci. Lett.* 258, 428–441.
- Agard, P., Yamato, P., Jolivet, L., Burov, E., 2009. Exhumation of oceanic blueschists and eclogites in subduction zones: timing and mechanisms. *Earth-Sci. Rev.* 92, 53–79.
- Baldwin, J.A., Powell, R., Brown, M., Moraes, R., Fuck, R.A., 2005. Modelling of mineral equilibria in ultrahigh-temperature metamorphic rocks from the Anápolis-Itaucu Complex, central Brazil. *J. Metamorph. Geol.* 23, 511–531.
- Boudier, F., Ceuleneer, G., Nicolas, A., 1988. Shear zones, thrusts and related magmatism in the Oman ophiolite: initiation of thrusting on an oceanic ridge. *Tectonophysics* 151, 275–296.
- Burov, E.B., 2007. Plate rheology and mechanics. In: *Treatise on Geophysics*, vol. 6. Elsevier, pp. 99–151.
- Casey, J.F., Dewey, J., 1984. Initiation of subduction zones along transform and accreting plate boundaries, triple-junction evolution, and forearc spreading centres: implications for ophiolitic geology and obduction. *Geol. Soc. (Lond.) Spec. Publ.* 13, 269–290.
- Çelik, Ö.F., Marzoli, A., Marschik, R., Chiaradia, M., Neubauer, F., Öz, I., 2011. Early–Middle Jurassic intra-oceanic subduction in the Izmir–Ankara–Erzincan Ocean, Northern Turkey. *Tectonophysics* 509, 120–134. <http://dx.doi.org/10.1016/j.tecto.2011.06.007>.
- Ceuleneer, G., Nicolas, A., Boudier, F., 1988. Mantle flow patterns at an oceanic spreading centre: the Oman peridotites record. *Tectonophysics* 151, 1–26.
- Coleman, R.G., 1981. Tectonic setting for ophiolite obduction in Oman. *J. Geophys. Res.* 86, 2497–2508.
- Crameri, F., Tackley, P.J., Meilick, I., Gerya, T., Kaus, B.J.P., 2012. A free plate surface and weak oceanic crust produce single-sided subduction on Earth. *Geophys. Res. Lett.* 39, L03306.
- de Capitani, C., Petrakakis, K., 2010. The computation of equilibrium assemblage diagrams with Theriax/Domino software. *Am. Mineral.* 95, 1006–1016.
- Dewey, J., 1976. Ophiolite obduction. *Tectonophysics* 31, 93–120.
- Dewey, J.F., Casey, J.F., 2013. The sole of an ophiolite: the Ordovician Bay of Islands Complex, Newfoundland. *J. Geol. Soc. Lond.* 170, 715–722. <http://dx.doi.org/10.1144/jgs2013-017>.

- Diener, J.F.A., Powell, R., White, R.W., Holland, T.J.B., 2007. A new thermodynamic model for clino- and orthoamphiboles in the system  $\text{Na}_2\text{O}-\text{CaO}-\text{FeO}-\text{MgO}-\text{Al}_2\text{O}_3-\text{SiO}_2-\text{H}_2\text{O}-\text{O}$ . *J. Metamorph. Geol.* 25, 631–656. <http://dx.doi.org/10.1111/j.1525-1314.2007.00720.x>.
- Diener, J.F.A., Powell, R., 2012. Revised activity–composition models for clinopyroxene and amphibole. *J. Metamorph. Geol.* 30, 131–142.
- Duretz, T., Agard, P., Yamato, P., Ducassou, C., Burov, E.B., Gerya, T.V., 2015. Thermo-mechanical modeling of the obduction process based on the Oman Ophiolite case. *Gondwana Res.* <http://dx.doi.org/10.1016/j.gr.2015.02.002>.
- Dymkova, D., Gerya, T., 2013. Porous fluid flow enables oceanic subduction initiation on Earth. *Geophys. Res. Lett.* 40, 5671–5676.
- Escartin, J., Hirth, G., Evans, B.W., 2001. Strength of slightly serpentinised peridotites: implications for the tectonics of oceanic lithosphere. *Geology* 29, 1023–1026.
- Faccenda, M., 2014. Water in the slab: a trilogy. *Tectonophysics* 614, 1–30.
- Faul, U.H., Jackson, I., 2007. Diffusion creep of dry, melt-free olivine. *J. Geophys. Res.* 112, B04204. <http://dx.doi.org/10.1029/2006JB004586>.
- García-Casco, A., Torres-Roldán, R.L., Iturralde-Vinent, M., Millán, G., Cambra, K.N., Calisalvo, C.L., Vega, A.R., 2006. High pressure metamorphism of ophiolites in Cuba. *Geol. Acta* 4, 63–88.
- Getsinger, A.J., Hirth, G., 2014. Amphibole fabric formation during diffusion creep and the rheology of shear zones. *Geology* 42, 535–538.
- Gnos, E., 1998. Peak metamorphic conditions of garnet amphibolites beneath the semi-oceanic ophiolite: implications for an inverted pressure gradient. *Int. Geol. Rev.* 40, 281–304.
- Green, E., Holland, T.J.B., Powell, R., 2007. An order-disorder model for omphacitic pyroxenes in the system jadeite–diopside–hedenbergite–acmite, with applications to eclogitic rocks. *Am. Mineral.* 92, 1181–1189.
- Green, E.C.R., White, R.W., Diener, J.F.A., Powell, R., Holland, T.J.B., Palin, R.M., in press. Activity–composition relations for the calculation of partial melting equilibria for metabasic rocks. *J. Metamorph. Geol.* <http://dx.doi.org/10.1111/jmg.12211>.
- Gurnis, M., Hall, C., Lavier, L., 2004. Evolving force balance during incipient subduction. *Geochem. Geophys. Geosyst.* 5, Q07001.
- Hacker, B.R., 1990. Simulation of the metamorphic and deformational history of the metamorphic sole of the Oman ophiolite. *J. Geophys. Res.* 95, 4895–4907.
- Hacker, B.R., Mosenfelder, J.L., Gnos, E., 1996. Rapid emplacement of the Oman ophiolite: thermal and geochronologic constraints. *Tectonics* 15, 1230–1247.
- Hacker, B.R., Gnos, E., 1997. The conundrum of Samail: explaining the metamorphic history. *Tectonophysics* 279, 215–226.
- Hansen, L.N., Zimmerman, M.E., Kohlstedt, D.L., 2011. Grain boundary sliding in San Carlos olivine: flow law parameters and crystallographic-preferred orientation. *J. Geophys. Res.* 116, B08201.
- Hilairet, N., Reynard, B., Wang, Y., Daniel, I., Merkel, S., Nishiyama, N., Petitgirard, S., 2007. High-pressure creep of serpentine, interseismic deformation and initiation of subduction. *Science* 318, 1910–1913.
- Hirth, G., Kohlstedt, D.L., 2003. Rheology of the upper mantle and the mantle wedge: a view from the experimentalists. In: Eiler, J. (Ed.), Inside the Subduction Factory. In: Geophys. Monogr., vol. 138. American Geophysical Union, Washington, DC, pp. 83–105.
- Hirth, G., Kohlstedt, D.L., 2015. The stress dependence of olivine creep rate: implications for extrapolation of lab data and interpretation of recrystallized grain size. *Earth Planet. Sci. Lett.* 418, 20–26.
- Holland, T.J.B., Powell, R., 1998. An internally consistent thermodynamic data set for phases of petrological interest. *J. Metamorph. Geol.* 16, 309–343.
- Holland, T.J.B., Baker, J., Powell, R., 1998. Mixing properties and activity–composition relationships of chlorites in the system  $\text{MgO}-\text{FeO}-\text{Al}_2\text{O}_3-\text{SiO}_2-\text{H}_2\text{O}$ . *Eur. J. Mineral.* 10, 395–406.
- Homburg, J.M., Hirth, G., Kelemen, P.B., 2010. Investigation of the strength contrast at the Moho: a case study from the Oman ophiolite. *Geology* 38, 679–682.
- Ishikawa, T., Fujisawa, S., Nagaihi, K., Masuda, T., 2005. Trace element characteristics of the fluid liberated from amphibolite-facies slab: inference from the metamorphic sole beneath the Oman ophiolite and implication for boninite genesis. *Earth Planet. Sci. Lett.* 240, 355–377.
- Jamieson, R.A., 1981. Metamorphism during ophiolite emplacement—the petrology of the St Anthony Complex. *J. Petrol.* 22, 397–443.
- Jamieson, R.A., 1986.  $P-T$  paths from high temperature shear zones beneath ophiolites. *J. Metamorph. Geol.* 4, 3–22.
- Karato, S., 2010. Rheology of the Earth's mantle: a historical review. *Gondwana Res.* 18, 17–45.
- Kessel, R., Ulmer, P., Pettke, T., Schmidt, M.W., Thompson, A.B., 2005. The water–basalt system at 4 to 6 GPa: phase relations and second critical endpoint in a K-free eclogite at 700 to 1400 °C. *Earth Planet. Sci. Lett.* 237, 873–892.
- Kimura, G., Ludden, J., 1995. Peeling oceanic crust in subduction zones. *Geology* 23, 217–220.
- Linckens, J., Herwegen, M., Müntener, O., 2011a. Linking temperature estimates and microstructures in deformed polymimetic mantle rocks. *Geochem. Geophys. Geosyst.* 12, Q08004.
- Linckens, J., Herwegen, M., Müntener, O., Mercalli, I., 2011b. Evolution of a polymimetic mantle shear zone and the role of second phases on the localization of deformation. *J. Geophys. Res.* 116, B06210. <http://dx.doi.org/10.1029/2010JB008119>.
- Malpas, J., 1979. The dynamothermal aureole of the Bay of Islands ophiolite suite. *Can. J. Earth Sci.* 16, 2086–2101.
- McCaig, A.M., 1983.  $P-T$  conditions during emplacement of the Bay of Islands ophiolite complex. *Earth Planet. Sci. Lett.* 63, 459–473.
- Michibayashi, K., Mainprice, D., 2004. The role of pre-existing mechanical anisotropy on shear zone development within oceanic mantle lithosphere: an example from the Oman ophiolite. *J. Petrol.* 45, 405–414.
- Nicolas, A., 1989. Structures in Ophiolites and Dynamics of Oceanic Lithosphere (Petrology and Structural Geology). Kluwer, Dordrecht.
- Nicolas, A., Boudier, F., Ildefonse, B., Ball, E., 2000. Accretion of Oman and United Arab Emirates ophiolite – discussion of a new structural map. *Mar. Geophys. Res.* 21, 147–179.
- Petrini, K., Podladchikov, Y., 2000. Lithospheric pressure–depth relationship in compressive regions of thickened crust. *J. Metamorph. Geol.* 18, 67–77.
- Plunder, A., Agard, P., Chopin, C., Pourteau, A., Okay, A.I., 2015. Accretion, underplating and exhumation along a subduction interface: from subduction initiation to continental subduction (Tavşanlı zone W. Turkey). *Lithos* 226, 233–254.
- Plunder, A., Agard, P., Chopin, C., Soret, M., Okay, A.I., Whitechurch, H., in press. Metamorphic sole formation, emplacement and blueschist-facies overprint: early subduction dynamics witnessed by western Turkey ophiolites. *Terra Nova*. <http://dx.doi.org/10.1111/ter.12225>.
- Regenauer-Lieb, K., Yuen, D.A., Branlund, J., 2001. The initiation of subduction: criticality by addition of water? *Science* 294, 578–580.
- Rioux, M., et al., 2013. Tectonic development of the Samail ophiolite: high-precision U–Pb zircon geochronology and Sm–Nd isotopic constraints on crustal growth and emplacement. *J. Geophys. Res.* 118, 2085–2101.
- Roberts, N.M.W., Thomas, R.J., Jacobs, J., in press. Geochronological constraints on the metamorphic sole of the Samail ophiolite in the United Arab Emirates. *Geosci. Front.* 7, 609–619. <http://dx.doi.org/10.1016/j.gsf.2015.12.003>.
- Searle, M.P., Malpas, J., 1980. Petrochemistry and origin of sub-ophiolitic metamorphic and related rocks in the Oman Mountains. *J. Geol. Soc.* 139, 235–248.
- Searle, M.P., Cox, J., 2002. Subduction zone metamorphism during formation and emplacement of the Samail ophiolite in the Oman Mountains. *Geol. Mag.* 139, 241–255.
- Sizova, E., Gerya, T., Brown, M., Perchuk, LL., 2010. Subduction styles in the Precambrian: insight from numerical experiments. *Lithos* 116, 209–229.
- Spray, J.G., 1984. Possible causes and consequences of upper mantle decoupling and ophiolite displacement. *Geol. Soc. (Lond.) Spec. Publ.* 13, 255–268.
- Stern, R.J., Bloomer, S., 1992. Subduction zone infancy: examples from the Eocene Izu–Bonin–Mariana and Jurassic California arcs. *Geol. Soc. Am. Bull.* 104, 1621–1636.
- Stern, R.J., 2004. Subduction initiation: spontaneous and induced. *Earth Planet. Sci. Lett.* 226, 275–292.
- Syracuse, E.M., van Keken, P.E., Abers, G.A., 2010. The global range of subduction zone thermal models. *Phys. Earth Planet. Inter.* 183, 73–90.
- Tasaka, M., Hiraga, T., Michibayashi, K., 2014. Influence of mineral fraction on the rheological properties of forsterite + enstatite during grain size sensitive creep: 3. Application of grain growth and flow laws on peridotite ultramylonite. *J. Geophys. Res., Solid Earth* 119, 840–857. <http://dx.doi.org/10.1002/2013JB010619>.
- Ulmer, P., Trommsdorff, V., 1995. Serpentinite stability to mantle depths and subduction-related magmatism. *Science* 268, 858–861.
- van Dinter, Y., Gerya, T.V., Dalguer, L.A., Mai, P.M., Morra, G., Giardini, D., 2013. The seismic cycle at subduction thrusts: insights from seismo-thermo-mechanical models. *J. Geophys. Res.* 118, 6183–6202.
- Wakabayashi, J., 1990. Counterclockwise  $P-T-t$  paths from amphibolites, Franciscan Complex, California: relics from the early stages of subduction zone metamorphism. *J. Geol.* 98, 657–680.
- Wakabayashi, J., Dilek, Y., 2000. Spatial and temporal relationships between ophiolites and their metamorphic soles: a test of models of forearc ophiolite genesis. In: Dilek, Y., Moores, E.M., Elthon, D., Nicolas, A. (Eds.), Ophiolites and Oceanic Crust: New Insights from Field Studies and the Ocean Drilling Program. In: Geological Society of America Special Paper, vol. 349. Boulder, Colorado, pp. 53–64.
- Wakabayashi, J., Dilek, Y., 2003. What constitutes emplacement of an ophiolite? Mechanisms and relationship to subduction initiation and formation of metamorphic soles. *Geol. Soc. (Lond.) Spec. Publ.* 218, 427–447.
- White, R.W., Powell, R., Holland, T.J.B., 2007. Progress relating to calculation of partial melting equilibria for metapelites. *J. Metamorph. Geol.* 25, 511–527. <http://dx.doi.org/10.1111/j.1525-1314.2007.00711.x>.
- Williams, W., Smyth, R., 1973. Metamorphic aureoles beneath ophiolite suites and Alpine peridotites: tectonic implications with west Newfoundland examples. *Am. J. Sci.* 273, 594–621.
- Yuen, D.A., Fleitout, L., Schubert, G., Froidevaux, C., 1978. Shear deformation zones along major transform faults and subducting slabs. *Geophys. J. R. Astron. Soc.* 54, 93–119.



7.2 Soret et al. (2016) : *Strain localization and fluid infiltration in the mantle wedge during subduction initiation : Evidence from the base of the New Caledonia ophiolite*





ELSEVIER

Contents lists available at ScienceDirect

Lithos

journal homepage: [www.elsevier.com/locate/lithos](http://www.elsevier.com/locate/lithos)

## Strain localization and fluid infiltration in the mantle wedge during subduction initiation: Evidence from the base of the New Caledonia ophiolite



M. Soret <sup>a</sup>, P. Agard <sup>a,b</sup>, B. Dubacq <sup>a</sup>, A. Vitale-Brovarone <sup>a,c</sup>, P. Monié <sup>d</sup>, A. Chauvet <sup>d</sup>, H. Whitechurch <sup>e</sup>, B. Villemant <sup>a</sup>

<sup>a</sup> Sorbonne Universités, UPMC Univ Paris 06, CNRS, Institut des Sciences de la Terre de Paris (ISTeP), 4 place Jussieu, 75005 Paris, France

<sup>b</sup> Institut Universitaire de France, F-75005, Paris, France

<sup>c</sup> Institut de Minéralogie, de Physique des Matériaux, et de Cosmochimie, Sorbonne Universités, UMR CNRS 7590, Université Pierre et Marie Curie Paris 06, Muséum National d'Histoire Naturelle, Institut de Recherche pour le Développement UMR 2064 place Jussieu, 75005 Paris, France

<sup>d</sup> Université Montpellier, Géosciences Montpellier, UMR CNRS 5243, Place E. Bataillon, 34095, Montpellier Cedex 05, France

<sup>e</sup> IPGS, Université de Strasbourg, UMR CNRS 7516, 1 rue Blessig, 67000 Strasbourg, France

### ARTICLE INFO

#### Article history:

Received 5 March 2015

Accepted 12 November 2015

Available online 8 December 2015

#### Keywords:

Subduction initiation

Obducted ophiolite

Amphibolite shear bands

Supra-subduction zone metasomatism

### ABSTRACT

Despite decades of petrological and geochemical studies, the nature and setting of obducted ophiolites remain controversial: the influence of supra-subduction zone environments on pre-existing oceanic lithosphere is yet to assess, and the processes leading to subduction/obduction initiation are still poorly constrained. Our study documents successive influx of slab-derived fluids and progressive strain localization within the upper mantle in a supra-subduction environment during the first few My of the subduction history. We focus on strongly sheared mafic amphibolites intruding peridotites near the mantle–crust transition of the New Caledonia obducted ophiolite and ~50 to 100 m above the basal thrust contact of the ophiolite. These m- to hm-long and several m-thick shear bands are interpreted as inherited small-scale intrusions of mafic melts, probably dikes or sills, which were derived from a moderately refractory mantle source refertilized by supra-subduction zone fluids.  $^{40}\text{Ar}/^{39}\text{Ar}$  age constraints on pargasite at ca. 90 Ma suggest that they could be inherited from the former Pacific west-dipping subduction.

Secondary deformation of these mafic intrusions is intimately associated to three major stages of fluid infiltration: (1) the first stage of deformation and metasomatism is marked by syn-kinematic growth of Ca-amphibole (at 700–800 °C and 3–5 kbar) with a distinctive supra-subduction zone signature, and controlled later channelization of aqueous fluids.  $^{40}\text{Ar}/^{39}\text{Ar}$  dating on magnesio-hornblende indicates that this deformation episode occurred at ca. 55 Ma, coincident with east-dipping subduction initiation; (2) the main metasomatic stage, characterized by the development of a phlogopite-rich matrix wrapping peridotites and amphibolite boudins, points to the percolation of alkali-rich aqueous fluids at still high temperature (650–750 °C); (3) the last, low temperature (<600 °C) metasomatic stage results in the formation of deformed veinlets containing talc, chlorite and serpentine.

© 2015 Elsevier B.V. All rights reserved.

### 1. Introduction

Obduction emplaces fragments of dense oceanic lithosphere on top of continents over several hundreds of kilometers (e.g. Oman, Newfoundland, Turkey, New Caledonia; Coleman, 1971). Despite numerous petrological and geochemical studies, the exact nature and setting of many obducted ophiolites remain unclear. The Oman ophiolite is a typical example where there are evidences for both a MORB-type signature (Boudier et al., 1988; Ceuleneer et al., 1988; Godard et al., 2000, 2003; Le Mée et al., 2004; Nicolas et al., 2000) and a supra-subduction zone (SSZ) geochemical imprint (Ernewein et al., 1988; McLeod et al., 2013; Shervais, 2001; Stern and Bloomer, 1992).

The origin of obducted ophiolites has long been debated (Coleman, 1971; Dewey and Bird, 1971; Moores et al., 2000; Nicolas, 1989), with recent studies focusing on subduction–obduction initiation and early emplacement of ophiolites (Agard et al., 2007, 2014; Lagabrielle et al., 2013; Vaughan and Scarrow, 2003). Most of our knowledge on the initiation of the subduction–obduction system comes from the amphibolite to granulite facies metamorphic soles found at the base of most large-scale non-metamorphosed ophiolites and from magmatic dikes emplaced at different levels of the mantle sequence. These dikes generally record partial refertilization of the mantle wedge by subduction-derived fluids and show little deformation (e.g. Pirard, 2012; Xiong et al., 2014) whereas metamorphic soles are highly deformed portions

of upper oceanic crust and sediments, heated and metamorphosed along the interface between the subducting slab and the hotter mantle wedge during early subduction (e.g. Wakabayashi and Dilek, 2003). Metamorphic soles typically predate the final emplacement of the ophiolite onto the continental margin by several millions of years (~20 My for Oman; Agard et al., 2007).

We document sheared mafic amphibolite and feldspar-rich veins outcropping over a scale of hundreds of meters, within the peridotites of the New Caledonia ophiolite. They occur near the crust–mantle transition zone (e.g. Pirard et al., 2013; Prinzhöfer et al., 1980) and ~50 to 100 m above the basal contact of the ophiolite, south east of Nouméa (Fig. 1). As these deformed, metamorphosed rocks occur at the base of the New Caledonia ophiolite, it is tempting to relate them to subduction initiation, as for metamorphic soles. These sheared amphibolites could represent metamorphic sole fragments (outcropping in the Thio area; Cluzel et al., 2001, 2012) tectonically imbricated with basal peridotites, or be derived from melt products triggered by subduction-derived fluids (e.g. as the SSZ amphibole-bearing dikes in the Massif du Sud peridotites; Cluzel et al., 2006; Pirard, 2012; Pirard et al., 2013). Alternatively, they could also be inherited from earlier melting processes during ocean basin formation (e.g. near transform fault; Constantin, 1999; Gaggero and Cortese, 1997).

In this study, we provide a detailed petrological, geochemical and geochronological study to constrain the nature, the tectonic setting and the origin of these deformed amphibole-bearing dikes, and discuss implications for the New Caledonia subduction system in terms of geological setting and refertilization.

## 2. Geological setting

New Caledonia is located at the northern termination of the Norfolk Ridge, a stretched continental fragment rifted off the eastern Australian margin during the Early Cretaceous rollback of the Western Pacific subduction zone and the opening of New Caledonia and Loyalty basins (Schellart et al., 2006; Van de Beuck et al., 1998; Weissel and Hayes, 1977).

The present-day structure of New Caledonia (Fig. 1a) results from a Paleogene episode of convergence. This event led to the closure of the

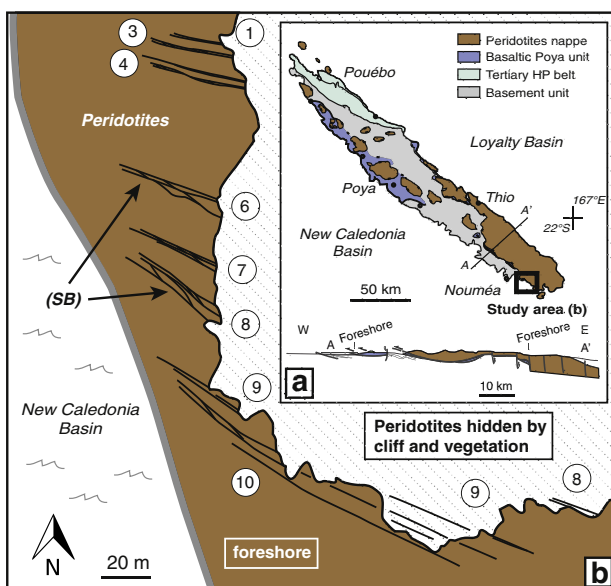


**Fig. 1.** a) Simplified geological map and cross-section of New Caledonia Island (after Cluzel et al., 2001); b) structural map of the study area near to Plum Beach (S.E. of Nouméa) showing the distribution of m-scale shear mafic bands within the peridotite of the ophiolite. Shear band (SB) #2 is not represented at this scale.

South Loyalty Basin after the initiation of a north-east-dipping intra-oceanic subduction (Cluzel et al., 2001; Matthews et al., 2015; Schellart et al., 2006) and was responsible for the obduction of the New Caledonia ophiolite rooted in the Loyalty Basin (Collot et al., 1987). Geochronological and thermochronological data on mafic rocks from the metamorphic sole (Cluzel et al., 2012) and mafic dikes intruding the ultramafic ophiolite (Cluzel et al., 2006; Pirard, 2012) suggest that subduction inception occurred at ca. 56 Ma. At ca. 34 Ma, this intra-oceanic subduction led to the obduction of the South Loyalty Basin lithosphere towards the south-west onto the Norfolk Ridge (e.g. Collot et al., 1987; Paris et al., 1979; Prinzhöfer, 1981).

The ophiolite complex of New Caledonia is composed of three allochthonous units of Cretaceous–Eocene age accreted over a calc-alkaline, island-arc derived basement (Fig. 1a) (Aitchison et al., 1995; Cluzel et al., 2001). This basement was created from the Permian to the Early Cretaceous with the accretion of three major volcano-sedimentary terranes (i.e. Teremba, Boghen and Koh terranes) along the eastern Gondwana margin. Above this basement, the Tertiary subduction complex is composed of four main units:

1 – a Tertiary high-pressure metamorphic belt at the northern end of New Caledonia (Fig. 1a) made of volcano-sedimentary and mafic blueschist and eclogite facies rocks, some of which are interbedded in a serpentinite matrix and minor metasediments (Carson et al., 2000; Clarke et al., 2006; Cluzel et al., 2001; Vitale Brovarone and Agard, 2013). Mafic eclogites have Late Cretaceous to Eocene protolith ages and share geochemical affinities with the Poya terrane (Cluzel et al., 2001; Spandler et al., 2005)

2 – the Poya terrane, a weakly metamorphic mafic rocks unit (e.g. Cluzel et al., 1997, 2001; Eissen et al., 1998), outcrops along most of the west coast of New Caledonia and also forms several isolated exposures along the eastern side (Fig. 1a). This terrane consists mainly of massive and pillow basalt, dolerite, and gabbro associated with chert and volcaniclastic rocks (Eissen et al., 1998). The origin of the Poya Terrane is controversial. Geochemical associations of back-arc basin and enriched-MORB signatures constrain its formation to a back-arc environment (Cluzel et al., 1997, 2001). Paleontological studies date its formation between 83 and 55 Ma (Cluzel et al., 2001). This unit was interpreted as representing the crustal cover of the South Loyalty Basin (Lagabrielle et al., 2013; Spandler et al., 2005), with the above ages likely indicating the opening period of the basin.

3 – the ultramafic ophiolite (named “Nappe des Péridotites”) found on the south-eastern portion of New Caledonia (Fig. 1a) is constituted mainly of a 2–3 km thick depleted mantle sequence (spinel-bearing harzburgite) above a 20 to 100 m thick porphyroclastic serpentine mylonite. In the northern part of New Caledonia, lherzolite is present in the Tiebaghi and the Poum massifs (e.g. Moutte, 1979; Ulrich et al., 2010). This suite of ultramafic rocks is interpreted as representing upper mantle rocks of the South Loyalty Basin (Lagabrielle et al., 2013) and documents a complex history with several supra-subduction zone settings, as attested by magmatic intrusions.

In the Massif du Sud, Marchesi et al. (2009) and Pirard et al. (2013) reported gabbronorites and olivine gabbro sills at the top of ophiolitic sequence. These gabbros represent the lower crust of the ophiolite. They are separated from the underlying harzburgite by a dunite complex composed of dunite channels with the presence of dunite cumulates, wherlite, clinopyroxenite and websterite sills and dikes. Amphibole is commonly present in clinopyroxenite bodies but absent from the lower crust gabbronorites (Pirard, 2012; Pirard et al., 2013). These authors interpret this complex as the crust–mantle transition with mafic sills and dikes being the result of percolating, hydrous primitive

arc magmas within the peridotite during early stages of the subduction system and nascent arc crust formation.

The Massif du Sud is also extensively cross-cut by Early Eocene felsic, anhydrous and hydrous coarse grained dikes (leucodiorite, granitoid, micro-diorite, dolerite and hornblendite; Cluzel et al., 2005, 2006; Pirard, 2012; Pirard et al., 2013; Prinzhoffer, 1981) discordant with the harzburgite and/or the gabbro sills from the lower crust. These dikes are generally unmetamorphosed and undeformed with the exception of few diorite dikes which are boudinaged, locally micro-folded and where amphibole shows a preferred orientation (Cluzel et al., 2012). Upon geochemical and geochronological features, these dikes have been interpreted as formed in a supra-subduction zone setting. These dikes are essentially considered as synchronous or immediately posterior to magma injection in active faults that formed during the first stages of the 55 Ma subduction (Cluzel et al., 2006, 2012). However, Prinzhoffer (1981) obtained 2 different K-Ar ages (i.e.  $90 \pm 10$  Ma and  $42 \pm 5$  Ma) for dolerite dikes intruding the Massif du Sud. The youngest dikes coincide with the Eocene New Caledonia subduction. The Late Cretaceous dikes could be an evidence of the ocean spreading stage of the South Loyalty Basin (Matthews et al., 2015; Prinzhoffer, 1981). The Late Cretaceous age of 85 Ma was also measured in zircon cores from the high-pressure Pouebo unit (Spandler et al., 2005). In addition, Cluzel et al. (2005) report granitoid dikes intruding the Massif du Sud at 27 and 24 Ma. They interpret these dikes, coeval with the final obduction stages, as related to the inception of a new subduction along the west coast of New Caledonia in response to the blocking of the previous Eocene subduction. Altogether these dikes appear to record several subduction-related events, suggesting that the ophiolite witnesses several and distinctive stages of migration, accumulation and re-equilibration of different melts (including hydrous melts) in a supra-subduction environment (e.g. Marchesi et al., 2009; Pirard, 2012; Ulrich et al., 2010), rather than being the result of a fractional crystallization from a single magma-type during oceanic spreading (Prinzhoffer and Allègre, 1985).

4 – an amphibolite to granulite facies metamorphic sole is found in places between the ophiolite and the Poya and Pouebo underlying terranes (Cluzel et al., 2012). This metamorphic sole is interpreted to have been welded to the ophiolite during subduction inception. Using various thermobarometers, Cluzel et al. (2012) estimate peak crystallization conditions around 5 kbar and 800 to 950 °C. Thermochronology on hornblende ( $^{40}\text{Ar}/^{39}\text{Ar}$ ), zircon and sphene (U-Pb) indicate that these mafic rocks crystallized at ca. 56 Ma (Cluzel et al., 2012). This result and inferred pressure-temperature conditions for the New Caledonia metamorphic sole give a geothermal gradient greater than 40 °C/km, consistent with subduction inception occurring at or near the spreading ridge of the South Loyalty Basin.

### 3. Outcrop-scale deformation patterns and mineralogy

The study area is exposed at low tide on the foreshore of Plum Beach (south-east of Noumea), across a  $\sim 150 \times 100$  m surface (Fig. 1b). This area is bounded to the west by the New Caledonia Basin and by a densely vegetated cliff to the east. It is located near the base of the ophiolite, 50 to 100 m above the north-east dipping contact with the underlying Poya unit, which outcrops 2 km to the north.

The study area is a major deformation zone characterized by large-scale mafic shear bands (up to 100 m long in places) and centimetric to decimetric orthopyroxenite veins away from the deformed area. The shear bands and veins cross-cut the peridotite, which is constituted mainly of highly serpentinized harzburgite and rare dunite. One to two meters away from the shear bands, the peridotite is massive and has only a tectonite porphyroclastic texture with a high temperature foliation steeply dipping to the NE (parallel to the paleo-Moho according

to Prinzhoffer et al., 1980). The orientation of this foliation is discordant with respect to the deformation observed in the mafic shear bands.

Ten major shear bands have been recognized in the study area. Shear bands #1 to #7 are 30 to 50 m long and strike ~N150 (Fig. 1b). They disappear under the eastern cliff but likely extend further to the south-east, where similar shear bands are found in apparent continuity along the coast (#8 to #10). The overall length of these shear bands is thus greater than 150 m.

The shear bands are m- to several m-thick and commonly outlined by 10–50 cm thick amphibolite bands, mostly found at the core of the shear bands (and, when found on the margins, only on their south-west side; Fig. 2).

Peridotite and amphibolite are strongly boudinaged within the amphibolite-bearing shear zones (Fig. 3a, b, c). Strain increases towards the core of the shear bands, as shown by the marked decrease in boudin size, from the m- to the cm-scale. Both ultramafic and mafic boudins are sigmoidal and indicate consistent sinistral-reverse, top to the north-west shear senses across the whole outcrop (Figs. 2, 3a). These boudins are embedded in a phlogopite-rich matrix described below.

A network of distributed leucocratic feldspar-rich veins also cross-cuts the peridotite. This network is mainly found on the margins of the high strain bands. Mutual cross-cutting relationships between the dark amphibolites and the feldspar-rich veins suggest that they formed coevally. The vein network is developed only on one side of the amphibolite bands (to the NE); the density, thickness and length of the veins decrease away from the amphibolites (Fig. 3c, d, f, g). The mafic shear

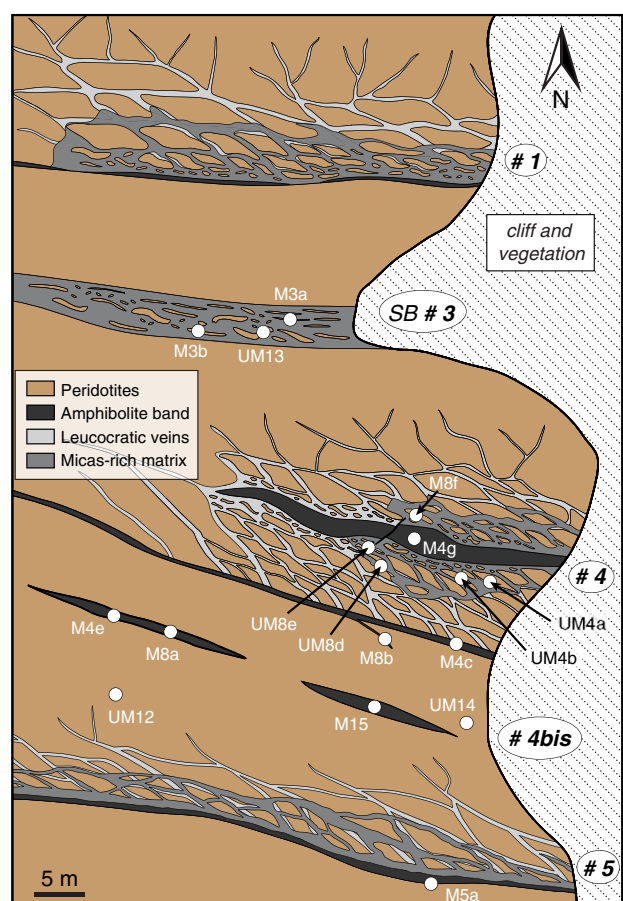


**Fig. 2.** Structural map of the northern shear bands. Schematizing the relations between shear bands within the undeformed peridotite of the ophiolite. White dots indicate sample location (Table 1). Shear band (SB) #2 is not represented at this scale.

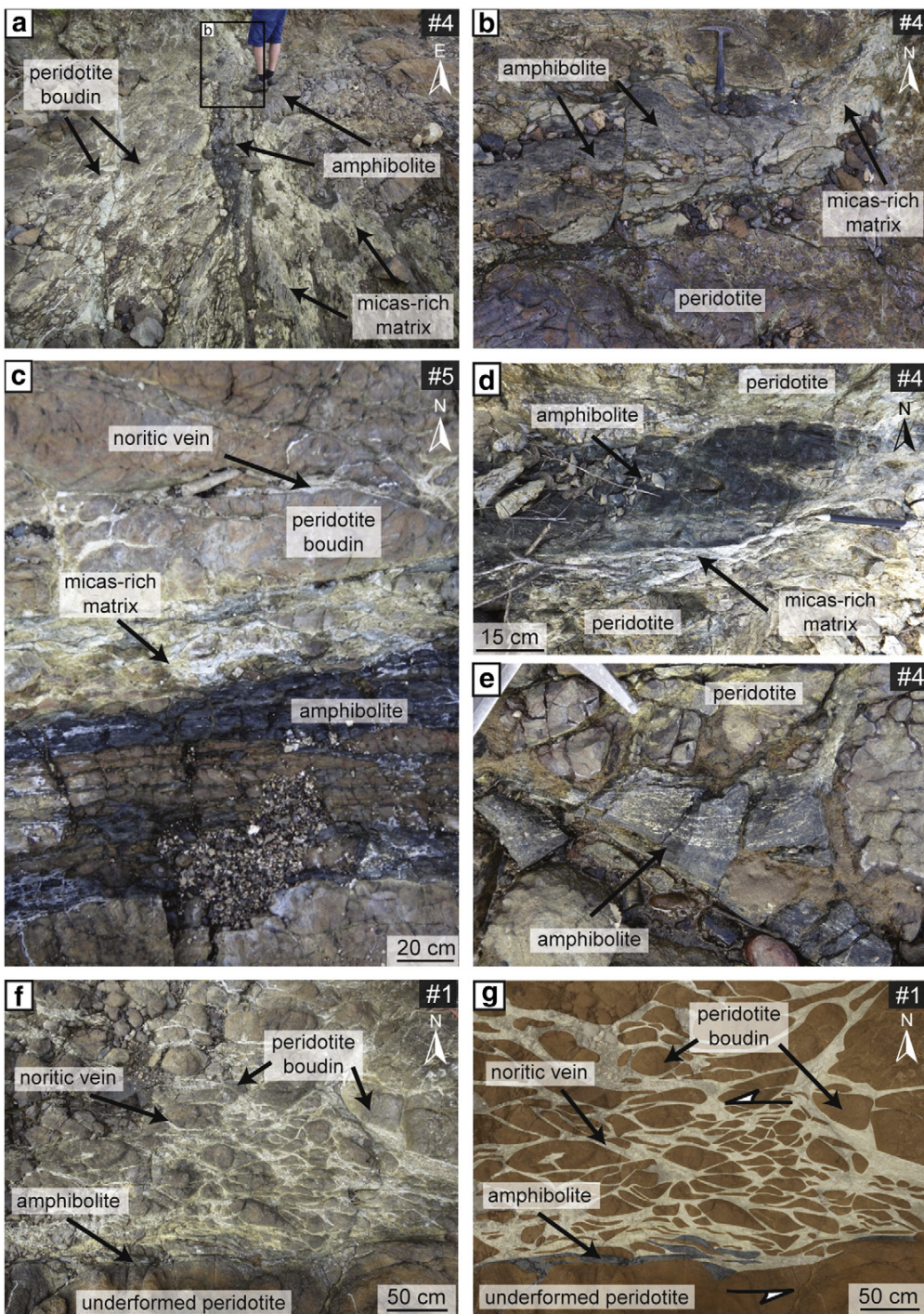


**Fig. 3.** Structures of the mafic shear bands. Note that peridotite is highly boudinaged near dark dm-scale amphibolite bands. a) Amphibolite band found at the core of shear band #4. b) A small-scale amphibolite band cut by the major amphibolite #4. c) Shear band #5 is asymmetrical. The vein network is developed only on one side of the amphibolite band (to the NE). d) and e) Boudinaged and foliated amphibolite. f) and g) Photograph and corresponding schematized sketch of asymmetrical shear band #1. Vein density, thickness and length decrease away from the amphibolites.

band #4bis is a dm-thick dark amphibolite without feldspar-rich veins (Fig. 2).

Amphibolite bands (Fig. 3e) chiefly comprise calcic amphibole with 10 to 50 vol.% plagioclase, variably altered to reddish-to-yellowish low-grade oxidized aggregates. Pyroxene (always orthopyroxene, as detailed below) amounts to 15–30 vol.%.

Leucocratic feldspar-rich veins are characterized by a predominance of plagioclase with up to 20 vol.% coarse-grained orthopyroxene crystals (Fig. 4a, b). Most orthopyroxenes are rimmed by calcic-amphibole.

A light colored, green to gray matrix comprising phlogopite, chlorite, talc and serpentine is observed within the shear bands and appears to form at the expense of both the mafic and ultramafic rocks

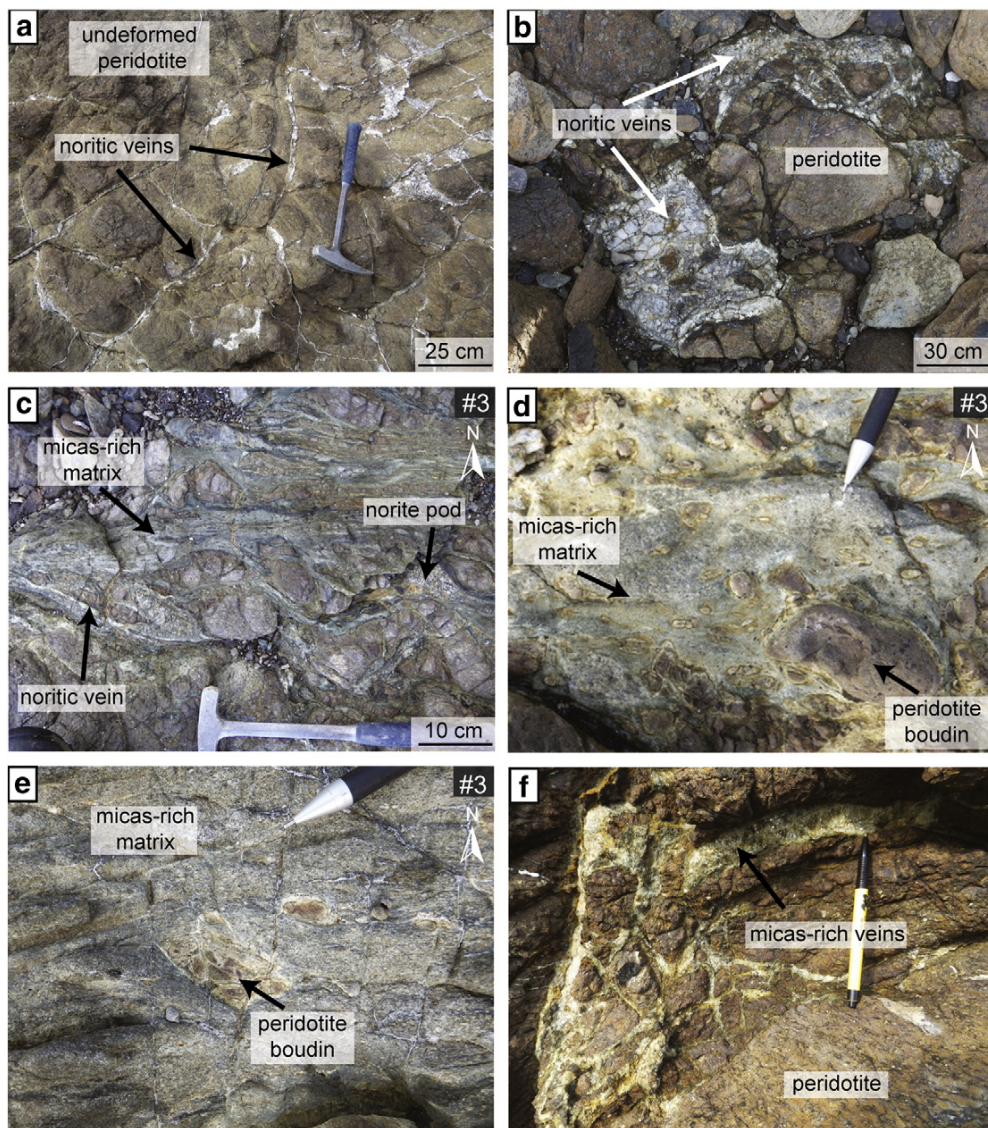


**Fig. 4.** Photographs of the peridotite and the micas-rich matrix within and away from shear bands. a) and b) Weakly deformed feldspar-rich veins within undeformed peridotites away from shear bands. c), d), e) and f) Late light colored matrix with biotite, chlorite, talc and serpentine minerals within the shear bands. The matrix appears to form at the expense of both the mafic and ultramafic rocks.

(Fig. 3c, d, e, f). Late, milky white cm-thick serpentine veinlets rim peridotite boudins and also cross-cut the boudins and the matrix. Phlogopite is also observed concentrated in m-scale veins next to some of the shear bands (#9).

#### 4. Sampling strategy and analytical techniques

##### 4.1. Sample selection

60 samples (Table 1) were collected in the field across the whole range of textures and mineralogical assemblages of the shear bands (both for mafic – M – and ultramafic – UM – protoliths; Fig. 2). 15 samples are dark amphibolites, either within deformation bands (e.g. M4d; Figs. 2, 5a) or isolated in undeformed peridotite (e.g. M8a), whereas 5 samples are deformed feldspar-rich mafic veins (e.g. M8e; Fig. 5b), including an undeformed feldspar-rich veinlet isolated in peridotite (sample M9). Ultramafic samples comprise 17 peridotite boudin samples surrounded by deformed feldspar-rich veins and phlogopite-rich

matrix (e.g. UM13, UM10; Fig. 5c, d), 14 undeformed peridotite samples (e.g. UM12, UM14) and one orthopyroxenite vein sample.

##### 4.2. Electron probe microanalysis (EPMA)

EPMA was carried out at CAMPARIS (UPMC–IPGP, Paris, France) on amphibolites ( $n = 7$ ), feldspar-rich veins ( $n = 5$ ), peridotite boudins ( $n = 5$ ), undeformed peridotites ( $n = 2$ ) and on the biotite-rich matrix ( $n = 7$ ), using classical analytical conditions for spot analyses (1–2  $\mu\text{m}$  spot size; 15 kV, 10 nA, wavelength-dispersive spectroscopy mode), using  $\text{Fe}_2\text{O}_3$  (Fe),  $\text{MnTiO}_3$  (Mn, Ti), diopside (Mg, Si),  $\text{CaF}_2$  (F), orthoclase (Al, K), anorthite (Ca) and albite (Na) as standards for bracketed elements. Representative analyses are given in Table 2.

##### 4.3. Thermobarometry

Pressure and temperature conditions of crystallization have been estimated using the hornblende-plagioclase geothermobarometer of

**Table 1**  
Mineral occurrence for selected samples.

Unit	Sample	ol	opx	fsp	Ba-fsp	hbl	ath	phl	chl/tlc	srp
Undeformed peridotite	M12	x	x							1
	M14	x	x							1
Peridotite boudin	M9	x	x	v			o	o	1	1
	M10	x	x	v	o		o	o	1	1
	M16	x	x	v		o	o	o	1	1
	M8a	x	x	x			o			1
Ol-bearing amphibolite	M8b	x	x	x			o			1
	M4e	x	x	x			o			
Ol-free amphibolite	M15	x	x	x			o			
	M3c	x	x				o			
	M3b	x	x				o			
	M4c	x	x				o			
	Mx	x	x				o			
	M4d	x	x				o		1	1
	M4g	x	x				o		1	1
	8e	x	x				o			

x: primary phases; o: secondary phases; l: late phases; v: vein wrapping peridotite boudin.  
Mineral abbreviations after Whitney and Evans (2010). Ba-fsp: celsian.

Holland and Blundy (1994) modified by Anderson and Smith (1995) in three olivine-bearing amphibolites and in six olivine-free amphibolites. This geothermobarometer is based on the reaction: edenite + albite = richterite + anorthite. The absence of Ti-rich phases in amphibolites invalidates the use of Ti-based geothermobarometers. Representative pressure–temperature estimates are given in Table 2.

The  $\text{Fe}^{3+}$  estimation method in amphibole given in Holland and Blundy (1994) provides the minimum ( $\text{Fe}^{3+}/\text{Fe}_{\text{tot}}$ ) ratio for which sufficient Na is allocated to the A-site.  $\text{Fe}^{3+}/\text{Fe}_{\text{tot}}$  here averages around 0.4 in late amphibole (i.e. magnesio-hornblende). With a ( $\text{Fe}^{3+}/\text{Fe}_{\text{tot}}$ ) ratio = 1, estimated after the method of Leake et al. (1997), the

estimated temperature is  $\sim 70$  °C higher than that calculated with  $\text{Fe}^{3+}/\text{Fe}_{\text{tot}} = 0.4$ .

#### 4.4. ICPMS and LA-ICPMS

Whole-rock major element analysis was performed on 7 samples (Table 3) at EOST in Strasbourg, France, by ICP-AES and ICP-MS (see Table 2; analytical procedure given in Omrani et al., 2008) and at UPMC Univ. Paris 6 (following the procedure of Salaün et al., 2010).

LA-ICPMS was performed on amphibole in at IRD Bondy using a 7500 cx AGILENT NI Standards coupled with a laser NWR-213 nm. Analyses were carried out using a 10 Hz laser repetition rate and 50  $\mu\text{m}$  beam diameter for amphibole. All analyses were conducted at fixed beam position. For internal standardization  $^{43}\text{Ca}$  was used for amphibole. For external standardization, NIST SRM 610 and 612 glasses were used after Pearce et al. (1997). Raw data were processed using GLITTER (GEMOC, Macquarie University, Australia). The following masses were analyzed (Table 4):  $^7\text{Li}$ ,  $^{11}\text{B}$ ,  $^{47}\text{Ti}$ ,  $^{85}\text{Rb}$ ,  $^{88}\text{Sr}$ ,  $^{89}\text{Y}$ ,  $^{90}\text{Zr}$ ,  $^{93}\text{Nb}$ ,  $^{133}\text{Cs}$ ,  $^{138}\text{Ba}$ ,  $^{139}\text{La}$ ,  $^{140}\text{Ce}$ ,  $^{141}\text{Pr}$ ,  $^{146}\text{Nd}$ ,  $^{147}\text{Sm}$ ,  $^{153}\text{Eu}$ ,  $^{157}\text{Gd}$ ,  $^{159}\text{Tb}$ ,  $^{169}\text{Dy}$ ,  $^{165}\text{Ho}$ ,  $^{166}\text{Er}$ ,  $^{172}\text{Yb}$ ,  $^{175}\text{Lu}$ ,  $^{178}\text{Hf}$ ,  $^{181}\text{Ta}$ ,  $^{208}\text{Pb}$ ,  $^{238}\text{U}$ ,  $^{232}\text{Th}$ .

#### 4.5. Radiometric dating

The selected samples were crushed and sieved; single grains of amphibole were handpicked under binocular microscope and cleaned in ultrasonic bath with acetone and distilled water. They were packaged in Al foils and irradiated for 40 h in the core of the Triga Mark II nuclear reactor of Pavia (Italia) with several aliquots of the Fish Canyon sanidine standard ( $28.03 \pm 0.08$  Ma; Jourdan and Renne, 2007) as flux monitor. Argon isotopic interferences on K and Ca were determined by irradiation of KF and  $\text{CaF}_2$  pure salts from which the following correction

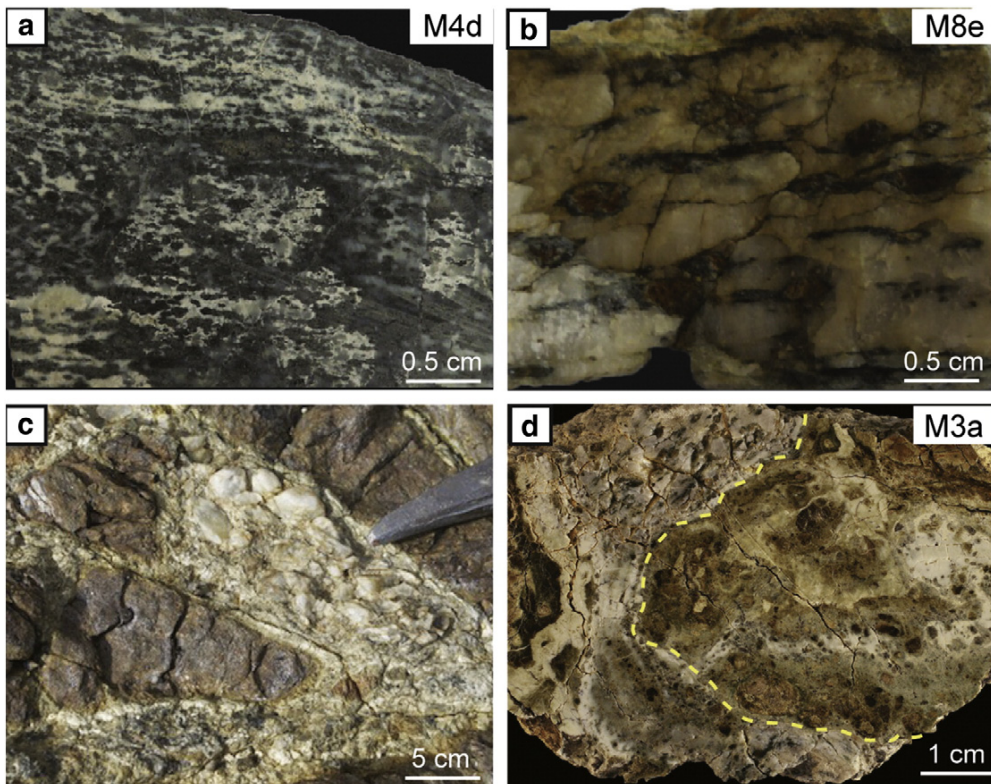


**Fig. 5.** Representative samples of the different units observed in shear bands. a) Foliated amphibolite. White layers are mainly composed of plagioclase, darker layers contain amphibole and orthopyroxene. b) Feldspar-rich veins with brown coarse-grained orthopyroxene rimmed by green amphiboles. c) Feldspar-rich vein wrapping around a peridotite boudin. Note the serpentine-bearing white rim around the boudin. d) Peridotite boudin wrapped by feldspar-rich vein and cross-cut by serpentine-talc-chlorite-rich white veinlets.

**Table 2**Selected representative EPMA analyses for olivine, orthopyroxene, plagioclase and amphibole. Fe<sup>3+</sup> for amphibole calculated after Leake et al. (1997).

Min. Olivine				Min. Orthopyroxene								Min. Feldspar								
Samp.	M4e	M8a1	M8b	UM10	Samp.	M3c	M4e	M8a1	M8a2	M8b	M8e	UM10	UM16	Samp.	M8a1	M8a1	M8e	UM9	UM10	
SiO <sub>2</sub>	40.05	39.56	40.24	41.62	SiO <sub>2</sub>	55.85	55.02	54.51	54.69	56.04	55.86	57.44	58.08	SiO <sub>2</sub>	43.24	43.55	56.68	56.62	51.19	
TiO <sub>2</sub>	b.d.l	b.d.l	b.d.l	b.d.l	TiO <sub>2</sub>	b.d.l	b.d.l	b.d.l	b.d.l	0.12	b.d.l	b.d.l	b.d.l	TiO <sub>2</sub>	b.d.l	b.d.l	b.d.l	b.d.l	b.d.l	
Al <sub>2</sub> O <sub>3</sub>	b.d.l	b.d.l	b.d.l	b.d.l	Al <sub>2</sub> O <sub>3</sub>	1.34	2.12	1.88	1.23	1.60	1.55	1.50	0.70	Al <sub>2</sub> O <sub>3</sub>	37.18	36.77	27.62	26.70	22.52	
Cr <sub>2</sub> O <sub>3</sub>	b.d.l	b.d.l	b.d.l	b.d.l	Cr <sub>2</sub> O <sub>3</sub>	b.d.l	b.d.l	0.08	b.d.l	0.07	b.d.l	0.72	0.09	Cr <sub>2</sub> O <sub>3</sub>	b.d.l	b.d.l	b.d.l	b.d.l	b.d.l	
FeO	14.25	18.31	16.12	8.14	FeO	11.12	10.00	13.74	14.78	10.85	10.38	5.24	6.69	FeO	b.d.l	b.d.l	b.d.l	b.d.l	b.d.l	
MnO	0.23	0.28	0.36	0.08	MnO	0.23	0.25	0.49	0.42	0.28	0.25	0.08	0.11	MnO	b.d.l	b.d.l	b.d.l	b.d.l	b.d.l	
MgO	45.46	41.73	43.11	50.38	MgO	31.24	32.28	28.76	28.13	30.26	31.78	34.94	34.89	MgO	b.d.l	b.d.l	b.d.l	b.d.l	b.d.l	
CaO	b.d.l	b.d.l	b.d.l	b.d.l	CaO	0.28	0.47	0.53	0.57	0.54	0.39	0.42	0.20	CaO	20.33	19.40	9.13	9.48	0.13	
Na <sub>2</sub> O	b.d.l	b.d.l	b.d.l	b.d.l	Na <sub>2</sub> O	b.d.l	b.d.l	b.d.l	b.d.l	b.d.l	b.d.l	b.d.l	b.d.l	Na <sub>2</sub> O	0.21	0.54	6.47	6.61	0.46	
K <sub>2</sub> O	b.d.l	b.d.l	b.d.l	b.d.l	K <sub>2</sub> O	b.d.l	b.d.l	b.d.l	b.d.l	b.d.l	b.d.l	b.d.l	b.d.l	K <sub>2</sub> O	b.d.l	b.d.l	b.d.l	7.92		
BaO	n.a	n.a	n.a	n.a	BaO	n.a	n.a	n.a	n.a	n.a	n.a	n.a	n.a	BaO	n.a	n.a	n.a	n.a	15.78	
Sum	100.0	99.9	99.8	100.2	Total	100.1	100.1	100.0	99.8	99.7	100.3	100.3	100.8	Sum	101.0	100.3	99.9	99.4	98.0	
<i>Formula unit</i>																				
Si	1.00	1.01	1.02	1.01	Si	1.96	1.92	1.94	1.96	1.98	1.95	1.97	1.99	Si	1.98	2.00	2.46	2.54	2.65	
Ti	0.00	0.00	0.00	0.00	Ti	0.00	0.00	0.00	0.00	0.00	0.00	0.00	0.00	Ti	0.00	0.00	0.00	0.00	0.00	
Al	0.00	0.00	0.00	0.00	Al	0.06	0.09	0.08	0.05	0.07	0.06	0.06	0.03	Al	2.00	1.99	1.52	1.42	1.37	
Cr	0.00	0.00	0.00	0.00	Cr	0.00	0.00	0.00	0.00	0.00	0.02	0.00	0.00	Cr	0.00	0.00	0.00	0.00	0.00	
Fe <sup>3+</sup>	0.00	0.00	0.00	0.00	Fe <sup>3+</sup>	0.02	0.08	0.03	0.02	0.00	0.02	0.00	0.00	Fe <sup>3+</sup>	0.00	0.00	0.00	0.00	0.00	
Fe <sup>2+</sup>	0.30	0.39	0.34	0.00	Fe <sup>2+</sup>	0.31	0.21	0.38	0.42	0.32	0.28	0.15	0.19	Fe <sup>2+</sup>	0.00	0.00	0.00	0.00	0.00	
Mn	0.00	0.01	0.01	0.17	Mn	0.01	0.01	0.01	0.01	0.01	0.00	0.00	0.00	Mn	0.00	0.00	0.00	0.00	0.00	
Mg	1.70	1.59	1.63	0.00	Mg	1.64	1.68	1.53	1.50	1.60	1.66	1.78	1.78	Mg	0.00	0.00	0.00	0.00	0.03	
Ca	0.00	0.00	0.00	1.82	Ca	0.01	0.02	0.02	0.02	0.02	0.01	0.02	0.01	Ca	1.00	0.95	0.53	0.46	0.01	
Na	0.00	0.00	0.00	0.00	Na	0.00	0.00	0.00	0.00	0.00	0.00	0.00	0.00	Na	0.02	0.05	0.48	0.58	0.05	
K	0.00	0.00	0.00	0.00	K	0.00	0.00	0.00	0.00	0.00	0.00	0.00	0.00	K	0.00	0.00	0.00	0.00	0.36	
Ba	–	–	–	–	Ba	–	–	–	–	–	–	–	–	Ba	–	–	–	–	0.52	
Mg#	0.85	0.80	0.83	0.92	Mg#	0.83	0.85	0.79	0.77	0.83	0.85	0.92	0.90	Ca#	0.98	0.95	0.52	0.44	0.13	
<i>Min. Amphibole</i>																				
Samp.	M3c mhb	M3c mhb	M8a1 prg	M8a1 tr	M8a2 mhb	M8b prg	M8b mhb	M8e mhb	M8e mhb	M09 mhb	UM10 mhb	UM10 tr	UM10 ath	UM16 mhb	UM16 tr					
SiO <sub>2</sub>	47.08	45.41	43.33	55.40	46.30	46.11	46.04	49.96	46.99	48.13	53.96	57.08	51.52	54.23						
TiO <sub>2</sub>	0.19	1.01	0.40	b.d.l	0.79	0.39	0.06	0.06	0.68	0.44	0.07	b.d.l	b.d.l	b.d.l						
Al <sub>2</sub> O <sub>3</sub>	11.10	11.47	15.16	3.14	11.82	12.24	11.54	8.42	11.66	10.58	5.73	1.57	8.44	4.76						
Cr <sub>2</sub> O <sub>3</sub>	b.d.l	b.d.l	b.d.l	b.d.l	0.10	0.44	b.d.l	b.d.l	b.d.l	0.85	b.d.l	0.05	b.d.l	b.d.l						
FeO	7.03	7.38	8.20	4.16	8.85	6.11	7.20	6.32	5.86	4.09	3.51	9.14	3.83	3.05						
MnO	0.18	0.05	0.10	0.12	0.09	0.08	0.15	0.17	0.09	0.06	0.04	0.26	0.05	0.12						
MgO	18.26	17.64	15.27	21.91	16.08	17.47	17.55	19.28	18.88	19.62	21.81	28.58	20.97	22.41						
CaO	11.51	11.27	12.03	12.73	11.71	12.35	11.38	11.29	11.52	11.72	12.06	0.73	12.02	11.90						
Na <sub>2</sub> O	2.20	2.50	2.80	0.53	2.13	2.38	2.47	1.82	2.20	2.48	1.26	0.12	1.67	1.09						
K <sub>2</sub> O	0.12	0.15	0.10	b.d.l	0.06	0.07	0.13	0.08	0.13	0.14	0.05	b.d.l	0.08	b.d.l						
Sum	97.67	96.89	97.38	97.99	97.94	97.63	96.51	97.41	98.04	98.11	98.50	97.51	98.58	97.56						
<i>Formula unit</i>																				
Si	6.57	6.41	6.18	7.56	6.52	6.49	6.51	6.94	6.52	6.66	7.33	7.77	7.03	7.42						
Ti	0.02	0.11	0.04	0.00	0.08	0.42	0.01	0.01	0.07	0.05	0.01	0.00	0.00	0.00						
Al	1.83	1.90	2.55	0.51	1.96	2.03	1.92	1.38	1.90	1.73	0.92	0.25	0.97	0.77						
Cr	0.00	0.00	0.00	0.00	0.01	0.05	0.00	0.00	0.00	0.09	0.00	0.01	0.00	0.00						
Fe 3+	0.82	0.87	0.55	0.47	0.70	0.48	0.85	0.73	0.68	0.47	0.40	0.17	0.35	0.44						
Fe 2+	0.00	0.00	0.43	0.00	0.34	0.24	0.00	0.00	0.00	0.00	0.00	0.87	0.00	0.00						
Mn	0.02	0.01	0.01	0.01	0.00	0.01	0.02	0.02	0.01	0.01	0.01	0.03	0.01	0.01						
Mg	3.70	3.72	3.24	0.46	3.37	3.66	3.70	3.99	3.90	4.05	4.42	5.80	4.57	4.26						
Ca	1.72	1.71	1.84	1.86	1.77	1.86	1.73	1.68	1.71	1.74	1.76	0.11	1.75	1.76						
Na	0.60	0.69	0.78	0.14	0.58	0.65	0.68	0.49	0.59	0.66	0.33	0.03	0.29	0.44						
K	0.02	0.03	0.02	0.00	0.01	0.01	0.02	0.02	0.02	0.02	0.01	0.00	0.01	0.01						
Mg#	0.82	0.81	0.77	0.49	0.76	0.84	0.81	0.84	0.86	0.90	0.92	0.85	0.93	0.91						
<i>Geothermobarometry after Holland and Blundy (1994) modified by Anderson and Smith (1995)</i>																				
An#	0.52	0.52	0.95	–	0.52	0.52	0.52	0.52	0.44	0.44	–	–	0.44	–						
T (°C)	718	776	1013	–	756	963	739	702	680	677	–	–	615	–						
P (kbar)	5.16	4.33	Error	–	4.98	error	5.23	3.34	5.97	3.61	–	–	3.78	–						

b.d.l: below detection limit; n.a.: non-analyzed

An#: Ca/(Ca + Na) in plagioclase

factors were obtained:  $(^{40}\text{Ar}/^{39}\text{Ar})_K = 0.00969 \pm 0.00038$ ,  $(^{38}\text{Ar}/^{39}\text{Ar})_K = 0.01297 \pm 0.00045$ ,  $(^{39}\text{Ar}/^{37}\text{Ar})_{\text{Ca}} = 0.0007474 \pm 0.000021$  and  $(^{36}\text{Ar}/^{37}\text{Ar})_{\text{Ca}} = 0.000288 \pm 0.000016$ . Argon analyses were performed at Géosciences Montpellier (France) with two analytical devices that each consist of: (a) an IR-CO<sub>2</sub> laser of 100 kHz used at 5–15% during 60 s, (b) a lenses system for beam focusing, (c) a steel chamber, kept at  $10^{-8}$ – $10^{-9}$  bar, with a drilled copper plate, (d) an inlet line for purification of gases including two Zr-Al getters, (e) a multi-collector

mass spectrometer (Argus VI from Thermo-Fisher) or an MAP215-50 single collector mass spectrometer depending on the used device. A custom-made software controls the laser intensity, the timing of extraction/purification and the data acquisition. To measure the Ar background within the system, one blank analysis was performed every three sample analyses. ArArCalc© v2.5.2 was used for data reduction and plotting. The one-sigma errors reported on plateau, isochron and total gas ages include the error on the irradiation factor J. Atmospheric <sup>40</sup>Ar was

**Table 3**

Whole rock geochemistry for representative amphibolite dikes.

Sample	M15_Z1 amph	M4f amph	M15_Z2 ol-amph	M8a ol-amph	M4e ol-amph	M4a amph(1)	M4g amph(1)
SiO <sub>2</sub> (wt.%)	43.83	49.45	43.61	44.66	43.09	46.96	45.81
TiO <sub>2</sub>	0.38	1.38	0.00	0.26	0.24	0.19	0.64
Al <sub>2</sub> O <sub>3</sub>	7.41	14.09	9.35	10.41	8.94	7.29	10.13
Fe <sub>2</sub> O <sub>3</sub>	9.59	9.78	11.10	8.12	9.89	5.88	5.59
MnO	0.18	0.15	0.17	0.14	0.15	0.07	0.08
MgO	21.54	8.12	20.99	20.30	25.40	25.86	21.90
CaO	7.65	9.71	8.25	9.21	7.03	2.60	8.56
Na <sub>2</sub> O	1.42	3.96	1.70	1.80	1.61	1.53	1.61
K <sub>2</sub> O	b.d.l.	0.74	b.d.l.	0.02	b.d.l.	0.10	0.07
P <sub>2</sub> O <sub>5</sub>	0.03	0.13	0.03	0.06	0.03	0.02	0.03
Perte	6.41	1.52	3.16	4.72	3.54	9.47	5.21
1000							
Sum	98.43	99.03	98.60	99.69	99.91	99.78	99.00
Cr (ppm)	960.00	336.00	1249.00	1652.00	2212.00	1140.00	802.00
Ni	348.00	94.00	523.00	544.00	819.00	922.00	648.00
Cs	0.14	0.19	0.17	0.12	0.09	0.16	0.56
Rb	3.90	11.10	4.00	4.00	3.90	4.40	5.30
Ba	20.70	49.40	14.90	12.80	15.10	n.d.	7.10
Th	0.25	0.27	0.22	0.22	0.21	0.26	0.30
U	0.09	0.11	0.07	0.08	0.07	0.09	0.17
Nb	0.37	2.24	0.34	0.40	0.31	1.42	2.28
Ta	0.04	0.18	0.05	0.04	0.03	0.13	0.16
La	1.76	3.49	1.53	2.37	1.39	3.19	5.96
Ce	4.56	10.26	3.48	6.16	3.29	8.03	20.82
Pb	6.19	0.62	0.50	0.66	0.64	1.36	2.12
Pr	0.66	1.72	0.49	0.90	0.46	1.22	4.01
Sr	19.40	95.60	60.60	91.80	208.50	20.90	33.60
Nd	3.45	9.07	2.42	4.20	2.25	5.44	21.72
Zr	20.00	74.00	14.00	24.00	14.00	45.00	65.00
Hf	0.80	2.30	0.51	0.84	0.49	1.50	2.72
Sm	1.14	3.13	0.76	1.17	0.72	1.33	6.45
Eu	0.48	1.15	0.33	0.43	0.30	0.39	1.84
Gd	1.27	3.45	0.83	1.11	0.75	1.10	5.44
Tb	0.28	0.68	0.17	0.22	0.16	0.19	0.90
Dy	2.00	4.39	1.30	1.53	1.21	1.18	5.11
Ho	0.48	1.00	0.32	0.37	0.29	0.26	1.10
Y	11.00	25.00	6.00	9.00	6.00	6.00	32.00
Er	1.29	2.51	0.83	0.97	0.78	0.68	2.80
Yb	1.39	2.48	0.90	1.07	0.87	0.74	2.94
Lu	0.22	0.38	0.15	0.17	0.14	0.12	0.47

(1) Mafic amphibolite altered by 1 – the phlogopite-rich matrix and 2 – late chlorite-rich matrix.

b.d.l.: below detection limit.

estimated using a value of the initial  $^{40}\text{Ar}/^{36}\text{Ar}$  of 295.5. Data are portrayed as age spectra on Fig. 11 and summarized in Table 5.

## 5. Petrography

### 5.1. Mafic rocks

Dark mafic bands (Fig. 6a, b, c) contain abundant amphibole (40–70 vol.%) plagioclase (10–50 vol.%) orthopyroxene (10–20 vol.%) ± olivine (0–25 vol.%). Olivine is only found in some mafic layers (i.e. shear band #4bis; M8a, Fig. 6c). No clinopyroxene is found. Sulfide inclusions in amphibole, iron oxides and rare apatite (samples M8a and M8b) are also present.

Amphibole surrounds all other mineral phases and appears texturally as a late crystallization product with respect to olivine, orthopyroxene (Figs. 6d, e, g, 7a, b, c, d). Sample M8a shows two distinct amphibole-bearing layers as an olivine-free amphibolite vein cross-cut a boudinaged olivine-bearing amphibolite band (Fig. 6c). In olivine-bearing amphibolites (shear band #4bis), amphibole (referred to as early amphibole) is strongly pleochroic from blue to green under the microscope with a sub-automorphic habitus and marked cleavages (Fig. 6d, g). By contrast, amphibole in olivine-free amphibolite (referred to as late amphibole) shows a distinctly paler pleochroism and presents a higher degree of deformation (Fig. 6e).

**Table 4**

LA-ICP-MS geochemistry for representative Ca-amphibole in amphibolite dikes.

Sample mineral	M8a1 prg	M8a1 prg	M8a1 prg	M8a2 mhb	M8a2 mhb	M8a2 mhb
SiO <sub>2</sub> (wt.%)	43.12	45.46	43.98	48.14	43.82	46.32
TiO <sub>2</sub>	0.30	0.09	0.21	0.53	0.77	0.85
Al <sub>2</sub> O <sub>3</sub>	13.99	12.79	14.11	10.48	13.13	11.82
Cr <sub>2</sub> O <sub>3</sub>	0.07	0.15	0.24	0.17	0.10	0.07
FeO	8.97	6.53	7.85	7.70	9.29	8.76
MnO	0.16	0.07	0.10	0.13	0.08	0.06
MgO	15.84	17.43	16.28	16.80	15.24	16.10
CaO	11.83	12.37	12.12	11.64	11.89	12.01
Na <sub>2</sub> O	2.79	2.39	2.44	1.82	2.48	2.14
K <sub>2</sub> O	0.07	0.04	0.05	0.04	0.07	0.07
Sum	97.13	97.31	97.37	97.47	96.87	98.20
Cs (ppm)	b.d.l.	b.d.l.	b.d.l.	b.d.l.	0.24	0.07
Rb	b.d.l.	b.d.l.	b.d.l.	b.d.l.	3.72	b.d.l.
Ba	2.18	2.05	2.77	2.68	5.21	3.79
Nb	0.36	0.31	0.40	0.68	0.65	0.87
Ta	b.d.l.	b.d.l.	b.d.l.	b.d.l.	0.11	0.15
La	2.23	1.90	2.26	2.57	2.67	2.81
Ce	6.31	5.76	6.63	7.95	7.09	9.64
Pb	b.d.l.	b.d.l.	b.d.l.	b.d.l.	b.d.l.	b.d.l.
Pr	0.95	0.92	1.23	1.60	1.21	1.67
Sr	73.11	68.75	67.36	41.47	46.78	48.35
Nd	4.05	4.59	5.67	7.81	8.66	10.30
Zr	24.49	23.12	30.51	48.31	38.45	56.43
Hf	1.13	0.85	1.04	1.95	1.62	2.08
Sm	1.50	b.d.l.	1.64	3.23	2.96	2.74
Eu	0.87	0.76	0.81	1.08	1.09	1.46
Gd	b.d.l.	1.41	3.34	3.10	3.62	6.02
Tb	0.33	0.32	0.62	0.82	0.69	1.20
Dy	2.76	2.86	3.86	5.97	6.50	8.42
Ho	0.67	0.68	0.93	1.31	1.18	2.03
Er	2.36	1.60	2.80	4.20	3.43	5.65
Yb	2.26	1.44	2.53	4.72	4.13	5.58
Lu	0.22	0.36	0.49	0.62	0.67	0.76

See Fig. 10 for spider diagram graphic.

Abbreviations after Whitney and Evans (2010).

Textural relationships between plagioclase, orthopyroxene and olivine are obscured by the amphibolitization stage. Olivine appears as fine-grained clusters closely associated with, and generally included in, orthopyroxene (Figs. 6g, 7a, b). In sample M4e, olivine was replaced by orthopyroxene before the crystallization of large amphibole grains (Fig. 7c, d). Olivine is also partially destabilized by tremolite. Primary Cr-rich spinel crystals are present in olivine (Fig. 7a). In olivine-bearing samples, plagioclase is rare and partially to totally replaced by amphibole (Fig. 6g).

Leucocratic feldspar-rich veins are mainly composed of plagioclase (70–100%) with subordinate orthopyroxene (0–20%) and rare amphibole (0–10%). Undeformed leucocratic veins show euhedral amphibole in a groundmass of large plagioclase crystals (Fig. 6f). Close to the shear bands, veins of plagioclase evidence deformation and grain size reduction. Orthopyroxene is only partially preserved yet retaining textural evidence of former equilibrium with plagioclase. Orthopyroxene is included in amphibole or rimmed by amphibole pressure shadows (Fig. 6e), again suggesting the partial destabilization of coarse grained primary assemblage of orthopyroxene (± olivine) and plagioclase to form various generations of amphibole. A network of late serpentine, chlorite and talc is observed in orthopyroxene fractures (Fig. 6d).

As for ultramafic rocks, mafic bands are locally replaced by a phlogopite-rich matrix (in which phlogopite is in turn replaced by chlorite). Orthopyroxene and calcic-amphibole appear only as relicts into layers of phlogopite and acicular ortho-amphibole. Plagioclase is destabilized and rimmed by a Ba-rich K-feldspar.

### 5.2. Ultramafic rocks (UM) and matrix

The mineralogy of undeformed peridotites is dominated by an isotropic network of serpentine (75–90%), with rare relicts of brown

**Table 5**<sup>40</sup>Ar/<sup>39</sup>Ar age performed on amphiboles from mafic dikes cross-cutting the peridotite of the New Caledonia ophiolite.

Sample	Lithology	Location	Total fusion age	Plateau age	% <sup>39</sup> Ar	Intercept age	( <sup>40</sup> Ar/ <sup>36</sup> Ar) <sub>i</sub>	MSWD	Preferred age	<sup>38</sup> Ar/ <sup>37</sup> Ar	<sup>38</sup> Ar/ <sup>39</sup> Ar
C10 (1)	MS amphibolite	Thio	59.12 ± 2.24	56.21 ± 2.14	95.6	nd	nd	nd	56.21 ± 2.14	nd	nd
C10 (2)	MS amphibolite	Thio	68.23 ± 2.97	56.85 ± 4.79	96.0	nd	nd	nd	nd	nd	nd
SNC01 (1)	Pegmatite dike	Massif du Sud	53.67 ± 3.14	60.20 ± 4.62	92.5	nd	nd	nd	60.20 ± 4.62	0.011	0.41
SNC01 (2)	Pegmatite dike	Massif du Sud	87.66 ± 5.94	62.87 ± 5.54	61.8	nd	nd	nd	nd	0.01	0.36
SNC03 (1)	Gabbro	Massif du Sud	51.13 ± 4.49	51.25 ± 3.12	81.5	51.32 ± 4.18	295.7 ± 21.1	0.65	51.25 ± 3.12	0.013	0.53
SNC04 (1)	Gabbro	Massif du Sud	47.59 ± 4.36	49.56 ± 3.98	97.8	52.22 ± 5.34	287.5 ± 10.5	0.93	52.22 ± 5.34	0.007	0.27
M3b (1)	ol-free amphibolite	Plum beach	53.64 ± 4.27	53.35 ± 3.39	78.0	54.10 ± 3.40	293.6 ± 5.0	1.25	54.10 ± 3.40	0.005	0.18
M4d (1)	ol-free amphibolite	Plum beach	238.54 ± 7.50	/	/	/	/	/	/	0.02	1.72
M4d (2)	ol-free amphibolite	Plum beach	73.10 ± 5.49	68.67 ± 6.37	97.4	67.59 ± 5.06	303.7 ± 5.0	1.02	67.59 ± 5.06	0.02	1.73
M8f (1)	ol-free amphibolite	Plum beach	58.34 ± 3.61	56.29 ± 3.28	95.8	52.86 ± 5.34	318.6 ± 20.6	1.79	56.23 ± 4.42	nd	nd
M8f (2)	ol-free amphibolite	Plum beach	62.08 ± 2.61	60.82 ± 3.06	92.2	60.25 ± 2.84	299.6 ± 4.2	1.77		0.004	0.11
M8f (3)	ol-free amphibolite	Plum beach	93.78 ± 3.08	49.34 ± 4.47	49.31	56.46 ± 7.40	282.5 ± 12.1	0.23		0.004	0.07
M8f (4)	ol-free amphibolite	Plum beach	53.43 ± 2.85	54.86 ± 2.04	99.5	55.36 ± 2.11	293.1 ± 2.9	0.38		0.003	0.08
M8a-Z1 (1)	Ol-bearing amphibolite	Plum beach	107.69 ± 7.09	107.94 ± 10.80	67.7	92.81 ± 13.43	349.1 ± 19.0	1.56		0.017	1.71
M8a-Z1 (2)	Ol-bearing amphibolite	Plum beach	125.24 ± 4.51	111.22 ± 6.93	70.8	92.50 ± 11.65	351.7 ± 3.7	1.28	92.50 ± 11.65	0.017	1.68
M8a-Z2 (1)	Ol-free amphibolite	Plum beach	76.61 ± 7.31	72.54 ± 5.83	86.1	73.85 ± 6.74	297.0 ± 9.6	1.55	73.85 ± 6.74	0.024	1.87
M15 (2)	Ol-bearing amphibolite	Plum beach	81.80 ± 4.20	/	/	/	/	/		0.019	1.59
M15 (3)	Ol-bearing amphibolite	Plum beach	89.97 ± 8.42	85.94 ± 7.50	87.9	86.54 ± 7.58	296.1 ± 1.8	2.09		0.017	1.28
M15 (4)	Ol-bearing amphibolite	Plum beach	167.09 ± 21.48	/	/	/	/	/		0.013	1.74

Preferred age is determined after plateau age, intercept age or a mean of different analysis for a same sample when the plateau age is not significant.

MS: metamorphic sole; MSWD: mean square weighted deviation.

orthopyroxene, olivine phenocrysts and black chromiferous spinels. These peridotites belong to the highly depleted harzburgites of the Massif du Sud (i.e. Pirard et al., 2013; Prinzhöfer and Allègre, 1985; Ulrich et al., 2010). Few deformation textures are observed, where the extensive late serpentinization may have erased former deformation textures.

Peridotites boudinaged in shear bands (Fig. 7b) show a similar mineral assemblage. However, a reaction rim around peridotite boudins contains coarse-grained hornblende pseudomorphing orthopyroxene, and containing chromite inclusions (Fig. 7g). Light colored phlogopite (Fig. 7b, f, h) and acicular ferro-magnesian ortho-amphibole (Fig. 5f) co-crystallized around peridotite boudins as a result of the partial destabilization of ultramafic orthopyroxene and secondary hornblende. Therefore, this assemblage postdates the boudinage of the peridotite and the first hydration recorded by the crystallization of hornblende. Phlogopite increases in modal proportion towards the amphibole-rich mafic bands, along with a grain size decrease but shows no preferred orientation. Chlorite is interlayered with phlogopite and crystallizes as a late stage alteration product responsible for the macroscopically greenish to grayish color of the matrix. Millimetric veinlets of talc-chlorite-serpentine, slightly sheared in places, also cross-cut peridotites boudins (Fig. 7h). These veinlets are themselves cross-cut by a late isotropic serpentine network.

## 6. Mineralogy

### 6.1. Orthopyroxene

Orthopyroxene from harzburgites displays a typical Mg# [Mg/(Mg + Fe)] of 0.92 ± 0.02 (Fig. 8a). In mafic rocks, the Mg# of orthopyroxene shows lower values ranging between 0.77 and 0.85.

Cr<sub>2</sub>O<sub>3</sub> and CaO contents (Fig. 7a) show small yet systematic variations between the mafic bodies, with higher values in olivine-bearing rocks (<0.20 wt.% Cr<sub>2</sub>O<sub>3</sub>; 0.35–0.65 wt.% CaO, except for three points with 0.82 and 0.97 wt.% CaO) than in leucocratic feldspar-rich rocks (<0.04 wt.% Cr<sub>2</sub>O<sub>3</sub>; 0.15–0.35 wt.% CaO). Cr<sub>2</sub>O<sub>3</sub> and CaO contents are higher in ultramafic rocks, with large intra-sample variations (0.40–0.80 wt.% Cr<sub>2</sub>O<sub>3</sub>; 0.40–1.80 wt.% CaO). Al contents are low (~0.02 p.f.u.) and show no systematic variation.

Orthopyroxene in harzburgite falls within the composition domain of orthopyroxene-poor harzburgite described by Prinzhöfer et al. (1980) and Pirard et al. (2013; Fig. 8a). Orthopyroxene in olivine-bearing and olivine free amphibolites overlaps the range of orthopyroxene in

amphibolite and hornblendite dikes described by Pirard (2012). Orthopyroxene in mafic bands have similar Mg# orthopyroxene from gabbronorite sills of Pirard et al. (2013), but show lower Ca content.

### 6.2. Olivine

The patterns of Mg# of olivine (Fig. 8b) in harzburgite and in olivine-bearing mafic rocks mirror those of orthopyroxene described above (Fig. 8b). Mg# in ultramafic olivine is 0.91–0.92 and the MnO content varies between 0.06 and 0.22 wt.% (Fig. 8b), in the same range as those of nearby harzburgites (Pirard et al., 2013). Olivine in mafic bands shows similar Mg# (0.78–0.85 wt.%) to amphibolite and hornblendite dikes of Pirard (2012). The Mg# is lower and the MnO content (0.20–0.39 wt.%) is higher than reported for mafic cumulates by Pirard et al. (2013; Fig. 8b). NiO content in mafic olivine varies between 0.16 and 0.21 wt.%, which is consistent with the most evolved olivine found in olivine-bearing cumulates (Pirard et al., 2013). Compositional trends in NiO and MnO vs. Mg# match the fractional crystallization trends evidenced by Pirard et al. (2013).

### 6.3. Feldspar

Plagioclase occurs only in mafic rocks, as veins in leucocratic feldspar-rich rocks (with a composition of a norite), or as scarce, isolated crystals in olivine-bearing rocks. In noritic rocks, albite content [Na# = Na/(Na + Ca)] ranges from 0.46 to 0.66 (from labradorite to andesine; Fig. 8c), in the domain of amphibolite dikes described by Pirard (2012). In olivine-bearing rocks, plagioclase corresponds to anorthite (Na#: 0.02–0.07; Fig. 8c), in the range of amphibolite dikes of Pirard (2012). Secondary feldspar rimming norite veins are rich in alkalis (~5.5 wt.% Na<sub>2</sub>O; ~3.5 wt.% K<sub>2</sub>O; ~12.5 wt.% BaO) and have intermediate composition between anorthoclase and hyalophane.

### 6.4. Ca-amphibole

Amphibole shows Mg# comparable to that of orthopyroxene and olivine in both mafic (0.90–0.74; Fig. 9a) and ultramafic rocks (~0.91 ± 0.01; Fig. 9a), and Na < 0.5 p.f.u. and (Ca + Na)<sub>B</sub> > 1.0 p.f.u. typical of calcic-amphibole (Leake et al., 1997).

In olivine-bearing mafic bodies, early amphibole is pargasitic with (Na + K)<sub>A</sub> ≥ 0.5 p.f.u. and Si ranging from 6.12 to 6.30 p.f.u. (Fig. 9b). Late amphibole destabilizing this pargasite hornblende

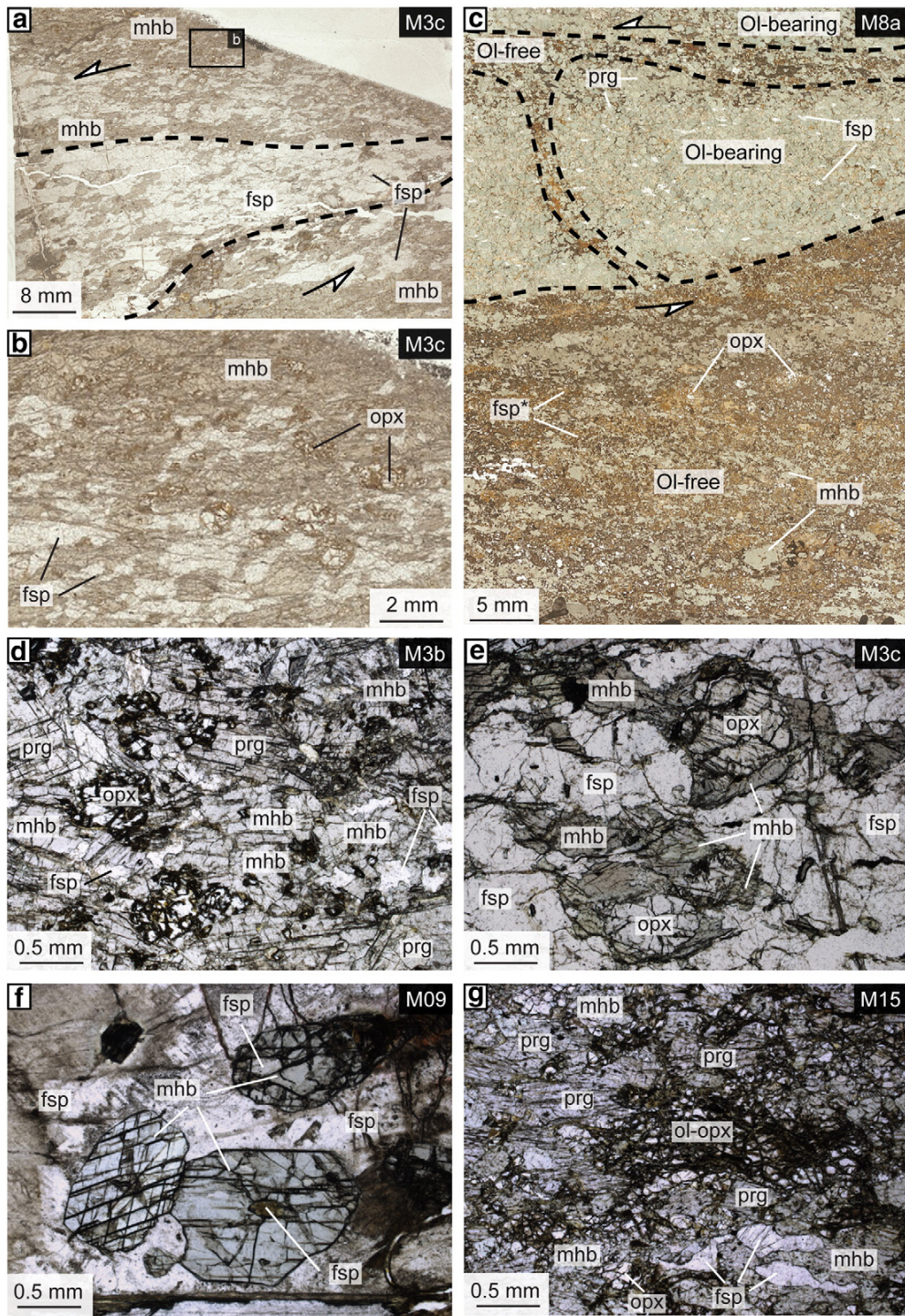


**Fig. 6.** Representative mineral assemblages in amphibolite dikes. a) Olivine-free amphibolite with a boudinaged feldspar-rich layer within a hornblende-rich matrix. b) Zoom into the hornblende-rich matrix showing the destabilization of orthopyroxene. c) Pale olivine-bearing amphibolite band boudinaged and cross-cut by an olivine-free amphibolite layer. d) e) Assemblage of orthopyroxenes and plagioclases destabilized by the growth of amphiboles. f) Euhedral blue-pale amphibole growing in feldspar-rich vein away from deformation. g) Olivine, orthopyroxene and plagioclase boudinaged and destabilized by the syn-cinematic growth of amphibole. Abbreviations after Whitney and Evans (2010).

has  $(\text{Na} + \text{K})_A \leq 0.5$  p.f.u. and a higher Si content (6.50–7.00 p.f.u.; Fig. 9b), and belongs to the magnesio-tschermarkite hornblende (Leake et al., 1997). In olivine-free samples (i.e M3c), late amphibole shows a decrease in  $(\text{Na} + \text{K})_A$  and an increase of the Si content (6.37–6.88 p.f.u.; Fig. 9b). This evolution is also observed with the

content in Ti (0.15–0.05 p.f.u.). This composition is similar to the composition of amphibole from undeformed mafic dikes described by Pirard (2012), and partially fall in the domain of the metamorphic sole amphibolites from Thio considering their Ti and  $(\text{Na} + \text{K})_A$  contents, yet with a much lower Mg# (see Cluzel et al., 2012).

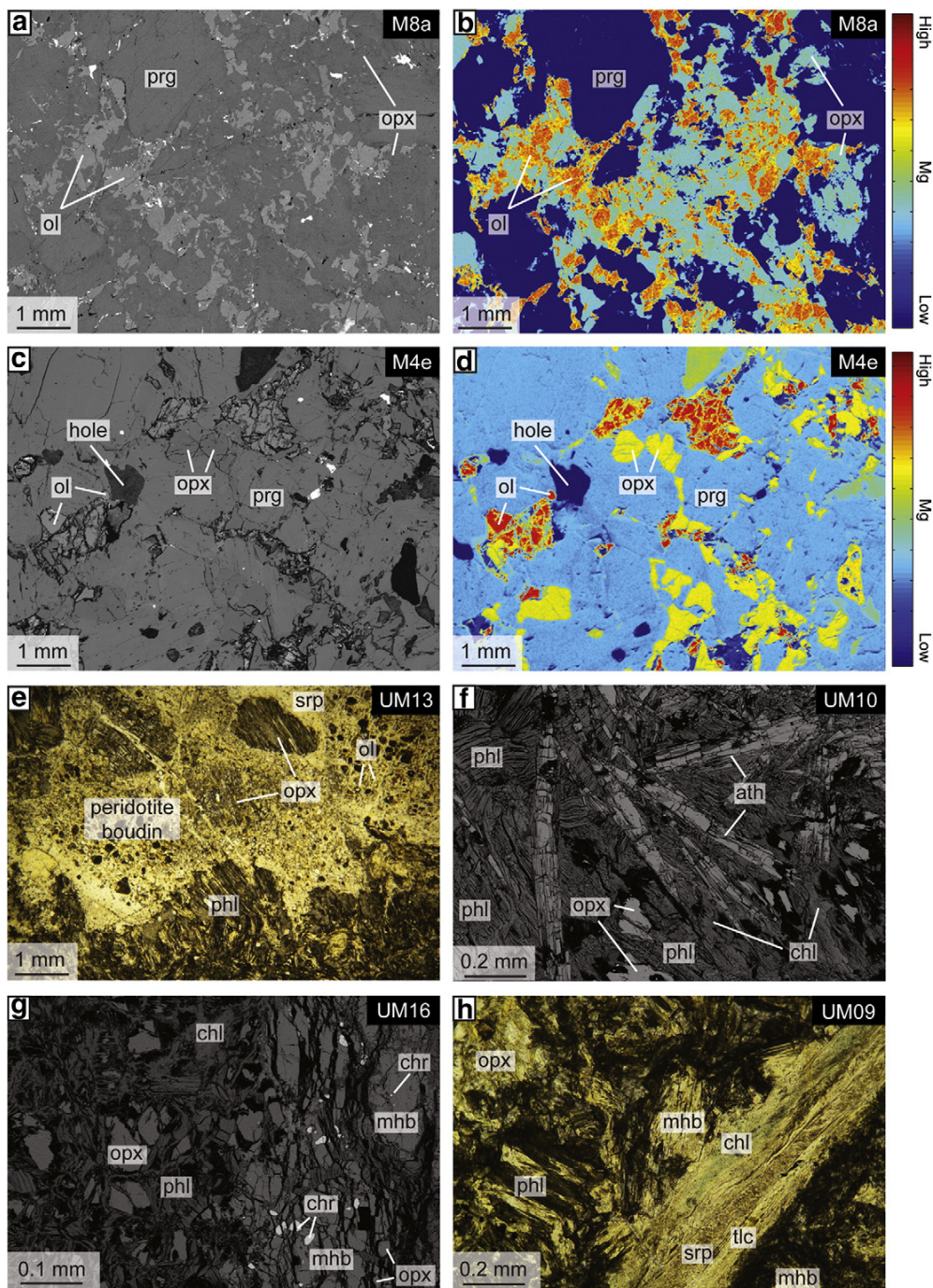


**Fig. 7.** Representative mineral assemblages in olivine-bearing amphibolite and in micas-rich matrix. a), b), c) and d) Olivine and plagioclase destabilized by orthopyroxene and then amphibole. a) and c) are SEM back-scattered electron images, b) and d) are corresponding SEM abundance maps for Mg, where relative concentration is scaled on the right-end side color bar. e) and f) Microphotograph and SEM back-scattered electron image of peridotites boudins destabilized by the phlogopite-rich matrix associated to the anthophyllitic amphiboles. g) Coarse-grained hornblende pseudomorphing orthopyroxene and partially destabilized by phlogopite. h) Phlogopite-rich matrix cross-cut by veins of talc, chlorite and serpentine. Abbreviations after Whitney and Evans (2010).

Early amphibole in olivine-bearing amphibolite has the lowest Ti (0.01 and 0.05 p.f.u.) and does not fall in the domains of amphibole-bearing dikes (Pirard, 2012) or of the metamorphic sole (Cluzel et al., 2012) (Fig. 9c). Amphibole with the highest Si content is again the poorest in  $(\text{Na} + \text{K})_{\text{A}}$  content (Fig. 9b). Tremolite is only present in olivine-bearing rocks and texturally associated to mafic olivine (Fig. 9b).

Calcic-amphibole destabilizing ultramafic orthopyroxene are magnesio-hornblende with high Si content (7.19–7.46 p.f.u.),  $(\text{Na} + \text{K})_{\text{A}}$  between 0.25 and 0.12 p.f.u. (Fig. 9b) and  $\text{Ti} < 0.10$  p.f.u. (Fig. 9c).

Late acicular amphibole crystallizing within the phlogopite-rich matrix belongs to the ferro-magnesian anthophyllite series ( $\text{Si} \sim 8$  p.f.u.;  $\text{Al}_{\text{tot}} \leq 0.23$  p.f.u.;  $(\text{Ca} + \text{Na})_{\text{B}} \leq 0.15$  p.f.u.; Leake et al., 1997).

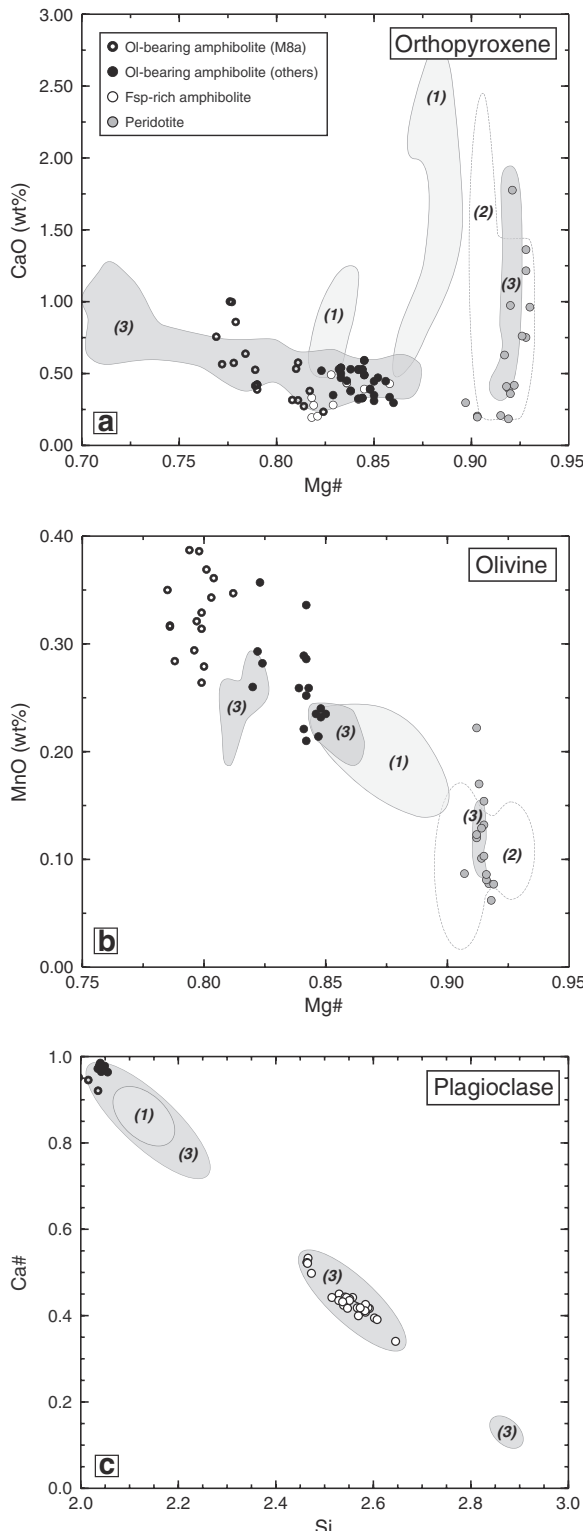


**Fig. 8.** EPMA composition of selected minerals. a) Mg# [ $Mg/(Mg + Fe)$ ] vs. CaO (wt%) in mafic and ultramafic orthopyroxene. b) Mg# vs. MnO (wt%) in mafic and ultramafic olivine. c) Si (p.f.u.) vs. Ca# [ $Ca/(Ca + Na)$ ] in plagioclase. (1) Gabbronorite sills (crustal cumulates; Pirard et al., 2013); (2) peridotites from Massif du Sud (Marchesi et al., 2009); (3) horblendite and amphibolite dikes (Pirard, 2012).

### 6.5. Phlogopite

Phlogopite presents a Mg# of 0.89, regardless of its structural position in the shear band (Table 1). Only few crystals display the K<sub>2</sub>O content of a regular mica owing to retrogression by chlorite. Cr<sub>2</sub>O<sub>3</sub> (<0.02 wt%) and TiO<sub>2</sub> (0.05 wt%) are present in small amounts.

### 6.6. Accessory minerals

Early amphibole grains (i.e. pargasite) host various inclusions (e.g. spinel, magnetite, sulfides). Magnetite inclusions derive from the oxidation of iron-sulfide and spinel. Spinel in harzburgite is a chromite with a Cr# [Cr# =  $(Cr/(Cr + Al + Fe^{3+}))$ ] of  $0.72 \pm 0.05$  and a Mg# of  $0.35 \pm 0.05$  (Fig. 9d). Spinel is consistently more aluminous in mafic rocks, with a Cr# from 0.18 to 0.38 for a Mg# varying between 0.25 and 0.32 (Fig. 9d). TiO<sub>2</sub> in mafic and ultramafic spinel is below the detection limit. Cu- and Ni-rich Fe-sulfides (i.e. pentlandite-pyrrhotite) are found as inclusions in early amphibole in olivine-bearing mafic rocks.

## 7. Geochemistry

### 7.1. Whole rock geochemistry

Rare earth elements (REE) normalized to N-MORB of both olivine-bearing and olivine-free amphibolites display values lower than 1 [ $(\text{REE})_N \sim 0.4$ ], with the exception of the sample M4f [ $(\text{REE})_N \sim 1$ ] (Fig. 10a). They display a slight enrichment in light REE (LREE) relative to heavy REE (HREE) [ $(La/Lu)_N = 1.89 \pm 0.35$ ]. High field strength elements (HFSE; Ti, Hf, Zr, Nb, Ta) are slightly depleted relative to REE [ $(Nb/Lu)_N = 0.41 \pm 0.05$ ] (Fig. 10a). Large Ion Lithophile Elements (LILE; Pb, U, Th, Ba, Rb, Cs) show large enrichments relative to REE, increasing with their degree of mobility and incompatibility [ $(Cs/Lu)_N = 62 \pm 39$ ] (Fig. 10a).

The compositions range of metamorphic sole (Cluzel et al., 2012) display a similar pattern to amphibolites though slightly shifted towards higher values by a factor of ~2 (Fig. 10a). Gabbronorite sills (Pirard et al., 2013) are highly depleted in all incompatible elements. However, they display a pattern roughly similar to that of amphibolites, with a mean relative depletion factor of ~10 but with larger Pb and Sr relative anomalies (Fig. 10a). Arc tholeiitic dikes (Cluzel et al., 2006) have incompatible elements compositions overlapping with those amphibolites (Fig. 10a). It strongly suggests that tholeiitic dikes and amphibolites have a same origin.

In phlogopite-rich rocks, concentrations in HREE are similar to those of olivine-free and olivine-bearing amphibolite (Fig. 10a). However, phlogopite-rich rocks have a larger enrichment in LREE relative to HREE [ $(La/Lu)_N = 3.55 \pm 1.77$ ]. These rocks are depleted in HFSE relative to REE but less depleted than olivine-bearing and olivine-free amphibolite (with the exception of the sample M4f). Sr shows a large depletion relative to REE and LILE display a large enrichment especially in Cs.

### 7.2. In-situ trace elements

Incompatible trace elements compositions of early and late amphibole, respectively found in olivine-bearing and olivine-free amphibolites display similar N-MORB normalized patterns (Fig. 10b) with however slightly higher content in late amphibole (i.e. magnesio-hornblende) compared to early amphibole (i.e. pargasite). REE patterns from heavy REE (HREE) to light REE (LREE) are flat and close to N-MORB values, with  $(La/Lu)_N = 0.87 \pm 0.39$ . HFSE are slightly depleted relative to REE [ $(Nb/Lu)_N = 0.21 \pm 0.07$ ]. LILE show positive anomalies [ $(Cs/Lu)_N = 12.1 \pm 5.9$ ]. Overall, similar behaviors (i.e. negative anomalies in HFSE and positive anomalies in LILE) are observed in whole-rock data on amphibolites and in-situ data on amphibole, suggesting that the trace

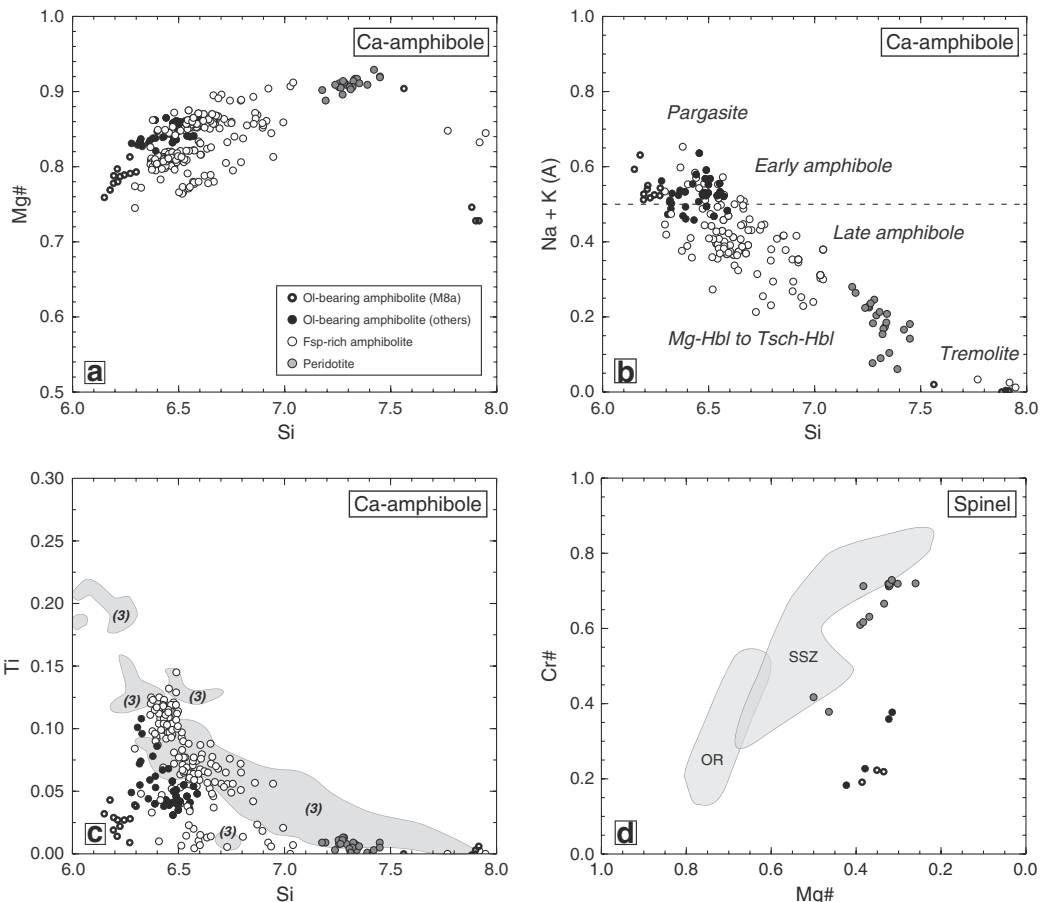


**Fig. 9.** EPMA composition of amphibole and spinel in selected samples. a) Si (p.f.u.) vs. Mg# in Ca-amphibole. b) Si (p.f.u.) vs. (Na + K)<sub>A</sub> in Ca-amphibole after the classification of Leake et al. (1997). The dash line separates the pargasite domain (early amphibole) from the Mg-hornblende to tsch-horblende domains (late amphibole). c) Si (p.f.u.) vs Ti (p.f.u.) in Ca-amphibole. d) Mg# vs. Cr# in spinel. OR: Ocean ridge domain. SSZ: suprasubduction domain. (3) Horblende and amphibolite dikes (Pirard, 2012).

element budget in the rocks is mainly controlled by amphibole. However, higher HREE content in late amphibole compared to that in early amphibole is difficult to explain with a fluid mediated recrystallization. This higher content more likely mirrors the more differentiated nature of the norite dikes compared to the troctolite dikes (prior to metamorphic hydration).

Amphibole in mafic amphibole-bearing dikes analyzed by Pirard (2012) displays a pattern similar to that of the amphibole reported here (gray overlay; Fig. 10b): it shows a similar enrichment in Pb and depletions in Ti-Sr-Nb-Ta with comparable absolute values, including in the most mobile and incompatible trace elements, advocating for similar origins. Ba-content is similar in both analyses series and Rb-content is lower in the amphibole of Pirard (2012) than all our early and late amphiboles (Fig. 10b). Cs has not been measured.

#### 8. $^{40}\text{Ar}/^{39}\text{Ar}$ constraints on mafic rocks formation

$^{40}\text{Ar}/^{39}\text{Ar}$  laser probe step-heating dating was carried out on 20 isolated single amphibole crystals from 11 different rocks, using the procedure described above. These samples are mainly olivine-free and olivine-bearing amphibolites from the Plum beach. They also include amphibolites from the Thio metamorphic sole (sample C10) and undeformed gabbroic dikes from the Massif du Sud (samples SNC03 and SNC04, col des Deux Tétons). Age spectra and inverse isochron plots are reported in Fig. 11 for some of these samples. The closure temperature for the  $^{40}\text{Ar}/^{39}\text{Ar}$  method in hornblende is around

550 ± 50 °C (Harrison, 1980). For most samples, errors are relatively large due to the fact that only one grain was analyzed each time and that the K content (and therefore the amount of radiogenic Ar) is low in these amphiboles.

Amphibole from the Thio metamorphic sole provides an age of 56.9 ± 2.6 Ma (Figs. 11a, 12) consistent with the age reported by Cluzel et al. (2012) from a nearby exposure. Similar ages are obtained on the two undeformed gabbros from the Massif du Sud for which intercept ages are in the range 51–52 ± 4 Ma (Figs. 11a, 12; see the Online Fig. S1 for isotope correlation plot), with initial  $^{40}\text{Ar}/^{36}\text{Ar}$  values close to the present-day atmospheric ratio (see Table 5). Large amphibole from a partially weathered pegmatite dike yields more scattered results with some evidence of excess argon as a result of fluid infiltration and only a maximum age of 60 ± 5 Ma can be attributed to this sample.

At Plum beach, 8 hornblende crystals from 4 olivine-free amphibolites (M3d, M4d, M8a-Z2, M8f) and 5 hornblende crystals from two weakly deformed olivine-bearing amphibolite (M15 and M8a-Z1) yield ages ranging between 54 and 93 Ma, with the exception of one crystal (M15) that displays a strongly discordant age pattern and an integrated age of 167 ± 21 Ma likely related to trapped excess argon. For M8f, 4 amphiboles were analyzed and representative age spectra are shown on Fig. 11b, with plateau dates ranging from 54.9 ± 2.0 Ma to 59.2 ± 2.7 Ma and a similar age in the isotope correlation plot with an initial atmospheric ratio (reported in the Online Fig. S1). The consistency of the results on 4 grains from M8f and the lack of evidence of excess argon for this sample suggest that amphibolitization and related

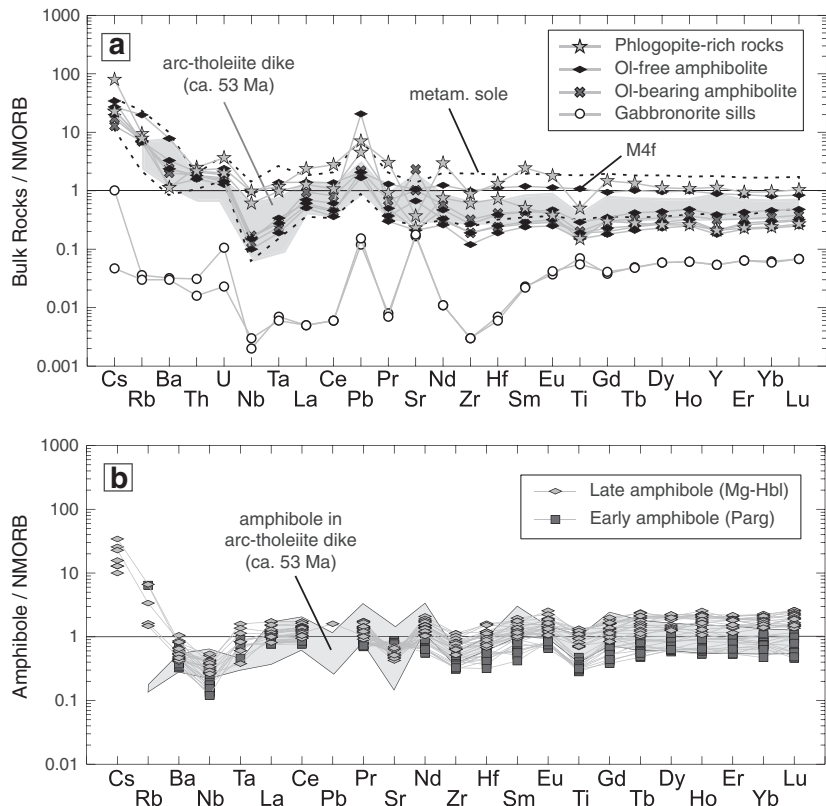


**Fig. 10.** (a) Trace elements concentrations of amphibolite. The N-MORB normalization values are from Sun and McDonough (1989). Data for the metamorphic sole are from Cluzel et al. (2012) and for pre-obduction dikes (53 Ma) from Cluzel et al. (2006). Gabbronorite sills from the crustal cumulates are from Pirard et al. (2013). (b) Trace elements spider-diagrams of hornblende in olivine-free and olivine-bearing amphibolite M8a. Normalization values for the NMORB are from Sun and McDonough (1989). Gray area represents the trace elements values for amphibole in hornblendite and diorite dikes described by Pirard (2012).

deformation occurred at ca. 55 Ma, which is supported by the age of  $54.1 \pm 3.4$  Ma obtained on amphibolite M3b from another shear zone. According to microprobe analyses and textural observations, it is likely that this age of ca. 55 Ma corresponds to the crystallization of secondary magnesio-hornblende that partially replaced pargasite and orthopyroxene. This age range coincides with the formation of the metamorphic sole at Thio (sample C10 and Cluzel et al., 2012), the emplacement of some gabbros (samples SNC03 and SNC04) and pre-obduction felsic dikes (53 Ma; Cluzel et al., 2006).

8 amphiboles from 5 olivine-bearing samples yield older ages ranging from 73 to 93 Ma (Table 5) with relatively discordant age spectra (Fig. 11c) and large experimental errors due to the low amount of K. However, the isotope correlation diagram and the flat K/Ca ratios do not provide evidence of excess argon (reported in the Online Fig. S1), which could indicate that ages around 90 Ma are meaningful. This suggests that early amphibole is preserved in the dated rocks, which is consistent with the chemical data that point to the coexistence of primary pargasite predating synkinematic magnesio-hornblende developed around it.

## 9. Interpretations and discussion

### 9.1. Nature of the protolith and subduction signature

The sharp contact between mafic rocks and surrounding peridotites (preserved from metasomatic alteration in places) suggests that these mafic rocks were emplaced, prior to amphibolitization, as 100 m-scale intrusions, most likely as dikes or melt lenses. The lack of pervasive deformation in the peridotite a few meters away from the shear

bands, and the presence of olivine and orthopyroxene in mafic rocks, rule out the possibility that the mafic bands represent sheared metamorphic sole amphibolites imbricated within mantle wedge peridotites. The protolith of the mafic bands is therefore interpreted as emplaced in the form of small-scale melt intrusions at temperatures where peridotites were comparatively brittle.

Partially preserved orthopyroxene, anorthitic plagioclase and high Mg# olivine indicate that the protolith of the amphibolite bands was a norite or a troctolitic norite. Late hornblende (i.e. magnesio-hornblende) and Ca-Na plagioclase, which abound in amphibolite bands, may have recrystallized from orthopyroxene, olivine and anorthitic plagioclase (such as found in the “noritic” pods) during amphibolitization and/or later fluid infiltration. Clinopyroxene was either absent or is now completely replaced (undeformed hornblendite dikes from Rivière des Pirogues show late amphibole replacing large clinopyroxene crystals; Pirard, 2012).

Olivine-bearing domains cross-cut by olivine-free domains (Fig. 6c) point to evolving compositions of the magma intruding the peridotite. The positive correlation between Cr# of spinel and Mg# of olivine in olivine-bearing amphibolites suggests that the mafic protolith formed through melting of harzburgite with a supra-subduction signature followed by fractional crystallization (Marchesi et al., 2009). The presence of orthopyroxene, plagioclase and early amphibole (i.e. pargasite) is consistent with peridotite melting triggered by aqueous slab-derived fluids (Pirard, 2012).

Amphibolites display flat N-MORB normalized patterns with lower REE abundances than N-MORB ( $\text{REE}_{\text{Amphibolite}}/\text{REE}_{\text{N-MORB}} \sim 0.5$ ; Fig. 10). A simple melting model shows that these amphibolites are too enriched, however, to derive directly from melting of the host

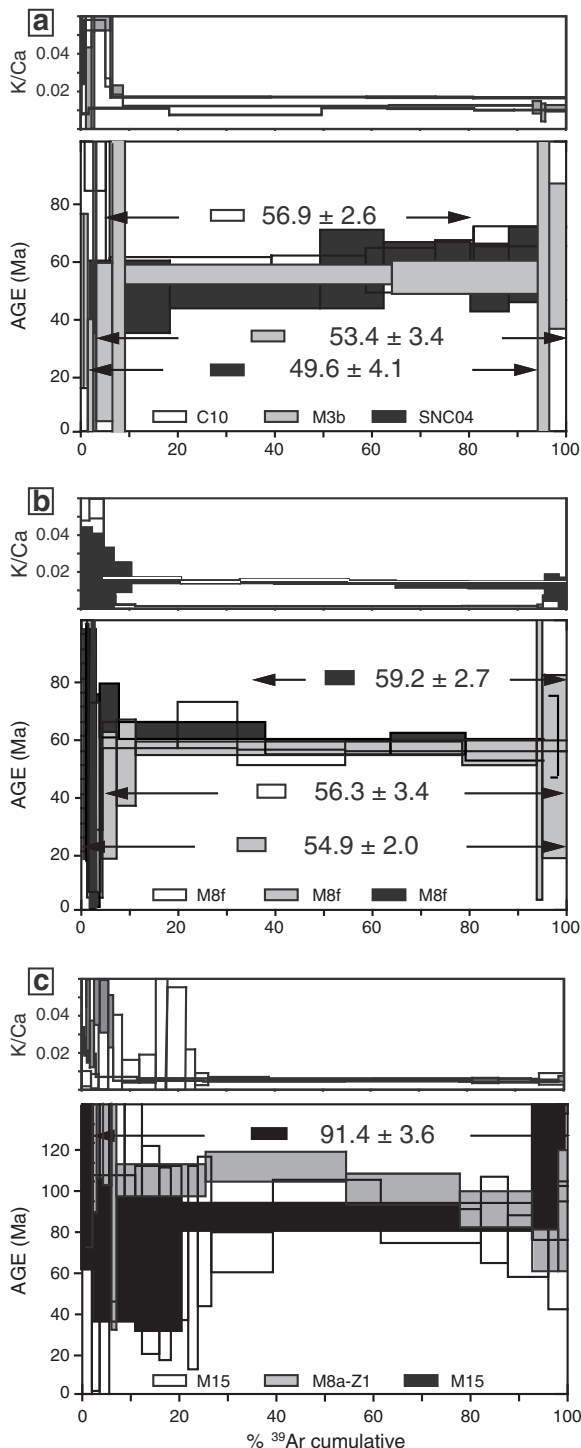


**Fig. 11.** Representative  $^{40}\text{Ar}/^{39}\text{Ar}$  age spectra of amphibole where K/Ca and calculated age are plotted as function of the cumulative fraction of  $^{39}\text{Ar}$  released. Samples: C10: metamorphic sole sampled of Thio; SNC04: undeformed gabbroic dikes cross-cutting the Massif du Sud ophiolite; M8a-Z1 and M15: olivine-bearing; M8f and M3b: olivine-free amphibolite. Corresponding reverse isochron plots ( $^{36}\text{Ar}/^{40}\text{Ar}$  vs.  $^{39}\text{Ar}/^{40}\text{Ar}$ ) with intercept age are reported in the Online Fig. S1.

depleted harzburgite and require a less depleted ultramafic source (either refertilized by fluids or silica-rich melts). Trace elements patterns of amphibolites in fact closely fit those of unmetamorphosed

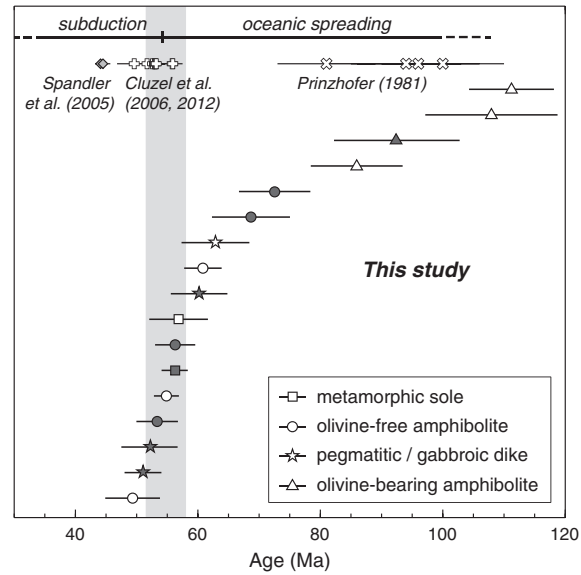


**Fig. 12.** Plots of  $^{40}\text{Ar}/^{39}\text{Ar}$  plateau age on amphibole from the different mafic units of the New Caledonia ophiolite in comparison of the timing of intrusion of pre-obduction dikes from Cluzel et al. (2006) and the metamorphic sole is from Cluzel et al. (2012). High-pressure rocks are from Spandler et al. (2005) and Cretaceous gabbroic dikes cross-cutting the peridotite are from Prinzhofer (1981). White-colored data are for  $^{40}\text{Ar}/^{39}\text{Ar}$  plateau ages. Black-colored data are for  $^{40}\text{Ar}/^{39}\text{Ar}$  preferred ages (plateau age or intercept age). See also Table 5.

microdioritic dikes found in the Massif du Sud, interpreted as subduction-related magma intrusions by Cluzel et al. (2006).

The slab signature is best recorded by HFSE and LILE. HFSE in the bulk rock display negative anomalies relative to REE (Fig. 10). These are characteristic of subduction zone magmas, as these elements are retained in rutile and zircon in the subducting slab (e.g. Coltorti et al., 2007; Zack and John, 2007). The enrichment in LILE (and to a lesser extent in LREE) is also consistent with a subduction signature, since LILE are mobilized during the dehydration of the upper part of the slab (e.g. Pearce et al., 1984). Such enrichments are observed in metamorphic soles for Rb, Ba and also Pb (Ishikawa et al., 2005). These enrichments cannot result from late sub-surface alteration, since LILE and HFSE are mainly concentrated in high temperature amphiboles which impose their geochemical signature in the whole rock (Fig. 10b; Table 4).

#### 9.2. Petrological evolution, deformation and fluid ingression

Field relationships and mineralogy suggest that the dark amphibolite bands and the more leucocratic noritic veins are cogenetic, with percolation apparently favored towards the north. This direction is compatible with upward melt migration expected at plate boundary (e.g. Matthews et al., 2015) within the mantle wedge (Figs. 2, 13a) and close to the nascent crust (e.g. Pirard et al., 2013). Progressive aqueous fluid infiltration and amphibolitization of the preexisting mafic bands would have preferentially localized deformation in the former dikes during the first stages of the Eocene subduction. Fig. 4c and Fig. 5c exemplify mafic veins with peridotite boudins. Deformation localization is here closely tied with fluid infiltration, consistently with the weaker rheology of amphibole and plagioclase compared to pyroxene (Homburg et al., 2010) and olivine.

Three main hydration stages can be seen in these rocks and related to deformation events, as schematized in Fig. 13:

– (a) amphibolitization stage:

Replacement of orthopyroxene by late amphibole is the second event of hydrous fluid intrusion and the major deformation stage

(Fig. 13b). Whereas magnesio-hornblende in undeformed leucocratic veins has an euhedral shape and are associated to a groundmass of large plagioclase crystals (Fig. 6f), magnesio-hornblende within the shear bands makes up the foliation, together with plagioclase (Fig. 6e), and presents syn-kinematic texture (e.g. pressure shadow around orthopyroxene; Fig. 6e). Euhedral late amphibole could be of magmatic origin, but syn-kinematically deformed late amphibole has likely crystallized from an aqueous fluid. Nonetheless, evolving late amphibole (and possibly plagioclase) compositions (Figs. 8c, 9b, c) indicate that mafic bands underwent progressive recrystallization during fluid infiltration and deformation (localized within the shear bands).

Although mafic bands are strongly boudinaged and folded, amphibole crystals themselves are only mildly deformed. This is consistent with plagioclase being weaker than amphibole (Getsinger and Hirth, 2014) and with some static recrystallization after the peak of deformation. Peridotites in contact with mafic dikes are also boudinaged during this stage and record hydration through the crystallization of amphibole with a Mg# around 0.92 (Fig. 9a).

Magnesio-hornblende (i.e. late amphibole) compositions yield pressure-temperature conditions 3–5 kbar and  $750 \pm 50$  °C

(Table 2). These estimations are similar to that calculated for leucodiorite dikes in the uppermost harzburgite (i.e.  $3.5 \pm 0.6$  kbar and  $800 \pm 45$  °C; Pirard, 2012). As for metamorphic sole, the pressure estimates for the dikes cannot be explained by the present ophiolite thickness.

Age constraints on amphibole reveal an age cluster at  $55 \pm 2$  Ma (Fig. 12), which is well defined for late amphibole. Although the closure temperature for the  $^{40}\text{Ar}/^{39}\text{Ar}$  method in hornblende is ~200 °C lower than our temperature estimates for amphibole formation, we interpret these ages as crystallization ages in a context of fast cooling. Considering available constraints on the latest oceanic magmatic events, pressure-temperature estimates and the age of the New Caledonia metamorphic sole (Cluzel et al., 2012 and this study), high temperature metamorphism and cooling below the closure temperature must have occurred in a very short lapse of time after the Eocene subduction initiation.

– (b) formation of the alkali-rich matrix:

The alkali-rich matrix is composed of an association of Ba-rich feldspar, phlogopite and ortho-amphibole crystallized at the expense of pyroxene, olivine and Ca-amphibole, from both the mafic and

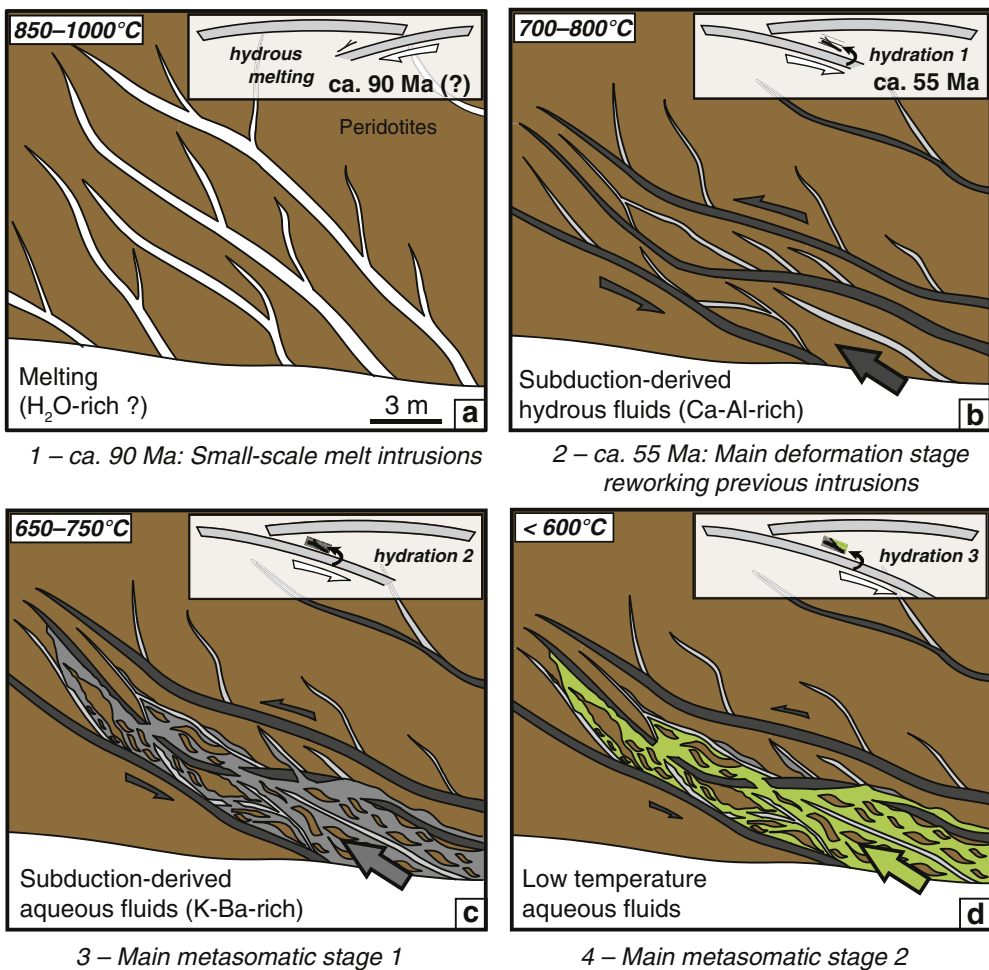


**Fig. 13.** Schematized crystallization and deformation events for the emplacement of the mafic dikes at the study area scale. The inset shows the corresponding simplified geodynamic evolution with successive stages of infiltration of subduction-related fluids. a) Small-scale melt intrusions, enriched in Ca and Al compared to the surrounding harzburgites. Fluids at the origin of these mafic veins (with orthopyroxene, olivine, plagioclase ± early amphibole) were probably gabbroic melts derived from hydrated melting of the peridotite, caused by slab dehydration. b) Amphibolitization stage is the main deformation stage reworking previous mafic intrusions mechanically weaker than the peridotite host. Sheared amphibolites indicate that these mafic intrusions were deformed shortly after emplacement, as suggested by amphibole ages at  $55 \pm 2$  Ma. c) The following emplacement of the phlogopite-rich matrix records the main metasomatic stage. Anthophyllite indicates temperature around 700 °C. The intensity of deformation decreased significantly compared to b). d) Talc–chlorite–serpentinite assemblage representing the last stage of metasomatism affecting the shear bands and likely starting around temperatures of 600 °C.

ultramafic protoliths, with less deformation than during the main amphibolitization stage (Fig. 13c). This matrix points to an episode of fluid ingress postdating amphibolitization, with a markedly distinct fluid composition (i.e. richer in K, Na and Ba). Ortho-amphibole (anthophyllite) indicates temperatures of  $\sim 700 \pm 50^\circ\text{C}$  (Chernosky and Autio, 1979; Nozaka, 2011).

— (c) Late reaction with serpentine, talc, chlorite:

Finally, veinlets composed of hydrous phases (serpentine, talc and chlorite) form mm to cm-scale rims around mafic and peridotite boudins or cross-cut the matrix (Fig. 13d). With temperatures lower than 500–600 °C, according to presence of the talc–chlorite assemblage, this stage reflects the latest and coldest episode of reequilibration of these shear bands.

### 9.3. Geodynamics implications

Both petrology and geochemistry (through the similarity to undeformed amphibole-bearing dikes reported in the Massif du Sud; Cluzel et al., 2006; Pirard, 2012) suggest that mafic shear bands correspond to former hm- to km-scale mafic intrusions emplaced in the highly refractory host harzburgite, deriving from the melting of a moderately depleted mantle source fluxed by subduction-derived fluids (see § 9.1).

Trace element geochemistry (i.e. HFSE depletion and LILE enrichment) and age constraints at ca. 55 Ma (Fig. 12) show that secondary amphibolitization coincides with the east-dipping subduction initiation preluding to obduction (Cluzel et al., 2001, 2012; Spandler et al., 2005). Fluid infiltration and at least part of the trace element enrichment could result from dehydration of the upper part of the slab (as for metamorphic sole dehydration; Ishikawa et al., 2005). In this interpretation, the shear bands reported here are a direct record of early subduction processes in New Caledonia, deformation and mantle metasomatism in an active subduction setting.

By contrast, the magmatic origin of the mafic protoliths remains uncertain. The high degree of amphibolitization affecting these mafic dikes hampers modeling the degree of partial melting of the peridotites and to constrain the exact origin of the mafic protoliths.

Age constraints on amphiboles at both ca. 90 Ma (early pargasite) and ca. 55 Ma (magnesio-hornblende) can be accounted for in two different ways:

- (1) amphibole-bearing troctolite to norite mafic intrusions would have formed at ca. 55 Ma as a result of the east-dipping subduction preluding to obduction, as for the relatively abundant dikes interpreted as supra-subduction and dated at ca. 55 Ma by Cluzel et al. (2006) or dikes found in the nearby Massif du Sud exposures (also interpreted as Eocene, based on structural data; Pirard, 2012), both interpreted as formed in a supra-subduction setting at the expense of a metasomatized, HFSE-depleted mantle. In this view, ages at ca. 90 Ma would be attributed to excess argon.
- (2) mafic intrusions would represent inherited mafic melts from the Cretaceous South Loyalty basin accretion (dating back to  $\geq 90$  Ma; e.g. Cluzel et al., 2012 and this study), as several early amphiboles yield an age of ca. 90 Ma (Fig. 12). This hypothesis is supported by the similarity with ages found in amphibole-bearing dikes in the Massif du Sud by Prinzhofer (1981). Hydrous mafic melt intrusions would have been emplaced possibly as a result of the west-dipping Pacific subduction, and later been fluxed by fluids leading to late amphibole crystallization and ages at ca. 55 Ma (during the second, east-dipping subduction initiation). This secondary high temperature event has only partially reset the ca. 90 Ma age in pargasite.

The second interpretation is favored by the lack of evidence for excess argon, early amphibole (pargasite) compositions that are distinct

from those of Pirard (2012), and the peculiar deformation of these dikes (those of Pirard and Cluzel are not or only mildly deformed).

Deformation and fluid infiltration later localized on these preexisting mafic intrusions. Shear bands developed as a result of a threefold stage of fluid infiltration from slab-derived fluids. These mafic bands (and the later metasomatic matrix) are good witnesses of the subduction initiation processes, both in terms of fluid influx and progressive deformation near the base of the obducted New Caledonia ophiolite, from temperatures of 800–700 °C down to less than 600 °C. Localization of deformation along inherited structures such as mafic dike swarms also supports the view that subduction initiation is generally triggered near a preexisting weakness zone (i.e. Agard et al., 2014).

## 10. Conclusions

This study focuses on strongly sheared mafic amphibolites within the uppermost mantle of the New Caledonia obducted ophiolite, near the transition zone and  $\sim 50$ –100 m above the basal thrust contact. Using a combination of petrological, geochemical, and geochronological data, we show that these amphibolites record melting and polyphase metasomatism within the mantle wedge during the early history of the subduction.

Shear bands indicate that deformation and high temperature fluid infiltration (from  $\sim 800$  to  $\sim 500^\circ\text{C}$ ) localized along preexisting hm-scale mafic intrusions emplaced within the upper mantle of the New Caledonia ophiolite and derived from peridotites refertilized by slab-derived fluids in a supra-subduction zone environment. The timing of these melt intrusions remains uncertain. Age constraints on early amphibole at ca. 90 Ma and the lack of evidence for argon excess suggest that they could be inherited from the former west-dipping Pacific subduction.

Secondary deformation and amphibolitization of these mafic dikes were the result of a threefold infiltration of slab-derived fluids. The age cluster of amphibole at ca. 55 Ma indicates that amphibolitization of the mafic protoliths (as well as later alkali-metasomatism) relate to the onset of the Eocene east-dipping subduction initiation preluding to the obduction of the New Caledonia ophiolite.

These outcrops bring important information on the processes and timing of fluid influx, progressive deformation and peridotites refertilization during subduction initiation, showing how m- to hm-scale heterogeneities (inherited or early-emplaced magmatic dikes) localize deformation and metasomatism in the oceanic lithosphere. In turn this suggests that similar small-scale heterogeneities may have controlled the development of larger thrusts, ultimately leading to the tectonic slicing (and later emplacement) of the New Caledonia ophiolite.

Supplementary data to this article can be found online at <http://dx.doi.org/10.1016/j.lithos.2015.11.022>.

## Acknowledgments

We thank M. Cannat (IPGP, France) and M. Ulrich (IPGS, France) for interesting discussions. We also thank B. Caron and O. Boudouma (ISTeP-UPMC, France), M. Fialin and N. Rividi (CAMPARIS), F. Le Cornec (IRD Bondy, France) and D. Deldicque (ENS Paris, France) for analytical support, M. Moroni (ISTeP-UPMC) for the scanning of thin-sections. C. Pirard and J. Hermann are warmly thanked for their constructive reviews and suggestions, and Marco Scambelluri for his editorial handling. This work was essentially funded through the ONLAP project (ANR blanche, SIMI6; 2010 BLAN 615 01). Additional support was provided by an IUF grant (Institut universitaire de France) to Philippe Agard.

## References

- Agard, P., Jolivet, L., Vrielynck, B., Burov, E., Monié, P., 2007. Plate acceleration: the obduction trigger? *Earth and Planetary Science Letters* 258 (3–4), 428–441. <http://dx.doi.org/10.1016/j.epsl.2007.04.002>.

- Agard, P., Zuo, X., Funiciello, F., Bellahsen, N., Faccenna, C., Savva, D., 2014. Obduction: why, how and where. Clues from analog models. *Earth and Planetary Science Letters* 393, 132–145. <http://dx.doi.org/10.1016/j.epsl.2014.02.021>.
- Aitchison, J.C., Clarke, G.L., Meffre, S., Cluzel, D., 1995. Eocene arc-continent collision in New Caledonia and implications for regional southwest Pacific tectonic evolution. *Geology* 23 (2), 161–164. <http://dx.doi.org/10.1130/0091-7613>.
- Anderson, J.L., Smith, D.R., 1995. The effects of temperature and  $f_{O_2}$  on the Al-in-hornblende barometer. *American Mineralogist* 80, 549–559.
- Boudier, F., Ceuleneer, G., Nicolas, A., 1988. Shear zones, thrusts and related magmatism in the Oman ophiolite: initiation of thrusting on an oceanic ridge. *Tectonophysics* 151 (1–4), 275–296. [http://dx.doi.org/10.1016/0040-1951\(88\)90249-1](http://dx.doi.org/10.1016/0040-1951(88)90249-1).
- Carson, C., Clarke, G., Powell, R., 2000. Hydration of eclogite, Pam Peninsula, New Caledonia. *Journal of Metamorphic Geology* 18, 79–90. <http://dx.doi.org/10.1046/j.1525-1314.2000.00245.x>.
- Ceuleneer, G., Nicolas, A., Boudier, F., 1988. Mantle flow patterns at an oceanic spreading The Oman peridotites record. *Tectonophysics* 151, 1–26. [http://dx.doi.org/10.1016/0040-1951\(88\)90238-7](http://dx.doi.org/10.1016/0040-1951(88)90238-7).
- Chernosky, J.V., Autio, L.K., 1979. The stability of anthophyllite in the presence of quartz. *American Mineralogist* 64, 294–303.
- Clarke, G.L., Aitchison, J.C., Cluzel, D., 2006. Eclogites and blueschists of the Pam Peninsula, NE New Caledonia: a reappraisal. *Journal of Petrology* 38 (7), 843–876. <http://dx.doi.org/10.1093/petroj/38.7.843>.
- Cluzel, D., Picard, C., Aitchison, J.C., Laporte, C., Meffre, S., Parat, F., 1997. The Poya Nappe, ex-“Formation des Basaltes” (New Caledonia, southwest Pacific): a Campanian to Upper Palaeocene oceanic plateau obducted in the late Eocene. *Comptes Rendus de l'Académie des Sciences* 324, 443–451.
- Cluzel, D., Aitchison, J.C., Picard, C., 2001. Tectonic accretion and underplating of mafic terranes in the Late Eocene intraoceanic fore-arc of New Caledonia (Southwest Pacific): geodynamic implications. *Tectonophysics* 340 (1–2), 23–59. [http://dx.doi.org/10.1016/S0040-1951\(01\)00148-2](http://dx.doi.org/10.1016/S0040-1951(01)00148-2).
- Cluzel, D., Bosch, D., Paquette, J.L., Lemennicier, Y., Montjoie, P., Ménot, R.P., 2005. Late Oligocene post-obduction granitoids of New Caledonia: a case for reactivated subduction and slab break-off. *Island Arc* 14 (3), 254–271. <http://dx.doi.org/10.1111/j.1440-1738.2005.00470.x>.
- Cluzel, D., Meffre, S., Maurizot, P., Crawford, A.J., 2006. Earliest Eocene (53 Ma) convergence in the Southwest Pacific: evidence from pre-obduction dikes in the ophiolite of New Caledonia. *Terra Nova* 18 (6), 395–402. <http://dx.doi.org/10.1111/j.1365-3121.2006.00704.x>.
- Cluzel, D., Jourdan, F., Meffre, S., Maurizot, P., Lesimple, S., 2012. The metamorphic sole of New Caledonia ophiolite: 40Ar/39Ar, U-Pb, and geochemical evidence for subduction inception at a spreading ridge. *Tectonics* 31 (3), TC3016. <http://dx.doi.org/10.1029/2011TC003085>.
- Coleman, R.G., 1971. Tectonic erplacement upper mantle peridotites along continental edges. *Journal of Geophysical Research* 76 (5), 1212–1222. <http://dx.doi.org/10.1029/JB076i005p01212>.
- Collot, J.Y., Malahoff, A., Recy, J., Latham, G., Missegue, F., 1987. Overthrust emplacement of New Caledonia Ophiolite: Geophysical evidence. *Tectonics* 6 (3), 215–232. <http://dx.doi.org/10.1029/TC006i003p00215>.
- Coltorti, M., Bonadiman, C., Faccini, B., Grégoire, M., O'Reilly, S.Y., Powell, W., 2007. Amphiboles from suprasubduction and intraplate lithospheric mantle. *Lithos* 99 (1–2), 68–84. <http://dx.doi.org/10.1016/j.lithos.2007.05.009>.
- Constantin, M., 1999. Gabbroic intrusions and magmatic metasomatism in harzburgites from the Garrett transform fault: implications for the nature of the mantle–crust transition at fast-spreading ridges. *Contributions to Mineralogy and Petrology* 136 (1–2), 111–130. <http://dx.doi.org/10.1007/s004100050527>.
- Dewey, J.F., Bird, J.M., 1971. Origin and emplacement of the ophiolite suite: appalachian ophiolites in Newfoundland. *Journal of Geophysical Research* 76 (14). <http://dx.doi.org/10.1029/JB076i014p03179>.
- Eissen, J., Crawford, A., Cotten, J., Meffre, S., 1998. Geochemistry and tectonic significance of basalts in the Poya Terrane, New Caledonia. *Tectonophysics* 284, 203–219. [http://dx.doi.org/10.1016/S0040-1951\(97\)00183-2](http://dx.doi.org/10.1016/S0040-1951(97)00183-2).
- Ernewein, M., Pflumio, C., Whitechurch, H., 1988. The death of an accretion zone as evidenced the magmatic history of the Sumail ophiolite (Oman). *Tectonophysics* 151, 247–274. [http://dx.doi.org/10.1016/0040-1951\(88\)90248-X](http://dx.doi.org/10.1016/0040-1951(88)90248-X).
- Gaggero, L., Corteseño, L., 1997. Metamorphic evolution of oceanic gabbros: recrystallization from subsolidus to hydrothermal conditions in the MARK area (ODP Leg 153). *Lithos* 40 (2–4), 105–131. [http://dx.doi.org/10.1016/S0024-4937\(97\)00006-6](http://dx.doi.org/10.1016/S0024-4937(97)00006-6).
- Getsinger, a.J., Hirth, G., 2014. Amphibole fabric formation during diffusion creep and the rheology of shear zones. *Geology* 42 (6), 535–538. <http://dx.doi.org/10.1130/G35327.1>.
- Godard, M., Jousselin, D., Bodinier, J.L., 2000. Relationships between geochemistry and structure beneath a palaeo-spreading centre: a study of the mantle section in the Oman ophiolite. *Earth and Planetary Science Letters* 180 (1–2), 133–148. [http://dx.doi.org/10.1016/S0012-821X\(00\)00149-7](http://dx.doi.org/10.1016/S0012-821X(00)00149-7).
- Godard, M., Dautria, J.-M., Perrin, M., 2003. Geochemical variability of the Oman ophiolite lavas: relationship with spatial distribution and paleomagnetic directions. *Geochemistry, Geophysics, Geosystems* 4 (6). <http://dx.doi.org/10.1029/2002GC000452>.
- Harrison, T.M., 1980. Diffusion in  $^{40}\text{Ar}$  in Hornblende. *Contributions to Mineralogy and Petrology* 78 (3), 324–331. <http://dx.doi.org/10.1007/BF00398927>.
- Holland, T., Blundy, J., 1994. Non-ideal interactions in calcic amphiboles and their bearing on amphibole-plagioclase thermometry. *Contributions to Mineralogy and Petrology* 116 (4), 433–447. <http://dx.doi.org/10.1007/BF00310910>.
- Homburg, J.M., Hirth, G., Klemenc, P.B., 2010. Investigation of the strength contrast at the Moho: a case study from the Oman Ophiolite. *Geology* 38 (8), 679–682. <http://dx.doi.org/10.1130/G30880.1>.
- Ishikawa, T., Fujisawa, S., Nagaishi, K., Masuda, T., 2005. Trace element characteristics of the fluid liberated from amphibolite-facies slab: inference from the metamorphic sole beneath the Oman ophiolite and implication for boninite genesis. *Earth and Planetary Science Letters* 240 (2), 355–377. <http://dx.doi.org/10.1016/j.epsl.2005.09.049>.
- Jourdan, F., Renne, P.R., 2007. Age calibration of the Fish Canyon sanidine  $^{40}\text{Ar}/^{39}\text{Ar}$  dating standard using primary K-Ar standards. *Geochimica et Cosmochimica Acta* 71 (2), 387–402. <http://dx.doi.org/10.1016/j.gca.2006.09.002>.
- Lagabrielle, Y., Chauvet, A., Ulrich, M., Guillot, S., 2013. Passive obduction and gravity-driven emplacement of large ophiolitic sheets: the New Caledonia ophiolite (SW Pacific) as a case study? *Bulletin de la Société Géologique de France* 184 (6), 545–556. <http://dx.doi.org/10.2113/gsgfbull.184.6.545>.
- Le Mé, L., Girardeau, J., Monnier, C., 2004. Mantle segmentation along the Oman ophiolite fossil mid-ocean ridge. *Nature* 432 (7014), 167–172. <http://dx.doi.org/10.1038/nature03075>.
- Leake, B.E., Woolley, A.R., Arps, C.E.S., Gilbert, M.C., Grice, J.D., Hawthorne, F.C., Whittaker, E.J.W., 1997. *Nomenclature of amphiboles*. *The Canadian Mineralogist* 35, 219–246.
- Marchesi, C., Garrido, C.J., Godard, M., Belley, F., Ferré, E., 2009. Migration and accumulation of ultra-depleted subduction-related melts in the Massif du Sud ophiolite (New Caledonia). *Chemical Geology* 266 (3–4), 171–186. <http://dx.doi.org/10.1016/j.chemgeo.2009.06.004>.
- Matthews, K.J., Williams, S.E., Whittaker, J.M., Müller, R.D., Seton, M., Clarke, G.L., 2015. Geologic and kinematic constraints on Late Cretaceous to mid Eocene plate boundaries in the southwest Pacific. *Earth-Science Reviews* 140, 72–107. <http://dx.doi.org/10.1016/j.earscirev.2014.10.008>.
- McLeod, C.J., Lissenbourg, J., Bibby, L.E., 2013. “Moist MORB” axial magmatism in the Oman ophiolite: the Evidence against a mid-ocean ridge origin. *Geology* 41 (4), 459–462. <http://dx.doi.org/10.1130/G33904.1>.
- Moore, E.M., Kellogg, L.H., Dilek, Y., 2000. Tethyan ophiolites, mantle convection, and tectonic “historical contingency”: a resolution of the “ophiolite conundrum”. *Geological Society of America Special Paper* 349.
- Moutte, J., 1979. Le massif de Tiébaghi, Nouvelle Calédonie et ses gîtes de chromite. *Ecole Nationale Supérieure des Mines de Paris*, p. 160.
- Nicolas, A., 1989. In: Masson (Ed.), *Principes de Tectonique*, p. 190.
- Nicolas, A., Boudier, F., Ildefonse, B., Ball, E., 2000. Accretion of Oman and United Arab Emirates ophiolite – discussion of a new structural map. *Marine Geophysical Research* 21, 147–179. <http://dx.doi.org/10.1023/A:1026769727917>.
- Nozaka, T., 2011. Constraints on anthophyllite formation in thermally metamorphosed peridotites from southwestern Japan. *Journal of Metamorphic Geology* 29 (4), 385–398. <http://dx.doi.org/10.1111/j.1525-1314.2010.00921.x>.
- Omran, J., Agard, P., Whitechurch, H., Benoit, M., Prouteau, G., Jolivet, L., 2008. Arc-magmatism and subduction history beneath the Zagros Mountains, Iran: a new report of adakites and geodynamic consequences. *Lithos* 106 (3–4), 380–398. <http://dx.doi.org/10.1016/j.lithos.2008.09.008>.
- Paris, J.P., Andreieff, P., Coudray, J., 1979. Sur l'âge Eocène supérieur de la mise en place de la nappe ophiolitique de Nouvelle-Calédonie. *Comptes Rendus de l'Académie des Sciences Paris* 288, 1659–1661.
- Pearce, J.A., Lippard, S.J., Roberts, S., 1984. Characteristics and tectonic significance of supra-subduction zone ophiolites. *Geological Society, London, Special Publications* 16 (1), 77–94. <http://dx.doi.org/10.1144/GSLSP.1984.016.01.06>.
- Pearce, N.J.G., Perkins, W.T., Westgate, J.A., Jackson, S.E., Neal, C.R., Chereny, S.P., Gorton, M.P., 1997. A compilation of new and published major and trace element data for NIST SRM 610 and NIST SRM 612 glass reference materials. *The Journal of Geostandards and Geoanalysis* 21 (1), 115–144. <http://dx.doi.org/10.1111/j.1751-908X.1997.tb00538.x>.
- Pirard, C., 2012. Transfer of Melts in the Sub-arc Mantle: Insights from High-pressure Experiments and from the New Caledonia Ophiolite. *College of Physical and Mathematical Sciences*.
- Pirard, C., Hermann, J., O'Neill, H.S.C., 2013. Petrology and Geochemistry of the Crust–Mantle Boundary in a Nascent Arc, Massif du Sud Ophiolite, New Caledonia, SW Pacific. *Journal of Petrology* 54 (9), 1759–1792. <http://dx.doi.org/10.1093/petrology/egt030>.
- Prinzhofer, A., 1981. *Structure et pétrologie d'un cortège ophiolitique: le Massif du Sud (Nouvelle Calédonie): la transition manteau-croûte en milieu océanique*. *École Nationale Supérieure des Mines de Paris*, p. 185.
- Prinzhofer, A., Allègre, C.J., 1985. Residual peridotites and the mechanisms of partial melting. *Earth and Planetary Science Letters* 74, 251–265.
- Prinzhofer, A., Nicolas, A., Cassard, D., Moutte, J., Leblanc, M., Paris, J.-P., Rabinovitch, M., 1980. Structures in the new calédonia peridotites-gabbros: implications for oceanic mantle and crust. *Tectonophysics* 69, 85–112.
- Salaün, A., Villemant, B., Semet, M.P., Staudacher, T., 2010. Cannibalism of olivine-rich cumulate xenoliths during the 1998 eruption of Piton de la Fournaise (La Réunion hotspot): Implications for the generation of magma diversity. *Journal of Volcanology and Geothermal Research* 198, 187–204. <http://dx.doi.org/10.1016/j.jvolgeores.2010.08.022>.
- Schellart, W.P., Lister, G.S., Toy, V.G., 2006. A Late Cretaceous and Cenozoic Reconstruction of the Southwest Pacific Region: Tectonics Controlled by Subduction and Slab Roll-back Processes. *Earth-Science Reviews* 76 (3–4), 191–233. <http://dx.doi.org/10.1016/j.earscirev.2006.01.002>.
- Shervais, J.W., 2001. Birth, death, and resurrection: the life cycle of suprasubduction zone ophiolites. *Geochemistry, Geophysics, Geosystems* 2. <http://dx.doi.org/10.1029/2000GC000080>.
- Spandler, C., Rubatto, D., Hermann, J., 2005. Late Cretaceous–Tertiary tectonics of the southwest Pacific: insights from U–Pb sensitive, high-resolution ion microprobe (SHRIMP) dating of eclogite facies rocks from New Caledonia. *Tectonics* 24 (3). <http://dx.doi.org/10.1029/2004TC001709>.
- Stern, R., Bloomer, S.H., 1992. Subduction zone infancy: examples from the Eocene Izu-Bonin–Mariniana and Jurassic California arcs. *Bulletin of the Geological Society of America* 104 (12), 1621–1636. <http://dx.doi.org/10.1130/0016-7606>.

- Sun, S.S., McDonough, W.F., 1989. Chemical and isotopic systematics of oceanic basalts: implications for mantle composition and processes. Geological Society, London, Special Publications 42 (1), 313–345. <http://dx.doi.org/10.1144/GSL.SP.1989.042.01.19>.
- Ulrich, M., Picard, C., Guillot, S., Chauvel, C., Cluzel, D., Meffre, S., 2010. Multiple melting stages and refertilization as indicators for ridge to subduction formation: the New Caledonia ophiolite. *Lithos* 115 (1–4), 223–236. <http://dx.doi.org/10.1016/j.lithos.2009.12.011>.
- Van De Beucke, S., Auzende, J., Lafoy, Y., Bernardel, G., Nercessian, A., Reginier, M., Exon, N., 1998. Transect sismique continu entre l'arc des Nouvelles-Hebrides de l'Australie: programme FAJST (French Australian Seismic Transect) Continuous seismic transect between the New Hebrides Arc and the Eastern. *Earth and Planetary Sciences* 327, 761–768. [http://dx.doi.org/10.1016/S1251-8050\(99\)80048-2](http://dx.doi.org/10.1016/S1251-8050(99)80048-2).
- Vaughan, A.P.M., Scarrow, J.H., 2003. Ophiolite obduction pulses as a proxy indicator of superplume events? *Earth and Planetary Science Letters* 213 (3–4), 407–416. [http://dx.doi.org/10.1016/S0012-821X\(03\)00330-3](http://dx.doi.org/10.1016/S0012-821X(03)00330-3).
- Vitale Brovarone, A., Agard, P., 2013. True metamorphic isograds or tectonically sliced metamorphic sequence? New high-spatial resolution petrological data for the New Caledonia case study. *Contributions to Mineralogy and Petrology* 166 (2), 451–469. <http://dx.doi.org/10.1007/s00410-013-0885-2>.
- Wakabayashi, J., Dilek, Y., 2003. What constitutes “emplacement” of an ophiolite?: Mechanisms and relationship to subduction initiation and formation of metamorphic soles. Geological Society, London, Special Publications 218 (1), 427–447. <http://dx.doi.org/10.1144/GSL.SP.2003.218.01.22>.
- Weissel, J.K., Hayes, D.E., 1977. Evolution of the Tasman Sea reappraised. *Earth and Planetary Science Letters* 36, 77–84. [http://dx.doi.org/10.1016/0012-821X\(77\)90189-3](http://dx.doi.org/10.1016/0012-821X(77)90189-3).
- Whitney, D.L., Evans, B.W., 2010. Abbreviations for names of rock-forming minerals. *American Mineralogist* 95, 185–197.
- Xiong, Q., Zheng, J.P., Griffin, W.L., O'Reilly, S.Y., Pearson, N.J., 2014. Pyroxenite dykes in orogenic peridotite from North Qaidam (NE Tibet, China) track metasomatism and segregation in the mantle wedge. *Journal of Petrology* 55 (12), 2347–2376. <http://dx.doi.org/10.1093/petrology/egu059>.
- Zack, T., John, T., 2007. An evaluation of reactive fluid flow and trace element mobility in subducting slabs. *Chemical Geology* 239 (3–4), 199–216. <http://dx.doi.org/10.1016/j.chemgeo.2006.10.020>.